UNIVERSIDADE ESTADUAL DE CAMPINAS

INSTITUTO DE FÍSICA ‘GLEB WATAGHIN’

Leonardo Marcon Corrêa

Estudo das Propriedades Estruturais de Nanossistemas por Difração Elétrons com Precessão (PED)

Study of the Structural Properties of Nanosystems by Precession Electron Diffraction (PED)

Campinas

2024

Leonardo Marcon Corrêa

Estudo das Propriedades Estruturais de Nanossistemas por Difração Elétrons com Precessão (PED)

Study of the Structural Properties of Nanosystems by Precession Electron Diffraction (PED)

Tese apresentada ao Instituto de Física Gleb Wataghin da Universidade Estadual de Campinas como parte dos requisitos exigidos para a obtenção do título de Doutor em Ciências, na área de Física Aplicada.

Orientador: Daniel Mario Ugarte

ESTE TRABALHO CORRESPONDENTE À VERSÃO FINAL DA TESE DEFENDIDA PELO ALUNO LEONARDO MARCON CORRÊA, E ORIENTADO PELO PROF. DR. DANIEL MARIO UGARTE

Campinas

2024

Ficha catalográfica
Universidade Estadual de Campinas (UNICAMP)
Biblioteca do Instituto de Física Gleb Wataghin
Lucimeire de Oliveira Silva da Rocha - CRB 8-9174

C817e

Corrêa, Leonardo Marcon, 1995-
Estudo das propriedades estruturais de nanossistemas por difração elétrons com precessão (PED) / Leonardo Marcon Corrêa. – Campinas, SP : [s.n.], 2024.

Orientador(es): Daniel Mario Ugarte.
Tese (doutorado) – Universidade Estadual de Campinas (UNICAMP), Instituto de Física Gleb Wataghin.

1. Microscopia eletrônica de transmissão. 2. Elétrons - Difração. 3. Nanomateriais. 4. Cristalografia. 5. Nanociência. I. Ugarte, Daniel Mario, 1963-. II. Universidade Estadual de Campinas (UNICAMP). Instituto de Física Gleb Wataghin. III. Título.

Informações complementares

Título em outro idioma: Study of the structural properties of nanosystems by precession electron diffraction (PED)
Palavras-chave em inglês:
Transmission electron microscopy
Electrons - Diffraction
Nanomaterials
Crystallography
Nanoscience
Área de concentração: Física Aplicada
Titulação: Doutor em Ciências
Banca examinadora:
Daniel Mario Ugarte [Orientador]
Diego Muraca
Daniela Zanchet
Jefferson Bettini
Fábio Furlan Ferreira
Data de defesa: 11-10-2024
Programa de Pós-Graduação: Física

Identificação e informações acadêmicas do(a) aluno(a)
- ORCID do autor: https://orcid.org/0000-0002-0823-4085
- Currículo Lattes do autor: http://lattes.cnpq.br/8703335107651128

MEMBROS DA COMISSÃO EXAMINADORA DA TESE DE DOUTORADO DO ALUNO LEONARDO MARCON CORRÊA – RA 211796 APRESENTADA E APROVADA AO INSTITUTO DE FÍSICA GLEB WATAGHIN, DA UNIVERSIDADE ESTADUAL DE CAMPINAS, EM 11/10/2024.

COMISSÃO JULGADORA:

- Prof. Dr. Daniel Mario Ugarte (IFGW/ UNICAMP) - Presidente e Orientador

- Prof. Dr. Diego Muraca (IFGW/ UNICAMP)

- Profa. Dra. Daniela Zanchet (IQ/ UNICAMP)

- Prof. Dr. Jefferson Bettini (Central Nacional de Pesquisa em Energia e Materiais)

- Prof. Dr. Fabio Furlan Ferreira (Universidade Federal do ABC – Campus Santo André)

OBS.: Ata da defesa com as respectivas assinaturas dos membros encontra-se no SIGA/Sistema de Fluxo de Dissertação/Tese e na Secretaria do Programa da Unidade.

Campinas

2024

Agradecimentos

Gostaria de agradecer aos meus pais (Gilberto e Marcia) e aos meus irmãos (Andréia, Fabiano, Eduardo e Mariana) por me darem a oportunidade e o suporte para seguir as minhas escolhas. Sem eles nada seria possível.

A minha gratidão ao Prof. Daniel Mario Ugarte pela oportunidade de participar desse trabalho, pela orientação, suporte, confiança e compreensão. Seus ensinamentos e comportamentos mostram a ética de trabalho que deve guiar um bom cientista que vise evitar transformar a busca por conhecimento em somente mais uma linha de produção.

Agradeço aos diversos colaboradores que possibilitaram os trabalhos do doutorado: Prof. Varlei Rodrigues, Prof. Mônica Cotta, Profa. Laura Fabris, Profa. Caterina Ducati, Prof. Arturo Ponce, Dr. Eduardo Ortega, Dr. Simon Fairclough e Msc. Diego Davi Coimbrão. Também agradeço todos os laboratórios que utilizamos durante esse trabalho.

Agradeço aos membros do Grupo de Física de Nanoestruturas e Materiais Nanoestruturados (Riul, Gabriel, Rafael, Malu, Leon, Vlad, Marcos, Maria, Tatiana, Shirley, Luísa, Henrique e Eduardo).

Por fim, um salve para meus amigos de Curitiba que me acompanharam (Alan e Leonardo e Vinícius), e a aqueles que ficaram (Cenedese, Felipe, Leonardo, Bruno, Leozão, Maruan e Luís), assim como os que conheci durante esse anos em Campinas (Murilo, Levi, Gabriel, Leon, Shirley).

O presente trabalho foi realizado com apoio do Conselho Nacional de Desenvolvimento Científico e Tecnológico (CNPq), bolsa processo nº 140596/2020-8, e da Fundação de Desenvolvimento da Unicamp (FUNCAMP), protocolo nº 54755-24. O presente trabalho foi realizado com apoio da Coordenação de Aperfeiçoamento de Pessoal de Nível Superior – Brasil (CAPES) - Código de Financiamento 001.

Resumo

O desenvolvimento de métodos para caracterização estrutural especialmente adaptado a nanomaterias é fundamental para novas tecnologias. Usualmente, fatores instrumentais impõem limitações na capacidade de obter informação na escala nano, no entanto, existem limitações intrínsecas associadas ao baixo sinal devido a pequeno volume desses materiais. Técnicas de cristalografia por difração (comumente por raios X), não são adequadas para caracterizar nanocristais, já que essas dependem da existência da ordem de longo alcance presente somente em cristais macroscópicos. Alternativamente, a difração de elétrons (ED: *electron diffraction*) é uma alternativa para realizar cristalografia de nanocristais, principalmente pela capacidade de medir massas muito menores que a possível com raios X. Mais especificamente, a difração de elétrons com precessão (PED: *precession electron diffraction*) permite a possibilidade de análise quantitativa da intensidades do feixes difratados devido possuir menos influências de espalhamento múltiplo, que limitam significativamente a análise quantitativa de intensidade em EDs. Devemos enfatizar que existem muitos desafios instrumentais e básicos nos estudos de nanocristalografia, e ainda é necessário explorar as capacidades de PED de fornecer novas respostas.

Nesse trabalho, vamos utilizar o uso quantitativo de intensidades de PED para aprimorar a caracterização de nanomateriais complexos. Exploraremos aqui 3 fundamentos importantes para técnicas de cristalografias de elétrons: i) adaptar metodologias estabelecidas em difração de raios X para poderem se utilizadas em ED; ii) aproveitar análise quantitativa de intensidade de PED para melhorar técnicas de microscopia eletrônica de transmissão (TEM: *transmission electron micrsocopy*); iii) aplicar novos métodos de difração de elétrons para resolver aspectos estruturais de nanoestruturas, onde técnicas comuns não sejam viáveis. Em mais detalhes:

1) Determinação da célula unitária de nanopartículas (NPs) decaédricas (Dh: *decahedral*) de AuAg, por meio de refinamento estrutural pela função de distribuição de pares (PDF: *pair distribution function*) derivada de PED. 2) Desenvolvimento de mapeamento de orientação de cristais automatizada (ACOM: *automated crystal orientation mapping*) analisando as intensidades de PED em experimentos visando um aumento da resolução angular possível nesses experimentos. 3) Caracterização de forma e estrutura cristalina de nanoestrelas (NS) de

AuAg a partir de um único mapeamento de difração PED (4D-STEM: *four dimensional scanning* TEM).

Nossos resultados indicam que o uso de PED + PDF (geralmente associada a raios X) fornece informação estrutural de alta precisão utilizando baixa dose de irradiação de elétrons e com uma quantidade de amostra várias ordens de magnitude melhor que o requerido para experimentos similares em fonte de radiação sincrotron. O método desenvolvido de ACOM forneceu uma grande melhoria da resolução angular (~0,03º) que a abordagem comum aplicada na atualidade (limitada a ~1º). A análise do mapeamento 4D-STEM da NS nos permitiu determinar a estrutura atômica e a morfologia tridimensional da NS. Determinamos que o centro e constituído de nanopartícula icosaédrica e as pernas são nanofios decaédricos, que crescem numa configuração planar no espaço sobre os vértices do núcleo icosaedro. O conjunto de resultados abre várias novas linha promissoras para a caraterização de nanoestruturas com alta qualidade.

Abstract

The development of methods for structural characterization especially adapted to nanomaterials is fundamental for new technologies. Usually, instrumental factors impose limitations on the ability to obtain nanoscale information, in addition, there are intrinsic limitations associated with low signal due to the small volume of these materials. Diffraction crystallography techniques (commonly based on X-rays) are not suitable for characterizing nanocrystals, since they depend on the existence of the long-range order present only in macroscopic crystals. Alternatively, electron diffraction (ED) is an alternative to perform nanocrystallography, mainly due to the ability to measure masses much smaller than possible with X-rays. More specifically, precession electron diffraction (PED) allows the possibility of quantitative analysis of diffracted beam intensities due to reduction of multiple scattering effects, which significantly limit quantitative intensity analysis in EDs. We must emphasize that there are many challenges in the instrumental and basic aspects of nanocrystallography studies, and it is still necessary to explore the capabilities of PED to provide new answers.

In this work, we will exploit the quantitative use of PED intensities to improve the characterization of complex nanomaterials. Here, we will explore 3 important fundamental issues for electron crystallography techniques: i) adapt established methodologies in X-ray diffraction to be used in ED; ii) use quantitative analysis of PED intensity to improve transmission electron microscopy (TEM) techniques; iii) apply new electron diffraction methods to solve structural aspects of nanostructures, where common techniques are not feasible. In more detail:

1) Determination of the decahedral nanoparticle (Dh: decahedral) unit cell of AuAg, from the structural refinement by the pair distribution function (PDF) derived from PED. 2) Development of automated crystal orientation mapping (ACOM) analyzing the PED intensities in experiments aiming to increase the angular resolution. 3) Characterization of the shape and crystal structure of AuAg nanostars (NS) from a single diffraction mapping PED (4D-STEM: four-dimensional scanning TEM).

Our results indicate that the use of PED + PDF (usually associated with X-rays) provides high-precision structural information using low-dose electron irradiation with a sample quantity several orders of magnitude lower than that required in synchrotron radiation studies. The

developed ACOM method provided a greater improvement in angular resolution (~0.03º) when compared with current common approach (limited to ~1º). The single 4D-STEM mapping allowed us to determine NS's atomic structure and three-dimensional morphology. We have determined that the center is an icosahedral nanoparticle and that the legs are decahedral nanowires, which grow in a planar configuration 3D over the vertices of the icosahedral nucleus. This set of results opens several promising new lines of work for the characterization of nanostructures with high quality.

Sumário

Capítulo 1

Introdução

Recentemente, o desenvolvimento de nanomateriais tem se direcionado a estruturas de maior complexidade morfológica e estrutural devido a possibilidade de utilizar processos de síntese com alto controle ou em diversos passos [1]. Essas estruturas possuem propriedades físicas (opticas, térmicas, elétricas, magnéticas, *etc*) ideais para aplicação em dispositivos de alta eficiência ou qualidade.

A maior complexidade estrutural trouxe a necessidade de métodos de caracterização mais avançados que possam atender certas demandas práticas, por exemplo, capacidade de medir baixas quantidades de massa, informação média de um volume da amostra e alta resolução espacial para medir variações estruturais locais. Distintas técnicas de caracterização podem atender uma ou mais dessas demandas, tal que é comum na caracterização de materiais combinar diversas técnicas para obter informação estrutural mais completa. No entanto, a caracterização de nanoestruturas possui dificuldades experimentais intrínsecas além de aspectos práticos e que prejudicam a capacidade de obter informação estrutural de sistemas com dimensões limitadas.

Idealmente uma caracterização da estrutura forneceria a posição de todos os átomos num volume, tal que teríamos toda informação possível sobre o material: grau de cristalinidade (amorfo, mono ou policristalina), organização de domínios cristalinos, defeitos, forma, *etc*. Num material macroscópico é inviável obter individualmente a posição de todos os átomos devido a quantidade incontável deles no volume; no entanto, a posições média pode ser obtida pela simetria proveniente do ordenamento dos átomos em dimensões significativas (micrométricas). Isso é comumente realizado em técnicas de difração, por exemplo, em difração de raios X de monocristais (XRD: *x-ray diffraction*) ou de pó (XRPD: *x-ray powder diffraction*); os picos de difração possuem todas as informações referentes a simetrias do cristal e da organização dos átomos [2]. Nesse caso, XRPD é a técnica mais utilizada para caracterizar materiais macroscópicos, sendo acessível e facilmente encontrada em laboratórios.

Materiais nanométricos possuem organização atômica restrita a nanômetros, não sendo possível obter informação das posições atômicas através das simetrias. Por exemplo, XRPD de nanopartículas (NPs) apresentam picos de difração largos e sobrepostos, que se assemelham a

materiais amorfos, consequentemente, existe uma grande dificuldade em determinar a estrutura cristalina da NP com confiabilidade. A dificuldade em obter informação estrutural em nanomateriais é conhecido como o "problema da nanoestrutura" e foi extensivamente discutida por Billinge e Levin na referência [3]. Eles propõem que a solução pode ser obtida ao medir a maior quantidade de informação possível sobre a estrutura: químico por técnicas espectroscópicas e estrutural por técnicas de imagem e difração. Isso demanda o uso de diversas técnicas em instrumentações distintas que demandam logísticas complexas para obter informação reprodutível e representativa da amostra. Portanto, a viabilidade desse processo seria significativamente melhor caso fosse possível utilizar uma mesma instrumentação em todos os experimentos distintos.

A microscopia eletrônica de transmissão (TEM: *transmission electron microscopy*) é usualmente relacionada a capacidade de obter imagens com resolução atômica em modo de alta resolução (HRTEM: *high resolution* TEM) [4]. Diversos trabalhos mostram uma solução direta para o "problema da nanoestrutura" ao reconstruir a posição dos átomos em experimentos de tomografia com imagens de resolução atômica; por exemplo, NPs de Au (Ø ~ 6 nm), Pt (Ø ~ 7nm), AuAg (Ø ~ 4 nm), FePt (Ø ~ 8 nm) e até mesmo NPs de NiPdPt (Ø ~ 4 nm) com alto grau de amorfização [5,6]. No entanto, esses trabalhos possuem limitações em relação ao tamanho e forma do nanomaterial, e principalmente a possíveis danos de irradiação por elétrons, comuns ao obter imagens com resolução atômica [4]. Alternativamente, em um TEM existe a possibilidade de obter informação estrutural no espaço recíproco e química por técnicas de espectroscopia de raios X ou elétrons, que torna TEM um instrumento versátil o suficiente para resolver o problema da nanoestrutura, como proposto por Billinge e Levin [3,4]. Isso foi demonstrado para caracterização de uma NPs de PdNi (Ø ~ 5 nm), no entanto, a solução combina técnicas de imagem e espectroscopia em TEM com XRPD, que torna o procedimento significativamente mais complexo [7].

Técnicas de difração são um dos pilares para solucionar a estrutura de materiais, especialmente cristalinos, por permitir procedimentos de refinamento estrutural, exemplificado por procedimentos de Rietveld em XRPD. Como mencionado anteriormente, o uso de Rietveld em nanocristais é imprecisa devido à falta de ordenamento atômico de longo alcance, no entanto, o padrão de difração ainda contém informação sobre o ordenamento dos átomos em curto e médio que pode ser explorada. Nesse caso, a cristalografia de nanocristais é realizado com a função de distribuição de pares (PDF: *pair distribution function*) que descreve a distância entre átomos vizinhos no volume do material [8]. A PDF é obtida a partir de padrões de difração de pó e uma subsequente transformada de Fourier (TF), sendo uma descrição no espaço real do

ordenamento atômico do material. Mais importante, é possível realizar análises de refinamento estrutural no espaço real com PDF, por exemplo, para determinar o ordenamento de domínios de NPs policristalinas, a tamanho de nanocristais, defeitos em nanoestruturas e deformações localizadas na ordem de curto alcance [9].

A difração de elétrons (ED: electron diffraction) possui vantagens em relação a raios X e nêutrons para estudar nanocristais, especialmente relacionada a baixa massa necessária para obter um padrão de difração de alta qualidade, fundamental ao estudar nanocristais de difícil síntese/cristalização (ver Capítulo 2). No entanto, a análise quantitativa de ED é comumente inviabilizada pela presença de difração dinâmica dos elétrons (múltiplos eventos de espalhamento), em contraste com a difração cinética de raios X e nêutrons (somente um evento de espalhamento). Alternativamente, a difração de elétrons com precessão (PED: *precession electron diffraction*) modifica a trajetória do feixe de elétrons para minimizar os efeitos de espalhamento múltiplo [10,11]. Consequentemente, PED possui as mesmas vantagens de ED comuns, mas também pode ser utilizada análises quantitativas; procedimentos de refinamento estrutural, tipo Rietveld, foram utilizados com PED para resolver a estrutura de diversos nanocristais (proteínas, moléculas, zeólitas, sólidos amorfos, *etc*) [11]. Com PED podemos explorar novas possibilidades em cristalografia com elétrons, principalmente visando uma solução do problema da nanoestrutura, para isso o desenvolvimento de um método utilizando a combinação de PDF e PED é fundamental. Trabalhos anteriores mostraram a capacidade de realizar solução estrutural de PDF derivado com PED com qualidade similar as obtidas com PDF derivados de radiação síncrotron [12,13]. Portanto, é possível explorar diferentes problemas estruturais que antes eram inacessíveis com os métodos comuns de caracterização de nanoestruturas. O desenvolvimento de uma técnica robusta de difração de elétrons permite tornar TEM uma ferramenta otimizada a solução de nanoestrutura complexas, principalmente quando combinada com a capacidade de obter informação estrutural com alta resolução espacial.

Na microscopia eletrônica de transmissão em modo varredura (STEM: scanning TEM) o feixe de elétrons é focalizado a tamanhos de 0.05 nm a 10 nm e então varrido pela amostra [4]; o sinal adquirido (intensidade de difração, emissão de raios x, número de elétrons, corrente elétrica etc.) é medido pixel a pixel. Nesse caso, é possível mapear variações estruturais na amostra com resolução espacial limitada a aproximadamente o tamanho do feixe de elétrons. No caso de ED, desenvolvimentos recentes tornaram mais acessíveis detectores bidimensionais de elétrons de alta velocidade, que permite a medida de diversos padrões de difração em tempos viáveis para experimentos de STEM (milhares de frames por segundo). São então obtidos

conjuntos de dados onde em cada posição do feixe (duas coordenadas no espaço real) possuem um padrão de difração completo (duas coordenadas no espaço recíproco), o que dá o nome de 4D-STEM a técnicas de mapeamento de difração de elétrons [14]. O uso de PED com 4D-STEM permite explorar as capacidades de análise quantitativa PED com a alta resolução espacial do TEM.

1.1 Objetivos

Nesse trabalho vamos explorar o uso quantitativo de intensidade de feixes difratados medidas em modo PED para caracterização de nanomateriais de alta complexidade estrutural e onde técnicas de caracterização tradicionais não fornecem respostas satisfatórias.

O Capítulo 2 descreva a utilização da difração de pó com PED para determinar a deformação média em pequenas nanopartículas policristalinas de AuAg (<5 nm). Mais especificamente, diferenciamos modelos de deformações para nanopartículas decaédricas (modelo de Bagley [15] e um modelo de baixa deformação tetragonal [16,17]), que anteriormente não foi possível determinar com HRTEM ou XRD [16,17].

Nos Capítulos 3 e 4 descreve o uso combinado de PED e 4D-STEM para estudos que envolvam a medida da orientação de cristais. O Capítulo 3 descreve o desenvolvimento de uma metodologia para utilizar as intensidades de PED para medir a orientação de nanocristais com alta resolução angular (<0.1º). No Capítulo 4 caracterizamos nanoestrelas (NS) de AuAg que apresentam pernas alta anisotropia e razão de aspecto (~6). As NS atraem grande interesse na comunidade de Raman devido as suas expressivas propriedades plasmônicas, as quais são dependentes da distribuição espacial das pernas. Para poder medir a forma tridimensional das nanostrelas aplicamos a metodologia desenvolvida no Capítulo 3. Também determinar a estrutura cristalina do núcleo e das pernas da NS o que permitiu obter nova compreensão sobre o processo de crescimento das mesmas.

1.2 Sobre está dissertação

Essa dissertação possui uma estrutura alternativa, onde artigos descrevendo cada trabalho realizado é incluso em capítulos. O Capítulo 2 descreve os métodos experimentais e teóricos, os Capítulos 3 – 5 descrevem essencialmente os resultados científicos incluso em cada um dos artigos. O Capítulo 6 apresenta conclusão e perspectivas da tese, incluindo uma

contextualização sobre os desafios do projeto. Finalmente, o Apêndice A descreve em detalhes os procedimentos associados aos métodos descritos no Capítulo 2.

Capítulo 2

Materiais e Métodos

Nesse capítulo são descritos os métodos experimentais e teóricos utilizados ao longo do trabalho de doutorado. Além disso, descrições mais detalhadas são dadas para métodos que não são descritos em detalhes nos artigos apresentados a seguir.

2.1 Microscopia Eletrônica de Transmissão

A microscopia TEM é uma das técnicas de caracterização estrutural mais aplicadas na ciência de materiais pela sua capacidade de obter informação com alta resolução espacial. Por exemplo, na caracterização de nanopartículas (NP: *nanoparticle*), é possível obter uma imagem que contenha diversas NPs para medir a distribuição de tamanhos (resolução de sub micrometro) e uma onde seja possível observar o ordenamento dos átomos dentro de cada uma delas para medir a estrutura cristalina (resolução sub ångström) [18]. Essa versatilidade não se restringe a imagens, e TEM também permite obter informação sobre composição química, estrutura eletrônica, domínios magnéticos, *etc* [4].

O microscópio eletrônico funciona como um sistema óptico de projeção. Uma fonte de elétrons é utilizada para iluminar a amostra de interesse, que terá sua imagem aumentada e formada por uma lente magnética (denominada lente objetiva, ver Fig. 2.1). A imagem invertida do objeto iluminado é formada no plano imagem da lente, e no plano focal é formado um padrão de difração de elétrons(eDP: *Electron Diffraction Pattern*) ou TF da amostra.

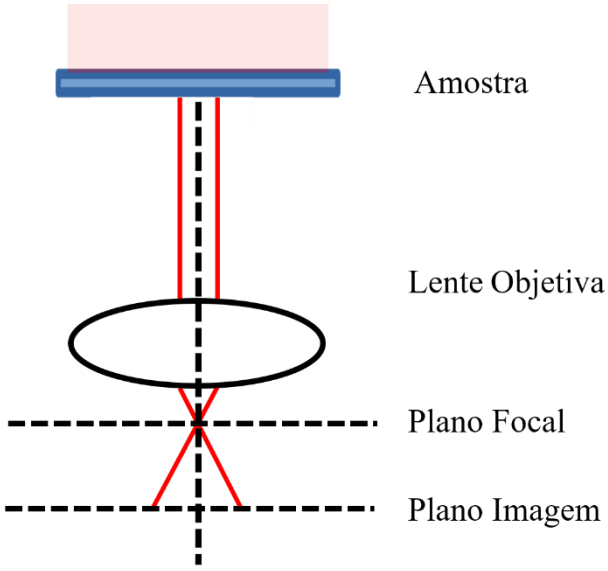

Figura 2.1: Diagrama simplificado do princípio de funcionamento de um TEM. A óptica é a mesma utilizada em um sistema de projeção. Imagens são obtidas no plano imagem e padrões de difração são obtidos no plano focal.

A caracterização da estrutura cristalina comumente utiliza imagens de Microscopia Eletrônica de Alta Resolução (HRTEM: *High Resolution Transmission Electron Microscopy*) para observar, por exemplo, o ordenamento dos átomos, fronteira entre grãos e defeitos estruturais [4]. Comparado a técnicas de difração de raios X tradicional na caracterização de cristais, o uso de imagens fornece uma maneira mais intuitiva e direta para observar aspectos morfológicos (forma e tamanho) e o arranjo atômico de um material. No entanto, embora seja intuitiva, HRTEM possui diversas limitações relacionadas a necessidade de observar o material ao longo de direções de alta simetria (necessidade de alinhar as colunas atômicas ao longa da direção do feixe de elétrons[4]). Além disso, não é possível obter informação nas três dimensões (3D) devido as imagens serem projeções (uma integração) da estrutura ao longo da direção de observação. Considerando todos esses fatores, pode ser bastante complexo obter informação da estrutura dos materiais de baixa simetria cristalina, como amorfos e policristais nanométricos. Alternativamente, técnicas de difração fornecem informação estrutural em cristal fora de eixos de simetria. Mas essa informação está no espaço recíproco o que dificulta a interpretação direta; no entanto ele contém informação da orientação do cristal no espaço com a análise da distribuição e das intensidades dos feixes difratados.

2.2 Difração de Elétrons

A caracterização de cristais é feita principalmente com medidas no espaço recíproco, ao obter o padrão de difração de um cristal temos acesso a uma grande quantidade de informação estrutural com uma única medida. Por exemplo, XRPD é utilizado corriqueiramente na determinação da estrutura de diversos materiais (metais, cerâmicos, moléculas, proteínas, *etc*.), sendo capaz de determinar estruturas complexas com o mínimo de informação inicial e sem necessidade de análises numéricas complexas [19].

A técnica de difração mais comum em TEM é a Difração de Elétrons de Área Selecionada (SAED: *Selected Area Electron Diffraction*), nela é utilizada uma abertura no plano imagem para obter o ED de uma região de interesse (Fig. 2.2). Em SAED a frente de onda eletrônica incidente é usualmente plana ao chegar na amostra, condição é obtida ao iluminar áreas muito maiores que somente a selecionada com a abertura (5 µm a 0.1 µm). Consequentemente, em SAED são utilizadas baixas doses de elétrons, geralmente menores que 10 $e^-/Å^2$ ideal para caracterizar materiais sensíveis a irradiação (número de elétrons por área é a unidade comumente utilizada em TEM) [4,20]. De maneira geral, em condições óticas equivalentes, as doses utilizadas em técnicas de difração de elétrons são menores que em imagens. Isso é devido as características de cada tipo de sinal: um DP mostra discos de alta intensidade localizada num fundo comparativamente baixo (por exemplo, picos claros num fundo escuro), já a imagem apresenta variedades sutis de intensidade entorno da intensidade média (por exemplo, mudanças numa escala de cinza) .

A interação dos elétrons com átomos é mais forte que a de raios X ou nêutrons, portanto a massa mínima necessária em SAED (menor que ng) é muito menor que a necessária para raios X (mg) e nêutrons (g). Com SAED torna-se possível caracterizar cristais individuais com tamanho reduzido (milhares de átomos) ou de difícil síntese (biomoléculas, cristais metaestáveis) [21] .

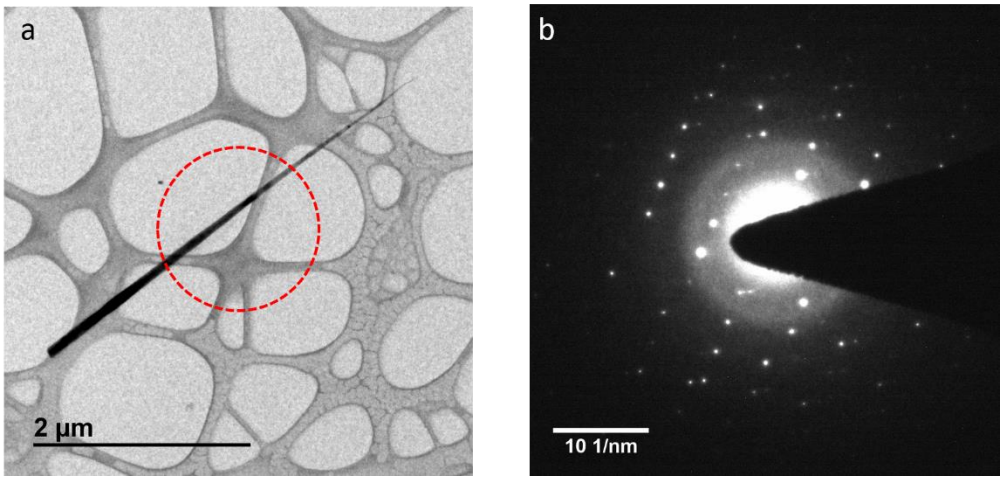

Figura 2.2: a) Imagem de baixa magnificação de um nanofio de InP; a área indicada pela linha tracejada representa a abertura de utilizada para obter o padrão de difração SAED em b).

O raio típico da esfera de Ewald para elétrons (400 nm^{-1} num microscópio 200 keV) é maior que a de raios X e nêutrons (10 nm^{-1}), sendo efetivamente quase-plana, tal que uma esfera de Ewald de baixa curvatura excita mais pontos de uma mesma zona de Laue (ver Fig 2.3). Dessa forma sempre há mais reflexões excitadas em SAED que em diagramas gerados utilizando raios X ou nêutrons; isso facilita o estudo de monocristais onde pode ocorrer dificuldade de excitar diversas reflexões simultaneamente. No entanto, comparativamente a raios X/nêutrons, SAED fornece majoritariamente informação bidimensional do cristal, mas ainda é possível obter informação 3D pelas intensidades difratadas (ver Fig 2.3)[22] .

A máxima espessura dos cristais utilizados em TEM é limitada pela necessidade de transmissão dos elétrons incidentes através da amostra (geralmente espessuras menores que 100 nm [4]). Portanto, ocorro o efeito de filme fino da difração (*thin film effect*), tal que os 'pontos' da rede recíproca (transformada de Fourier da forma do cristal) possuem um tamanho finito (ver Fig. 2.3) [23]. Efetivamente a condição de Bragg de um cristal fino é 'relaxada' por um desvio $\boldsymbol{s}$ (erro de excitação) em relação a condição de Bragg do cristal infinito (vetor do espação recíproco $\boldsymbol{g}$), e ocorre excitação de uma reflexão com vetor de difração $\boldsymbol{K}$ (Eq. 2.1):

$$\boldsymbol{K} = \boldsymbol{k_D} - \boldsymbol{k_0} = \boldsymbol{g} + \boldsymbol{s} \tag{2.1}$$

onde $\boldsymbol{k_0}$ e $\boldsymbol{k_D}$ são os vetores de onda dos feixes incidente e difratado, respectivamente.

A difração de elétrons permite medir volumes muito pequenos devido à forte interação dos elétrons com o material, no entanto, isso também torna comum eventos de espalhamento

múltiplo e a interpretação das medidas fica mais complexa em relação à quando somente ocorre um único evento de espalhamento.

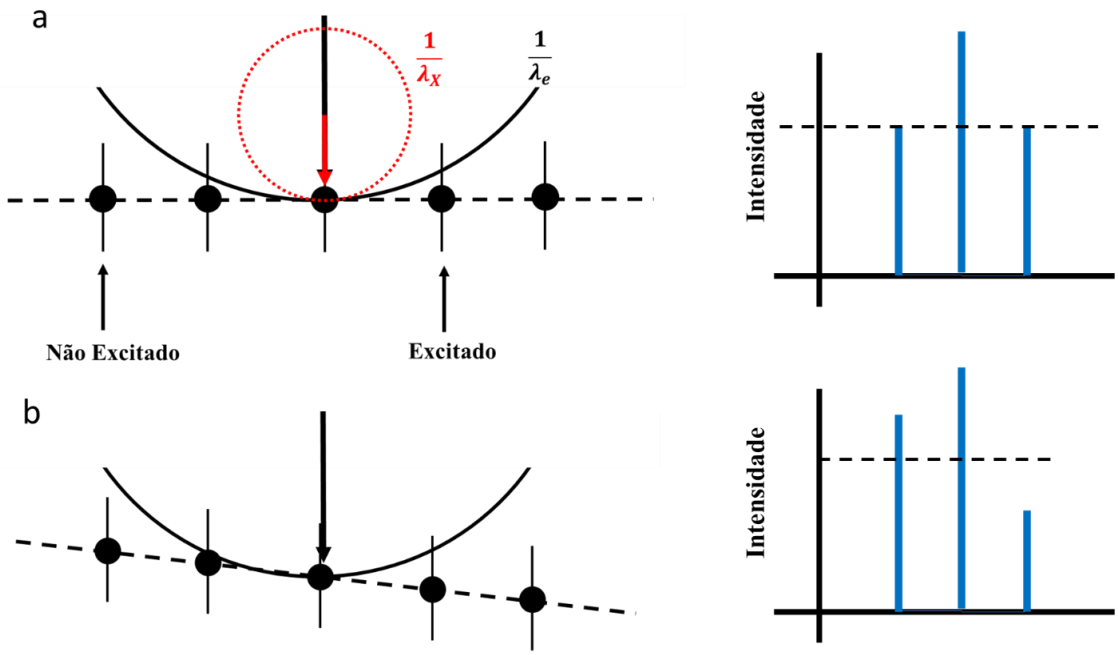

Figura 2.3: Direita) Os pontos da rede recíproca possuem tamanhos finitos devido ao efeito de filme fino, que nesse caso é representado pelos traços sobre os pontos da rede recíproca. Os círculos representam a relação entre as esferas de Ewald de raios X (linha pontilhada) e elétrons (linha continua). Esquerda) Representação dos perfis de intensidade dos pontos interceptados pela esfera de Ewald. Representação para o cristal a) perfeitamente orientado ao longo do eixo de zona e b) desorientado do eixo de zona. Perceba que quanto mais próximo a esfera de Ewald está do ponto, mais intensa é a intensidade do pico de difração.

2.2.1 Intensidades Medidas em Difração de Elétrons

A descrição completa da estrutura de um cristal pode ser realizada ao calcular o fator de estrutura (F_{hkl}) por esse conter informação sobre o tipo atômico e a localização dos N presentes na célula unitária:

$$F_{hkl} = \sum_{n=1}^{N} f_n e^{2\pi(hu_n+kv_n+lw_n)} \tag{2.2}$$

onde f_n é o fator de espalhamento atômico (informação interação onda-átomo), hkl os índices de Miller e (u_n, v_n, w_n) as posições do átomo na célula unitária. No caso da difração cinética (difração de raios X e nêutrons), onde somente um evento de espalhamento da onda incidente

ocorre, a relação entre a intensidade difratada medida I_{hkl} e o quadrado do fator de estrutura é diretamente proporcional (Eq. 2.3) [23]. Essa relação torna simples realizar diversos cálculos de intensidade rapidamente, já que somente é necessário calcular uma somatória em poucos átomos (células unitárias com mais de 50 átomos são consideradas incomuns) [24].

$$I_{hkl} = |F_{hkl}|^2 \tag{2.3}$$

Durante a propagação dos elétrons no cristal ocorrem múltiplos eventos de espalhamento, por consequência a intensidade observada num eDP não é relacionada diretamente com $|F_{hkl}|^2$ e as intensidades difratas devem ser descritas pela teoria dinâmica da difração [25]. O cálculo completo e preciso de um ED dinâmico não possui descrição analítica, sendo processos numéricos ou interativos como *Multiple-Beam* (mais de 2 feixes) ou pelo formalismo de Bloch [4]. Ambos os casos exigem cálculos que são complexos e demorados, o que limita a possibilidade de realizar análises quantitativas das intensidades, seja em materiais complexos ou em aplicações que exigem a análise de uma grande quantidade de EDs (como será visto no capítulo 4) [26].

É importante destacar que mesmo em amostras de pequena espessura, como no caso de nanopartículas, os efeitos de difração dinâmica podem ser consideráveis. Simulações indicam que há forte presença de efeitos dinâmicos no padrão de difração de pó com elétrons, mesmo em NPs de Au com diâmetros de 1 nm (Fig. 2.4) [27].

Esforços de refinamento estrutural são limitados em TEM pelas dificuldades em lidar com difração dinâmica por exigir processos números complexos. Para expandir a capacidade de análise estrutural quantitativa em TEM é necessária uma técnica que diminua os efeitos de espalhamento múltiplo nas intensidades difratadas medidas. Na seção seguinte descrevemos uma proposta instrumental que tenta reduzir esses efeitos.

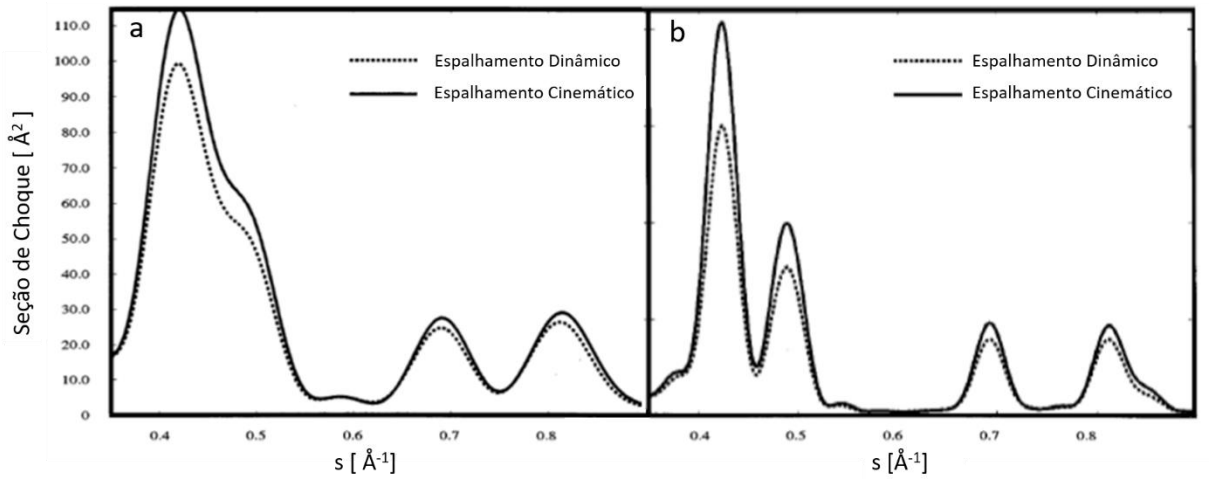

Figura 2.4: Simulações da seção de choque diferencial elástica (intensidade difratada) em função do modulo do vetor de espalhamento $s\ (2sen(\theta)/\lambda)$, com elétrons a 100 kV. Foram simulados padrões de difração de pó dinâmico (linha pontilhada) e cinemáticos (linha continua) em NPs de Au monocristalinas e com diâmetros de: a) ~1 nm, b) ~3 nm. Imagem adaptada de [28].

2.3 Difração de Elétrons com Precessão

O desenvolvimento de Difração de Elétrons com Precessão (PED) por Vicente e Midgley visou obter padrões de difração que fossem mais apropriado para uso quantitativo em processos de solução estrutural similar ao realizado em raios X [10]. Acima da amostra o feixe de elétrons é manipulado em um movimento de precessão em torno do eixo ótico do TEM; esse movimento forma um cone oco (com meio-ângulo de abertura φ) no espaço real, e o movimento da esfera Ewald, formando um volume contínuo no espaço recíproco. Consequentemente, as intensidades medidas em PED são o resultado da integração em torno da condição de Bragg (ver Fig. 2.5) e há uma significativa diminuição da influência de orientações do cristal que favoreçam espalhamento múltiplo. Portanto, ocorre uma redução significativa dos efeitos de espalhamento dinâmico nas intensidades medidas, que as tornam mais próxima das esperadas pela difração cinemática; no entanto, as intensidades de PED são consideradas Quase-Cinemáticas por ainda possuírem efeitos residuais da difração dinâmica [29,30]. Efetivamente, PED traz uma relação mais próxima ao fator de estrutura do cristal, onde são reveladas as simetrias esperadas do cristal que não eram visíveis com SAED convencional (ver Fig. 2.6).

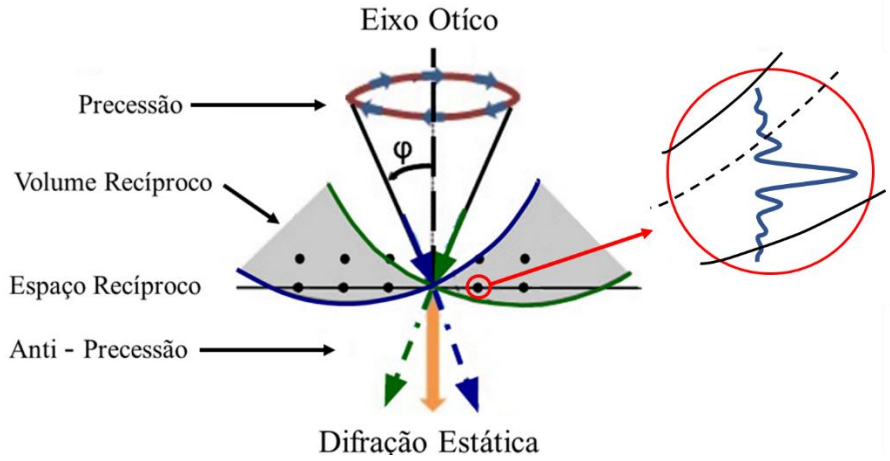

Figura 2.5: O feixe precessiona acima da amostra com meio-ângulo φ, e sofre uma contra-precessão abaixo dela para obter um eDP estático. Portanto, é gerado um volume continuo (marcado em cinza) no espaço recíproco, e as intensidades de PED são consequência da integração em torno da condição de Bragg relaxada pelo efeito de filme fino.

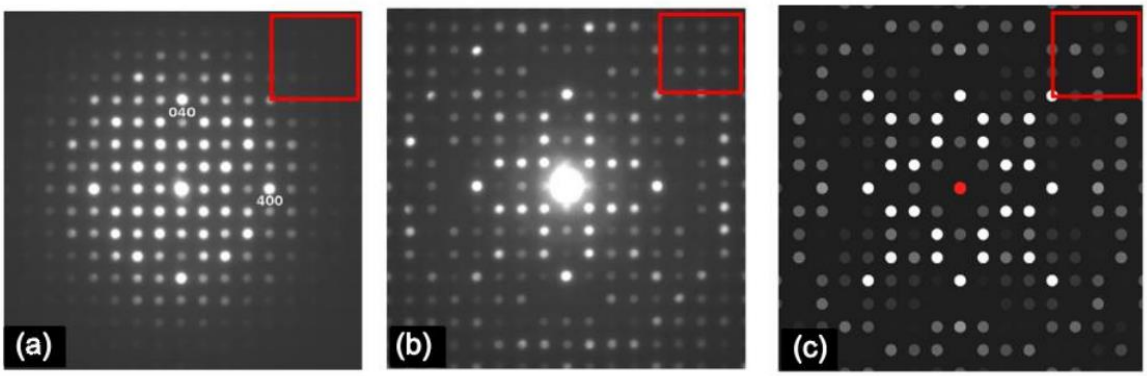

Figura 2.6: eDP de um cristal de $Er_2Ge_2O_7$, a) sem precessão, b) com precessão (φ = 2º) e c) fator de estrutura do cristal. As caixas vermelhas indicam regiões onde ocorre o aumento do número de reflexões excitadas ao utilizar precessão. Imagem adaptada de [31].

2.3.1 Intensidades Quase-Cinemáticas

Uma característica importante de PED é a diminuição da influência de espalhamento múltiplo nas intensidades com o aumento do ângulo de abertura do cone de precessão, onde a relação entre as intensidades medidas em PED (I_{hkl}^{PED}) e o fator de estrutura tornam-se significativamente mais próximas a partir de somente alguns graus (> 0.5º) [30,32–34]:

$$I_{hkl}^{PED} \sim |F_{hkl}|^2 \tag{2.4}$$

Seria esperado que esforços de análise quantitativas das intensidades de PED cutilizando como base o fator de estrutura fosse inviabilizado pela difrença entre as intensidades medidas e calculadas. Embora as intensidades individualmente não sejam "corretamente" iguais, a ordem relativa entre intensidades é corrigida pela precessão. Por exemplo, se no caso cinemático, as intensidades de picos de difração podem ser categorizadas como 'fortes/fracos', com PED elas podem ser separadas nas mesmas categorias de 'fortes/fracas' [33]. Efetivamente, em um processo de refinamento estrutural, a correta relação relativa entre intensidade é mais importante que os valores absolutos delas, tal que é possível realizar refinamento estrutural somente considerando o ordenamento grosseiro das intensidades [33,34]. A natureza quase-cinemática das intensidades de PED é evidente ao considerar a diminuição significativa das intensidades de picos de difração cinematicamente proibidos (hkl com $F_{hkl} = 0$), mas sem que ocorra o anulamento desses pico; eles são ainda detectáveis mesmo em altos ângulos de precessão (por exemplo, o (002) do Si na Fig. 2.7) [4,31].

É importante enfatizar a complexidade das intensidades medidas em PED, tal que não é possível tirar conclusões gerais sobre o seu comportamento; mesmo cálculos complexos e completos das intensidades de PED somente fornecem as conclusões qualitativas ou particulares ao cristal usado na simulação/cálculos. Novamente, reflexões proibidas deixam evidente características de PED, tal que estudos mais completos, que aliam simulações considerando a difração dinâmica e medidas, mostram que individualmente as intensidades dessas reflexões possuem comportamento complexo com aumento do ângulo de precessão, mas ainda é possível observar a tendência geral da queda de suas intensidades (Fig. 2.7) [29,30]. No geral, podemos esperar a atenuação significativa de efeitos de espalhamento múltiplo com PED, e o aumento do ângulo de precessão torna analises quantitativas mais precisas. No entanto, existe um valor máximo do ângulo devido a aspectos: i) instrumentais provenientes das aberrações das lentes (alargamento e distorção dos picos de difração); ii) geométricos devido a aproximação das zonas de Laue com o aumento do ângulo de precessão e iii) reflexões de comportamento complexo, como (222) das estruturas do tipo diamante/silício [29,30,35].

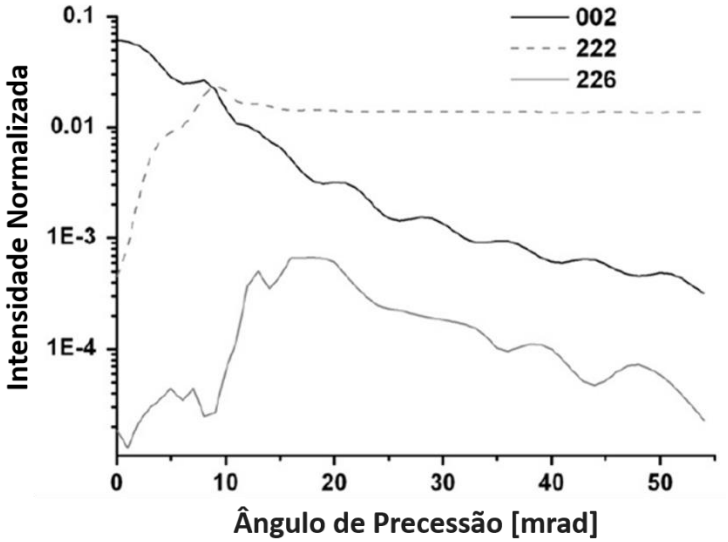

Figura 2.7: Simulação de PED para diversos ângulos da abertura do cone de precessão, para feixes proibidos de um cristal de Si (espessura ~ 48 nm). Figura adaptada de [30].

O aspecto prático mais importante é as intensidades difratadas em PED são bem comportadas (num diagrama SAED a relação de intensidade entre feixes é imprevisível) e a ordenação apropriada das intensidades dos feixes difratados permite utilizar o modelo cinemático para refinar a estrutura cristalina.

2.4 Mapeamento de Difração em 4 Dimensões

Até agora descrevemos medidas de SAED onde o sinal de difração vem de uma grande área, o que é benéfico para obter, por exemplo, informação média sobre um conjunto de cristais ou média de um cristal homogêneo (sem mudanças significativas no volume da estrutura) [13]. Também temos que considerar que técnicas onde um feixe de elétrons focalizado é varrido sobre a amostra (STEM) são bastante comuns em microscopia eletrônica.

Recentemente, existe grande interesse em obter dados por 4D-STEM, onde o feixe de elétrons é varrido pela amostra e para cada posição do feixe (pixel) é medido um ED (ver Figura 2.8) [36]. Nesse caso, são formados dados multidimensionais conhecido como bloco de dados; para 4D-STEM há duas dimensões no espaço recíproco (as duas dimensões do ED medido) e duas no espaço real (localizam a posição do ED medido) [14].

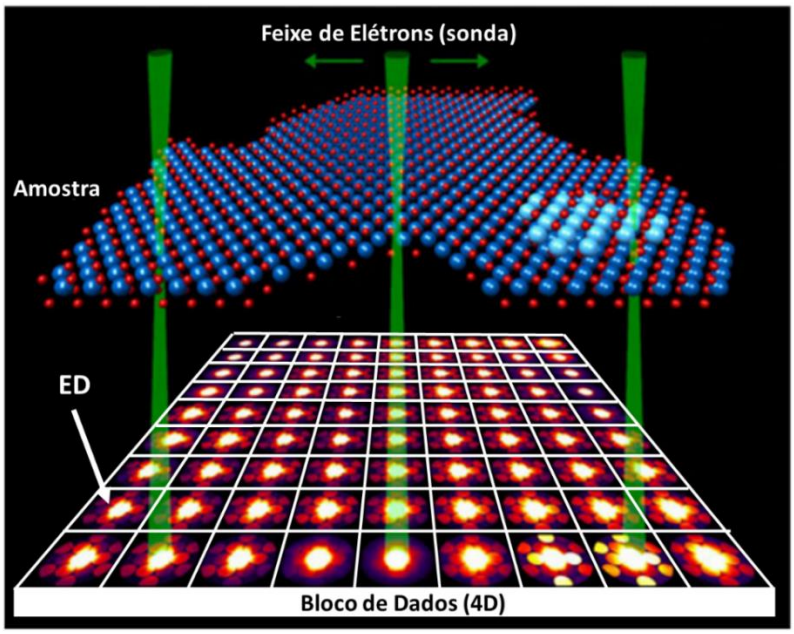

Figura 2.8: Ilustração de uma medida de 4D-ED. Para cada posição do feixe de elétrons é medido um padrão de difração daquele local da amostra. O bloco de dados é formado pela associação de uma posição espacial (um pixel no espaço real), localizado por duas coordenadas, a uma medida de um padrão de difração (uma imagem bidimensional do espaço recíproco). Figura adaptada da referência [14].

A aplicação dessa técnica está muito relacionada a capacidade de adquirir imagens bidimensionais com velocidade o suficiente para que a aquisição de mapeamento de difração demore de alguns minutos. Assim, o desenvolvimento de 4D-STEM está relacionado a recente comercialização de detectores de alta velocidade [37]. O uso de detectores lentos torna as medidas demoradas e doses de elétrons altas são depositadas no material. Um exemplo preliminar da necessidade de detectores de alta velocidade são sistemas comerciais para experimentos de 4D-STEM com PED (Nanomegas). Esses sistemas incluem uma câmera CCD (*Charge Coupled Device*) ótica de alta velocidade colocada fora do microscópio TEM gravando a imagem da tela de fósforo do microscópio (ver Fig. 2.9) [38,39]. Embora esse conjunto permita a detecção rápida de padrões PED, a intensidade difratada é perdida devido ao baixo intervalo dinâmico da câmera (8 bits), a não linearidade da tela de fósforo (a quantidade de elétrons incidentes e de luz emitida não são proporcionais) e as fortes distorções geométricas nas medidas (o eixo ótico, tela de fosforo e a câmera tem orientações relativas que distorcem significativamente o ED medido) [40]. Detectores de elétrons mais modernos de tecnologia CMOS (*Complementary Metal–Oxide–Semiconductor*) tem a capacidade de realizar capturas em alta velocidade (CCD: 1 captura por segundo, CMOS: mais de 200 capturas por segundo) [40]. Adicionalmente, detectores de elétrons direto (DED: *Direct Electron Detector*) aumentaram muito a velocidade de detecção (mais de 1000 capturas por segundo). É importante

também considerar que o tempo de medida por pixel (*dwell time*) é limitada por outros fatores, por exemplo, a necessidade de alta intensidade (acumulação de contagem) ou a frequência de precessão utilizada em PED.

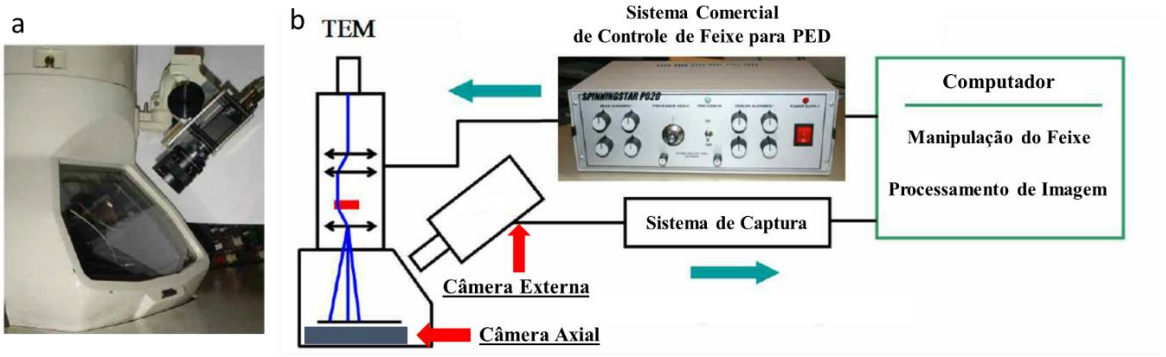

Figura 2.9: Sistema comercial SpinningStar P020 para PED desenhado para experimentos de 4D-ED. a) Câmera CCD externa que acompanha o sistema. b) Esquemático do funcionamento: o sistema controla o feixe de elétrons para o movimento de precessão e a câmera CCD externa captura os padrões de difração gerado. Ambos estão sincronizados por meio do computador. Observe que a câmera axial não é utilizada durante o experimento e está coberta pela tela de fosforo, que é observada pela câmera externa. Figura adaptada de [39].

A principal vantagem de 4D-STEM vem da versatilidade de ter um conjunto de dados com padrões de difração medidos com resolução nanométrica (aproximadamente o tamanho do feixe eletrônico). Por exemplo, num mesmo dado é possível formar imagens de campo escuro e claro, medir localmente fase, distorções, espessura, orientação, distribuição de campo eletromagnético selecionando imagens formadas por alguns feixes presente em cada diagrama de difração por pixel [14]. É evidente que dados de 4D-STEM contém muita informação sobre a amostra, o que traz muito interesse em desenvolver e aplicar técnicas de análise cristalográfica. No entanto, embora a qualidade dos dados tenha avançado consideravelmente, a análise quantitativa das intensidades ainda é bastante complexa devido as mesmas limitações que a difração dinâmica impõe a SAED. Portanto, é comum que 4D-STEM seja combinado com PED para obter dados onde a análise utilize a aproximação cinemática no cálculo da difração eletrônica. Um exemplo, são medidas de textura por o método chamado *pattern-matching* (também comumente chamado de *template-matching*), onde o PED em cada pixel é comparado com uma biblioteca de simulações de padrões de difração cinemática do cristal em diversas orientações (essa técnica será mais explorada no Capítulo 4) [39–41]. Outro aspecto importante de 4D-STEM é uso de aprendizado de máquina (ML: machine learning) para, por exemplo, redução de dimensionalidade, categorização não supervisionada (clustering) e

redução de ruídos. Nesse caso, PED torna ML muito mais simples e precisa por homogeneizar as variações de intensidade que ocorrem no interior dos discos de difração devido a espalhamento múltiplo (ver Figura 2.10) [42,43].

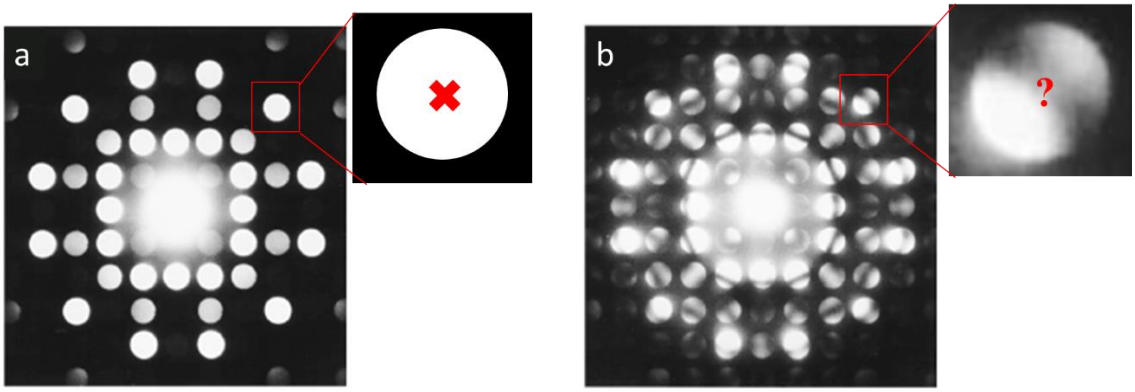

Figura 2.10 Comparação entre padrões de difração a) cinemático e b) dinâmico. A estrutura no interior de discos de difração em b) torna a determinação do centro e analises por ML mais complexas [42,43].

As vantagens de combinar PED, seja com SAED ou 4D-STEM, são evidentes ao facilitar o uso quantitativo das intensidades; ainda assim, pouco foi feito visando desenvolver métodos para o uso das intensidades e ainda são muito dependentes de técnicas desenvolvidas em dados sem intensidades de qualidade.

2.5 Função de Distribuição de Pares

Como descrito na introdução, a cristalografia de nanocristais possui limitações conceituas devido a dependência das técnicas comumente aplicadas a existência de ordem de longo alcance (‘*the nanostructure problem*’) [3]. Na difração de pó, ao diminuir o tamanho de um cristal ocorre perda de informação sobre a estrutura do cristal, evidenciado pelo aumento da largura dos picos com a diminuição das dimensões do cristal (ver Fig. 2.11), a maior atenuação das intensidades devido ao movimento mais acentuado dos átomos e ao aumento do fundo de difração [2]. No espaço recíproco, a quantificação das intensidades, numa análise de Rietveld, é baseada na altura, largura e centro dos picos de difração medidos [44,45]. No entanto, em nanocristais a perda de ordem de longo alcance implica que a informação da organização atômica está distribuída sobre todo o padrão de difração e o uso exclusivo dos picos usualmente não resulta numa solução estrutural precisa. Alternativamente, é possível realizar quantificação estrutural utilizando todo o padrão de difração (*full-pattern analysis*),

principalmente realizado através da análise por Função de Distribuição de Pares (PDF), originalmente desenvolvida para o estudo da estrutura de materiais amorfos [8].

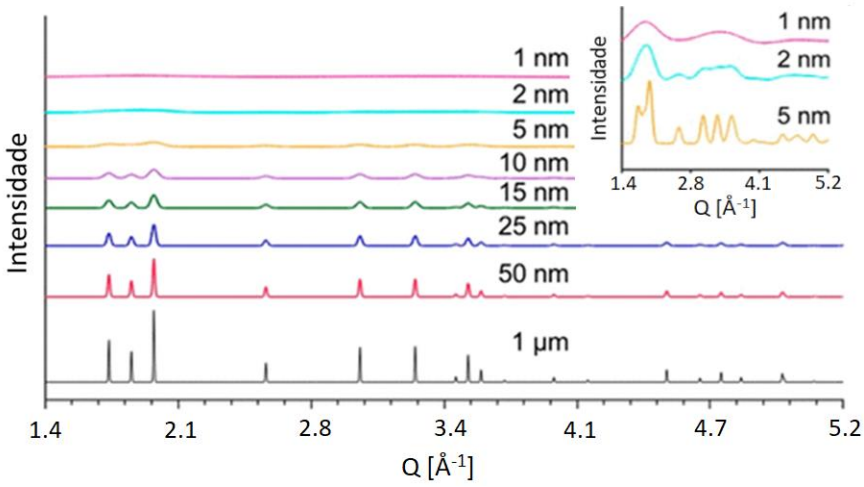

Figura 2.11: Simulações dos XRPD em NPs de wurtizita CdS esféricas de diversos diâmetros (1 µm – 1 nm). Na parte superior em destaque estão as simulações para as NPs de 1 nm, 2 nm e 5 nm. Note o claro alargamentos dos picos de difração. Figura adaptada de [2].

PDF descreve a distribuição de distâncias entre pares de átomos num volume de material, como ilustrado na Fig. 2.12a. A PDF é sensível as distâncias interatômicas e quais são os átomos presentes em cada par. Muitas das informações estruturais do material podem ser obtidas de maneira direita em uma curva PDF, por exemplo, a distância e número de vizinhos dos átomos (Fig. 2.12). Com a PDF toda informação estrutural do material está presente no espaço real, a vantagem é ser possível obter informação da estrutura local dos cristais de maneira mais intuitiva [8].

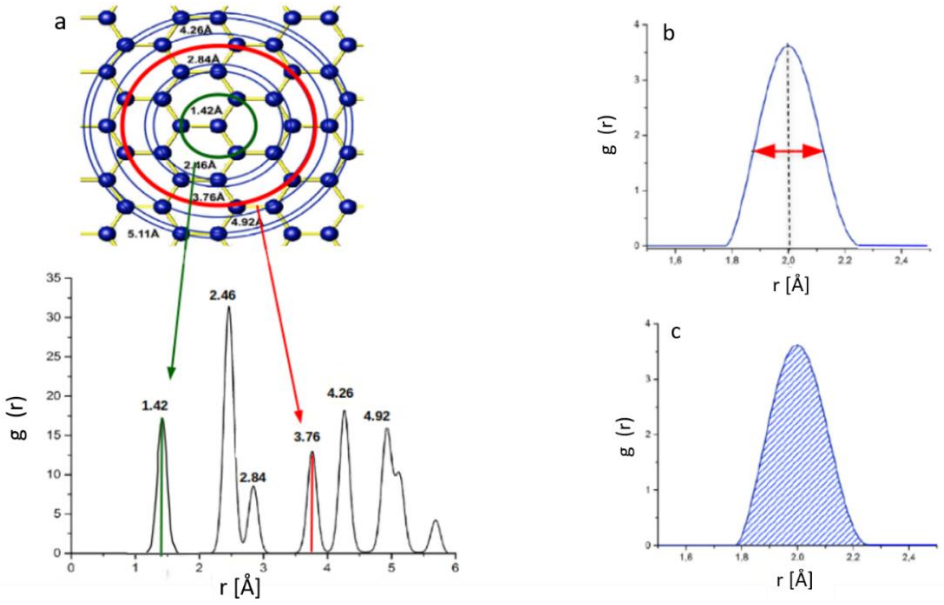

Figura 2.12: a) Representação da relação entre os picos da PDF ($g(r)$) e a estrutura do material. b) A largura do pico é relacionada com distorções na estrutura. c) A área abaixo de um pico é o número de átomos vizinhos a uma determinada distância. Figuras adaptadas de [46] .

A PDF é obtida a partir de padrões de difração de pó; no caso da difração de elétrons isso corresponde a medida SAED escolhendo uma abertura que inclua diversos (>1000) nanocristais. Durante o mestrado, desenvolvemos um programa (software) para derivação da PDF a partir de medidas de PED, visando uma metodologia de análise dos dados especifica para difração de elétrons. Os detalhes da metodologia desenvolvida podem ser encontrados no artigo publicado descrevendo os procedimentos adotados, em anexo no fim desse manuscrito. Mais importante, a análise quantitativa de PDF com PED mostrou-se capaz de caracterizar a estrutura de nanocristais complexos (em nosso trabalho nanopartículas de AuAg) com a qualidade similar a PDF obtida com difração de raios X em fontes d luz síncrotron. O próximo capítulo explora PDF + PED para determinar as distorções em partículas decaédricas com alta precisão e confiabilidade.

Capítulo 3

Função de Distribuição de Pares (PDF) para Caracterização de Nanopartículas Decaédricas

A cristalografia de elétrons é reconhecida como fundamental para obter a estrutura completa de cristais a partir de pequenos volumes de amostra (<μm^2) [47]. Tal reconhecimento é muito recente (~5 anos), sendo que no paradigma anterior a difração de elétrons (assim como imagens de TEM) eram limitadas a análises qualitativas devido à complexidade de analisar quantitativamente padrões de difração dinâmicos [4]. Consequentemente, a difração de elétrons era comumente utilizada de maneira complementar a técnicas já estabelecidas baseadas em raios X e nêutrons, quem usualmente são utilizadas para obter resultados com alta qualidade estatística e utilizando métodos de refinamento estrutural (por exemplo, Rietveld) [48].

Essa diferença se dá principalmente pela difração de elétrons ser significativamente afetada por eventos de espalhamento múltiplo ao propagar pela amostra, diferente de raios X/nêutrons onde somente uma interação/espalhamento ocorre [4]. O uso quantitativo da intensidade de feixes difratados quando acontece difração dinâmica demanda simulações muito demoradas complexas que as de difração cinemática. O desenvolvimento de difração de elétrons com precessão (PED, ver Capítulo 2) tornou possível utilizar as intensidades de difração de elétrons quantitativamente com maior confiabilidade e reprodutibilidade [11]. Hoje, PED é visto como uma técnica viável e precisa para resolver a estrutura de monocristais. Ainda assim, a caracterização de nanomateriais de tamanho reduzida (<10 nm) é um grande desafio para técnicas de difração, seja ela de raios X, nêutrons ou elétrons, devido dificuldades intrínsecas a pequena dimensionalidade desses sistemas [3].

Nanomateriais possuem estrutura de curto alcance bem definida (primeiros vizinhos, assim como materiais amorfos) e também possuem estrutura periódica em médio alcance (10-100 nm). No entanto, o conceito de cristal infinitamente periódico não é válido, tal que metodologias de cristalografia baseadas nesse princípio (como refinamento estrutural por Rietveld, que utiliza unicamente o fator de estrutura para calcular intensidades dos picos difratados) se tornam difíceis de aplicar com confiabilidade em nanomateriais [3].

Alternativamente, a cristalografia de materiais amorfos tem sido baseada por décadas na análise de padrões de difração por função de distribuição de pares (PDF, ver Capítulo 2), uma técnica de fronteira associada a facilidades de grande porte e alto custo (raios X: síncrotrons,

nêutrons: fontes nucleares) [8,9]. A PDF descreve as distâncias entre pares atômicos no espaço real, de maneira que contêm informação precisa da ordem atômica de curto e médio alcance, sendo também é possível utilizar a PDF para realizar análise estrutural quantitativa similar ao refinamento Rietveld [9]. A análise por PDF tem se tornado na última década uma técnica importante para a caracterização de nanopartículas (tamanho, estrutura de grãos, forma), amorfos (estrutura de primeiros vizinhos, grau de cristalinidade, identificação de tipos de amorfo) e até mesmo materiais macroscópicos que possuem ordem local complexa (ferroelétricos, materiais magnéticos,*etc*) [49].

A PDF é obtida partindo de padrões de difração de pó com alto ângulo de espalhamento, o que demanda fontes (de fótons, nêutrons, elétrons, etc.) de alta energia (35-70 keV). O uso de difração de elétrons para PDF é interessante por ser acessível mesmo em altas energias (usualmente microscópios de transmissão operam acima de 80 keV), simplificando a aplicabilidade dela no cotidiano da pesquisa científica com instrumentos na configuração padrão [4].

As diferenças entre difração de raios X/nêutrons e elétrons implica na necessidade de desenvolver metodologias especificas para derivar PDF de elétrons, portanto, diversas tratamento de melhor adaptados a ED foram propostas nos últimos anos [49,50]. Nosso grupo desenvolveu um software capaz de realizar todo os passos necessários para realizar a análise quantitativa de ePDF: i) correções de distorções óticas, ii) integração azimutal, iii) subtração de fundo, iv) cálculo da PDF, v) simulação de PDF, vi) cálculo e refinamento estrutural utilizando como métrica a minimização de resíduos [12]. Uma atenção especial foi dada a subtração de fundo do padrão de difração, que usualmente é tratada de maneira simplifica devido a complexidade de considerar simultaneamente duas contribuições significativas ao fundo medido (espalhamento incoerente e o substrato).

Além disso, aliamos a metodologia desenvolvida ao uso de PED para poder realizar quantificação com alta qualidade e precisão. Os resultados mostraram a capacidade de identificar a estrutura de nanopartículas (tamanho e organização dos cristalitos) com qualidade similar a obtidas com síncrotrons de alta performance; mesmo ao usar um microscópio com mais de 10 anos de utilização e muito mais simples (microscópio 200 keV, canhão de elétrons LaB6, resolução > 0.2 nm) quando comparado a microscópios modernos com corretores de aberração esférica (resolução ~0.05 nm).

Nesse presente trabalho utilizamos a técnicas de PDF derivado de PED para caracterizar a estrutura de nanopartículas metálicas decaédricas, visando obter informação sobre as deformações associadas a essas partículas. Diversos metais formam nanocristais policristalinos

de alta simetria na nanoescala usualmente chamados de multiply-twinned particles (MTPs) [51]. Entre elas, as nanopartículas decaédricas (Dh: decahedra) de metais nobres (Au, Ag,) são uma das variantes mais comuns. Nesse caso, 5 cristalitos (de forma tetraédrica) são organizados em torno de um único eixo de simetria (eixo de simetria 5) [51]. Os tetraedros em princípio deveriam ter a estrutura cúbico de face centrada (FCC: face-centered cubic) da fase macroscópica, no entanto, nesse caso, o decaedro resultante teria descontinuidades em sua estrutura [15,52]. Portanto, é necessário deformar os tetraedros para obter um decaedro sem descontinuidades. Diversos modelos foram propostos para explicar tais deformações (deformações inomogêneas, ou distorções homogêneas gerando cristais com célula unitária ortorrômbica ou tetragonal) [15–17,52]. No entanto, pouca evidência experimental foi obtida para determinar sem ambiguidades o modelo correto, principalmente por dificuldades em medir a estrutura tridimensional de NPs individuais, ou a diminuição de precisão associado a alargamento dos feixes difratados induzidos pela diminuição de tamanho do domínio cristalino.

O manuscrito do artigo relacionada a esse capítulo (Apêndice A), que está em fase de submissão, foca em obter informação sobre a estrutura cristalina média (célula unitária) de Dh presente em uma amostra composta de NPs de AuAg de poucos nm de diâmetro (2-4 nm). Mais especificamente, contrapomos o modelo mais aceito, proposto por Bagley nos anos 60, de uma célula unitária ortorrômbica de corpo centrado (BCO: body centered ortorrombic), com uma observações mais recentes (aproximadamente na última década) que sugerem uma simetria tetragonal de corpo centrado (BCT: body centered tetragonal) [15–17,52].

Em nosso estudo tivemos especial cuidado em minimizar os números de parâmetros livres utilizados no refinamento estrutural relacionados as distancias/deformações do decaedro. É conhecido que padrão de difração de nanosistemas são propicio a perda de informação devido a suas dimensões limitadas e efeitos térmicos acentuados [3,8,9]. Consequentemente um número excessivo de parâmetros livres durante o refinamento/ajuste induz a ajustes excessivo (*overfiting*), gerando estruturas não realistas. Mais preocupante no caso estudado, é a possibilidade de não conseguirmos diferenciar apropriadamente (sem um intervalo de confiança) modelos muito distintos (como os decaedros baseados em células unitárias BCO e BCT) ao analisar a mesma informação experimental. Portanto um número limitado de parâmetros foi utilizado para os ajustes e critérios físicos (nesse caso o fator de empacotamento) foram utilizados para restringir a variação dos parâmetros.

Nossos resultados mostram conclusivamente que o modelo de Bagley (célula unitária ortorrômbica com 5% expansão na direção paralela ao eixo de simetria 5) não descreve satisfatoriamente a amostra medida. A célula unitária resultante de nosso refinamento sugere

que uma estrutura ortorrômbica de baixa distorção ao longo eixo de simetria 5 como a melhor descrição dos Dh de AuAg na amostra. Se consideramos a precisão na medida absoluta dos comprimentos dos vectores base (a_{BCO}, b_{BCO}, c_{BCO}) da célula identificada, não podemos excluir a existência da fase BCT (as distâncias a_{BCO} e b_{BCO} se superpõem considerando os intervalos de incerteza 3σ). Devemos mencionar que não é possível descartar a existência de deformações inomogênea na estrutura, pois nosso estudo não possui a precisão necessária para analisar modelos tão detalhados. Uma determinação mais precisa poderia ser obtida com experimentos de maior qualidade, por exemplo, ao utilizar detectores maiores para obter maior ângulo de espalhamento e filtros de energia para diminuir a influência do fundo inelástico nos resultados. Os resultados indicam que ePDF + PED é uma ferramenta importante para obter informação 3D completa da estrutura de nanomateriais com as vantagens de utilizar uma baixa dose de elétrons (< 10 $e^-/Å^2$).

Os trabalho está descrito no manuscrito presente no Apêndice A em conjunto com o material suplementar que acompanha o manuscrito (Apêndice B).

Capítulo 4

Aplicação das Intensidade de Difração de Elétrons com Precessão (PED) para Mapeamento de Orientação de Cristais Automatizado (ACOM) com Alta Resolução Angular

Recentemente, grande atenção tem sido dada ao desenvolvimento de nanofios (NW: Nanowires) semicondutores, principalmente devido a possibilidade de miniaturizar diversos sistemas eletrônicos [53]. A presença de defeitos estruturais nesses fios (maclas, discordâncias, interfaces, *etc*.) geram deformações estruturais e afetam significativamente o controle das propriedades físicas, como transporte elétrico e propriedades óticas [54]. Consequentemente, a reprodutibilidade da aplicação de NW em dispositivos ainda é limitada pela falta de informação precisa sobre deformações na estrutura do material [54]. A caracterização dessas deformações é bastante complexa por ocorrerem em nano-objetos individuais, tal que técnicas comuns não podem ser facilmente aplicadas. Nesse caso, são usualmente utilizadas técnicas de TEM devido sua alta resolução espacial (atualmente é possível atingir resoluções na faixa do sub ångström) [19]. Entre elas, técnicas de difração de elétrons são ideais para acessar informações sobre a estrutura cristalina e sua modificação em NWs. Principalmente pela baixa dose de elétrons (dada por $e^-/Å^2$) necessária, este valor baixo garante a preservação da estrutura de defeitos sem ser modificada pela observação em TEM.

Hoje, experimentos de ED são comumente realizados no modo 4D-STEM, onde o feixe de elétrons é varrido pelas amostras e para cada posição do feixe (pixel) é medido um ED [36]. Nesse caso, são formados dados multidimensionais conhecido como bloco de dados; para 4D-STEM há duas dimensões no espaço recíproco (as duas dimensões do ED medido) e duas no espaço real (localizam a posição do ED medido) [14]. A difração de elétrons com precessão é comumente utilizada para realizar medidas de 4D-STEM, por diminuir significativamente efeitos prejudiciais do espalhamento dinâmico, usualmente encontrados no caso de um feixe estático[11]. Por exemplo, PED fornece maior precisão nos valores de tensão (expansão ou compreensão) ou na identificação de fases, mas sem afetar significativamente a resolução espacial das medidas [55].

A técnica de PED já foi utilizada por nosso grupo para caracterizar nanofios de InP, sintetizados pela Prof. Dr. Monica Cotta (IFGW-DFA). Neste caso, foi possível obter informação quantitativa sobre a estrutura de defeitos dos NWs contendo uma discordância axial

do tipo parafuso [56]. Também foi possível reconstruir a forma 3D dele partindo de informações 2D, tal foi feito com doses significativamente menores que as utilizadas em técnicas de tomografia [4].

As informações que podem ser derivadas de 4D-STEM (com ou sem PED) são usualmente obtidas somente considerando as posições dos picos de difração [43]. O principalmente motivo tem sido a impossibilidade de utilizar o detector axial do microscópio (comumente uma CCD) integrado ao eixo ótico do microscópio para medir a intensidade relativa de elétrons transmitidos em EDs ou imagens [41]. Usualmente, esses detectores eram lentos demais para serem utilizados em experimentos em que um feixe de elétrons é varrido rapidamente pela amostra, que acaba por tonar as medidas significativamente demoradas e uma alta dose de elétrons é depositada no material [41,43].

Detectores de elétrons mais modernos de tecnologia CMOS tem a capacidade de realizar capturas em alta velocidade (CCD: 1 captura por segundo, CMOS: mais de 200 capturas por segundo). No entanto, mesmo nesses casos o uso das intensidades de difração ainda é usualmente ignorado, principalmente devido à dificuldade em analisar quantitativamente os valores relativos de intensidade (comparação entre medidas e modelos numéricos) [41]. Os cálculos de difração dinâmica são bastante complexos, de maneira que o cálculo de EDs para os milhares de padrões medidos é inviável; a técnica PED simplifica significativamente os cálculos necessários ao permitir a utilização do modelo cinemático, tal que o uso das intensidades é viável.

Esse panorama será explorado nesse trabalho ao considerar o uso das intensidades para realizar a medida da orientação de cristais, usualmente associada a medidas de textura em materiais policristalinos (ACOM: Automated Crystal Orientation Mapping) [41,43,57,58]. Essa é a aplicação mais comum de técnicas de 4D-STEM, tal que é um foco importante do desenvolvimento metodológico e instrumental, visível pelos diversos software's disponíveis para analisar esse tipo de dados. Os métodos convencionais de ACOM utilizam o procedimento de *pattern-matching* onde a identificação da orientação é realizada através de uma correlação cruzada entre o ED medido e uma biblioteca de padrões simulados. No entanto, tais procedimentos somente utilizam as posições dos picos e não suas intensidades, visando acelerar e simplificar a análise, mas limitando a precisão da determinação da orientação do cristal a 1-2 graus.

As intensidades de ED possuem informações significativas sobre a orientação do cristal, que pode ser bastante sensível, principalmente em cristais finos (*thin-film effect*).[19] Portanto, a exploração das intensidades pode ser fundamental para obter resultados mais

precisos. Recentemente, Palatinus *et al*. [59], mostraram a capacidade de utilizar as intensidades de PED para determinar a orientação de nanocristais visando realizar uma reconstrução tomográfica precisa do espaço recíproco. Surpreendente, a resolução angular obtida com as intensidades (~ 0.05°) é ordens de magnitude maior que a possível obter com *pattern-matching* (usualmente > 1°, mas análises mais refinadas podem obter >0.2°). Assim, a aplicação da análise das intensidades em ACOM pode trazer melhoras significativas na resolução angular das medidas.

Nesse trabalho desenvolvemos ACOM a partir de dados de 4D-STEM assistido por PED e usando um detector CMOS acoplado a um cintilador em TEM (medidas realizadas na University of Texas - San Antonio TX, USA). Para cada posição da sonda (um feixe de elétrons focalizado), um padrão PED de alta qualidade é adquirido e a orientação do cristal é derivada automaticamente em cada pixel pela análise quantitativa das intensidades difratadas (analise similar ao refinamento de Rietveld). A equação de Howie-Whelan (*two-beam*) foi utilizada para a análise quantitativa das intensidades difratadas por essa ser a única descrição de difração dinâmica que possui expressão analítica; isso é fundamental para tornar viável a simulação de intensidades em um grande volume de dados [19]. Aplicamos a metodologia desenvolvida para caracterizar os nanofios de InP semicondutores anteriormente mencionados. Nossos resultados indicam que foi possível obter uma precisão angular maior que as anteriormente reportadas na literatura (~0,03º). Mostramos como diferentes metodologias de ACOM se comportam no mesmo conjunto de dados para obter uma análise rigorosa da qualidade e confiabilidade dos resultados. Esta melhoria de precisão tem sido fundamental para observar a pequena desorientação cristalina associadas a discordância em parafuso nos nanofios com torção de Eshelby [60,61].

Nosso trabalho mostra que os avanços instrumentais devem ser acompanhados por metodologias de análise de dados mais complexas e completas para acessar a informação estrutural de maneira mais precisa e completa. Consequentemente, o trabalho desenvolvido em ACOM abre uma ampla gama de novas possibilidades para analisar com precisão pequenas mudanças na orientação do cristal, como torção de Eshelby NW, rugosidade em material bidimensional [62], *etc*. Veremos no próximo capítulo que a análise de orientação de cristais muito finos e complexos somente é possível devido a capacidade de analisar quantitativamente as intensidades difratadas de PED.

Nosso resultados foram publicados na revista *Ultramicroscopy* [63] (Apêndice C) em conjunto com o material suplementar que acompanha o artigo (Apêndice D).

Capítulo 5

Caracterização das Nanoestrelas de AuAg

Os trabalhos descritos nos capítulos anteriores mostraram a importância de metodologias avançadas para aproveitar a alta qualidade dos dados que é possível obter a partir dos recentes avanços em instrumentação. Dessa forma, podemos então utilizar tais avanços para caracterizar materiais de grande complexidade estrutural, sensíveis a irradiação ou grandes conjuntos de dados para obter informação estatisticamente significante.

Um exemplo desses sistemas complexos são nanoestrelas plasmonicas de AuAg (NS: *nanostar*), um material de interesse em diversas aplicações em dispositivos optoeletrônicos, medicinais, *etc* [64]. A caracterização dessas estruturas da grande ênfase em determinar a forma da nanoestrela, ou mais precisamente, a orientação das pernas no espaço [65] Diferentes distribuições das pernas afetam significativamente a resposta óptica dessas estruturas, tal que o controle de suas propriedades demanda a caracterização da morfologia tridimensional da estrela. Além disso, a caracterização da estrutura atômica permite determinar como parâmetros de síntese afetam a estrutura final da NS, como a distribuição das pernas e largura comprimento. As NSs são formadas por um processo de síntese em etapas: a) primeiro são formadas as sementes (*seeds*) que formaram os núcleos das NS, e b) num segundo estágio são formadas as pernas que crescem sobre os núcleos já constituído.

Técnicas de TEM são usualmente aplicadas para obter tanto informação da forma como da estrutura atômica. A informação da forma da estrela pode ser obtida por técnicas de tomografia com imagens de TEM, onde são obtidas imagens da estrela em muitas (50-70) orientações [65]. A reconstrução da forma 3D pode conter informação da estrutura atômica da amostra dependendo da resolução espacial das imagens utilizadas para realizar a reconstrução [6]. Usualmente são utilizadas imagens de TEM de varredura (STEM) ou mais especificamente imagens de campo escuro de alto ângulo (HAADF: *high angle anular dark field*) devido essas possuírem intensidades com efeitos reduzidos de difração dinâmica, gerando uma imagem onde as intensidades dos pixels são aproximadamente proporcionais a espessura/tipo atômico [19]. No entanto, a reconstrução com alta resolução em regiões extensas (> 200nm x 200nm) é complexa devido à dificuldade em obter as diversas imagens com resolução atômica sem danificar a amostra pela alta dose de elétrons utilizada ($>10^9$ $e^-/Å^2$)[19]. Portanto, tal método não é viável em estruturas que ocupem regiões maiores, como as NS que ocupam uma área

circular de ~ 180 nm de diâmetro. Ao utilizar imagens de menor resolução, a dose de elétrons é significativamente menor < 10^5 -10^6 $e^-/Å^2$ e a morfologia da NS pode ser obtida com resolução espacial de 1 - 2nm. Lamentavelmente, a informação do arranjo atômica não pode ser derivada desse tipo de estudo. Tal dose ainda é significativa para matérias com estrutura sensíveis a irradiação, como estrutura policristalina anteriormente observada nas NS.

Alternativamente, técnicas de 4D-STEM, onde um padrão de difração de elétrons é medido para posição do feixe de elétrons, utilizam baixas doses (<100 $e^-/Å^2$) para obter informação da estrutura atômica do material e da orientação do cristais nas pernas da NS a partir d e um único mapeamento de difração 4D-STEM [66]. Portanto, é possível medir a forma e as estrutura cristalina da NS sem alterar/danificar a estrutura do material.

Nesse trabalho utilizamos 4D-STEM com PED para poder obter a forma da NS com alta precisão e uma baixa dose de elétrons (<200 $e^-/Å^2$), O uso de PED é importante em experimentos com uma grande quantidade de dados coletas (como 4D-STEM) por simplificar o uso de métodos de aprendizado de máquina (ML: *machine learning*) visando a redução de um grande volume de dados a somente que contém informação essencial [40,42]. Em nosso trabalho utilizamos métodos de clusterização (K-means) e fatoração matricial não negativa (NMF: *non-negative matrix factorization*), ambas comumente utilizadas em dados de difração de elétrons [40,42].

A análise por ML separou a NS entre as pernas e o núcleo que a compõem; efetivamente o problema de reconstrução da estrutura e forma da NS não requer a análise da grande quantidade de dados medidas (40000 padrões medidos), sendo somente necessário somente a análise de 11 padrões de difração (núcleo + 6 pontas das pernas + 4 base de pernas).

Nosso estudo provou que as pernas possuem estrutura de decaédrica, similar a nanofios com eixo de simetria cinco (*five-fold nanowires*) e o núcleo da NS é uma partícula icosaédrica. As identificações aproveitam a capacidade de 4D-STEM de formar imagens com diferentes critérios para obter contraste a partir dos padrões de difração medidos. Assim podemos formar imagens que possuam maior sensibilidade a transição entre diferentes cristais (anti-correlação entre pixels) onde um máximo de intensidade indica bordas de grão. Outro tipo de imagens são imagens virtuais de campo escuro (VDF: *virtual dark field*) que indicam a distribuição espacial de algum detalhe do diagrama de difração (ex. um feixe difratado). Essas análises mostram a força de 4D-STEM proveniente da capacidade de correlacionar informação no espaço recíproco com sua localização e organização no espaço real.

A determinação da forma vem da medida da orientação de cada perna por métodos de ACOM, que somente foi possível pela utilização do método de análise de intensidade

desenvolvido neste doutorado e descrito no Capítulo 4. A amostra tem características (e pequenos grãos de espessura ~5 nm nas pernas decaédricas) que tornam a aplicação de ACOM complexa, tal que a resolução angular das medidas é significativamente afetada pelas características da amostra. Os métodos que somente utilizam as posições dos picos têm resolução angular limitada a ~3-5°, tal que não consegue fornecer informação 3D para pernas próximas ao plano perpendicular ao feixe de elétrons. Com as intensidades, foi possível obter resolução angular de ~ 0.1°, um valor mais alto que os anteriormente reportados para análises similares, ver Capítulo 4, (<0.05°), mas que ainda é significativamente mais preciso que analises sem uso das intensidades (>1°).

As medidas da orientação das pernas mostram que elas estão numa configuração muito próxima a um plano em comum (desvio máximo de ~ 20° do plano em comum). A análise da orientação e posições das pernas em relação a orientação do núcleo (determinada independente) indica que as pernas crescem nos vértices de simetria 5 presentes no icosaedro que forma o núcleo da NS. Isto demostra uma relação de epitaxial perna-núcleo o que é consistente com a estrutura decaédrica das pernas.

A distribuição planar das 6 pernas sobre núcleo de simetria icosaédrica não é esperada, pois há 12 vértices distribuídos regularmente no espaço sobre um icosaedro, onde as pernas podem crescer. Nossa interpretação para esse resultado, que não está somente associado ao arranjo atômico do núcleo, vem da nucleação de uma perna em um dos eixos de simetria 5 implicar na redistribuição do passivante presente na superfície do NP, tal que os eixos de simetria 5 vizinhos se tornam as posições mais prováveis para nucleação da próxima perna. À medida que a pernas nucleiam, o passivante se compacta nas posições ortogonais na linha de cisalhamento da capa de surfactante determinada pelas duas primeiras pernas formadas. Isso inibe nucleação nessas regiões e permite crescimento das pernas somente num plano.

O trabalho aqui desenvolvido mostra que 4D-STEM + PED pode ser utilizada para caracterizar completamente estrutura muito complexas, como as NS medidas, com uma baixa dose de elétrons (<200 $e^-/Å^2$). Uma compreensão maior sobre o processo de crescimento das NS exige a análise de outras variações morfológicas (NS com 5 ou 7 pernas). Além disso, a caracterização estrutural completa desses sistemas envolve conhecer as estruturas envolvidas nos diferentes estágios da síntese. Portanto ainda é necessário caracterizar com ePDF a estrutura das sementes iniciais utilizadas para crescer as estrelas. Assim, a cristalografia de elétrons quantitativa, com o auxílio de PED, fornece todas as ferramentas necessárias para estudar em detalhe esse complexo processo de síntese.

Os resultados do trabalho foram publicados na revista *ACS Nano* (Apêndice E) em conjunto com o material suplementar que acompanha o artigo (Apêndice F).

Capítulo 6

Conclusões e Perspectivas

Devido ao formato da tese ser um compilado dos artigos publicados durante o doutorado, esse capítulo resume os principais resultados em conjunto com uma contextualização dos principais problemas de nossa pesquisa.

A forte seção eficaz de interação entre elétrons e a matéria permite obter padrões de EDs de alta qualidade com amostras pequenas [4]. No entanto, essa forte interação também induz que o elétron sofra múltiplos eventos de espalhamento ao atravessar os materiais, fenômeno que leva a geração de difração dinâmica [4]. A simulação da difração no caso dinâmico requer ferramentas numéricas e, em particular demanda o conhecimento preciso da espessura e orientação do cristal. Devido a complexidade do cálculo de difração dinâmica, não é possível realizar um procedimento de refinamento estrutural de forma prática. Ainda assim, a capacidade de obter sinal de difração de amostras pequenas ou contendo átomo de baixo número atômico traz um grande interesse a cristalografia de elétrons na indústria farmacêutica. De fato, nos últimos anos temos visto a comercialização de difratômetros de elétrons, equivalentes ao comumente encontrado difratômetros de raios X. Utilizando elétrons é possível medir os cristais micrométricos como contidos em medicamentos que chegam ao consumidor, o que torna os processos de desenvolvimento de fármacos mais eficientes e seguros [47,67].

A confiabilidade da cristalografia de elétrons tem sido considerada baixa devido falta de correlação direta entre intensidades da difração de elétrons e, intensidades calculadas pelo simples modelo cinemático baseado no fator de estrutura. A difração de elétrons PED recupera a uma relação razoável entre as intensidades de difração de elétrons e o fator de estrutura; por isso a PED pode ser considerada quase-cinemática, onde as intensidades experimentais são muito próximas das esperadas cinematicamente [10,11]. Portanto, PED é uma técnica com as características necessárias para desenvolver e explorar as potencialidades da cristalografia de elétrons.

Nesta tese, temos apresentado o estudo do arranjo atômico em nanopartículas decaédricas que demostra a grande potencialidade da cristalografia de elétrons para estudar pequenas NPs (diâmetro < 5 nm), pelo refinamento estrutural no espaço real usando PDF derivada de um padrão de difração de pó [8,9]. Este tipo de informação não pode ser derivado

de métodos tradicionais; por exemplo, imagens com resolução atômica demandam que o cristal esteja alinhado ao longo de um eixo de simetria (eixo de zona) do cristal [52]. Assim, a maior parte dos estudos de decaedros explora imagens de partículas é observada ao longo do eixo de simetria cinco, e não é possível obter informação ao longo dessa direção devido à natureza de projeção em 2D do objeto 3D. O uso baseado na PDF ameniza a perda de informação estrutural acessível no espaço recíproco (alargamento de picos de difração) devido a limitação no ordenamento dos átomos; de fato a PDF representa o principal método de análise materiais amorfos [8,9] . A obtenção da função PDF com boa resolução requer medir padrões de difração de pó com vetor de espalhamento significativamente maiores que o comumente utilizados em cristalografia comum [8,9]. Consequentemente, PDF é associada a difração de ondas de alta energia (pequenos comprimentos de onda) geradas com fontes de radiação síncrotron de alta energia (40 – 120 keV) o que a torna uma técnica menos acessível. Alternativamente microscópios eletrônicos são instrumentos mais numerosos e acessíveis, que fornecem medidas de padrões de difração de elétrons de alta qualidade e que pode ser obtido em TEM considerados de baixa performance quando comparada a instrumentação moderna. Durante o meu mestrado, foi desenvolvida a metodologia de PED + PDF que possibilita o refinamento estrutural com qualidade similar a obtida com radiação síncrotron, mas utilizando massas muito menores (~ fg) [12]. No Capítulo 3, apresentamos uma medida estrutural de alta qualidade utilizando os métodos aqui desenvolvido de nanocristalografia baseada em PDF para a caracterização de NPs decaédricas. Nesse estudo, demostramos que o refinamento estrutural indica uma célula unitária BCO que se superpõe com BCT dentro da barra de erro [16,17]. Também provamos que podemos descartar o modelo de BCO Bagley com expansão da distância inter atômica de 5% ao longo de eixo de simetria 5 (no BCT essa distorção não ocorre) [15]. É importante enfatizar que ao utiliza uma métrica de qualidade (resíduo) é possível determinar com precisão a rica informação estrutural presente nas intensidades e posições dos picos de difração de PED.

No Capítulo 4, abordamos o problema da nanocristalografia de monocristais, novamente baseado na análise quantitativa das intensidades de PED, e neste caso explorado para medir a orientação de cristais de forma automática (ACOM) [41,43,57,58]. Nesses estudos, aliamos a alta resolução espacial possível em um TEM com o poder da análise cristalográfica de PED. Usualmente, os métodos ACOM identificam a orientação através de uma correlação cruzada (*pattern-matching)* entre o ED medido e uma biblioteca de padrões simulados. As intensidades do ED não são utilizadas para aumentar a velocidade do cálculo, tal que as posições dos picos difratados é a principal informação utilizada. No entanto, essa análise compromete a

resolução angular a valores da ordem do grau. De ponto de vista físico, devemos esperar que as intensidades difratadas forneçam informações detalhadas sobre a orientação do cristal; de fato, o trabalho realizado por Palatinus *et al* [59], mostrou que procedimentos de análise de intensidade podem fornecer a orientação de nanocristais com uma resolução angular (~ 0.05°), ordens de magnitude maior que a possível obter com *pattern-matching*.

A análise das intensidades pode trazer melhoras significativas aos procedimentos em ACOM, mas o mapeamento de orientação requer detectar milhares padrões de difração de alta qualidade; neste aspecto detectores bidimensionais de alta velocidade são necessários. Detectores CCD possuem a velocidade de captura limitada a 1x imagem por segundo, e não são apropriados para mapeamento ACOM (por exemplo, a medida de 10000 PED demanda quase 3h). Detectores de elétrons CMOS podem realizar 200 capturas por segundo (10000 PED demanda menos de 1 minuto), e também possuem um nível de ruido menor que detectores CCD. Nos colaboramos com o Prof. Dr. Arturo Ponce (UTSA – San Antonio) que possui um instrumento TEM com sistema PED e o detector CMOS que viabilizava o nosso experimento sugerido (no Brasil ainda não é possível encontrar instrumentação similar). A nossa análise de intensidade baseia-se numa célula unitária onde os parâmetros estruturais são mantidos fixos e somente a orientação do cristal e a espessura do cristal são otimizadas. Utilizamos um modelo de dois feixes (*two-beam*) [4] pois ele permite uma estimação aproximada de intensidades PED utilizando uma expressão analítica, garantindo o tratamento viável de milhares de ED num mapeamento. A resolução angular resultante é de 0.03º, valor similar ao obtido por Palatinus, e muito mais preciso que o método tradicional utilizando *pattern-matching* [63].

É importante enfatizar que a capacidade de medir orientação de cristais com alta precisão é fundamental para o estudo de deformação (*strain*) de cristais. O estudo de deformação de nanomateriais usualmente se limita a medir a tensão (tração ou compreensão) da célula unitária no plano perpendicular ao feixe incidente ao medir a posição dos picos de difração [55]. No entanto, uma deformação estrutural genérica é composta de tensão e cisalhamento, sendo a última presente em mudanças na orientação dos vetores base da célula unitária [68]. Portanto a metodologia desenvolvida é fundamental para a medida completa de uma deformação, combinando a medida no plano ortogonal ao feixe com mais uma possível sutil rotação do cristal.

Os estudos precedentes descrevem as nossas contribuições a nanocristalografia de elétrons para a análise de amostras bem-comportadas ou casos teste. Para demostrar claramente o avanço atingido, é importante provar que esses desenvolvimentos são uteis para resolver casos complexos onde métodos de caracterização comuns não são apropriados. A esse fim, decidimos

estudar nanoestrelas plasmônicas de AuAg (produzidas pela Prof. Dra. Laura Fabris, Politecnico di Torino), que representam um problema de alta importância científica e tecnológica onde é necessário determinar a estrutura atômica e a morfologia (distribuição espacial das pernas) para aprimora a resposta óptica [65] .

Usualmente, técnicas de imagem TEM de resolução atômica são combinadas com tomografia (STEM-ET) para reconstruir a estrutura atômica em 3D [6]. A medida de imagens com resolução atômica requer um feixe de elétron com dimensões usuais de 0.05 nm em diâmetro que utiliza ângulos de convergência na ordem de 20 – 25 mrad. Tais ângulos de convergência implica num ponto focal com tamanho longitudinal (na direção do feixe) limitado a 5 – 7 nm [69]. Durante o experimento de ET o objeto é comumente rotacionado entre -70º e + 70 graus para reconstruir a estrutura 3D. Em objetos extensos como na nanoestrela, objeto ficaria fora de foco, inviabilizado ET baseada no modo HAADF-STEM. Nossa abordagem foi diferente: a) utilizamos um mapeamento de difração PED para obter informações da estrutura atômica com resolução manométrica; b) medimos as posições espaciais das pernas combinando os comprimentos obtidos das imagens e a orientação dos cristais nas pernas pela análise de intensidades PED medidas numa câmera de alta velocidade e alta gama dinâmica.

A necessidade de alta resolução espacial e PED requer instrumentação especial disponível em poucos lugares no mundo, a qual tivemos acesso através de colaboração com Prof. Dr. Caterina Ducatti (Cambridge University). Trata-se de um microscópio ThermoFisher Spectra 300 (300 keV) com corretor de aberração esférica, equipado com um detector de detecção direta Quantum Detector Merlin e um sistema de precessão de alta frequência (1 kHz). O corretor de aberração esférica permite atingir 1º sem perdas significativas na resolução espacial (em nosso experimento o feixe possui ~ 2 nm) e melhora significativamente a correspondência entre intensidades medidas e simuladas pelo modelo baseado na aproximação *two -beam* (Capítulo 4). A NS ocupa uma área de ~ 800 nm^2, portanto o mapeamento de difração demanda a medida de uma quantidade expressiva de padrões de difração. Isto foi solucionado pela câmera Merlin que realiza aproximadamente 2000 capturas por segundo, e um sistemas de precessão poco convencional que opera a de 1 kHz (normalmente utiliza-se 100 Hz limitando o tempo de captura por imagem). Portanto, podemos medir conjunto de dados extensos (em nosso experimento 40000 padrões PED são medidos) em tempos de poucos minutos.

Primeiro, a análise dos padrões de difração das pernas da NS indica que elas possuem estrutura decaédricas, e foi possível medir a orientação das pernas no utilizando a metodologia desenvolvida para o uso das intensidades (Capítulo 4). Também determinamos que o núcleo é uma nanopartícula icosaédrica, e as pernas crescem sobre os vértices do icosaedro. Este

resultado contradiz o modelo geralmente aceito na comunidade de nanopartículas plasmônicas que associam estrelas a núcleos decaédricos. Outro resultado inesperado é uma distribuição quase-planar das pernas no espaço, contradizendo a alta simetria de um núcleo icosaédrico. A morfologia da estrela nos permitiu desenvolver um novo modelo da formação da nanoestrela, que envolve um papel determinante da reordenação da camada de surfactante sobre o núcleo icosaedrico. Finalmente, devemos ressaltar que nosso estudo revelo muitos novos aspectos da estrutura de nanoestrela, com informações obtidas de único mapeamento 4D-STEM + PED aplicando uma baixa dose de elétrons (<200 $e^-/Å^2$).

Consideramos que o trabalho desenvolvido mostra o grande poder da cristalografia de elétrons para caracterização de nanocristais, O uso quantitativo das intensidades de PED, traz vantagens significativas, e demos enfatizar nossos esforços para derivar medidas estruturais com intervalos de confiança, fornecendo clara informação da resolução e representatividade das propriedades estruturais medidas.

Perspectivas

A análise de PDF + PED pode atingir resultados de altíssima qualidade mesmo com instrumentações simples, mas é importante reconhecer que limitações instrumentais encontradas em nosso trabalho podem ser facilmente superadas utilizando microscópios modernos. A mais evidente está relacionada a resolução limitada da PDF derivada devido ao tamanho do detector utilizado (2048x2048 pixels). O uso de detectores CMOS modernos fornece áreas maiores (4096x4096) para medir padrões de difração com vetores de espalhamento maiores (CCD: ~ 12 $Å^{-1}$, CMOS ~ 24 $Å^{-1}$), comparáveis as obtidos em experimentos de raios X utilizando fontes de luz sincrotron. A razão sinal-ruido dos experimentos também pode ser significativamente melhorada ao utilizar filtros de energia para reduzir o fundo proveniente do espalhamento inelástico dos elétrons. As doses também podem ser significativamente reduzidas ao utilizar detectores diretos de elétrons, já que hoje já é possível encontrar essa classe de detectores com tamanho suficiente para análise de PDF (por exemplo, a câmera K3 da Gatan possui ~ 5000x5000 pixels). Também é possível realizar melhorias significativas na modelagem utilizadas nas simulações de PDF, por exemplo, ao incluir efeitos mais realísticos dos movimentos dos átomos devido a temperatura (por exemplo, simulações com *fronzen-phonos* [4]) ou ao incluir deformações mais precisas na estrutura que poderiam ser analisadas ao melhorar a resolução da curva PDF. Todos esses fatores são essenciais para expandir o nosso estudo da estrutura das NPs decaédricas como a diferenciação entre modelos de deformação uniforme ou inomogênea.

A aplicação da análise quantitativa das intensidades necessita principalmente de melhoras práticas para simplificar, tornar mais acessível e acelerar os procedimentos numéricos utilizados. É importante enfatizar, que o artigo trás questões em relação a acurácia da metodologia que foram posteriormente respondidas no trabalho de caracterização das nanoestrelas, portanto, não há razão para realizar outros trabalhos sobre a confiabilidade da metodologia. Também é evidente no trabalho das nanoestrelas que a maior dificuldade em aplicar a metodologia está na necessidade de indexar os padrões de difração (o que requiriu a análise manual). A combinação entre *pattern-matching* e análise quantitativa das intensidades pode automatizar muitos dos passos iniciais da análise ao fornecer a indexação, eixo de zona e fase que melhor se adequem a cada padrão de difração medido. O tempo de análise também pode ser diminuído ao utilizar métodos de minimização mais eficientes e a paralelização dos mesmos.

As nanoestrelas são fabricadas por um método em duas etapas, crescimento dos núcleos (*seeds*) e o subsequente crescimento das pernas [21]. A caracterização completa da síntese ainda necessita da análise das sementes, e o método de PDF+ PED desenvolvido fornece a ferramenta ideal para tal. Estes experimentos estão sendo planejados para serem realizado com a instrumentação presente em Cambridge. Também é necessário caracterizar outras morfologias das nanoestrelas (5 ou 7 pernas) para determinar como os parâmetros da síntese afetam a distribuição e o número de pernas.

Finalmente, também planejamos explorar outras possibilidades como a combinação de 4D-STEM com PDF + PED para caracterizar materiais amorfos ou de baixa cristalinidade como metais amorfos.

Capítulo 7

Bibliografia

1. Baig, N., Kammakakam, I., Falath, W. & Kammakakam, I. Nanomaterials: A review of synthesis methods, properties, recent progress, and challenges. *Materials Advances* (2021) doi:10.1039/d0ma00807a.

2. Holder, C. F. & Schaak, R. E. Tutorial on Powder X-ray Diffraction for Characterizing Nanoscale Materials. *ACS Nano* 13, 7359–7365 (2019).

3. Billinge, S. J. L. & Levin, I. The Problem with Determining Atomic Structure at the Nanoscale. *Science (1979)* 316, 561–565 (2007).

4. Williams, D. B. & Carter, C. B. *Transmission Electron Microscopy: A Textbook for Materials Science*. (Springer Science, 2009).

5. Petkov, V., Prasai, B., Ren, Y., Shan, S., Luo, J., Joseph, P. & Zhong, C. J. Solving the nanostructure problem: Exemplified on metallic alloy nanoparticles. *Nanoscale* (2014) doi:10.1039/c4nr01633e.

6. Zhou, J., Yang, Y., Ercius, P. & Miao, J. Atomic electron tomography in three and four dimensions. *MRS Bulletin* (2020) doi:10.1557/mrs.2020.88.

7. Moniri, S., Yang, Y., Ding, J., Yuan, Y., Zhou, J., Yang, L., Zhu, F., Liao, Y., Yao, Y., Hu, L., Ercius, P. & Miao, J. Three-dimensional atomic structure and local chemical order of medium- and high-entropy nanoalloys. *Nature* (2023) doi:10.1038/s41586-023-06785-z.

8. Egami, T. & Billinge, S. J. L. *Underneath the Bragg Peaks*. *Materials Today* vol. 6 (Elsevier Ltd., 2003).

9. Christiansen, T. L., Cooper, S. R. & Jensen, K. M. O. There's no place like real-space: Elucidating size-dependent atomic structure of nanomaterials using pair distribution function analysis. *Nanoscale Adv* (2020) doi:10.1039/d0na00120a.

10. Vincent, R. & Midgley, P. A. Double conical beam-rocking system for measurement of integrated electron diffraction intensities. *Ultramicroscopy* 53, 271–282 (1994).

11. Midgley, P. A. & Eggeman, A. S. Precession electron diffraction – a topical review. *IUCrJ* 2, 126–136 (2015).

12. Corrêa, L. M., Moreira, M., Rodrigues, V. & Ugarte, D. Quantitative Structural Analysis of AuAg Nanoparticles Using a Pair Distribution Function Based on Precession Electron Diffraction: Implications for Catalysis. *ACS Appl Nano Mater* (2021) doi:10.1021/acsanm.1c02978.

13. Hoque, M. M., Vergara, S., Das, P. P., Ugarte, D., Santiago, U., Kumara, C., Whetten, R. L., Dass, A. & Ponce, A. Structural Analysis of Ligand-Protected Smaller Metallic Nanocrystals by Atomic Pair Distribution Function under Precession Electron Diffraction. *The Journal of Physical Chemistry C* 123, 19894–19902 (2019).

14. Ophus, C. Four-Dimensional Scanning Transmission Electron Microscopy (4D-STEM): From Scanning Nanodiffraction to Ptychography and Beyond. *Microscopy and Microanalysis* 25, 563–582 (2019).

15. BAGLEY, B. G. A Dense Packing of Hard Spheres with Five-fold Symmetry. *Nature* 208, 674–675 (1965).

16. Sun, Y., Ren, Y., Liu, Y., Wen, J., Okasinski, J. S. & Miller, D. J. Ambient-stable tetragonal phase in silver nanostructures. *Nat Commun* (2012) doi:10.1038/ncomms1963.

17. Mettela, G., Bhogra, M., Waghmare, U. V. & Kulkarni, G. U. Ambient Stable Tetragonal and Orthorhombic Phases in Penta-Twinned Bipyramidal Au Microcrystals. *J Am Chem Soc* 137, 3024–3030 (2015).

18. Zhiping Luo. *A Practical Guide to Transmission Electron Microscopy: Fundamentals*. (Momentum Press, 2016).

19. Carter, C. B. & Williams, D. B. *Transmission Electron Microscopy: Diffraction, Imaging and Spectrometry*. (Springer International Publishing, 2016). doi:10.1007/978-3-319-26651-0.

20. Ji, D. *et al.* Freestanding crystalline oxide perovskites down to the monolayer limit. *Nature* 570, 87–90 (2019).

21. Barringer, R. Illuminating the secrets of crystals: microcrystal electron diffraction in structural biology. *Bioscience Horizons: The International Journal of Student Research* 11, (2018).

22. Cowley, J. M. *Diffraction Physics*. (Elsevier, 1995).

23. De Graef, M. *Introduction to Conventional Transmission Electron Microscopy*. (Cambridge University Press, 2003).

24. Dinnebier, R. E. & Billinge, S. J. L. *Powder Diffraction*. (Royal Society of Chemistry, 2008).

25. Hirsch, P. B. *Electron Microscopy of Thin Crystals*. (Butterworth & Co., 1971).

26. Kirkland, E. J. *Advanced Computing in Electron Microscopy*. (Springer US, 2010).

27. Hall, B. D., Ugarte, D., Reinhard, D. & Monot, R. Calculations of the dynamic Debye–Scherrer diffraction patterns for small metal particles. *J Chem Phys* 103, 2384–2394 (1995).

28. Hall, B. D., Ugarte, D., Reinhard, D. & Monot, R. Calculations of the dynamic Debye–Scherrer diffraction patterns for small metal particles. *J Chem Phys* 103, 2384–2394 (1995).

29. White, T. A., Eggeman, A. S. & Midgley, P. A. Is precession electron diffraction kinematical? Part I: 'Phase-scrambling' multislice simulations. *Ultramicroscopy* (2010) doi:10.1016/j.ultramic.2009.10.013.

30. Eggeman, A. S., White, T. A. & Midgley, P. A. Is precession electron diffraction kinematical? Part II. A practical method to determine the optimum precession angle. *Ultramicroscopy* (2010) doi:10.1016/j.ultramic.2009.10.012.

31. Eggeman, A. S., White, T. A., Midgley, P. A., Eggeman, A. S. & Midgley, P. A. Is precession electron diffraction kinematical? Part I: *Ultramicroscopy* 110, 771–777 (2010).

32. Own, C. S., Sinkler, W. & Marks, L. D. Rapid structure determination of a metal oxide from pseudo-kinematical electron diffraction data. *Ultramicroscopy* 106, 114–122 (2006).

33. Klein, H. & David, J. The quality of precession electron diffraction data is higher than necessary for structure solution of unknown crystalline phases. *Acta Crystallogr A* 67, 297–302 (2011).

34. Eggeman, A. S. & Midgley, P. A. Refining structures against reflection rank: an alternative metric for electron crystallography. *Acta Crystallogr A* 68, 352–358 (2012).

35. Oleynikov, P., Hovmöller, S. & Zou, X. D. Precession electron diffraction: Observed and calculated intensities. *Ultramicroscopy* 107, 523–533 (2007).

36. Thomas, J. M., Leary, R. K., Eggeman, A. S. & Midgley, P. A. The rapidly changing face of electron microscopy. *Chem Phys Lett* 631–632, 103–113 (2015).

37. Clough, R. & Kirkland, A. I. Direct Digital Electron Detectors. in *Advances in Imaging and Electron Physics* (2016). doi:10.1016/bs.aiep.2016.09.001.

38. MacLaren, I., Frutos-Myro, E., McGrouther, D., McFadzean, S., Weiss, J. K., Cosart, D., Portillo, J., Robins, A., Nicolopoulos, S., Nebot del Busto, E. & Skogeby, R. A Comparison of a Direct Electron Detector and a High-Speed Video Camera for a Scanning Precession Electron Diffraction Phase and Orientation Mapping. *Microscopy and Microanalysis* 26, 1110–1116 (2020).

39. Moeck, P., Rouvimov, S., Rauch, E. F., Véron, M., Kirmse, H., Häusler, I., Neumann, W., Bultreys, D., Maniette, Y. & Nicolopoulos, S. High spatial resolution semi-automatic crystallite orientation and phase mapping of nanocrystals in transmission electron microscopes. in *Crystal Research and Technology* (2011). doi:10.1002/crat.201000676.

40. Eggeman, A. S., Krakow, R. & Midgley, P. A. Scanning precession electron tomography for three-dimensional nanoscale orientation imaging and crystallographic analysis. *Nat Commun* (2015) doi:10.1038/ncomms8267.

41. MacLaren, I., Frutos-Myro, E., McGrouther, D., McFadzean, S., Weiss, J. K., Cosart, D., Portillo, J., Robins, A., Nicolopoulos, S., Nebot del Busto, E. & Skogeby, R. A Comparison of a Direct Electron Detector and a High-Speed Video Camera for a Scanning Precession Electron Diffraction Phase and Orientation Mapping. *Microscopy and Microanalysis* 26, 1110–1116 (2020).

42. Martineau, B. H., Johnstone, D. N., van Helvoort, A. T. J., Midgley, P. A. & Eggeman, A. S. Unsupervised machine learning applied to scanning precession electron diffraction data. *Adv Struct Chem Imaging* 5, 3 (2019).

43. Rauch, E. F., Portillo, J., Nicolopoulos, S., Bultreys, D., Rouvimov, S. & Moeck, P. Automated nanocrystal orientation and phase mapping in the transmission electron microscope on the basis of precession electron diffraction. *Zeitschrift für Kristallographie* 225, (2010).

44. Rietveld, H. M. A profile refinement method for nuclear and magnetic structures. *J Appl Crystallogr* 2, 65–71 (1969).

45. Pecharsky, V. & Zavalij, P. *Fundamentals of Powder Diffraction and Structural Characterization of Materials*. (Springer US, 2009).

46. Willinger, E. Analysis of Local Structure by Atomic Pair Distribution Function. *Lecture series: Modern Methods in Heterogeneous Catalysis Research* 65 http://www.fhi-berlin.mpg.de/acnew/department/pages/teaching/pages/teaching__wintersemester__2016_2017/elena_willinger__analysis_of_local_structure_by_atomic_pair_distribution_function__170203.pdf (2016).

47. Gemmi, M., Mugnaioli, E., Gorelik, T. E., Kolb, U., Palatinus, L., Boullay, P., Hovmöller, S. & Abrahams, J. P. 3D Electron Diffraction: The Nanocrystallography Revolution. *ACS Cent Sci* 5, 1315–1329 (2019).

48. Cullity, B. D. & Stock, S. R. *Elementes of X-Ray Diffraction*. (Pearson Education Limited, 2014).

49. Tran, D. T., Svensson, G. & Tai, C.-W. SUePDF : a program to obtain quantitative pair distribution functions from electron diffraction data. *J Appl Crystallogr* 50, 304–312 (2017).

50. Gorelik, T. E., Neder, R., Terban, M. W., Lee, Z., Mu, X., Jung, C., Jacob, T. & Kaiser, U. Towards quantitative treatment of electron pair distribution function. *Acta Crystallogr B Struct Sci Cryst Eng Mater* 75, 532–549 (2019).

51. Marks, L. D. Experimental studies of small particle structures. *Reports on Progress in Physics* 57, 603–649 (1994).

52. Yang, C. Y. Crystallography of decahedral and icosahedral particles. *J Cryst Growth* 47, 274–282 (1979).

53. Jia, C., Lin, Z., Huang, Y. & Duan, X. Nanowire Electronics: From Nanoscale to Macroscale. *Chem Rev* 119, 9074–9135 (2019).

54. Güniat, L., Caroff, P. & Fontcuberta I Morral, A. Vapor Phase Growth of Semiconductor Nanowires: Key Developments and Open Questions. *Chem Rev* 119, 8958–8971 (2019).

55. Cooper, D., Denneulin, T., Bernier, N., Béché, A. & Rouvière, J. L. Strain mapping of semiconductor specimens with nm-scale resolution in a transmission electron microscope. *Micron* 80, 145–165 (2016).

56. Ugarte, D., Tizei, L. H. G., Cotta, M. A., Ducati, C., Midgley, P. A. & Eggeman, A. S. Analysis of structural distortion in Eshelby twisted InP nanowires by scanning precession electron diffraction. *Nano Res* 12, 939–946 (2019).

57. Cautaerts, N., Crout, P., Ånes, H. W., Prestat, E., Jeong, J., Dehm, G. & Liebscher, C. H. Free, flexible and fast: Orientation mapping using the multi-core and GPU-accelerated template matching capabilities in the Python-based open source 4D-STEM analysis toolbox Pyxem. *Ultramicroscopy* 237, 113517 (2022).

58. Savitzky, B. H. *et al.* py4DSTEM: A Software Package for Four-Dimensional Scanning Transmission Electron Microscopy Data Analysis. *Microscopy and Microanalysis* 27, 712–743 (2021).

59. Palatinus, L., Brázda, P., Jelínek, M., Hrdá, J., Steciuk, G. & Klementová, M. Specifics of the data processing of precession electron diffraction tomography data and their implementation in the program PETS2.0. *Acta Crystallogr B Struct Sci Cryst Eng Mater* (2019) doi:10.1107/S2052520619007534.

60. Eshelby, J. D. The twist in a crystal whisker containing a dislocation. *https://doi.org/10.1080/14786435808244565* 3, 440–447 (2006).

61. Eshelby, J. D. Screw Dislocations in Thin Rods. *J Appl Phys* 24, 176 (2004).

62. Shao, F. *et al.* Substrate influence on transition metal dichalcogenide monolayer exciton absorption linewidth broadening. *Phys Rev Mater* (2022) doi:10.1103/PhysRevMaterials.6.074005.

63. Corrêa, L. M., Ortega, E., Ponce, A., Cotta, M. A. & Ugarte, D. High precision orientation mapping from 4D-STEM precession electron diffraction data through quantitative analysis of diffracted intensities. *Ultramicroscopy* (2024) doi:10.1016/j.ultramic.2024.113927.

64. Ngo, N. M., Tran, H.-V. & Lee, T. R. Plasmonic Nanostars: Systematic Review of their Synthesis and Applications. *ACS Appl Nano Mater* 5, 14051–14091 (2022).

65. Atta, S., Beetz, M. & Fabris, L. Understanding the role of AgNO 3 concentration and seed morphology in the achievement of tunable shape control in gold nanostars. *Nanoscale* 11, 2946–2958 (2019).

66. Macpherson, S. *et al.* Local nanoscale phase impurities are degradation sites in halide perovskites. *Nature* (2022) doi:10.1038/s41586-022-04872-1.

67. Brown, A. & Clardy, J. Tiny crystals have big potential for determining structures of small molecules. *Nature* 564, 348–349 (2018).

68. Kelly, A. & Knowles, K. M. *Crystallography and Crystal Defects*. (Wiley, 2012). doi:10.1002/9781119961468.

69. Hovden, R. & Muller, D. A. Electron tomography for functional nanomaterials. *MRS Bull* 45, 298–304 (2020).

Apêndice A

Desvendando a Ordem Atômica Não Cúbica em Nanopartículas Decaédricas de AuAg Livres de Surfactante por Análise da Função de Distribuição de Pares (PDF)

A seguir está anexado o manuscrito do artigo nomeado *"Unraveling non-cubic atomic ordering in surfactant-free AuAg decahedral nanoparticles by Pair Distribution Function (PDF) analysis"* que descreve o trabalho descrito no Capítulo 2 da tese. O artigo ainda está em processo de submissão.

Unraveling non-cubic atomic ordering in surfactant-free AuAg decahedral nanoparticles by Pair Distribution Function (PDF) analysis

Leonardo M. Corrêa[1], Murilo Moreira[1], Varlei Rodrigues[1] and Daniel Ugarte[1,]*

1 Instituto de Física "Gleb Wataghin", Universidade Estadual de Campinas-UNICAMP, CEP 13083-859, Campinas - SP, Brazil.
* dmugarte@ifi.unicamp.br

Abstract

The atomic arrangement in 5-fold decahedral (Dh) nanoparticles (NPs) made of noble metals remains an open and contentious question. In the 60s, Bagley proposed a structural description, where the face centered cubic (*FCC*) crystal is homogeneously strained into a body centered orthorhombic (*BCO*) one; this construction requires a large 5% expansion of interatomic distances along the 5-fold axis. This model has been questioned due to evidence of localized deformations (inhomogeneous strain) and of Dh nanostructures with body centered tetragonal lattice (*BCT*) as revealed by x-ray diffraction. Transmission electron microscopy (TEM) has also been explored to visualize strain fields using images taken along the 5-fold axis. However, the 2D projection nature of TEM images inhibit the complete three-dimensional distortion field assessment, hindering the direct comparison between the proposed *BCO* and *BCT* ordering. Here, we have studied the average unit-cell symmetry and size in few-nm-wide surfactant-free noble metal (AuAg) nanoparticles; we have applied a structural refinement method based on Pair Distribution Function (PDF) derived from Precession Electron Diffraction (PED). This approach provides 3D information from a minute amount (< fg) of NPs deposed on a convention TEM grid. Two main conclusions can be derived from structure optimization; firstly, minimum residue is associated to a *BCO* unit-cell close to tetragonal symmetry (*BCT*). Secondly, the traditional Bagley *BCO* model is clearly unable to provide a good description of experiments, what suggests that it must be used with care for the modeling of Dh nanoparticles. Our structural refinement has followed rigorous error bars estimation and solution search procedures considering physical constrains and a minimal number of variables. This study demonstrates the exciting potential of (PDF +PED) to quantitatively obtain fine details of the average unit cell in small nanocrystals using a low electron irradiation dose (10 e/Å^2).

KEYWORDS: Pair Distribution Function (PDF), Decahedral Nanoparticles, 3D strain, Transmission Electron Microscope (TEM), Precession Electron Diffraction (PED), Nanocrystallography.

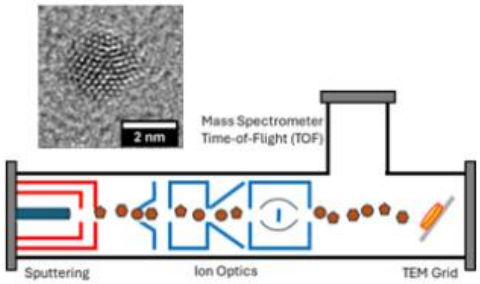

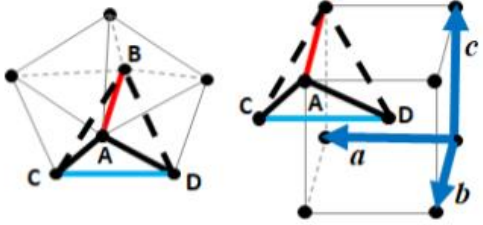

Pair Distribution Function

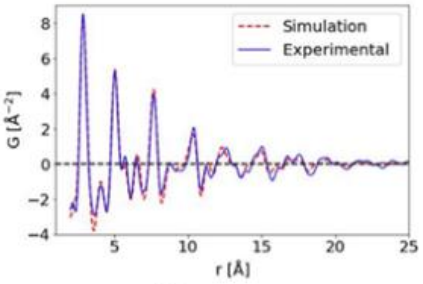

5-fold axis $\begin{cases} {}^{c}/_{a} = 1.376 \\ \overline{AC} = \overline{BC} = \overline{AD} = \overline{BD} \end{cases}$

Structural Refinement

$\overline{AB} = \overline{AC}$ ☞ ${}^{a}/_{b} = (1.02 \pm 0.01)$

Introduction

The term Multiply Twinned Particles (MTP) describe nanoparticles (NPs) which are formed by the assembly of several tetrahedral joined through twin planes, such as noble metal icosahedra or decahedra. The twin planes occur around one or several high symmetry axes, and in particular MTPs include 5-fold rotation axis[1]. Decahedral (Dh) symmetry contains a single 5-fold axis and it constitute the basis for a plethora of nanostructures such as nanorods, nanowires (NWs), bipyramids, nanostars, etc.[2,3]

The Dh atomic arrangement must form a closed structure filling space without gaps inside its volume; this condition cannot be fulfilled when Au or Ag atom are in the bulk stable phase, a face centered cubic (*FCC*) crystal structure. In the 60s, Bagley proposed a simple geometric construction based on optimizing the packing of rigid spheres into a Dh 5-fold motif [4]; this proposed arrangement contains a homogeneous distortion of the cubic lattice towards a body centered orthorhombic (*BCO*) unit cell (Figure 1), as discussed in detail by Yang.[5] One notable aspect of this *BCO* structure is a significant expansion (5%) of the interatomic distance along 5-fold axis direction. In contrast, several experimental and theoretical studies have suggested that inhomogeneous strain (localized deformations) should be the energetically preferred configuration in noble metal Dh NPs[6-9]. Also, recent x-ray diffraction studies of Dh nanostructures suggest a body center tetragonal (BCT) symmetry[10,11].

Transmission electron microscopy (TEM) has been the basic tool to characterize structural feature of Dh NPs. Atomic resolution images based on High Angle Annular Dark Field Scanning TEM (HAADF-STEM) or High-Resolution TEM modes (HRTEM) allow the easy identification of individual Dh NPs observed along the 5-fold symmetry axis[2,6,7,9]. However, these images represent a bi-dimensional (2D) projection of the imaged object; then only provide information averaged along the incident electron beam direction[12]. The 2D projection nature significantly hinders a complete picture of the three-dimensional (3D) deformation field and hides any interatomic distance expansion along observation direction. An atomic resolution electron tomography (ATM) study of a Au Dh (~17 nm in diameter) revealed the occurrence of inhomogeneous strain, but the Bagley´s 5% expansion along the 5-fold axis was not detected[7]. ATM requires the acquisition several tens of HAADF STEM images (50-70 images) with atomic resolution and the use of a rather high electron irradiation dose (10^5-10^7 $e^-/Å^2$)[13]. It is always important to note that high electron irradiation levels may induce modifications of nanostructures[13-15].

Powder x-ray diffraction (PXRD) techniques acquired in modern synchrotron sources have already been utilized to Dh atomic arrangement in macroscopic samples of long Dh Ag nanowires (60-80 nm in diameter, several microns in length)[8,10,16,17]. Some groups have reported that *BCT* structures provides a better description of PXRD patterns results; this unit cell is much closer from traditional noble metal *FCC* than the Bagley´s *BCO* structure[10,11]. Concerning few nm wide nanoparticles, the low interaction cross-section between x-ray and matter induces a rather low signal-to-noise ratio even using advanced synchrotron. Also, these experiments remain quite challenging as they require uniform samples of nanoparticles in the mg to gr range, which may be difficult to produce in practice.

Electron crystallography has recently gained renewed interest due to recent instrumentation development in electron optics, detectors and automation, but also because to the capacity to study tiny crystals and minutes quantities of matters[18,19]. Among electron diffraction (ED) available techniques, pair distribution function (PDF) based on precession electron diffraction (PED) has shown high potential to finely characterize the average atomic arrangement of NPs deposited in a conventional TEM sample grid[20-23]. The PDF+PED techniques allow quantitative structural refinement (or unit cell optimization) to gather 3D lattice distortion Au or Ag MTPS. Here, we have applied electron-based PDF (ePDF) to reveal that surfactant-free AgAu alloy Dh nanoparticles show an atomic arrangement better described as BCT, and that the Bagley BCO model based

on rigid sphere packing is not an appropriate to describe experimental results.

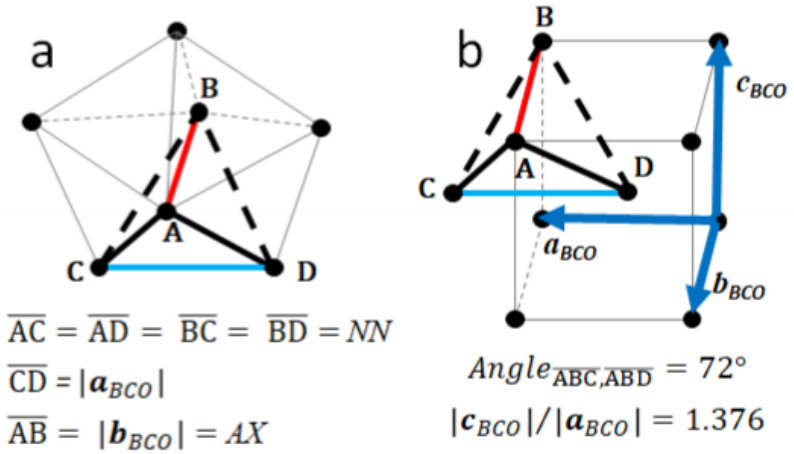

Figure 1. a) Schematic draw of the atomic arrangement inside an ideal decahedral particle; usually two main interatomic distances are used to define local order: a) AX represent distance along the 5-fold axis ($\overline{AB}$) and, b) NN represent interatomic distances between atoms along twin planes (($\overline{AC}$)= ($\overline{AB}$)= ($\overline{BC}$)= ($\overline{BD}$)). b) resulting atomic arrangement can be described by a BCO unit cell. When ($\overline{AB}$)= ($\overline{CD}$) a BCT structure is generated (noted as D-1 particle in the text); for a Bagley´s decahedra with BCO structure, ($\overline{AB}$)= 1.0515 ($\overline{CD}$).

Decahedral Nanoparticle Structure

The space filling constrain in a Dh particle implies in a 72 degrees angle between twins parallel to the 5-fold axis (Figure 1)[5]; a geometrical schemes of the atomic arrangement is represented in Figure 1, We may note that the angular constrain bounds the $\boldsymbol{c}_{BCO}$ and $\boldsymbol{a}_{BCO}$ vectors of a generic orthorhombic cell with $\tan^{-1}(a_{BCO}/c_{BCO}) = 36$ degrees or $c_{BCO}/a_{BCO} = 1.376$ (in contrast for a cubic *FCC* lattice, $c_{FCC}/a_{FCC} = 1/\sqrt{2}$, and an angle between twins of 70.5 degrees)[5]. We build this generic *BCO* unit cell using two interatomic distances (see Figure1a): 1) distance $\overline{AB}$ along 5-fold axis (equal to b_{BCO}, hereafter named *AX*) and, 2) distances $\overline{AC}$ =$\overline{AD}$ =$\overline{BC}$ =$\overline{BD}$ along to twin planes (hereafter named *NN*). Using simple trigonometrical calculation, a_{BCO} is derived from *AX* (*or* b_{BCO}) and *NN*; subsequently, c_{BCO} is calculated to fulfil the angular constrain due to filling space criteria. It must be emphasized that filling space restriction does not impose any bound on the relation AX/NN, then, the length of vectors $\boldsymbol{a}_{BCO}$ and $\boldsymbol{b}_{BCO}$ in the unit cell can vary independently meaning that Dh symmetry may be obtained with many different *BCO* atomic arrangements.

The Bagley´s packing of rigid spheres lead to a Dh particle with *BCO* structure where the following relations were defined: $\overline{CD} = NN$ and $AX/NN = 1.0515$ (or $b_{BCO}/a_{BCO} = 1.0515$, hereafter named DBa)[4]. Although this purely geometrical construction is very popular due do its simplicity, recent experimental studies of Dh nanostructures suggest a ratio that leads to a body center tetragonal (BCT)[10,11]. In this work, we have not attempted to analyze experimental data using inhomogeneous strain models (or localized deformations). The experimental ePDF data resolution is related to the maximum scattering vector in the measured diffraction pattern; this value is determined by the detector size (CCD camera) using for acquisition

of the electron diffraction pattern. Our experiments measured scattering vectors up to $Q_{max} \sim 12\ \AA^{-1}$, what may render extremely difficult the detection of fine details due to inhomogeneous strain. However, we must emphasize that this value of Q_{max} allows a reliable assessment of different mean atomic arrangement, for example, to differentiate cubic (*FCC*), icosahedral (rhombohedral arrangement) and different decahedral particle models (*BCO* or *BCT*, as shown in next sections).

Methods

The surfactant-free AuAg NPs samples have been produced using a home-built cluster source where metal particles are generated from the atom aggregation from a metallic gas[24]. Initially, the metallic gas is generated by sputtering of intertwisted wires (1x Au and 1x Ag) using a cylindrical magnetron sputtering. To initiate the agglomeration, the metal gas is cooled by an adiabatic expansion; the produced NP size distribution is controlled with the aid of ion optics and a Time-of-Flight Spectrometer (TOF) (see scheme in Figure 2a). The NP formation is composed of nucleation, growth of some nuclei within the gas, which subsequently agglomerate and coalesce to form larger clusters. This last step may favor the formation of MTPs[25] as observed in AuAg particles produced by gas aggregation[26]. The selected clusters are deposited with low kinetic energy (<0.5 eV/atom, soft land regime) onto an electron microscopy grid containing an amorphous carbon (a-C) thin film. The grid is afterwards transported to the microscope, so we cannot exclude that a thin Ag oxide layer may have been formed before electron diffraction measurements. The conventional electron microscopy characterization of these samples has already been thoroughly described in several previous publication of our group[21,27-29]. Figure 2 includes a low magnification TEM image of an ensemble of particles (mean diameter 3.2 nm, size distribution is shown in Figure S1), and several atomic resolution images where twinned and decahedral structures can be recognized.

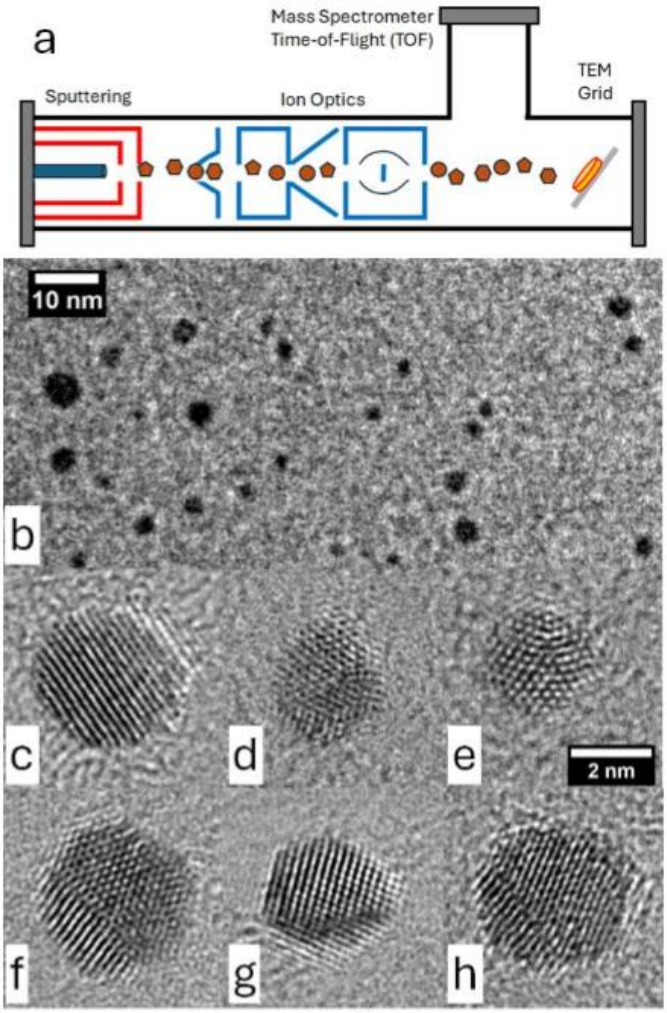

Figure 2. (a) Scheme illustrating the gas aggregation source[24]. b) Typical low magnification TEM image of the nanoparticle samples; c-h) Atomic resolution images of surfactant-free nanoparticles, note that the structure may present many twin defects.

Electron diffraction measurements were realized using a FEI TECNAI G2 STWIN microscope operated at 200 keV coupled with ASTAR (Nanomegas) beam precession control system at the Structural Characterization Laboratory (LCE-DEMa, UFSCAr, Brazil). The microscope has a LaB6 thermionic gun, a Gatan Orius CCD detector (14 bits, 2048x2048 pixels).

The whole procedure utilized to derive ePDF from the measured PED ring patterns (Figure S2) and the subsequent quantitative comparison between measurements and simulations has been described in a previous work (see Figure 3)[21]. Simulations of powder electron diffraction pattern have been based on the Debye scattering equation; this approach allows the calculation of diffraction intensity from any configuration of atomic positions, and no medium- or long-term periodicity is required[30]. The lattice parameter of the AuAg alloy was calculated using Vegard's law (measured chemical composition of the samples was $C_{Au} \sim 0.70$,

leading to a_{FCC}= 0.408 nm)[31].

The structural refinement follows a quantitative comparison of the measured PDF, $G_{meas}(r)$, with the simulated one from a structural model, $G_{sim}(r)$. A residual square difference R is used as the metric for optimization (Eq. 1):

$$R^2 = \frac{\sum(G_{me} - G_{sim})^2}{\sum {G_{me}}^2} \quad (1)$$

All residue minimization procedures are performed utilizing home-made Python software using the Powell algorithm provided by the Scipy library[32].

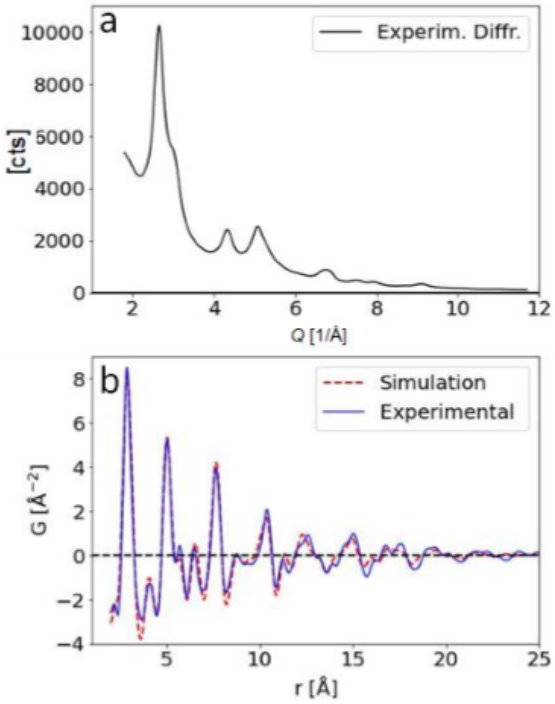

Figure 3. a) Powder diffraction pattern using obtained by the azimuthal integration of conventional PED ring pattern. b) Comparison between measured and optimized ePDF for the model that includes Dh and TW NPs with diameters of 2.6 nm and 2.2 nm, respectively.

Results

The optimization procedure (residue minimization) is initially performed using a library of diffraction patterns calculated as a function of NP diameter (from 1.4 nm to 4 nm, step 0.2 nm) for each proposed structure: *FCC*, twinned *FCC* (TW), Icosahedral (ICO) and Decahedral NPs. For each structure it is possible to find the NP size that yield the minimum residue when compared with experimental data. It is important to emphasize that the optimization only consider two free parameters for each structure: a) Q_{cal}: correction factor for the diffraction pattern calibration (perfect calibration imply Q_{cal} = 1) and b) DW: isotropic Debye-Waller

factor.

The PED-based powder diffraction pattern from the nanoparticles deposed on an amorphous carbon substrate is shown in Figure 3a, while derived ePDF curve is displayed in Figure 3b (after appropriate background subtraction and physical scattering constrain normalization, see Corrêa et al.[21] for details). Motivated by recent results suggesting Dh nanostructures with symmetry close to *BCT* and for the sake of completeness, we have also analyzed an exploratory Dh particle with $AX/NN = 1.0$ what leads to $b_{BCO}/a_{BCO} = 1.018$, hereafter named D-1). The resulting unit cell vectors are $a_{BCO} = 0.294$ nm, $b_{BCO} = 0.288$ nm and $c_{BCO} = 0.404$ nm, what represent an atomic arrangement ($a \sim b$) very close to *BCT* symmetry.

Figure 4 shows the residues as a function of NP diameter resulting from the comparison between experiments and simulations for the different NP models; note that the icosahedral structure generates a much higher residue than the others, so it has not been included in the plot. This figure shows that for all analyzed structures the residue behavior allows the clear identification of the particle size yielding the minimal residue (plot profiles display a well-defined single minimum).

The best experiment description is obtained by a D-1 particle with diameter of 2.6 nm; surprisingly, the DBa structure generated the worst experiment description showing a very large residue difference (~ 10%) for the global minimum (R_{DBa} = 30%, $R_{D\text{-}1}$ = 20%). A spherical twinned *FCC* particles twin crossing the particle center) also shows a very good description of experiments yielding a Residue just 1% above the D-1 NP (Figure S3 shows simulated electron diffraction and ePDF curves for D-1 and TW particle)

To analyze in more details this unexpected behavior, we have also constructed a library of diffraction patterns considering a fixed distance *NN* equal to bulk *FCC* one ($NN_{FCC} = a_{FCC}/\sqrt{2}$, indicated as *AB, BD, AC and BC* in Figure 1). Also, we analyzed the residue evolution while varying the interatomic distance *AX* along 5-fold axis (indicated as AB distance in Figure 1, $AX = NN_{FCC}\,\alpha_{AX}$, where α_{AX} represent the expansion factor). Figure 4b shows the residue evolution when α_{AX} varies in the range of 0.95-1.06 for decahedral particles of 2.6 nm and 2.8 nm in diameter; this plot confirms unambiguously that the DBa structure ($\alpha_{AX} \sim 1.0515$) generates much higher residues, and it clearly far away from the atomic arrangements that better describe the experimental measurements.

Discussion & Summary

Although our previous discussion has been focused on Dh particles, Figure 4a indicates that TW NPs (diameter of 2.2 nm) also yield a very good residue just ~1% above the global minimum. Decahedral particles with D-1 structure and 2.6 nm diameter should display at least 40% of atoms around the 5 twin planes in the Dh. Then, we must also expect that when a sample contains a significant fraction of decahedra, Twinned FCC NP will also produce a good description of the PDF curve. Looking carefully at the optimized PDF curves for TW and D-1 particles, experimental PDF peaks in the range between (8 – 16 Å) are better described by the TW NPs, although the local order is better described by the D-1 NPs (see Figure S3).

Considering that noble metal NP samples almost always a certain population distribution of NP structures in the sample, it is logical to consider that the sample may be formed by a dominant combination of the two kinds of particles whose residues were close to the residue global minimum (2.2 nm TW and 2.6nm D-1). Then, a more complete and reliable description of the experimental data should consider an optimization where both these structures are simultaneously included in the simulation. To do so, we have built a simulated electron powder diffraction pattern by the following expression (eq. 2):

$$I(Q) = w\, I_{D-1}(Q) + (1 - w)\, I_{TW}(Q) \quad (2)$$

where w is the proportion factor (0 – 1) of D-1 NPs in the sample. In our next optimization procedure, the diameter of both TW and D-1 has been kept fixed with the value that yielded the best residue when analyzed individually (2.2 nm and 2.6 nm respectively, see Figure 4a). This optimization was based on 3 free parameters (Q scale, DW and w) and it generated a further reduction of the residue to 18.8 % with $w \sim 0.6$. The optimized profile improved the description in the 2 – 16 Å range (Figure 3b), corresponding to the local and medium range order. However, proper description of the long-range order (>16 Å) may demand the inclusion of additional parameters such as a size distribution. This has not been attempted in this study with the aim of performing numerical optimization procedures with the minimal possible number of free parameters.

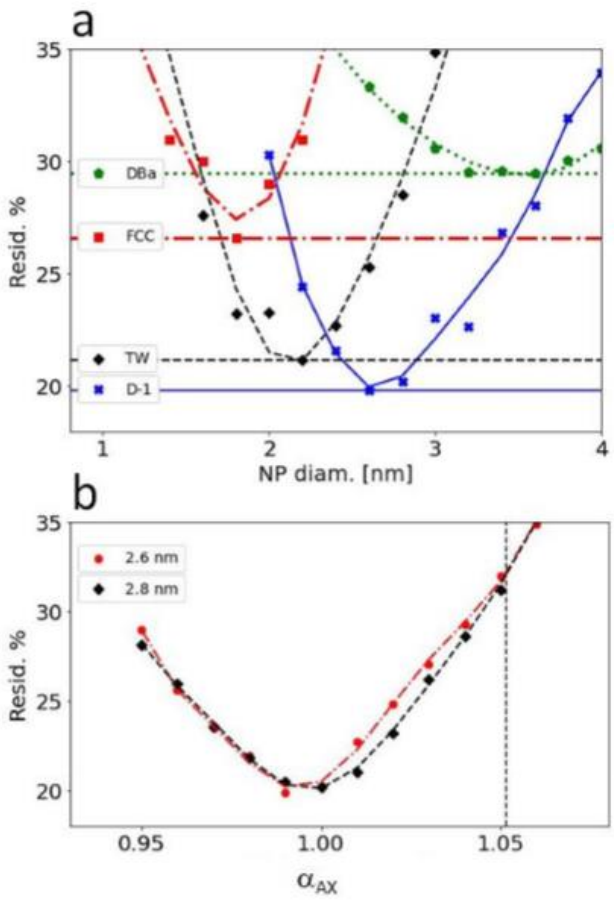

Figure 4. a) Residue as a function of NP diameter resulting from the comparison between experimental and simulated ePDF; this includes 4 different atomic arrangement: single crystal *FCC*, Twinned *FCC* (TW), DBa and D-1 (see text for more details). Note that the TW and D-1 structures provided excellent agreement with experiments by attaining minimal residue (NP diameter: $\varnothing_{TW}$ = 2.2 nm and $\varnothing_{D\text{-}1}$ = 2.6 nm). b) Plot of resulting residue as a function of the decahedral axis expansion factor (AX= α_{AX} NN) values range from 0.95-1.06), a well-defined minimum is recognizable for axial value around 1.0, indicating that the usually considered Bagley structure (indicated by a vertical dashed line) do not seem suitable to explain our experimental measurements.

At this point, it is clear that our results provide solid evidence that the DBa model provides a poor description for our ePDF measurements (high residue). It would be interesting to exploit even more deeply ePDF methods to try to extend our structural refinement to measure the *BCO* unit cell that best describe our experiments. To achieve that we must perform a residue optimization where distances *NN* and *AX* are allowed to vary simultaneously. This structure refinement analysis was implemented considering a sample containing with both TW and Dh particles with fixed diameter. Then, refinement procedure was implemented to optimize 5 free parameters*:* a) 2 parameters for *NN* and *AX* distances inside a 2.6 nm Dh (2.2 nm TW keeping fixed bulk *FCC* interatomic distances); b) 3 other parameters were scattering vector scale, *DW* factor and fractional weight of Dh presence in the sample (*Q* scale, DW and *w*).

We must remark that the inclusion of TW NPs in this refinement procedure fulfils a particularly key role. The atomic structure of TW particles is based on the *FCC* atomic arrangement using bulk interatomic distance (NN_{FCC}). In these terms, it adds robustness to the derived scaling of scattering vector *Q* in the diffraction pattern or, conversely (in real space), an internal interatomic distance calibration for the Dh particle interatomic distance. Then, we will be able to gather the subtle variation on *AX* and *NN* accurately measured and calibrated in relation with NN_{FCC}. This is an essential point if we consider that several experimental factors can affect the absolute distance measurement (calibration errors of scattering vectors, optical distortions due to intermediate lens, background subtraction, etc.). The optimization procedure usually yielded the *Q* calibration factor very close to 1.0 (differences < 2%) indicating that our data treatment and careful calibration had been very precise, what allows the derivation of absolute *AX* and *NN* distance values ($AX = \alpha_{AX,2}\ NN_{FCC}$ and $NN = \alpha_{NN,2}\ NN_{FCC}$).

Figure 4 shows the residue plotted as level curves showing the correlation between $\alpha_{NN,2}$ and $\alpha_{AX,2}$ parameters; the residue global minimal is 16.5% in the region with $\alpha_{NN,2}$ ~1.03 and $\alpha_{AX,2}$ ~1.10 and (this Dh structure is referred as Dh-Opt1). This residue value suggests a significative improvement, but the reliability of the fitting parameters should be carefully analyzed due to the very unusual value of estimated interatomic distances. The Dh-Opt1 display a significant expansion of the unit cell volume or, in other terms, unexpected reduction of atom packing factor to 0.66, while for FCC crystal the value is 0.74 (for Bagley decahedra packing attains 0.72, see in Figure S4 a plot of packing factors for the analyzed values of $\alpha_{NN,2}$ and $\alpha_{AX,2}$). In addition, the Dh-Opt1 contribution to sample diffraction is rather low ($w \sim 0.2$) suggesting a minor fraction in the NP sample; this somewhat is inconsistent with results shown in Figure 4 where the best NP structure to model experiments are Dh particles (precisely 2.6 nm D-1).

The refinement results, discussed above, seems open to doubt, and should be carefully examined. More likely, the global minimum low residue value may be associated to an overfit occurrence; it is known that an excessive number of variables during PDF optimization can provide structural parameters without any physical significance[33,34]. In fact, the resulting structure appear to have no influence in the PDF peaks positions and only affects the region between real space peaks in the ePDF. This can be clearly observed in Figure S3 where ePDF peaks of the simulated decahedra are severely shifted downwards from the experimental values. Most likely, overfitting of parameters compensates the lack of resolution in the experimental ePDF signal, which widens the bases of the ePDF peaks (ePDF minima between peaks are not as sharp in experiments in comparison with simulations, indicated with arrows in Figure S3). Briefly, we conclude that the overfit improves residue through the unrealistic use of the decahedra with large interatomic distances as a background contribution at the global minimum. Then, a more reliable optimization effort demands that we include more constrains based on known physical attributes of free parameters whose values are optimized.

The first constrain to consider is atomic packing of the optimized unit cell, which must be very close the expected value of the corresponding bulk FCC crystals. Consequentially, we will impose a minimal atomic packing factor of 0.72, what is the value for a Bagley decahedron DBa[5]. Furthermore, we can try to additional constrains, and Figure 4 provides an essential and strong information: both 2.2 nm TW and a 2.6 nm D-1 particle yield independently a very good description of experiments (residue ~20%). If we calculate the residue when comparing simulated PDF curves from these two model NPs, the residue results is again around ~20%. Then this residue value (~20%) seems to be a good estimate of the lower bound in our analysis considering the numerical comparison through a residue metrics between experiments and simulation or between simulation (TW vs D-1). This represent a limit to the structural information that can be derived for our ePDF analysis, considering our sample (polydisperse in size and structure, defects, oxidation), experimental data quality (counting noise, limited Q range, geometrical distortions associated to electron optics, background subtraction, precession angle, etc.) and the modelling (kinematical diffraction theory, no size distribution).

To put it more precisely, we have chosen to accept as physically correct all point in the $\alpha_{NN,2}$, $\alpha_{AX,2}$ residue map (Figure 5a), where the associated Dh structure shows: a) an atomic packing factor above 0.72; and, b) the simulated ePDF yields a residue < 20% difference with optimized 2.2 TW and 2.6 D-1 decahedra (Fig. 3). Fig. 4b shows the region in the $\alpha_{NN,2}$ and $\alpha_{AX,2}$ map that fulfill the precedent two physical constraint. A more detailed analysis of the validity of this assumption is discussed in the Supplementary Information, where we present examples of quantitative comparison between decahedral particles outside physically acceptable region, as well the overfitting effects and occurrence of correlation between free parameters.

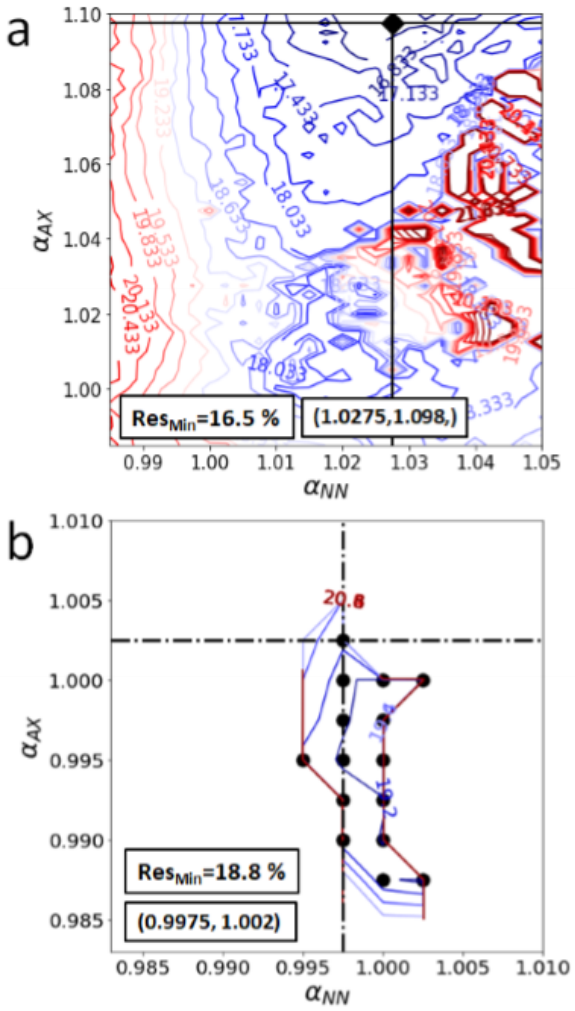

Figure 5. a) Residue in a contour map of the Dh distortion parameters, notice that the range includes the D-1 (α_{AX} ~ 1.0 and α_{NN} = 1.0) and DBa (α_{AX} ~ 1.0515 and α_{NN} =1.0). b) The region of the map in (a) built by imposing physically constrains as described in the text.

The selected region of physical significance in Figure 5b contains several local minima, so we will choose the mean value of them as result of our refinement. We have constructed the histogram of each parameter from local minima within 0.5% from the global minimum in the restricted region (see Figure 5). All parameters show well defined means and a further quantitative analysis provided an opportunity to estimate the error bars through the standard deviation or the point cloud size. We have estimated the error bar in a deliberately cautious way, taking it as the half-width of the cloud formed by the spread of the optimized parameters (see Figure S8). The following values are calculated: $Q_{cal,mean} = 0.994 \pm 0.002$, $\alpha_{NN,mean} = 1.005 \pm 0.003$, $\alpha_{AX,mean} = 1.00 \pm 0.01$ and $w_{mean} = 0.54 \pm 0.04$. Notice that, as expected, the scaling of the scattering vector has remained remarkably close to unity (less than 0.5 % deviation); also, it must be

noted that the precision for interatomic distance along the 5-fold axis direction (*AX*) is worse than for *NN*. The mix parameter w_{mean} provided a balanced contribution to the final diffraction intensity from the NP of each type (TW and Dh).

Both $Q_{cal,mean}$ and the mix parameter *w* are considered reasonable and consistent with all thorough analysis realized until this point. Consequently, we conclude that the determined $\alpha_{NN,mean}$ and $\alpha_{AX,mean}$ are also reliable and suitable for deeper further interpretation. The estimation of the ratio α_{AX}/α_{NN} is always found close to unity (1.00±0.01), which is compelling evidence that our sample is composed in majority by decahedra very well described by a D-1 structure. It must be noted that our results clearly indicate that the Bagley model (DBa) is outside of the experimental 3σ confidence interval (expected value $\alpha_{AX}/\alpha_{NN} = 1.0515$); DBa model incorporates a distortion of 5% along 5-fold axis that seems too high to properly describe the few-nm-wide particles studied here. We must note that this analysis seems to be very robust because if larger regions of acceptable physical solution space are considered (higher thresholds residue values of 25% and 30) similar conclusions are obtained (α_{AX}/α_{NN} ~1, see Figure S8).

The absolute *BCO* unit-cell derived from the ePDF analysis is: $a_{bco}^{opt} = (0.295 \pm 0.001)$ nm; $b = (0.288 \pm 0.003)$ nm; $c = (0.406 \pm 0.001)$ nm, yielding a filling factor 0.727. Considering the precision of measurements, a 3σ interval criterion indicates an overlapping of *a* nd *b* vector lengths; then, a rigorous error analysis suggest that our experiment cannot exclude the occurrence tetragonal symmetry (*BCT*), as our measurement are unable to prove the fact $a \neq b$ (i.e. the unambiguous identification of a *BCO* unit cell). These results are in agreement with previous reports that noble metal Dh nanowires or rods may show tetragonal symmetry as derived from XRPD studies[10,11].

Notice that both DBa and optimized Dh structures fulfill all requirement of 5-fold symmetry, 72° between twins and similar atomic packing factor (~0.724 and 0.727 respectively). So, our experiments do not necessarily exclude the occurrence of other atomic arrangement in another kind of NP sample (ex with different surfactants), because of the dominant role of surface energy in few-nm-wide particles. However, the lack of crystallography studies using advance analytical techniques confirming the identification of Bagley 5-fold structures may at least indicate that such structure must be considered with care to model Dh particles. In contrast, several experimental or theoretical studies support BCT unit cell description for homogenous strain [10,11], while the reliable measurement of inhomogeneous strain in the 3D (not addressed here) in small nm-wide NP remains a remarkable challenging experiment.

From another point of view, our study reveals the dangers of just looking at optimized structural parameters derived from numerically local/global minima search without considering the physical constrains associated with materials physical and chemical properties. Finally, we must conclude that PDF + PED show huge potential to contribute to quantitative refinement procedures in the field of crystallographic study of nanomaterials considering the low electron irradiation dose (10 e/Å^2) necessary to acquire a diffraction pattern in TEM.

.

Associated content

Supporting information

The Supporting Information is available free of charge at https://XXXXXXXX

Additional figures describing TEM experiments, Precession Electron diffraction, Data processing, kinematical simulation of nanoparticle electron diffraction patterns, Pair Distribution Function interpretation details.

AUTHOR INFORMATION

Corresponding Author

Daniel Ugarte- *Instituto de Física "Gleb Wataghin", Universidade Estadual de Campinas-UNICAMP, CEP 13083-859, Campinas - SP, Brazil; Email: dmugarte@ifi.unciamp.br*

Author

Leonardo M. Corrêa- *Instituto de Física "Gleb Wataghin", Universidade Estadual de Campinas-UNICAMP, CEP 13083-859, Campinas - SP, Brazil*

Murilo Moreira- *Instituto de Fsica "Gleb Wataghin", Universidade Estadual de Campinas-UNICAMP, CEP 13083-859, Campinas - SP, Brazil*

Varlei Rodrigues- *Instituto de Fsica "Gleb Wataghin", Universidade Estadual de Campinas-UNICAMP, CEP 13083-859, Campinas - SP, Brazil*

Notes

The authors declare no competing financial interest.

Acknowledgements

We thank D. Coimbrão from LCE-DEM-UFSCar for his invaluable assistance during TEM experiments. We also acknowledge Dr. Duncan Johnstone from University of Cambridge for illuminating discussions on PED diffraction applications. D. U. acknowledges financial support from the Brazilian Agencies FAPESP (No. 2014/01045-0), CNPq (402571/2016-9 & No. 306513/2017-0) and FAEPEX-UNICAMP. V. R. acknowledges funding from FAPESP (2007/01722-9) and CNPq (555647/2006-4 & 577046/2008-0). L. M. C. acknowledges financial support from CAPES (No. 1765876/2018) and CNPq (No. 140596/2020-8). M.M.

thanks funding from CNPq (No. 162541/2018-0). Access to the FEG-TEM/STEM from the Brazilian Nanotechnology National Laboratory is acknowledged (LNNANO, grant No. ME - 22329).

References

(1) Marks, L. D. Experimental Studies of Small Particle Structures. *Rep. Prog. Phys.* **1994**, 57, 603–649.

(2) Rogers, B.; Lehr, A.; Velázquez-Salazar, J. J; Whetten, R.; Mendoza-Cruz, R.; Bazan-Diaz, L.; Bahena-Uribe, D.; José Yacaman, M. Decahedra and Icosahedra Everywhere: The Anomalous Crystallization of Au and Other Metals at the Nanoscale. *Cryst. Res. Technol.* **2023**, 58, 2200259.

(3) Xia, Y.; Xiong, Y.; Lim, B.; Skrabalak, S. E. Shape-Controlled Synthesis of Metal Nanocrystals: Simple Chemistry Meets Complex Physics? *Angew. Chem. Int. Ed.* **2009**, 48, 60–103.

(4) Bagley, B. G. A Dense Packing of Hard Spheres with Five-fold Symmetry. *Nature* **1965**, 208**,** 674-675.

(5) Yang, C. Y. J. Crystallography of Decahedral and Icosahedral Particles: I. Geometry of Twinning. *Cryst. Growth* **1979**, 47, 274–282.

(6) Marks, L. D. Inhomogeneous Strains in Small Particles. *Surf. Scien.* **1985**, 150, 302-318.

(7) Wu, H.; Yu, R.; Zhu, J.; Chen, W.; Li, Y.; Wang, T. Size-Dependent Strain in Fivefold Twins of Gold. *Acta Crystallogr. B.* **2021**, 77, 93-98.

(8) Niekiel, F.; Bitzek, E.; Spiecker, E. Combining Atomistic Simulation and X-ray Diffraction for the Characterization of Nanostructures: A Case Study on Fivefold Twinned Nanowires. *ACS Nano* **2014**, 8, 1629-1638.

(9) Johnson, C. L.; Snoeck, E.; Ezcurdia, M.; Rodríguez-González, B.; Pastoriza-Santos, I.; Liz-Marzán, L. M.; Hÿtch, M. J. Effects of Elastic Anisotropy on Strain Distributions in Decahedral Gold Nanoparticles. *Nat. Mater.* **2008**, 7, 120-124.

(10) Sun, Y.; Ren, Y.; Liu, Y.; Wen, J.; Okasinski, J. S; Miller, D. J. Ambient-Stable Tetragonal Phase in Silver Nanostructures. *Nat. Commun.* **2012**, 3, 971 - 977.

(11) Mettela, G.; Bhogra, M.; Waghmare, U. V.; Kulkarni, U. Ambient Stable Tetragonal and Orthorhombic Phases in Penta-Twinned Bipyramidal Au Microcrystals. *J. Am. Chem. Soc.* **2015**, 137, 3024-3030.

(12) Carter, B. & Williams, D. B. (2016). *Transmission Electron Microscopy: Diffraction, Imaging, and Spectrometry*, pp. 343- 372, Springer: Switzerland.

(13) Zhou, J.; Yang, Y.; Ercius, P; Miao, J. Atomic Electron Tomography in Three and Four Dimensions. *MRS Bull.* **2020**, 45, 290–297.

(14) Hovden, R.; Muller, D. A. Electron Tomography for Functional Nanomaterials. *MRS Bull.* **2020**, 45 (4), 298–304.

(15) Albrecht, W.; Bals, S. Fast Electron Tomography for Nanomaterials. *J. Phys. Chem. C* **2020**, 124 (50), 27276–27286.

(16) Li, Z.; Okasinski, J. S.; Almer, J. D.; Ren, Y.; Zuo, X.; Sun, Y. Quantitative Determination of Fragmentation Kinetics and Thermodynamics of Colloidal Silver Nanowires by In Situ High-Energy Synchrotron X-ray Diffraction. *Nanoscale* **2013**, 6, 365-370.

(17) Zhou, Y.; Fichthorn, K. A. Internal Stress-Induced Orthorhombic Phase in 5-Fold-Twinned Noble Metal Nanowires. *J. Phys. Chem. C* **2014**, 118, 18746 – 18755.

(18) Gemmi, M.; Mugnaioli, E.; Gorelik, T. E.; Kolb, U.; Palatinus, L.; Boullay, P.; Hovmöller, S.; Abrahams J. P. 3D Electron Diffraction: The Nanocrystallography Revolution. *ACS Cent. Sci.* **2019**, 5, 1315 – 1329.

(19) Saha, A.; Nia, S. S.; Rodriguez, J. A. Electron Diffraction of 3D Molecular Crystals. *Chem. Rev.* **2022**, 122, 13883 – 13914.

(20) Egami, T.; Billinge, S. J. L. Underneath the Bragg Peaks Structural Analysis of Complex Materials; Elsevier: Oxford, 2003; pp 25– 51.

(21) Corrêa, L. M.; Moreira, M.; Rodrigues, V. & Ugarte, D. Quantitative Structural Analysis of AuAg Nanoparticles Using a Pair Distribution Function Based on Precession Electron Diffraction: Implications for Catalysis. *ACS. Appl. Nano* **2019**, 4, 12541 – 12551.

(22) Gorelik, T. E.; Neder, R.; Terban, M. W.; Lee, Z.; Mu, X.; Jung, C.; Jacob, T.; Kaiser, U. Towards Quantitative Treatment of Electron Pair Distribution Function. Acta Crystallogr., Sect. B: Struct. Sci., *Cryst. Eng. Mater.* **2019**, 75, 532– 549,

(23) Hoque, M. M.; Vergara, S.; Das, P. P.; Ugarte, D.; Santiago, U.; Kumara, C.; Whetten, R. L.; Dass, A.; Ponce, A. Structural Analysis of Ligand-Protected Smaller Metallic Nanocrystals by Atomic Pair Distribution Function Under Precession Electron Diffraction. *J. Phys. Chem. C* **2019**, 123, 19894– 19902.

(24) de Sá, A. D. T.; Abrao Oiko, V. T.; di Domenicantonio, G.; Rodrigues, V. New Experimental Setup for Metallic Clusters Production Based on Hollow Cylindrical Magnetron Sputtering. *J. Vac. Sci. Technol., B: Nanotechnol. Microelectron.: Mater., Process., Meas., Phenom.* **2014**, 32, 061804– 061812.

(25) Song, M.; Zhou, G.; Lu, N.; Lee, J.; Nakouzi, E.; Wang, H.; Li, D. Oriented Attachment Induces Fivefold Twins by Forming and Decomposing High-Energy Grain Boundaries. *Science* **2020**, 367, 40– 45.

(26) Huttel, Y. (2017). *Gas-phase Synthesis of Nanoparticles*, pp. 3−18, Wiley-VCH:Weinheim.

(27) Moreira, M.; Hillenkamp, M.; Divitini, G.; Tizei, L. H. G.; Ducati, C.; Cotta, M. A.; Rodrigues, V.; Ugarte D. Improving Quantitative EDS Chemical Analysis of Alloy Nanoparticles by PCA Denoising: Part I, Reducing Reconstruction Bias. *Microsc. Microanal.* **2022**, 28, 338-349.

(28) Moreira, M.; Felix, L. C.; Cottancin, E.; Pellarin, M.; Ugarte, D.; Hillenkamp, M.; Galvao, D. S.; Rodrigues, V. Influence of Cluster Sources on the Growth Mechanisms and Chemical Composition of Bimetallic Nanoparticles. *J. Phys. Chem. C* **2023**, 127, 1944-1954.

(29) Moreira, M.; Hillenkamp, M.; Rodrigues, V.; Ugarte, D. Ag Surface Segregation in Sub-10-nm Bimetallic AuAg Nanoparticles Quantified by STEM-EDS and Machine Learning: Implications for Fine-Tuning Physicochemical Properties for Plasmonics and Catalysis Applications. *ACS. Appl. Nano. Mater.* **2024**, 7, 1369-1378.

(30) Debye, P. Zerstreuung von Röntgenstrahlen. *Ann. Phys.* **1915**, 351, 809– 823

(31) Holder, C. F.; Schaak, R. E. Tutorial on Powder X-Ray Diffraction for Characterizing Nanoscale Materials. *ACS Nano* **2019**, 13, 7359– 7365.

(32) Virtanen, P.; Gommers, R.; Oliphant, T. E.; Haberland, M.; Reddy, T.; Cournapeau, D.; Burovski, E.; Peterson, P.; Weckesser, W.; Bright, J.; Van Der Walt, S. J.; Brett, M.; Wilson, J.; Millman, K. J.; Mayorov, N.; Nelson, A. R. J.; Jones, E.; Kern, R.; Larson, E.; Carey, C. J.; Polat, İ.; Feng, Y.; Moore, E. W.; VanderPlas, J.; Laxalde, D.; Perktold, J.; Cimrman, R.; Henriksen, I.; Quintero, E. A.; Harris, C. R.; Archibald, A. M.; Ribeiro, A. H.; Pedregosa, F.; Van Mulbregt, P.; SciPy 1.0 Contributors; Vijaykumar, A.; Bardelli, A. P.; Rothberg, A.; Hilboll, A.; Kloeckner, A.; Scopatz, A.; Lee, A.; Rokem, A.; Woods, C. N.; Fulton, C.; Masson, C.; Häggström, C.; Fitzgerald, C.; Nicholson, D. A.; Hagen, D. R.; Pasechnik, D. V.; Olivetti, E.; Martin, E.; Wieser, E.; Silva, F.; Lenders, F.; Wilhelm, F.; Young, G.; Price, G. A.; Ingold, G.-L.; Allen, G. E.; Lee, G. R.; Audren, H.; Probst, I.; Dietrich, J. P.; Silterra, J.; Webber, J. T.; Slavič, J.; Nothman, J.; Buchner, J.; Kulick, J.; Schönberger, J. L.; De Miranda Cardoso, J. V.; Reimer, J.; Harrington, J.; Rodríguez, J. L. C.; Nunez-Iglesias, J.; Kuczynski, J.; Tritz, K.; Thoma, M.; Newville, M.; Kümmerer, M.; Bolingbroke, M.; Tartre, M.; Pak, M.; Smith, N. J.; Nowaczyk, N.; Shebanov, N.; Pavlyk, O.; Brodtkorb, P. A.; Lee, P.; McGibbon, R. T.; Feldbauer, R.; Lewis, S.; Tygier, S.; Sievert, S.; Vigna, S.; Peterson, S.; More, S.; Pudlik, T.; Oshima, T.; Pingel, T. J.; Robitaille, T. P.; Spura, T.; Jones, T. R.; Cera, T.; Leslie, T.; Zito, T.; Krauss, T.; Upadhyay, U.; Halchenko, Y. O.; Vázquez-Baeza, Y. SciPy 1.0: Fundamental Algorithms for Scientific Computing in Python. *Nat. Methods* **2020**, 17 (3), 261–272.

(33) Banerjee, S.; Liu, C.-H.; Lee, J. D.; Kovyakh, A.; Grasmik, V.; Prymak, O.; Koenigsmann, C.; Liu, H.; Wang, L.; Abeykoon, A. M. M.; Wong, S. S.; Epple, M.; Murray, C. B.; Billinge, S. J. L. Improved Models for Metallic Nanoparticle Cores from Atomic Pair Distribution Function (PDF) Analysis. *J. Phys. Chem. C* **2018**, 122, 29498– 29506

(34) Yang, L.; Juhás, P.; Terban, M. W.; Tucker, M. G.; Billinge, S. J. L. Structure-Mining: Screening Structure Models by Automated Fitting to the Atomic Pair Distribution Function over Large Numbers of Models. *Acta Crystallogr A Found Adv* **2020**, 76 (3), 395–409.

Apêndice B

Material Suplementar ao Apêndice A

A seguir está anexado o material suplementar ao artigo que descreve o trabalho descrito no Capítulo 2 da tese.

Supporting Information

Unraveling non-cubic atomic ordering in surfactant-free AuAg decahedral nanoparticles by Pair Distribution Function (PDF) analysis

Leonardo M. Corrêa[1], *Murilo Moreira*[1], *Varlei Rodrigues*[1] *and Daniel Ugarte*[1,*]

1 Instituto de Física "Gleb Wataghin", Universidade Estadual de Campinas-UNICAMP, CEP 13083-859, Campinas - SP, Brazil.
* dmugarte@ifi.unicamp.br

Content

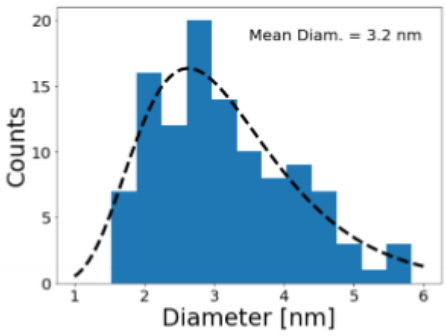

Figure S1. Size distribution of the NP used in our ePDF experiments, derived by TEM conventional imaging. The dashed curve represents the log-normal description of the distribution.

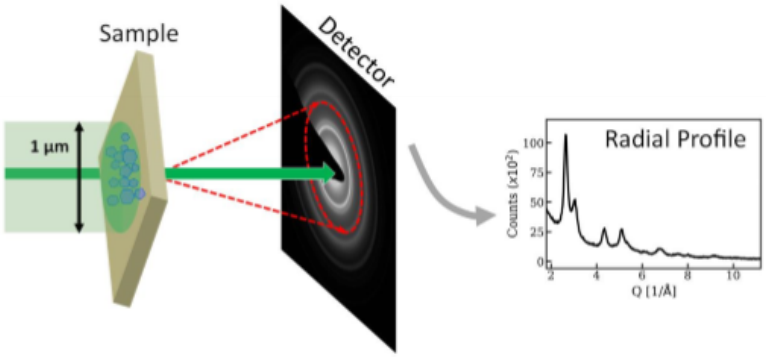

Figure S2. Schematic draw showing he input measurement to calculate the ePDF curve: a powder electron diffraction pattern calculated from TEM measurements. Polycrystalline samples generate ring diffraction patterns in a conventional TEM experiment; the radial profile extracted from this kind can be easily recognized as similar to a Powder X-ray Diffraction (PXRD) one. The measurements explored in this work used an incident beam precession along a cone of 2.0 degrees around the TEM optical axis, what allows a good description of measured intensity using the kinematical diffraction theory[2]. Also, we have performed an azimuthal integration of the ring patter to increase signal-to noise-ratio; all details of data treatment have been described in detail in a previous publication[3].

Defining physical constrains for the structural parameters of decahedral particles

This work aims to find the best Body Centered Orthorhombic (BCO) unit cell representing the average lattice in few NM wide noble metal decahedra. Two interatomic distances define the unit cell vector: a) distance between atom along 5-fold axis (AX) and distance between atoms along twin planes (NN). The requirement of space filling structure imposes an angle of 72 degrees between twin planes, what fixes the relation between the length of the three unitary cell vectors. The geometrical construction described above (see Figure 1, main text) does not impose any relation between *AX* and *NN* parameters, which can be varied independently ($AX = \alpha_{AX,2}\ NN_{FCC}$ and $NN = \alpha_{NN,2}\ NN_{FCC}$, where NN_{FCC} is the bulk interatomic distance). However there physical constrains that limit the values that these parameters may display. The first one if the atomic packing factor which must be close to the corresponding bulk phase (0.74, see main text and Figure S4a); in this work its value has been chose to be > than 0.72 (value corresponding to Bagley's BCO decahedral structure)[1].

From another point of view, our initial structure refinement trial has revealed that two model NPs generate the best description of experimental ePDF curve: a) 2.2 nm in diam. Twinned FCC particle (TW) with interatomic distance identical to the bulk phase (NN_{FCC}); and b) 2.6 nm in diameter decahedron where $AX = NN = NN_{FCC}$ (called D-1 in the main text). Both model NPs generated a residue in the range of 20% when compared with experiments; in addition, the comparison between the simulated ePDF curves also yielded a residue in the range of 20%. So, we have concluded that a residue value of ~20% seems to be approximatively the lowest possible value and also indicates the quality of the structural information that can be derived for our ePDF analysis. From another point of view, this also indicates that the simulated ePDF from decahedral particle with arbitrary value of AX and NN must be well suited to analyze experiments, only if its residue is < 20% when compared with the 2.2 nm twin or the 2.6 nm D-1 particles (the two NP structures that individually provide a good fit to experimental data).

If we use simulations to compare a 2.6 Dh particle with varying *AX* and *NN* distances with the 2.2 nm TW particles (nearest neighbor distance NN_{FCC}), the global minimum residue is ~16.5% at optimized parameters $\alpha_{NN,2}$ =0.992 and $\alpha_{AX,2}$ ~ 1.002 (very close to D-1 decahedra, see residue map as 3D plot in level curves in Figure S4b). In contrast, the Dh particle found at the global minimum of the TW+Dh combination (see Fig 5a, main text) not only displays a extremely low filling factor of 0.66 but it also attains a very high residue value of 76% when compared with 2.2 nm TW particle (Figure S5); this clearly indicates that a more careful and detailed hunt for the optimized decahedral structure should be discussed in detail. For the sake of completeness, we have also performed a similar calculation to get the residue map of comparing a simulated 2.6 nm Dh with varying α_{AX} and α_{NN} when compared with the simulated D-1 particles (Figure S4c). We can utilize both filling factor and residue maps in Figure S4 to define criteria fixing a valid range of $\alpha_{AX,2}$ and $\alpha_{NN,2}$.

To analyze the validity of the 20% residue criteria discussed above, we can observe the quality of the fits when comparing of Dh ($\alpha_{NN,2}$ and $\alpha_{AX,2}$) with the 2.2 nm TW model (optimizing *Q* scale and Debye-Waller factor, Figure S4b) for structures Dh structure with approximately 20%, 30% and 40% residue results (see Figure S6). It is possible to observe that Dh particles showing a 30% residue display clear major differences in the PDF curve profile and can be easily described as not well suited for detailed analysis (see Figure S6).

The visual analysis described above provides a value for the residue threshold, but a more precise determination can be obtained by detecting a correlation map between optimized free parameters. This represents an invaluable tool to reveal if fitting parameters are independent and to avoid the overfit behavior. This information is better uncovered by comparing α_{AX} and *w* (mix) (Figure S7), where it is clearly observable that those parameters are uncorrelated (less structured point distribution) only when we limit the accepted Dh structures to be within a residue of 20% from the 2.2 nm TW and from a 2.6 nm D-1. Beyond such values

parameters are strongly correlated, as the distance along 5-fold axis axial (α_{AX}) increases the relevance of decahedra in the sample (w) diminishes.

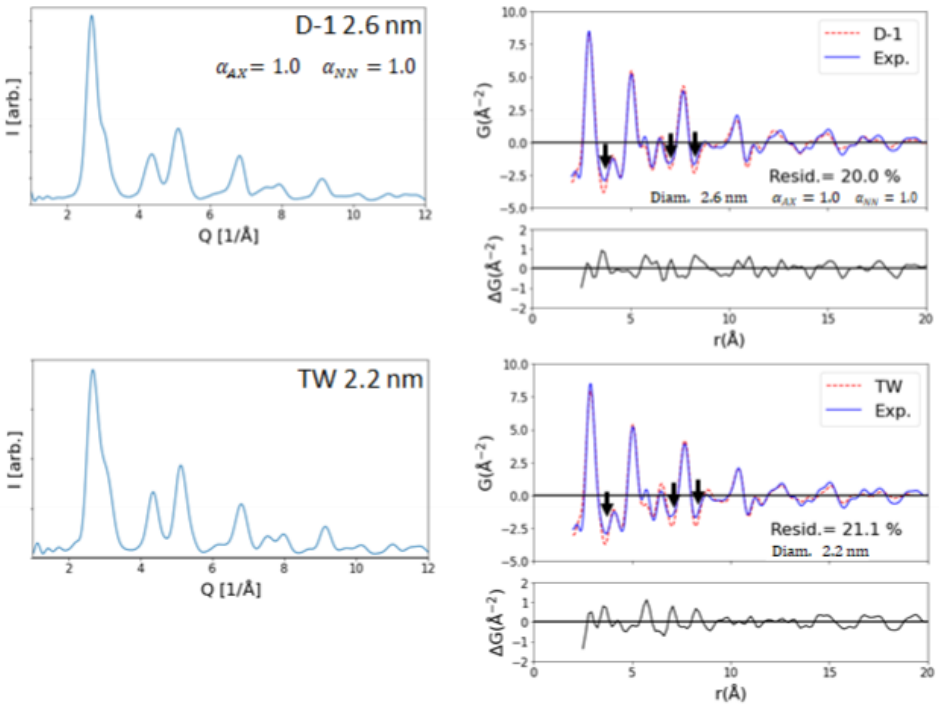

Figure S3. Simulated powder electron diffraction pattern (left) and comparison between measured and optimized ePDF (right) for: a) D-1 decahedron (where the body center orthorhombic was set to $a_{BCO} = b_{BCO}$; and b) spherical FCC particle containing a single twin crossing the particle center. Below each ePDF comparison, we show the difference curve. The arrows show the regions where the loss of resolution of the peaks are most evident.

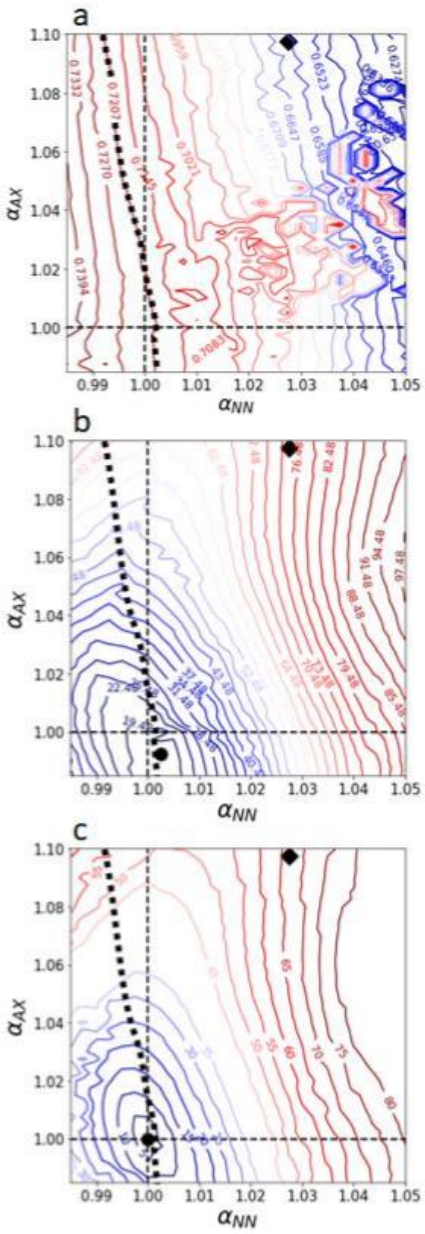

Figure S4. a) Atomic packing factor in relation to the variation in AX and NN. b) Residue variation in relation to the AX and NN variations for the optimization of the simulated Dh to the best optimized TW structure. c) Residue variation in relation to the AX and NN variations for the optimization of the simulated Dh to the best optimized D-1 structure. Vertical and horizontal line indicate AX and NN values for the D-1 decahedral structure.

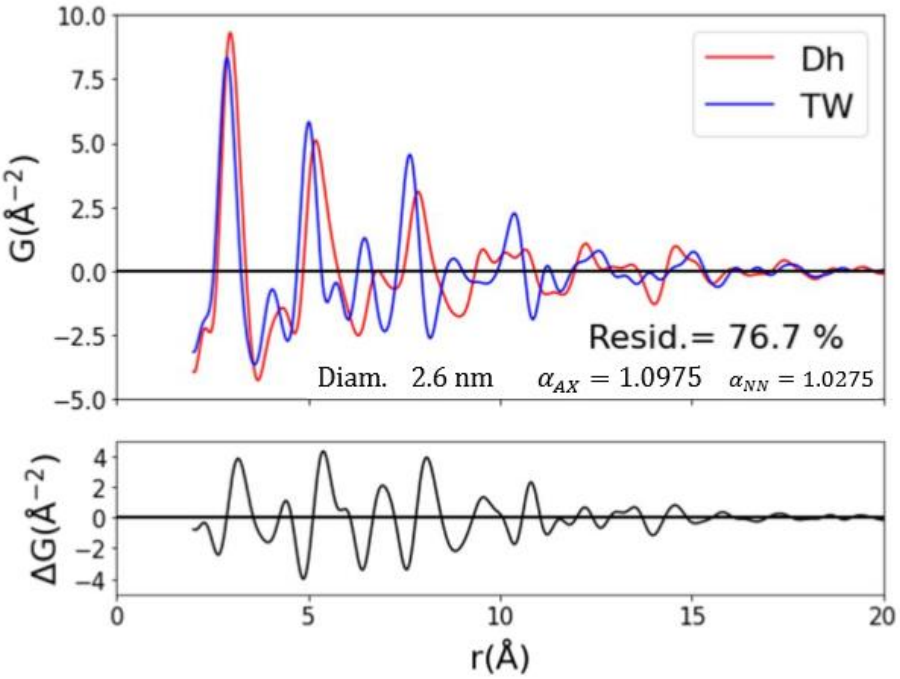

Figure S5. Comparison optimized ePDF for the TW model and the overfitted Dh particle D_Opt1. Below is plotted the difference between the two curves.

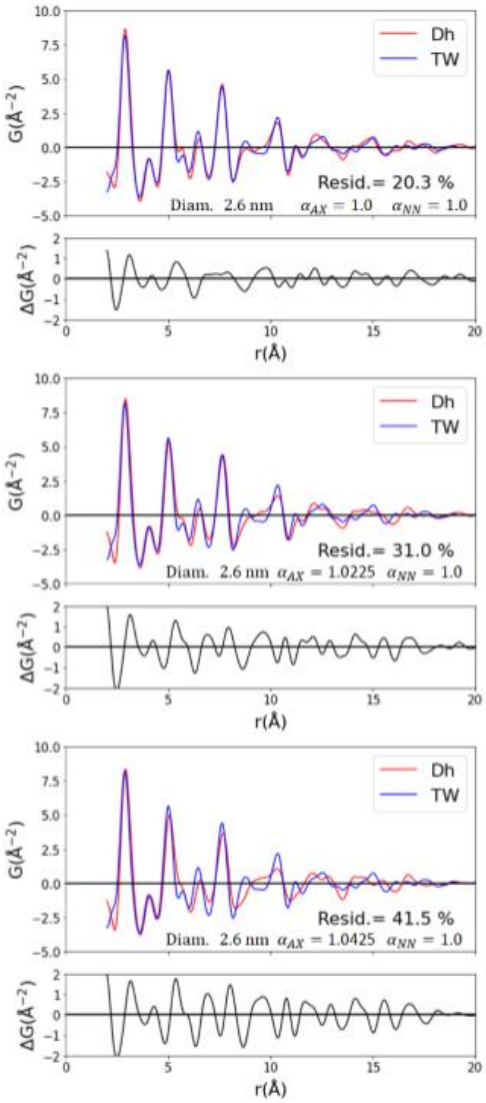

Figure S6. Comparison optimized ePDF for the TW model and the Dh particle for a) α_{NN} = 1.0 and α_{AX} = 1.0, b) α_{NN} = 1.0 and α_{AX} = 1.0225, c) α_{NN} = 1.0 and α_{AX} = 1.0425. Below each comparison is plotted the difference between the two curves.

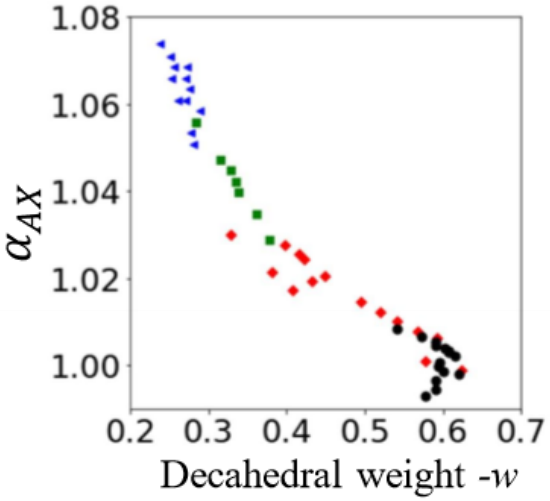

Figure S7. Correlation map (or scatter plot) for the α_{AX} and w for several threshold in residue (20%: circles, 30%: diamonds, 40%: squares, 50%: triangles, see text for explanation).

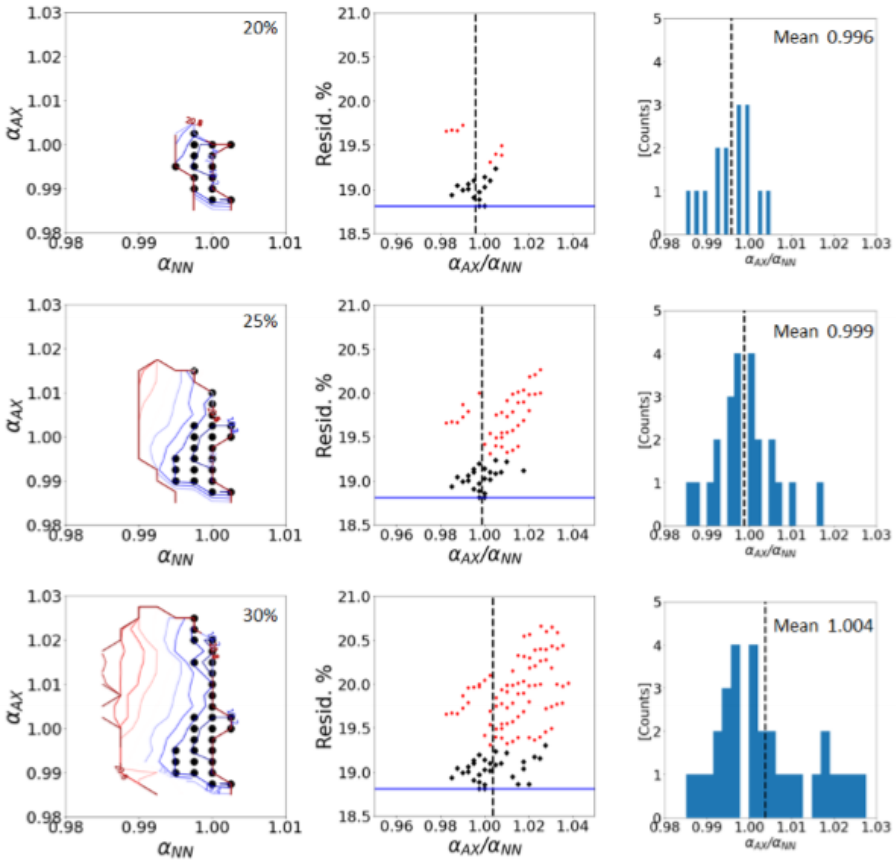

Figure S8. Left Column: areas in the α_{NN} , α_{AX} space which fulfil physical constrains related to atomic filling factor 0,.72 and a threshold residue (20%, 25 % and 30%) difference with NP yielding minimum residue when compared with experimental curves (twinned FCC particle 2.2 nm in diameter and D-1 2.6 nm in diameter, see main text). Central column: Point associated to the a region of the solution space considering different threshold values (left Column); Black diamond points indicate local minima at 0.5% from the lowest residue value . Right Columns: Histogram of local minima (diamond points central column). The histogram mean is indicated an remains very close to 1.0 value for t threshold residues 20, 25 and 30%.

References

1. Bagley, B. G. A Dense Packing of Hard Spheres with Five-fold Symmetry. *Nature* **1965**, 208, 674-675.

2. Carter, B. & Williams, D. B. (2016). Transmission Electron Microscopy: Diffraction, Imaging, and Spectrometry, pp. 343- 372, Springer: Switzerland.

3. Corrêa, L. M.; Moreira, M.; Rodrigues, V. & Ugarte, D. Quantitative Structural Analysis of AuAg Nanoparticles Using a Pair Distribution Function Based on Precession Electron Diffraction: Implications for Catalysis. ACS. Appl. Nano 2019, 4, 12541 – 12551.

Apêndice C

Mapeamento de Orientação com Alta Precisão por Meio da Análise Quantitativa das Intensidades Difratadas Obtidas de Dados de 4D-STEM e Difração de Elétrons com Precessão

A seguir está anexado o artigo nomeado "*High precision orientation mapping from 4D-STEM precession electron diffraction data through quantitative analysis of diffracted intensities*" que detalha o trabalho descrito no Capítulo 4. Ele foi publicado em 2024 na revista Ultramicroscopy 2024, 259, 113927 – 113940. Os direitos do artigo pertence a Elsevier que permite aos autores a reprodução do artigo em teses e dissertações, como exposto em: https://www.elsevier.com/about/policies-and-standards/copyright/permissions no item *"Can I include/use my article in my thesis/dissertation?"*.

Ultramicroscopy 259 (2024) 113927

Contents lists available at ScienceDirect

Ultramicroscopy

journal homepage: www.elsevier.com/locate/ultramic

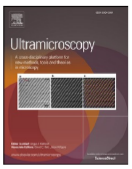

High precision orientation mapping from 4D-STEM precession electron diffraction data through quantitative analysis of diffracted intensities

Leonardo M. Corrêa [a], Eduardo Ortega [b], Arturo Ponce [b], Mônica A. Cotta [a], Daniel Ugarte [a,*]

[a] Instituto de Fisica "Gleb Wataghin", Universidade Estadual de Campinas-UNICAMP, 13083-859 Campinas, SP, Brazil
[b] Department of Physics and Astronomy, University of Texas, San Antonio, TX 78249, United States

ARTICLE INFO

Keywords:
Precession electron diffraction
Automated crystal orientation mapping
Eshelby twisted nanowires
Quantitative analysis of electron diffraction intensities
4D-STEM
High angular resolution crystal orientation measurement

ABSTRACT

The association of scanning transmission electron microscopy (STEM) and detection of a diffraction pattern at each probe position (so-called 4D-STEM) represents one of the most promising approaches to analyze structural properties of materials with nanometric resolution and low irradiation levels. This is widely used for texture analysis of materials using automated crystal orientation mapping (ACOM). Herein, we perform orientation mapping in InP nanowires exploiting precession electron diffraction (PED) patterns acquired by an axial CMOS camera. Crystal orientation is determined at each probe position by the quantitative analysis of diffracted intensities minimizing a residue comparing experiments and simulations in analogy to x-ray structural refinement. Our simulations are based on the two-beam dynamical diffraction approximation and yield a high angular precision (~0.03°), much lower than the traditional ACOM based on pattern matching algorithms (~1°). We anticipate that simultaneous exploration of both spot positions and high precision crystal misorientation will allow the exploration of the whole potentiality provided by PED-based 4D-STEM for the characterization of deformation fields in nanomaterials.

1. Introduction

The possibility of controlling chemical or physical properties of nanostructured materials have transformed then into essential constituents of many technological devices, such as sensors, electromagnetic or optical devices [1]. For example, semiconductor nanowires (NWs) are now proposed for many optoelectronic systems, where the application performance can be optimized by modifying their size, chemical composition, atomic structure, structural defects and other morphological and atomic structure aspects [2]. The presence of defects can affect their properties in unexpected ways, but usually inducing detrimental performance. Although the most common synthesis methods can provide high-quality crystalline order, the nanometric dimensions of NWs can favor the formation of metastable structure and defects/distortions may be unavoidable [3]. The control of such aspects requires precise analytical tools, which display unique challenges for such small systems.

Transmission electron microscopes (TEMs) are widely used in the characterization of nanomaterials because of the achievable high spatial resolution. The huge recent developments in instrumentation aspects (mainly aberration correctors and direct detection cameras) provides structural information at the atomic scale, which is considered accessible and reliable [4,5]. In general, advanced TEM methods are associated with atomic resolution imaging, but recently the development of the so-called four-dimensional scanning-TEM (4D-STEM) have raised the interest in electron diffraction techniques (ED) [6]. In this technique, a focused electron beam is scanned over the sample and a ED, or scattering pattern, is record for each pixel position. The resulting data can be utilized for several quantitative analysis methodologies to measure the structural properties of materials sample (as phase, strain and thickness) with nm resolution. From the local ED pattern, many different data types can be derived such as virtual detector imaging (VBF: virtual bright field, VDF: virtual dark field, VADF: virtual annular dark field) and higher-order Laue zone analysis [6]. Overall, 4D-STEM allows for versatile data acquisition and precise structural analysis without some of the limitations of atomic resolution imaging techniques, in particular reducing electron dose and allowing larger fields of view. Additionally, recently 4D-STEM has been applied to further developments in the collection and analysis of big data to extract the transmitted electron wave phase (lost during detection), in which the phase is encoded throughout a diffraction pattern at large convergence angle [7,6]. Alternatively, 4D-STEM analog analyses have been applied in the

* Corresponding author.
E-mail address: dmugarte@ifi.unicamp.br (D. Ugarte).

https://doi.org/10.1016/j.ultramic.2024.113927
Received 2 August 2023; Received in revised form 9 January 2024; Accepted 21 January 2024
Available online 24 January 2024

Fourier space of atomic resolution images and applied to crystal segmentation of multiple twinned small particles [8].

The fundamental and tricky problem associated with electron diffraction interpretation is the phenomenon described as dynamical diffraction. For example, the very strong interaction between the electron beam and the sample imply that electrons maybe scattered many times within the specimen, leading to complex effects on diffracted beam intensities, inhomogeneous illumination of diffracted spots and other deviations of the ideal kinematical regime [5]. The prediction of dynamical diffraction effects requires rather slow and complex numerical simulations [9]. An interesting alternative approach is the so-called precession electron diffraction (PED), where a pattern is generated by the incoherently addition of EDs acquired while the electron beam precesses around the microscope optical axis (forming a hollow cone) [10]. The resulting PED pattern display diffracted beam intensities with reduced dynamical diffraction effects. Such peculiar diffraction regime provides many characteristics that may be modelled using kinematical diffraction, as a reasonable quantitative interpretability of diffraction patterns, but we must always keep in mind that some non-kinematical effects will remain due to the unavoidable (although reduced) influence of dynamical diffraction [10–14]. In addition, diffraction disks show more homogeneous intensity, and more reflections are excited to high-scattering angles; this last attribute is fundamental to obtain information about small interatomic distances.

Scanning precession electron diffraction (SPED, can be included as a 4D-STEM method) is also widely used in materials science for texture analysis by means of the so-called automated crystal orientation mapping (ACOM) [14,15]. In fact, orientation indexing of each PED pattern can be carried out automatically by comparison with a library of kinematically calculated ED patterns. ACOM studies are usually performed in large areas, such that up to tens of thousands of EDs can be measured in a single experiment. Traditionally, TEM detectors are based on the charge coupled devices (CCD) technology, and usual read-out speeds are in order of ~1 frame/s (detectors with very limited size or complex electronics can achieve 1000 frames/s), which are unsuited for ACOM (*e.g.* 10,000 EDs imply in ~ 3 h of measurement) [16]. For that reason, the conventional PED set-up uses a high-speed external optical camera to capture diffraction patterns from the TEM fluorescent screen during nanobeam scanning [17]. The external optical camera captures the SPED patterns as images with an off-axis geometry, which must follow additional postprocessing steps, to correct different severe image distortions [17]. Although a high-frame rate is possible, acquired patterns contain afterimages from the last several probe positions because the fluorescent screen continues to emit light (~100 ms) after electron impact [17]. In addition, due to the low efficiency of detecting signal outside the microscope and high noise of the optical CCD, the signal-to-noise ratio (SNR) for this technique is suboptimal. Hence, this traditional SPED setup may introduce artifacts, obscuring the detection of weak reflections and strongly reduces angular resolution.

A much better measurement of PED patterns could be realized by using an on-TEM-axis camera to reduce geometrical distortions. The required high acquisition speed may be fulfilled at present by different available camera based on various technologies, such as direct electron detection (DDC) and complementary metal-oxide-semiconductor (CMOS) detectors based on monolithic active pixel sensors (APS) [16,18–22]. Recently, direct detectors acquisition have been fully synchronized with probe scan, allowing easy access to datablock already properly formatted for use in common analysis software/methodology. More importantly, new opportunities for analysis methods are possible as those detectors have shown linear intensities in common applications. Furthermore, their high detection speed and low noise compensates any possible non-linearity by allowing measurements with much lower electron doses which preserves the structure to beam damage. The conventional ACOM methods relies on a template-matching procedure where orientation identification is performed through a cross-correlation between the measured ED and a library of simulated patterns (see Fig. 1). This numerical calculation mostly takes into account diffraction peaks position, and intensities are usually rescaled. For example, in order to enhance angular resolution, high angle scattered beams intensity are rescaled by a gamma function or even binarized [21]. Other works utilize the intensities basically as a weight factor to ensure that low diffraction intensity peaks have influence in template-matching results (similar to the gamma function). The intensities basically work as a criterion for selection of peaks, but they will not be explored in any further analysis [22,23]. Some authors have applied the Laue circle method to fit diffraction spot positions and quickly determine sample disorientation [24,25].

The main strength of x-ray diffraction techniques (probably the most popular structural characterization method) is the quantitative use of the diffracted intensities though the comparison between measurement and simulations by mean of residue analysis [26]. In recent years, PED data has played a fundamental role to consolidate electron crystallography, allowing crystal structure solution/refinement analysis (as in x-ray or neutron diffraction) [11]. Previous works by the Palatinus group have shown that PED pattern intensity carries precise information about the orientation of the studied crystal, and that it is possible to recover such information though quantitative analysis of the PED intensities [27]. They applied such analysis to improve the angular position of frames in electron diffraction tomography experiments with an angular precision up to ~ 0.05° [27]. The precedent precision is much less than for common ACOM methods, where angular precision is usually accepted to be around ~ 1°, but with reports of the possibility to achieve ~ 0.2° in angular resolution [18,20–22,28,29]. Consequentially, the application of intensity analysis to ACOM could bring major improvements in angular precision to the technique.

Herein, we demonstrate orientation mapping with derived from the intensities of PED-assisted 4D-STEM measured using a scintillator-coupled CMOS detector in TEM. For each nanobeam probe position, a high-quality PED pattern is acquired, and the crystal orientation is automatically derived at each pixel by the quantitative analysis of diffracted intensities. The axial CMOS camera allows bigger arrays, faster readout (similar to the off-axis optical camera), higher-dynamical range, reduced noise, and reduced electron radiation damage [21]. We have studied semiconductor InP NWs displaying an axial screw dislocation and the corresponding crystal torsion (or Eshelby twist) [30,31]. Our results indicate that it has been possible to achieve much higher angular precision (~ 0.03°), well below normal ACOM method reports (~ 1°) and structure refinement efforts (~ 0.05°) [18,20–22,27,29]. We show a detailed comparison between different ACOM methodologies and make a rigorous analysis of the results quality and reliability. This precision improvement has been fundamental to observe the small crystal disorientations in the Eshelby twisted NWs.

2. Materials and methods

2.1. Sample and measurements

The In(Ga)P nanowires were grown using the vapor-liquid-solid (VLS) mechanism using a Au catalysts inside chemical beam epitaxy (CBE) process. The generation of the wires has already been described in detail in [32,29]. Briefly, thermally decomposed phosphine (PH_3), trimethyl Indium (TMI) and triethyl Gallium (TEGa) have been used as precursors, with H_2 as carrier gas. The electron microscopy samples have been generated by gently scraping the carbon grid (lacey type) on the substrate. The atomic arrangement in the wires is a wurtzite structure ($P6_3mc$, $a = b = 0.4150$ nm, $c = 0.6912$ nm); this hexagonal phase is not stable in macroscopic InP crystals.

The NWs represent a rather complex system to be analyzed (see Fig. 2); the wires contain an axial screw dislocation (wire axis along wurtzite hexagonal *c*-axis) such that the basal planes in the crystal form a helicoid of pitch B (dislocation Burgers vector) [30,31]. The normal to the helicoidal basal planes are tilted in relation to the wire geometrical

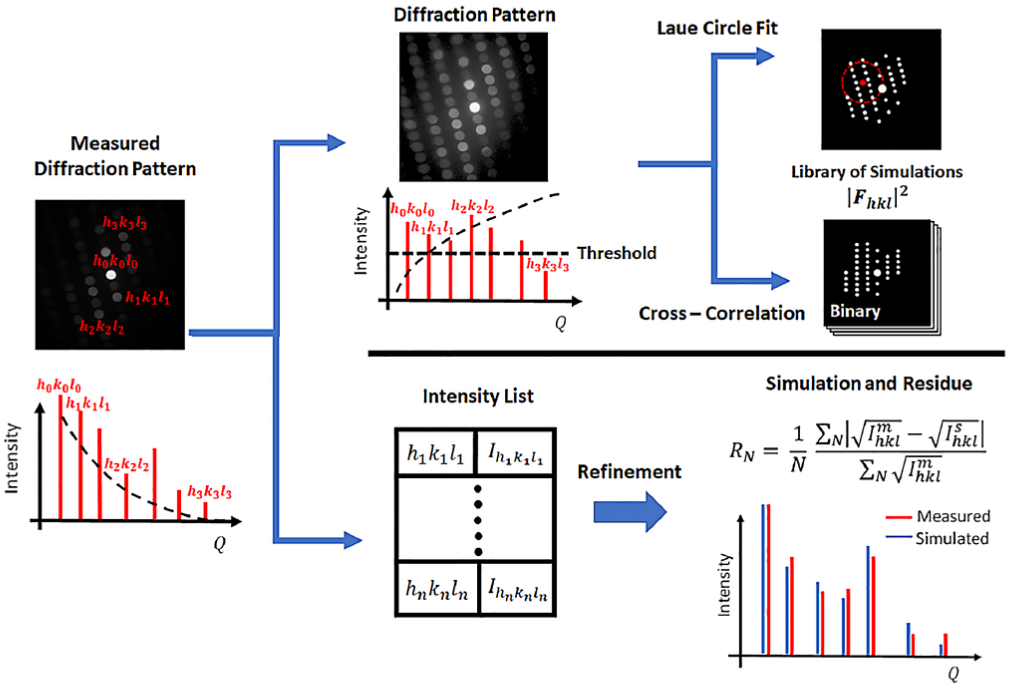

Fig. 1. Comparison between different ACOM methods. Explanation of differences between the template-matching method (threshold and binarization of intensities) and raw intensities use.

axis and the tilt display opposite sense at different sides of the dislocation line. In addition, the torque created by the screw dislocation induces a backwards torsion to get mechanical stability for a finite volume. This is so-called the Eshelby twist, which was initially proposed in the 50 s using classical elastic theory [30,31]. The twist rate α (given as radians per nm) is given by:

$$\alpha = \frac{B}{\pi R_w^2} \tag{1}$$

where B is the norm of the dislocation Burgers vector (in this case, $B = c$) and R_w is the NW radius. The twist should easily be revealed as a continuous rotation of the crystal normal along the wire. This effect has been first observed in 2008 in PbSe and PbS NWs [33,34]. A detailed description of Eshelby torsion in InP wires has been recently present by Ugarte et al. [29] and the combination of crystal torsion superimposed to helicoidal basal planes represent quite challenging case to test new ACOM methodologies. Furthermore, the interpretation of ACOM results is challenging due to changes in orientation along the electron probe path, which integrates a minor distortion at the NW surface with a much more distorted structure at the NW core. Ugarte et al. [29] has shown, using simulations, that the integration can greatly affect the measured dislocation field and imply in significative deviations from pure elastic theory at a precise radial distance of a screw dislocation.

TEM images and electron diffraction patterns have been acquired on a JEOL 2010F microscope at 200 kV. Diffraction patterns were recorded in a highly sensitive 16-megapixel F416 CMOS camera (TVIPS) and they were registered at 16-bit to ensure maximum dynamical range. This has allowed us to measure low intensity peaks (minimal intensity is ~ 200 counts) without the saturation of high intensity ones (maximum intensity is ~ 50,000 counts, close to the maximum possible in a 16bit system). Subsequently, the patterns have been binned to 512 × 512 pixels. Such procedure generates a larger data volume that is not utilized; however, more modern high-speed detectors are already limited in pixel number (usually < 512 × 512) with high-dynamical range and such cares are no longer necessary.

A Nanomegas PED unit was used to generate the precessing electron beam (frequency 100 Hz, precession half angle 0.5°). The beam full convergence angle was ~ 0.1° (measured from diffraction spot diameter), generating an approximately 2–4 nm diameter electron probe, estimated with the Barth and Kruit expression [5] with known values of probe current (2 pA) and expected instrumental parameters. The dwell time was ~ 125 ms, the electron dose is ~ 6000 $e^-/Å^2$ per pattern. The dose is much lower than the common values in many STEM experiments (usually higher than 10^5 $e^-/Å^2$). Also, the InP NW did not show modification indicating radiation damage due to electron beam incidence, such that we don't expect our results to be influenced by structural damage.

2.2. Data reduction

Data treatment has been performed with a home-made software developed in Python and, all the steps (from measurement, data reduction and quantitative analysis) are described below or in a more detailed way in Supplementary Information. A key point in our procedure is that the ACOM results are derived from structural refinement based on the analysis of diffraction intensities. Our approach relies on forming a list of intensities and their respective *hkl* values (or *hkil* for the hexagonal lattice), a common procedure in structural refinement efforts [11,27]. This greatly simplifies the simulations as only a limited set of *hkl* beam values (up to 30 in this work) needing to be calculated when compared to the required to calculate all pixels forming a PED pattern (each a 2D data, 512 × 512 pixels).

When crystallographic information is derived from the *hkl* intensities we must add the whole area under individual diffraction disk and also

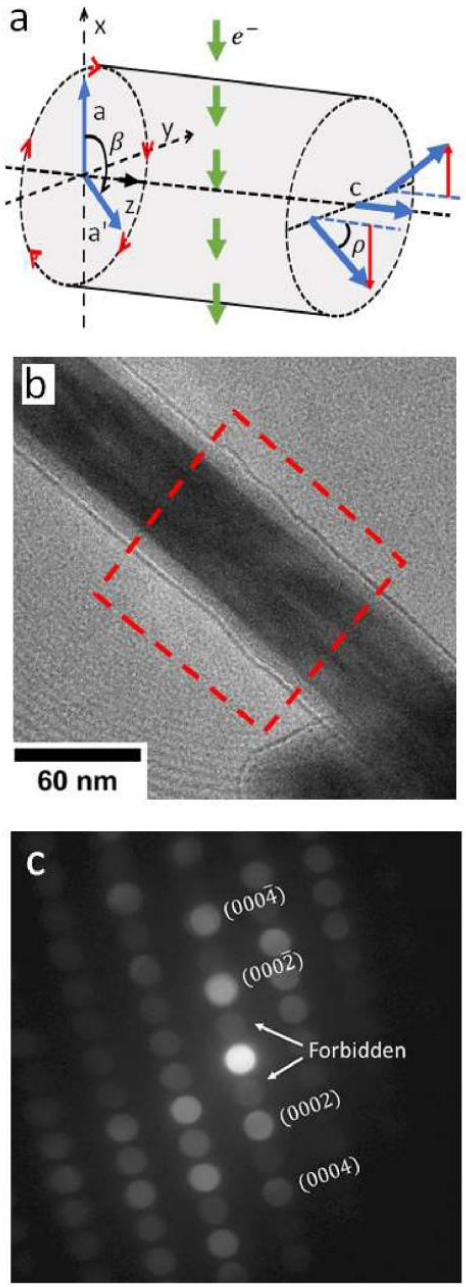

Fig. 2. a) Schematic draw of the NW crystal orientation changes due to the screw dislocation and Eshelby twist deformation fields [30,31]. Notice the a-axis rotation into the a' direction due to the crystal torsion and the change of orientation of the c-axis due to the dislocation core. b) TEM image of the nanowire; region indicated by the dashed rectangle has been scanned to generate the 4D-STEM-PED dataset. c) Example of a measured PED pattern, some peaks have been indexed along the wurtzite c–axis direction (or the NW growth direction) to show the presence of low intensity kinematical forbidden diffraction peaks.

further processing must preserve the intensity relation between different peaks. Consequentially, any data treatment that alters the peaks intensity value (enhancement filters) or the ratio between peaks (as a gamma function, that artificially increases low intensity peaks) will be impeditive for the quantitative use of intensities proposed in our work.

The original data was acquired as movie (time resolved) as the detection CMOS axial camera was not synchronized with the PED attachment used in our experiments. To convert the diffraction pattern series into 4D data, we have used VADF intensity from each pattern to assign a spatial position and build the NW VADF image (see Figs. 2 and 3). Once the 4D data set was generated, the area of the diffraction disk has been determined from the transmitted beam size and utilized as a template for the diffraction beams disk shape. This approach is only possible due to the use of PED, as there are no observable intensity variations within the *hkl* diffracted disks due of dynamical diffraction. The peak position detection is performed by cross-correlation with the template disk, allowing indexation and measurement of diffracted

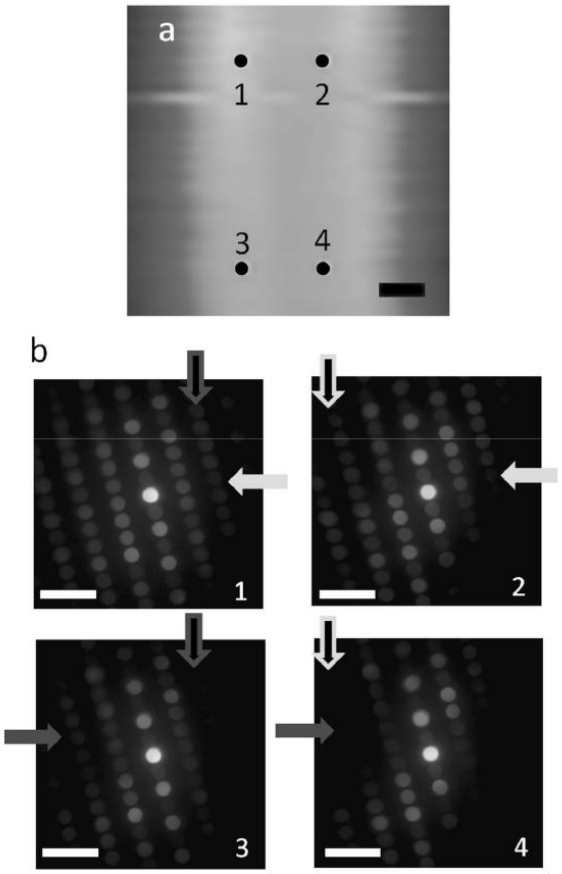

Fig. 3. Experimental data showing clear differences in PED patterns at different NW position. a) VADF image which shows the 4 distinct pixels in the NW, that are related to the 4 PED patterns below (b). The 4 arrow pairs show peaks or features displaying major distinctions between each ED both from the left to right or top to bottom. Notice that the differences are noticeable both across the NW center (where the screw dislocation is located) and along the NW length (due to Eshelby crystal torsion). The contrast of the displayed pattern images have been corrected to aid the visual analysis (gamma: 1.76, contrast: −18 and brightness: −29, IrfanView software). The scale bars are: a) 10 nm, b) 5 1/nm for all figures.

intensities from each diffraction disk (see Fig. 4 and details in Supplementary Information). Peaks which have intensity below a defined threshold have not been included as their information can be significantly affected by noise (see Supplementary Information). Background subtraction has not been utilized as no significative influence from background is observable due to the suspended nature of the sample, allowing us to minimize the amount of data processing.

This study aims the exploration of 4D-STEM PED intensities, so no attempt has been done to detect strain though the geometrical analysis of disk positions in the diffraction pattern [36–38]. Furthermore, Eshelby-twisted NWs may be too complex for strain analysis as the NW has two superimposed deformation fields (screw dislocation and crystal torsion). The dislocation strain field varies radially and the experiment performs an integration of different radial values along the electron path when traversing the NW (see [29]). This coupled with a possible non uniform relaxation of strain field due to a thick oxide layer suggest a system which may be rather complex for strain analysis.

Since, the realization of our experiments, the integration of PED and 4D-STEM with modern high-speed detectors had amazing improvement and several options are now available [18–22,39]. Many of the steps taken in our data processing (as the datablock creation) are a consequence of the utilized instrumentation, and recent developments makes then not necessary. Many native (experiment output) options for diffraction pattern data-blocks (data organization) are now available, and as long that the chosen experimental setup and data recording do not alter the measured diffraction intensities, they will be suitable to be analyzed with our proposed methodology.

2.3. Diffracted intensity calculation

The measured PED intensities include both dynamical diffraction effects (strongly dependent on crystal orientation and sample thickness) for each incident electron beam direction and, the incoherent integration along the beam precession circle. Due to the large number of diffracted patterns on an orientation mapping data set, we have chosen to use dynamical two-beam approximation for intensity calculation and a numerical integration to consider the change of excitation error associated to beam precession [12,40,41]. Our rather small 4D data-set includes more than 3000 measured EDs, and each one may need to be simulated many times during the residue (R_N) minimization procedure in order to perform the ACOM analysis or crystal orientation optimization by quantitative comparison of diffracted intensities. Although the two-beam expression may be considered a rather simplified approach to dynamical diffraction when compared with multi-slice calculation and Bloch wave formalism, it yields an analytical expression which can be utilized for quick calculation of diffracted intensity [5]. The two-beam approximation is considered of limited application to describe dynamical electron diffraction intensities from crystal oriented along a zone axis (strong many-beam condition) [5]. However, two-beam can provide good numerical descriptions of PED intensities, as beam precession reduces dynamical diffraction effects, as already reported by many studies [35,42,43]. Overall, two-beam has been reliable applied for structural refinement/solution of several types of crystal structures, and can be considered a well-established approach for quantitative analysis of PED intensities [35,44–46].

The two-beam model (Howie-Whelan equations) gives the most basic description of the diffracted intensities (I_{hkl}) in the dynamical regime: [5]

$$I_{hkl} = \frac{\pi^2}{\xi_{hkl}^2} \frac{sin^2(\pi t s_{eff})}{(\pi s_{eff})^2} \tag{2}$$

where $s_{eff} = \sqrt{s^2 + \xi_{hkl}^{-2}}$ is the effective excitation error, t is the crystal thickness and s is the excitation error for a given disorientation; ξ_{hkl} is the extinction distance and it is defined as $\xi_{hkl} = \pi V_c / \lambda F_{hkl}$, where V_c is

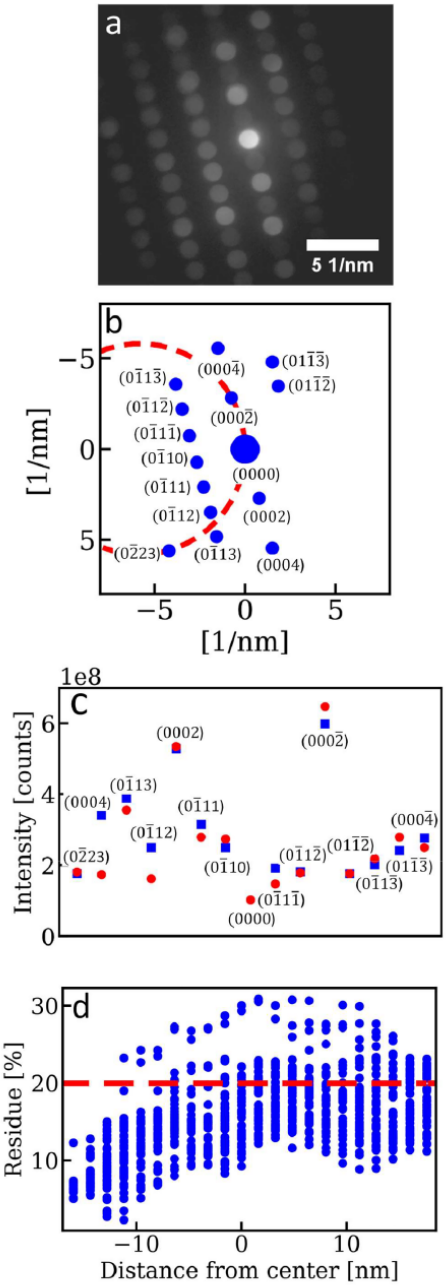

Fig. 4. Example of the intensity analysis procedure for: a) single pixel (the PED pattern). b) Indexed PED pattern, where hkil index have been retrieved, as well as intensity I_{hkil} (peak selection is based on a minimal intensity threshold of 7 % from I_{0000}); diffraction peak positions are utilized to fit a Laue circle in order to provide the initial of β and ρ for the crystal orientation optimization. c) Measured intensities (squares) and optimized simulation (circles) derived from the best model derived by residue factor minimization. d) Residue values for all the measured pixel positions along the NW (or PED patterns) in our analysis; the dashed line marks the 20 % residue value, which is considered a good quality factor for two-beam PED patterns refinement [35].

the volume of the primitive cell of the crystal, λ the electron wavelength and F_{hkl} the structure factor [47]. The application of this model requires knowledge of the thickness of the analyzed region and precise orientation (through excitation error) to calculate diffraction peak intensities.

Our simulations are based on a numerical integration to consider the effects of beam precession geometry where spot intensity is evaluated around the relaxed Bragg condition (integrating a range of s values). We have calculated this by considering the Laue circle center (O_L) movement, as the electron beam precession implies in a complete revolution of O_L around the transmitted beam position (T) [40,41]. If θ is the angle that defines projection of the scattering vector $\boldsymbol{k}$ ($k = 1/\lambda$) (azimuthal position of the precessing beam, see Figure S3) we can express the PED intensity as: [40,41]

$$I_{hkl}^{PED} = \int_0^{2\pi} I_{hkl}(\theta)d\theta \tag{3}$$

The precession geometry implies in a complex relation between the crystal orientation, precession angle and the excitation error. Such relation can be expressed by the equation derived by Gjonnes: [40]

$$s(\theta) = -\frac{2R_0 g_{xy}\cos(\theta) + 2kg_z + g^2}{2k} \tag{4}$$

where R_0 is the Laue circle radius ($R_0^2 = k_x^2 + k_y^2$), $\boldsymbol{g}$ is a point in reciprocal space, g_{xy} is its component in the plane perpendicular the component g_z parallel to the optical axis. Usually, the g_z factor in Eq. (4) is neglected due to the low value in the first Laue zone (most spots appear in this region due to the small curvature of the Ewald sphere for high energy electrons) [27,43,10]. Although this may be a sound argument for analyzing zone axis patterns, its implementation forces a symmetry to the diffraction intensities (not suitable for performing simulations targeting ACOM). For the pair of reflections hkl and $\overline{hkl}$, g_{xy} will be identical and both reflections will have equal intensities and independent of crystal orientation [48]. Then, it is fundamental to include the g_z term, as tiny value modification may induce asymmetry between intensities which carry the searched essential information about crystal orientation.

It is important to notice that Eqs. (2) and 3 can be utilized to account for the presence influence of several phases or overlapped crystal in the measured PED as each may be considered to contribute independently to the incoherent addition to form the total hkl intensity (independent intensity). This simplification is more realistic in PED, as it helps to avoid multiple scattering between crystals, for example, by reducing the influence of double diffraction in the overall intensity distribution [49].

In the following section, we will describe the crystalline structure and crystal orientation referential implement for PED intensity calculation based on the two-beam approximation.

2.4. PED intensity calculation and residue minimization

We have chosen our coordinate system such that initially the crystal is perfectly oriented at a zone axis set along the x axis (anti-parallel to the microscope optical axis), with prior correction of any possible in-plane rotation (rotation around the x-axis). Subsequently, the reciprocal lattice vector $\boldsymbol{g}$ of a reflection in a twisted crystal relates to the one in the ideal zone axis orientation ($\boldsymbol{g}_0$) by $R_y(\rho)R_z(\beta)\,\boldsymbol{g}_0$, where R_y and R_z are the rotations matrix around the y and z axis, respectively. This is used to calculate the excitation error as a function of β, ρ and θ (azimuthal position of the precessing beam) for any orientation of the crystal near the considered initial zone axis.

The next step involves the calculation of the structure factor for the estimation of ξ_{hkl}. In the case of InP wurtzite structure, two Debye-Waller factors (B_{In} and B_P, for the In and P atoms respectively) are necessary. In our residue minimization procedure, we included a single multiplicative factor m_{DB}, which modifies the amplitude of both B_{In} and B_P factors to account for possible variations in the Debye-Waller factors. This has been necessary to avoid complications due to correlation of B_{In} and B_P during optimization, a possibility as both have the same effect in the calculations (damping of intensities with increasing scattering angle). Then, m_{DB} imply in only one parameter to describe the intensity damping while preserving the proportion of B_{In} and B_P. In this approximation the structure factor is given by:

$$\begin{aligned} F_{hkl}(m_{DB}) &= \left(f_{In}e^{-m_{DB}B_{In}Q_{hkl}^2} + f_P e^{-m_{DB}B_P Q_{hkl}^2} e^{\frac{i3\pi l}{4}}\right) \\ &\times \left\{1 + \exp\left[i2\pi\left(\frac{h+2k}{3} + \frac{l}{2}\right)\right]\right\} \end{aligned} \tag{5}$$

where $B_{In} = 0.88$ Å^2 e $B_P = 0.57$ Å^2 (bulk values); f_{In} e f_P are the atomic scattering factor for the In e P, respectively [50,51].

Finally, utilizing Eqs. (4) & (5) in 2 & 3 we obtain the equation utilized to calculate the diffracted intensities:

$$\begin{aligned} I_{hkl}^{PED}(A,t,m_{DB},\beta,\rho) &= \frac{A\pi^2}{\xi_{hkl}^2(m_{DB})} \\ &\times \int_0^{2\pi} \frac{sen^2\left\{\pi t s_{eff}[\xi_{hkl}(m_{DB}), s(\beta,\rho,\theta)]\right\}}{\left\{\pi s_{eff}[\xi_{hkl}(m_{DB}), s(\beta,\rho,\theta)]\right\}^2} d\theta \end{aligned} \tag{6}$$

The integral in the expression is performed numerically and imply in five free parameters in our residue optimization procedure:

1) A : scale factor.
2) m_{DB} : changes in the Debye–Waller factors.
3) t : crystal thickness.
4) β : crystal rotation (ACOM parameter).
5) ρ : crystal rotation (ACOM parameter).

The crystal orientation is derived through a refinement based on the comparison between the measured and calculated intensities using a residual factor defined as: [35]

$$R_N = \frac{1}{N}\frac{\sum_N \left|\sqrt{I_{hkl}^m} - \sqrt{I_{hkl}^s}\right|}{\sum_N \sqrt{I_{hkl}^m}} \tag{7}$$

where I_{hkl}^m is the measured intensity and I_{hkl}^s the simulated one. This residue value is normalized by the number of peaks (N) in each diffraction pattern to allow for comparison between EDs with lower and higher values of N. In this work, when the residue R_N is shown in percentual units, the R_N is multiplied by N, such that we can compare the quality of the structural description obtained with previous works in the literature. The addition of $1/N$ in R_N do not change the minimization parameters for individual EDs, as it is only a scale factor in the residue evaluation.

The number of diffraction peaks (or fitting values) in each ED may be rather low (27 to 7 peaks have been utilized in this study), so we have chosen to further reduce the number of free parameters simultaneously fitted in our ACOM application. Our highest concern arises for the NW sides, where we have observed a strong thickness variation and significant effect of the amorphous oxide layer. It would be better to avoid any potential overfitting of the measurements due to the low information content over this wire region. In this sense, we have decided to optimize the Debye-Waller scaling factor m_{DB} globally, such that all EDs will have the same value. The thickness t has also been optimized globally, however the shape of the nanowire can be very complex, such that a more in-depth discussion may be need is this case (see practical details below). A cylindrical shape is the most reasonable expectation for the NW shape, however there are reports showing that semiconductor NW surfaces may show prominent faceting [52,53]. We have used VADF intensity to test which possibility would be the most appropriated for our data; the VADF NW profile does not follow the expected cylindrical shape, suggesting that it is reasonable to consider a faceted NW cross-section and uniform

thickness. This has been assumed for the wire region displaying highest SNR and that is suitable for the diffracted intensity analysis (see Supplementary Information section S.4 for more details). This constant thickness assumption may be refined in future works, but the comparison of both models (cylindrical and faceted) has not shown relevant differences in the results for the present study. The methodology applied here can be performed with any type of thickness variation model or even with thickness optimization in every pixel. In fact, one of the strengths of PED is that it its a well-recognized approach to diminish the sensibility of the intensities to small changes in sample thickness [11,12]. This is important to simplify the complexity of determining the optimal thickness in quantitative intensity analysis, as simple electron path variation models can be utilized and/or reliably tested even with the analytical two-beam simulations. Initially we have attempted to also refine the A value globally, however this was not possible as this demanded all diffractions patterns to be rescaled by the transmitted diffraction beam intensities. This procedure implied in severe discretization of the measured intensities (possible due to numerical truncation of very large numbers during division or by saturation of the transmitted beam intensity), which consequentially discretized all the optimized parameters.

In practice, the optimization is performed in two steps. First, a grid of m_{DB} and t values is manually formed, the interval between them is chosen to ensure sensitivity without overpopulating the grid (as performed in [54]). Concerning crystal rotation analysis, NW torsion induces the basal plane vectors (a, b, and d axes) to rotate by β (R_z) and the basal plane normal (hexagonal c axis) will tilt due to the screw dislocation by ρ (R_y, see data treatment section and Fig. S4b, c).

Then, for a pair of m_{DB} and t, the parameters A, β and ρ are optimized for each individual ED, with a common minimization algorithm (our data was best suited by differential evolution and Powell function optimization from Scipy [55]), but this may likely change with other systems). The pair m_{DB} and t (and the corresponding A, β and ρ) are chosen as the one that minimizes the mean residue of the whole dataset (always taking care with possible overfitting in the NW extremities). The choice of initial values in the optimization must be carefully performed to ensure convergence in a global minimum. The Laue circle fit (see Section S3) is utilized to find the initial values of β and ρ; the t initial value is found from the virtual images and m_{DB} is initialized equal to 1. Also, the thickness and m_{DB} are minimize through a brute force approach by a forming a grid of values, which allow us to better control the minimization. A template code (jupyter notebook) of the minimization algorithm is provided and a workflow of the method is present in the Supplementary Information (Section 8). Consequentially, the data analysis presented here is based on the optimization of the parameters A, β and ρ for each ED, such that we can obtain the orientation of each measured pattern of the NW through a residue factor comparing experimental and simulated intensities.

3. Results

Fig. 2 shows a TEM image of the Eshelby twisted InP NW, where we can observe a thin amorphous oxide layer and also a contrast variation at the NW center revealing the existence of the axial screw dislocation. Fig. 2b indicates the region scanned for the 4D-STEM data set (3500 patterns, 50 × 70 pixels, pixel step 1.59 nm). A quick look at a typical diffraction pattern (Fig. 2c) reveals that the crystal orientation is close to the $[2\bar{1}\bar{1}0]$ zone axis and that the misalignment is rather low. Using a simple Laue circle fit on the diffraction spot positions we may verify that zone axis misorientation is in 1–2° range [25].

Fig. 3 show diffraction patterns from pixels located such that their positions form a rectangle over the NW in such way that we are able to observe possible crystal orientation differences across the wire center (due to screw dislocation), and also along the wire due to the Eshelby torsion. As expected, the PEDs patterns show significant changes, which can be detected even with a simple visual inspection.

3.1. Results of acom based on intensity analysis

We have chosen as our coordinate system the case where the crystal is perfectly aligned along $[2\bar{1}\bar{1}0]$ zone axis along the x axis (anti-parallel to TEM optical axis); the c vector of wurtzite crystal is along the z axis.

Fig. 4 shows the different steps realized to perform the crystal orientation optimization based on the intensity of the diffraction spots. Firstly, the in-plane rotation of the ED must be correct or accounted prior to indexation; for the InP NW this can be performed by matching the [0001] direction of the ED with the anti-parallel of the NW growth direction (direction of increased diameter). Subsequently, the Laue circle (see section S.5 in the Supplementary Information) is fitted on spot positions to obtain initial angular values of β and ρ for orientation refinement (Fig. 4a and b). Then, the free refinement parameters are optimized to minimize the residue (R_N, Eq. (7)) comparing experimental and simulated intensities; an example of the result of this procedure is show in Figs. 4c and S11. Overall, the residue values are below 20 % (see Fig. 4d), such that we can confirm that a good structural description has been obtained for the ensemble of the NW; the residue value is similar to previous reports on structural refinement based on PED pattern analysis using two-beam approximation [35]. Also, the colormap of normalized residues (see Fig. S9c) is mostly homogeneous within large areas, ensuring optimization with minimal influence of noise. Furthermore, better structural descriptions (lower residues) are expected from crystal orientations that minimize the number of excited reflections, as they are closer to the two-beam condition expected by Eq. (2). However, the homogeneity of the residues in Fig. S9c show that such effect is not observable in our results. The optimized Debye–Waller factors are 0.6 $Å^2$ and 0.4 $Å^2$, for the In and P atoms, respectively. These values are slightly lower than the crystallographic base data for room temperature (In: 0.9 $Å^2$, P: 0.6 $Å^2$), but this can be explained by the increase in relative intensity for high scattering vector Q in PED patterns, which induces an effective reduction of the derived Debye–Waller factor [50,12]. The standard deviation of the optimized Debye–Waller factors along the NW center is approximately ~ 0.2 $Å^2$; only the center is utilized to avoid possible changes in thickness that can alter the Debye–Waller value. The combination of good residues and coherent Debye–Waller factors values ensure that the results obtained are reliable for the ensemble of diffraction patterns.

The quantitative analysis of diffracted intensity yields the crystal rotation angles β and ρ directly (two free parameters of the residue optimization). To reveal the screw dislocation, we plot the angle $\rho_{dis} = \rho - \rho_{center}$ (value of ρ_{center} is associated to pixels on the axis where the screw dislocation core is located) for each measured position at both sides of the NW (see Fig. 5c) [29]. A clear opposite behavior is observed when comparing the NW left and right sides. The Eshelby crystal torsion is observable by the plot of $\beta_{twist} = \beta - \beta_{base}$ (mean value of β_{base} across the wire in one of the NW extremities, see Fig. 5e). As expected, the basal plane rotation increases along the NW, revealing the crystal torsion around c -axis. Similar characteristics have been observed in crystal disorientation maps (Fig. 6), where a clear contrast can be observed across the NW center for screw dislocation detection (ρ_{dis}) and subtle torsion variation (β_{twist}) along the NW.

4. Discussion

As observed in the previous section the ACOM based on PED intensity analysis has easily revealed the helicoidal nature of the basal planes, as well as the induced crystal torsion in the NW crystal [30,31]. Nonetheless, it is important to corroborate these results by comparing them with other well-accepted ACOM methods, specially with the ones that only utilize the diffraction peak position as main source of information. In order to compare the quality of generated results, we can

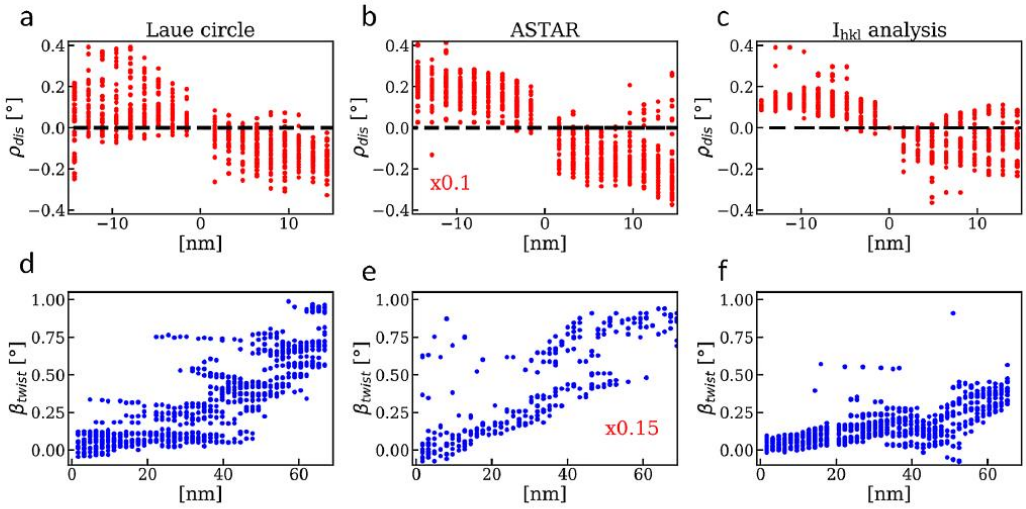

Fig. 5. Comparison between the results of dislocation deformation field (a–c) and Eshelby torsion (d–f) for the ACOM methods. Note that the ASTAR plots have been multiplied by a 0.1 or 0.15 factor to allow an easy comparison between different ACOM approaches with plots using display scales of identical value.

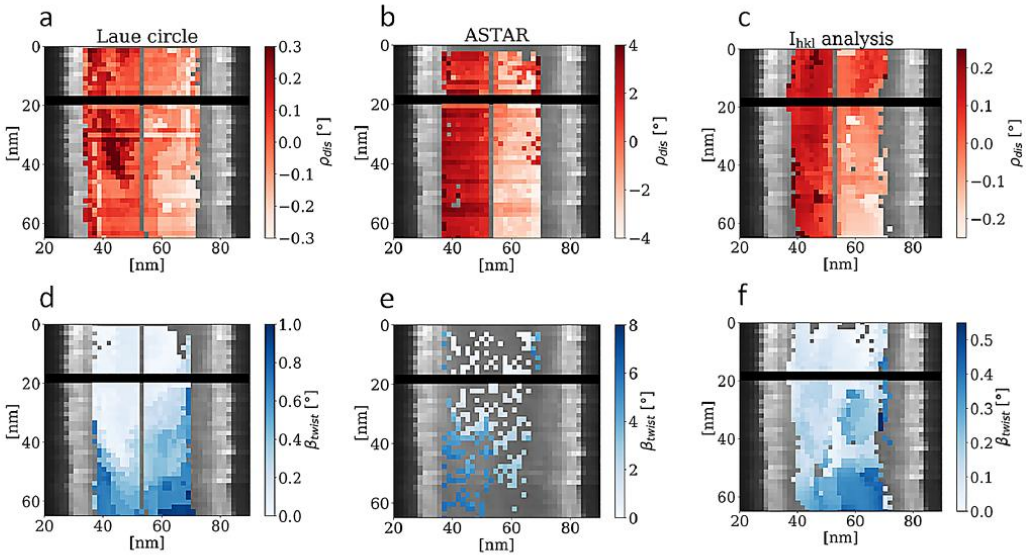

Fig. 6. Disorientation maps for the dislocation deformation field (a–c) and Eshelby torsion (d–f) for the ACOM methods. The colormap contrast represents the maximum and minimum disorientation values for each method, such that they are directly comparable (see Fig. 5).

quantify the dispersion of the values of ρ_{dis} and β_{twist} (named σ_ρ and σ_β, respectively) using the root mean square deviation; this will provide a reliable estimation of the angular precision and dispersion in crystal orientation determination.

The most popular methodology for ACOM is based on pattern matching, this approach has been initially proposed by Rauch [14] and also adopted by different available freeware programs [18,22,14]. In this work, we have used the proprietary software ASTAR for the comparison, which has already utilized for the characterization of Eshelby twisted InP NWs [29]. We must note that pattern matching ACOM is capable of identifying the presence of a screw dislocation and measure crystal torsion (Fig. 5). The angular precision obtained with ASTAR is ~1° (angular dispersion σ_ρ) what is about one order larger that the intensity analysis approach (see Table 1). This can be due to fact that initially ACOM has been designed to target the analysis of large areas

Table 1
Summary of the results obtained from ACOM based on different data treatment strategies (Laue circle, template matching-ASTAR and diffracted intensity analysis).

Method	Twist rate (°/nm)	σ_ρ(°)	σ_β (°)
Laue circle	0.010 ± 0.003	0.24	0.32
ASTAR	0.031 ± 0.008	3.0	1.2
Diffracted Intensity	0.006 ± 0.001	0.14	0.18

(several μ^2) where crystal grains suffer large and abrupt changes in crystal orientation ($> 10^\circ$). Usually, the number of PED patterns in the data set is in the several tens of thousands and this kind of crystal orientation study requires to map a large volume space in reciprocal space and with a high speed. The efficient cross-correlation metric has been chosen, but this metric is prone to get stacked in local minima [18]. Many researchers tried to improve the angular resolution of the pattern matching method with improved instrumentations, image treatment methodologies and better sampling of reciprocal space in simulations, but angular resolution has remained around $\sim 1^\circ$ [18,20–22,29]. Angular resolution of $\sim$ 0.2° has been achieved when the template-library calculation is modified to include and replicate the effect of beam precession in the intensity angular variation (rocking curve) [28].

The Laue circle approach only relies on simple fit of a circle to the PED spots positions, ignoring intensity of the diffraction spots. It is extremely fast and simple to apply; also, it does not request any kind of simulations library or previously knowledge about the crystalline structure. Nonwithstanding, the extracted information may be rather limited, being mainly appliable to derive the angular distance to the closest crystal zone axis [25]. Although its simplicity, the Laue circle method has been able to reveal the presence of the screw dislocation and crystal torsion for the rather small NW region analyzed here (see Fig. 5a and c). We can observe in Table 1 that the Laue circle angular dispersion σ_ρ is much lower than using the template-matching method, what enable us to observe changes below 1° in crystal orientation (see Section 5 in the Supplementary Information for more details). Overall, the Laue circle fit appears to be a good alternative to the common template matching procedure to derive small changes in orientation in a small sample region as required for a distortion/strain study. Finally, the derived angular dispersions are almost twice the ones obtained by the intensity analysis proposed in this work (Table 1).

The torsion angle derived from template-matching (Fig. 5e) appears to present two populations; this could be explained by the presence of two close local minima in the template-matching procedure, a tendency which has already been observed [18]. The Laue circle provided a twist evolution along the wire where several plateaus are clearly observable (Fig. 5d), this indicates the lack of precision to detect small PED features. In contrast, when using the diffracted intensity analysis, the twist evolution is mostly continuous with a monotonous positive slope (see Fig. 5**e**). Table 1 shows the comparison of measured twist rates, which measures the wurtzite basal plane rotation due to Eshelby torsion (it is supposed to be constant change rate along the NW due to the short NW section that has been analyzed). The twist rates derived from each ACOM methodology are significatively different (Table 1) and also differ from theoretically calculated value of $(0.0219 \pm 0.0001)^\circ$/nm (Eq. (1), for a cylindrical NW with (48 ± 7) nm in diameter and Burgers vector equal hexagonal axis c). The more precise torsion rate evaluations methods (Laue circle and intensity analysis) have superimposed values, but both underestimate the theoretical twist rate by at least a factor of 3×. It is important to notice that a quantitative comparison must be performed with care as the assumption of Eshelby equation relating Burgers vector and torsion rate (with $B = c$) has shown to be quite unreliable in several attempts to quantify NW torsion rates (usual values deviate by a factor in the 0.3–3× range) (see [29,32–34,56]). Such deviations could be explained by several different factors: i) faceted NW shape what is different from the theoretical cylindrical calculation; ii) oxide layer on NW surface which can relax the distortion in the structure (in our case is quite thick $\sim$ 7 nm); iii) a complex interplay between the dislocation core (unknown structure) and surface effects in the NW distortion field. Considering the available data, we have been able to discuss ACOM precision with the intensity analysis, but we are not able to estimate the accuracy. In order to estimate accuracy, we would need a Eshelby twisted nanowire with rotation of more than 30° along the analyzed region to cross two zone-axis (*e.g.* $[0\bar{1}10]$ and $[\bar{2}110]$, see Fig. 3 in [29]). These zone axes provide a good standard for calibration, but also require a very thin wire ($\sim$ 30 nm in diameter, torsion is inversely proportional to NW diameter), where crystal torsion is large (0.05°/nm). Otherwise, the required NW length is not viable for intensity analysis ACOM: our measure region is $\sim$ 0.07 μm in length, a 30 nm in diameter requires at least 0.5 μm and the measured NW (diameter $\sim$ 45 nm) requires almost 1.5 μm. The NW shape must also be straight, as any thickening due to lateral growth will lower the torsion rate and increase the required length.

Briefly, the three methods have been able to detect both dislocation and torsion deformation fields in the NW structure (see Fig. 5), however a quick visual inspection of the data indicates massive differences in the characteristics of the results. We took great care to ensure that each method was optimized to yield the best results, which required only some minor adaptations between data reduction for each method. The main difference was the threshold values utilized to select valid diffraction spots in the PED pattern (3 % and 7 % of I_{0000} for, respectively, the Laue circle and intensity analysis). For the ASTAR processing, we utilized a gamma function to enhance the low intensity peaks threshold value (traditional approach in pattern matching procedures), then the threshold cannot be directly compared with the other two approaches. We do not expect that such minor changes have had any major influence in the comparisons between methods. The above discussion shows that intensity analysis provides the crystal orientation and twist values with highest precision among all methods (Table 1).

Our analysis shows clear differences in sensibility to measure changes of the orientation of c axis (dislocation) or basal plane rotation (torsion). The colormaps in Fig. 6a–c shows that all the three methods detect the dislocation deformation field, however none of them appear to derive a well-behaved evolution of twist angle β_{twist} (see Fig. 6d–f). This is most critical for the ASTAR analysis as most derived β_{twist} values are not appropriate for torsion analysis (too large variations between neighboring pixels), such that only a very limited number of pixels are considered reliable to observe crystal torsion.

The previous study of Eshelby twisted InP NW have clearly shown the assessment of crystal torsion become imprecise when incident beam direction is perpendicular to hexagonal c-axis and close to zone axis the directions (2110) (see Fig. S5 in the supplementary information of [29]). For crystal close to these orientations (within $\sim 5^\circ$), assessment of disorientation can be significantly noisy and non-accurate. Consequentially, as the NW studied here is oriented close to a $[2\bar{1}\bar{1}0]$ axis ($\sim 2^\circ$ misorientation) we should expect that the measurement of such a small torsion rate (0.02 °/nm) will be extremely difficult from SPED. However, it is possible to recognize a subtle torsion along the NW (see Fig. 5d–f).

The exploration of diffracted intensity allows the measurement of disorientations with a precision much better than previous works for the case of deformation fields in nanowires [29]. The obtained angular dispersion agrees with reported precision of individual frames orientation during tomography of reciprocal space experiments [27]. These experiments must correct the angular values indicated by TEM goniometer mechanics, and the authors have used a PED diffracted intensity refinement to determine the correct crystal orientation. The intensity analysis procedure is analogous to structure refinement data treatment, such that the residue value is the important parameter to be considered. The residue normalized by the number of peaks (see Fig. S9a) tend to increase close to one of the NW sides (right) in relation to values for in the NW center (also observable along the right edge in Fig. S9c). This is expected considering the lower quantity of information (less diffraction spots) in such EDs and, also the increasing relevance of the amorphous oxide shell in relation to the crystalline phase. However, the other NW side, show a different behavior and the normalized residues remain at same values than the center. This may relate to a certain asymmetry observed in the virtual images and the number of peaks (see Supplementary Information, Figs. S5b, S7b and S9b), possibly related to small differences in thickness in each side of the NW. This indicate that we

must be careful in properly deciding the region in which the measured disorientation is reliable. A proper criterion may be determined in the region where the normalized residues start to deviate from the radial neighbor's tendency, as those appear to be homogeneous (see Figure S9c). It is important to understand how much changes in the number of diffractions peaks affect the quality of structural description, as this could be an important limitation for ACOM based intensity. It is evident that ACOM is most reliable when crystals are orientated far from zone axis, however, quantitative use of diffraction intensities is most precise when crystal is orientated near a zone axis (more diffraction peaks will imply in better structural descriptions). In our data, no significative degradation in the quality of structural description could be identified in our analysis for pixel close to the center of the NW (outside the increased residue edges in Fig. S9c), even with a variation of the number of diffraction peaks along the NW (see Fig. S9b). Although the residue map in Fig. S9c shows that the residues near the bottom of the NW are larger than in the top due to the lower number of diffraction peaks (see Fig. 3 for an example) the residues are still acceptable. Most of our fits have $R_N < 20\%$; this value is considered to be a good quality when analyzing PED patterns by two-beam simulations [35]. This implies that the crystal structure is well described by assumption taken to the optimized free parameters in our simulations: crystal orientation described by 2 angles and a simple rescaling of the Debye-Waller factor for In and P. It must be emphasized that the residue values are comparable with ones in previous works even through the precession angle is much lower. Our PED 4D-STEM data have used a precession angle of $\sim 0.5^\circ$ (typical angle for SPED experiments in uncorrected TEM instruments), while previous works targeting electron crystallography and structural refinement have used precession angles above 1° [11,13,54,57,58]. It is our understanding that the careful consideration of the precession geometry by the numerical integration along the excitation error g_z (Eq. (4)), represent an essential issue for the generated ACOM good quality refinements.

The analyzed Eshelby twisted NW represent a very interesting atomic arrangement due to the superposition of two orthogonal deformation fields. In fact, all pixels should show a crystal on a different orientation. However, as in our case only a small length of the twisted NW has been measured (~70 nm), it is reasonable to think that this wire sector is straight with a constant *c*-axis orientation for pixels on the wire center [29]. This provides us with a second opportunity to measure a constant optimized parameter (ρ) in the sample by observing the orientation of the wurtzite *c*-axis at the NW center. Both the Laue circle and intensity analysis corroborate that no significative tendency is observed for the changes in ρ along the NW axis or center region (see Fig. 7). In this case, the precision (dispersion for the values ρ in the NW center) for the Laue circle is $\sim 0.06^\circ$ and for the intensity analysis is $\sim 0.03^\circ$. This result indicates the high quality of the crystal orientation precision that can be obtained by the diffracted intensity analysis in 4D-STEM using PED.

It is important to corroborate the robustness of our results by observing the consistency of the several steps taken in our data treatment. During optimization, the 2 angles (β and ρ) describing crystal orientation are the most relevant free parameters for residue minimization in our analysis. A small variation of any of these parameters induce significant residue changes; we have observed that changes of $\sim 0.1^\circ$ are enough to produce a residue difference of ~ 1 % (see Supplementary Information, Fig. S10). As the precision of orientation values in our study is $\sim 0.03^\circ$, this implies that it is not possible to differentiate models (crystal in distinct orientations) with R_N differences around ~ 0.2 % for our experimental conditions (SNR, maximum scattering angle, *etc.*)

The use of high-speed and low noise detector is fundamental to the quantitative use of intensities in nanomaterials and to avoid structural damage by electron irradiation. However, the method itself can be applied to datasets captured with much less performant detectors. This is clearly observable in the crystallographic works by Palatinus where similar approach was taken in reciprocal space electron tomography

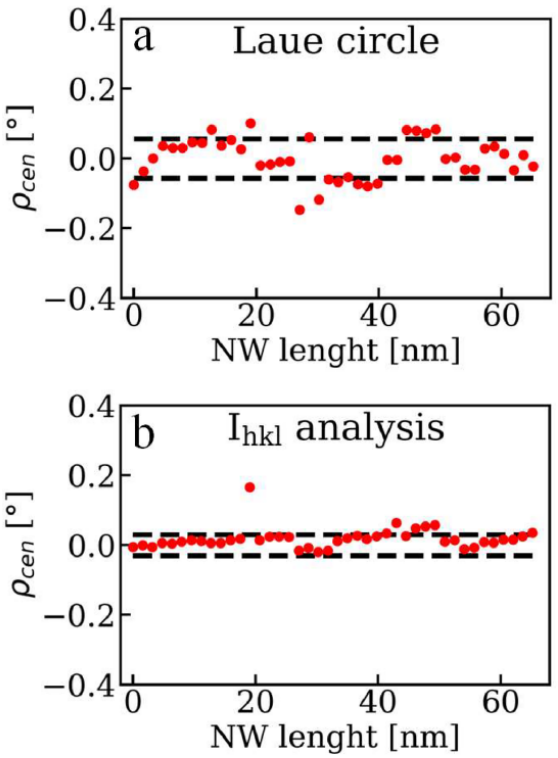

Fig. 7. Dispersion ρ_{cen} (in relation to the mean value) of ρ (hexagonal c-axis orientation) at the NW center derived from a) the Laue circle fit and, b) intensity optimization. The scales have been chosen such that the precision can be compared with the dispersions in Fig. 5a–c.

data capture by CCDs, where a good quality angular precision has been achieved [27,35,54]. Most detectors available in the market are appropriate for low to medium scattering angle (<12 1/nm) electron diffraction measurement (in relation to linearity and other aspects affected by the detector quantum efficiency). Regarding data quality, we do not expect that binning or detector size will influence the measured integrated intensities, as the main detrimental aspects to their quality (support background and Poisson noise) are mostly independent of the number of pixels that define the diffraction spots. Consequentially, angular precision is mostly dependent of diffracted intensity counts, quantity of peaks and PED reduction of dynamical diffraction effects. Then, the choice of instrumental parameters (dwell time, beam current, step size and probe size) must provide the maximum number of counts for the diffraction intensities, while minimizing sample damage by the electron beam and avoiding saturation of the detector. The probe convergence angle, and consequentially the probe size, must be limited to ensure that no overlap occurs between diffraction disks, as a one-to-one correspondence between peak intensity and indexation must exist to perform the two-beam modeling.

The work discussed in this manuscript uses a quite different approach to evaluate ACOM (diffracted intensity quantification) in which we focus on precision over a rather small dataset (few thousand of PED patterns). The residual factor metric is a very robust and popular approach in crystallography using x-ray, neutron or electron radiation for structural refinement. The residual metric has proved to be suitable even for cases where many local minima are present, although all the process (simulation, parameter variation and comparison) may be rather slow compared to the efficient pattern matching algorithm. Our analysis

has taken about ~ 22 h to be completed in common desktop computer: Intel i5–8400 CPU (2.8 GHz), 32 Gb of RAM DDR4, 1 Tb HD, UHD Intel 630 GPU. The ACOM results presented here are based on the analysis of ~ 750 PED patterns; similar crystal orientation optimizations has been reported for ED-based tomography of reciprocal space where 50–100 ED patterns constitute the data set. The speed of the method can greatly improve from parallelization as each PED pattern can be treated as independent from other. Others improvements could be performed, *e.g.* by more efficient minimization algorithms, proper vectorization in many sections of the algorithm, *etc*. This could allow the method to be applied to very large datasets or to contain multiple phases.

5. Conclusions

Our results show that PED-based ACOM can be significatively improved by exploring quantitative analysis of the intensities to attain an angular precision of ~ 0.03°. This opens a wide range of new possibilities to analyze precisely small crystal orientation changes such as Eshelby twist NW and roughness in bidimensional material [29,59,60]. After the crystal orientation optimization procedure, residue values for each pixel fully agree with previously reported structural refinement of PED data and two-beam dynamical diffraction analysis [35]. Although, the used precession angle is smaller (~ 0.5°) than conventionally accepted for electron crystallography structural refinement (1–3°, *e.g.* electron tomography in [35]), the high-quality results are most likely due to a proper integration of excitation error for PED provided by the Gjonnes formalism [40].

The structural complexity of the measured NW allowed the possibility to measure the small disorientation required to determine the method angular resolution, but also implied in a limited assessment of the accuracy. The method is accurate as the measured torsion rate are within the expected deviations from the Eshelby elastic theory, but further work must be performed for a reliable measurement of accuracy, *e.g.* by measuring a region of Eshelby NW containing two zone axis. Also, the structural complexity of the nanowires (screw dislocation and torsion) limited the possibilities to explore full-dynamical simulations to access the limits of angular resolution and accuracy. Thinner crystals with less structural distortions can provide the possibility to analyze limits and accuracy of ACOM based on intensities analysis. All the methods showed difficulty in yielding a reliable measure of NW torsion rates, which shows the importance of avoiding near-zone-axis (>5°) crystal orientations, independently of the utilized methodology.

The homemade developed software has performed the analysis of around 750 diffraction patterns in ~ 22 h of processing in desktop computer; but we estimate that this could be improved with more computational power and algorithm optimization. We must note that we have used a two-step approach to accelerate data treatment: 1) firstly, initial crystal orientation values are derived from the rapid and simple Laue circle fit and, 2) optimization based of intensity comparison between model and experiment. We think that a similar approach may be implemented by considering an initial step based on template-matching, but using a low sampling in reciprocal space to build the library.

More modern detectors can provide improvements in data quality due to their higher signal-noise-ratio, and higher acquisition speed that allow larger regions of the NW to be measured without beam damage. However, the data quality required for quantitative intensity analysis is much higher (much higher counting level) than the common ACOM ones, and not only instrumental limitations are significative. At present, template-matching routinely performed with good reliability and reasonably short acquisition times, but diffraction peaks typically have insufficient counts for proper intensity quantification. Template-matching only requires the identification of a diffraction peak, and this can be performed when its intensity is three times (3 ×) the background noise. The seminal work of Currie [61–64] shows that quantitative analysis requires a significant increase of the signal level (approximately 15 times higher than the uncertainty interval) to attain the measurement of a quantity with a 10 % relative error. This increases enormously the signal (counting level) required, in particular when the detection suffers from shot noise, given that in Poisson statistics intensity uncertainty is the square root of the intensity and it is unavoidable. Consequentially, experiments for intensity analysis requires acquisition speed limited by signal counting level of diffraction peaks, not detector speed or the precession cycle frequency.

The study described in this manuscript has focused on the analysis of experimental diffracted intensities to determine crystal orientation and no exploration of the peaks position has been attempted. If we remind that a small shear deformation can be describe as a pure strain plus a rotation, [65] the simultaneous exploration of both characteristics (diffraction disk positions and high precision crystal misorientation) can provide a much more complete characterization of the deformation in nanomaterials by exploring the whole potentiality provided by PED 4D-STEM dataset.

CRediT authorship contribution statement

Leonardo M. Corrêa: Writing – review & editing, Writing – original draft, Methodology, Visualization, Validation, Software, Investigation, Formal analysis, Data curation. **Eduardo Ortega:** Writing – review & editing, Resources, Methodology, Data curation. **Arturo Ponce:** Writing – review & editing, Supervision, Resources, Methodology, Funding acquisition, Data curation. **Mônica A. Cotta:** Supervision, Resources, Methodology, Funding acquisition, Data curation, Conceptualization. **Daniel Ugarte:** Writing – review & editing, Writing – original draft, Visualization, Validation, Supervision, Software, Resources, Project administration, Methodology, Investigation, Funding acquisition, Formal analysis, Data curation, Conceptualization.

Declaration of competing interest

The authors declare that they have no known competing financial interests or personal relationships that could have appeared to influence the work reported in this paper.

Data availability

The article is accompanied by a template code to utilize our method in other materials. For more information can be found in the Supplementary Information.

Acknowledgments

D. U. acknowledges financial support from the Brazilian Agencies FAPESP (No. 2014/01045-0), CNPq (402571/2016-9, 306513/2017-0, 402676/2021-1, 303025/2022-0) and FAEPEX-UNICAMP (2632/17). M. A. C acknowledges financial support from FAPESP (Nos. 15/16611-4 and 19/07616-3) and CNPq (No. 429326/2018-1). A. P. and E. O. gratefully acknowledge the financial support provided by U.S. Department of Defense W911NF1810439. L.M.C. acknowledges financial support from CAPES (no.1765876/2018) and CNPq (no. 140596/2020–8).

Supplementary materials

Supplementary material associated with this article can be found, in the online version, at doi:10.1016/j.ultramic.2024.113927.

References

[1] C.M. Lieber, Nanoscale science and technology: building a big future from small things, MRS Bull. 28 (2003) 486–491.
[2] C. Jia, Z. Lin, Y. Huang, X. Duan, Nanowire electronics: from nanoscale to macroscale, Chem. Rev. 119 (2019) 9074–9135.

[3] L. Güniat, P. Caroff, A.F. Morral, Vapor phase growth of semiconductor nanowires: key developments and open questions, Chem. Rev. 119 (2019) 85959–85971.
[4] J.M. Thomas, R.K. Leary, A.S. Eggeman, P.A. Midgley, The rapidly changing face of electron microscopy, Chem. Phys. Lett. 631 (2015) 103–113.
[5] D.B. Williams, C.B. Carter, Transmission Electron Microscopy: A Textbook for Materials Science, Springer Science, 2009.
[6] C. Ophus, Four-dimensional scanning transmission electron microscopy (4D-STEM): from scanning nanodiffraction to ptychography and beyond, Microsc. Microanal. 25 (2019) 563–582.
[7] G. Li, H. Zhang, Y. Han, 4D-STEM ptychography for electron-beam-sensitive materials, ACS Cent. Sci. 8 (2022) 1579–1588.
[8] G. Bárcena-González, A. Hernández-Robles, Á. Mayoral, L. Martinez, Y. Huttel, P. L. Galindo, A. Ponce, Unsupervised learning for the segmentation of small crystalline particles at the atomic level, Cryst. Res. Technol. 58 (2022) 2200211–2200218.
[9] E.J. Kirkland, Advanced Computing in Electron Microscopy, Springer, 2020.
[10] R. Vincent, P.A. Midgley, Double conical beam-rocking system for measurement of integrated electron diffraction intensities, Ultramicroscopy 53 (1994) 271–282.
[11] P.A. Midgley, A.S. Eggeman, Precession electron diffraction—a topical review, IUCrJ 2 (2015) 126–136.
[12] P. Oleynikov, S. Hovmöller, X.D. Zou, Precession electron diffraction: observed and calculated intensities, Ultramicroscopy 107 (2007) 523–533.
[13] C.S. Own, L.D. Marks, W. Sinkler, Precession electron diffraction 1: multislice simulation, Acta Crystallogr., Sect. A: Found. Crystallogr. 62 (2006) 434–443.
[14] E.F. Rauch, J. Portillo, S. Nicolopoulos, D. Bultreys, S. Rouvimov, P. Moeck, Automated nanocrystal orientation and phase mapping in the transmission electron microscope on the basis of precession electron diffraction, Z. Kristallogr. Cryst. Mater. 225 (2010) 103–109.
[15] D. Viladot, M. Véron, M. Gemmi, F. Peiró, J. Portillo, S. Estradé, J. Mendoza, N. Llorca-Isern, S. Nicolopoulos, Orientation and phase mapping in the transmission electron microscope using precession-assisted diffraction spot recognition: state-of-the-art results, J. Microsc. 252 (2013) 23–34.
[16] I. MacLaren, E. Frutos-Myro, D. McGrouther, S. McFadzean, J.K. Weiss, D. Cosart, J. Portillo, A. Robins, S. Nicolopoulos, E. Nebot del Busto, R.A. Skogeby, Comparison of a direct electron detector and a high-speed video camera for a scanning precession electron diffraction phase and orientation mapping, Microsc. Microanal. 26 (2020) 1110–1116.
[17] P. Moeck, S. Rouvimov, E.F. Rauch, M. Véron, H. Kirmse, I. Häusler, W. Neumann, D. Bultreys, Y. Maniette, S. Nicolopoulos, High spatial resolution semi-automatic crystallite orientation and phase mapping of nanocrystals in transmission electron microscopes, Cryst. Res. Technol. 6 (2011) 589–606.
[18] N. Cautaerts, P. Crout, H.W. Ånes, E. Prestat, J. Jeong, G. Dehm, C.H. Liebscher, Free, flexible and fast: orientation mapping using the multi-core and GPU-accelerated template matching capabilities in the Python-based open source 4D-STEM analysis toolbox Pyxem, Ultramicroscopy 237 (2022) 113517–113527.
[19] R. Clough, A.I. Kirkland, Direct digital electron detectors, in: P. Hawkes (Ed.), Advances in Imaging and Electron Physics, Elsevier, 2016, pp. 1–42.
[20] P. Harrison, X. Zhou, S.M. Das, P. Lhuissier, C.H. Liebscher, M. Herbig, W. Ludwig, E.F. Rauch, Reconstructing dual-phase nanometer scale grains within a pearlitic steel tip in 3D through 4D-scanning precession electron diffraction tomography and automated crystal orientation mapping, Ultramicroscopy 28 (2022) 113536–113544.
[21] J. Jeong, N. Cautaerts, G. Dehm, C.H. Liebscher, Automated crystal orientation mapping by precession electron diffraction-assisted four-dimensional scanning transmission electron microscopy using a scintillator-based CMOS detector, Microsc. Microanal. 27 (2021) 1102–1112.
[22] C. Ophus, S.E. Zeltmann, A. Bruefach, A. Rakowski, B.H. Savitzky, A.M. Minor, M. C. Scott, Automated crystal orientation mapping in py4DSTEM using sparse correlation matching, Microsc. Microanal. 28 (2022) 390–403.
[23] E.F. Rauch, P. Harrison, C. Zhou, M. Herbig, W. Ludwig, M. Véron, New features in crystal orientation and phase mapping for transmission electron microscopy, Symmetry (Basel) 13 (2021) 1675–1687.
[24] A. Ben-Moshe, A. da Silva, A. Muller, A. Abu-Odeh, P. Harrison, J. Waelder, F. Niroui, C. Ophus, A.M. Minor, M. Asta, W. Theis, P. Ercius, A.P. Alivisatos, The chain of chirality transfer in tellurium nanocrystals, Science 372 (2021) 729–733.
[25] J.W. Edington, Electron Diffraction in the Electron Microscope, Macmillan Education, London, UK, 1975.
[26] S.J.L. Billinge, I. Levin, The problem with determining atomic structure at the nanoscale, Science 316 (2007) 561–565.
[27] L. Palatinus, B. Petr, J. Martin, H. Jaromíra, S. Gwladys, K. Mariana, Specifics of the data processing of precession electron diffraction tomography data and their implementation in the programPETS2.0, Acta Crystallogr. B Struct. Sci. Cryst. Eng. Mater. 75 (2019) 512–522.
[28] E.F. Rauch, M. Véron, Crystal orientation angular resolution with precession electron diffraction, Microsc. Microanal. 22 (S3) (2016) 500–501.
[29] D. Ugarte, L.H.G. Tizei, M.A. Cotta, C. Ducati, P.A. Midgley, A.S. Eggeman, Analysis of structural distortion in Eshelby twisted InP nanowires by scanning precession electron diffraction, Nano Res. 12 (2019) 939–946.
[30] J.D. Eshelby, Screw dislocations in thin rods, J. Appl. Phys. 24 (1953) 176–179.
[31] J.D. Eshelby, The twist in a crystal whisker containing a dislocation, Philos. Mag. 3 (29) (1958) 440–447.
[32] L.H.G. Tizei, A.J. Craven, L.F. Zagonel, M. Tencé, O. Stéphan, T. Chiaramonte, M. A. Cotta, D. Ugarte, Enhanced Eshelby twist on thin wurtzite InP nanowires and measurement of local crystal rotation, Phys. Rev. Lett. 107 (2011) 195503–195508.
[33] M.J. Bierman, Y.K.A. Lau, A.V. Kvit, A.L. Schmitt, S. Jin, Dislocation-driven nanowire growth and Eshelby twist, Science 320 (2008) 1060–1063.
[34] J. Zhu, H.L. Peng, A.F. Marshall, D.M. Barnett, W.D. Nix, Y. Cui, Formation of chiral branched nanowires by the Eshelby twist, Nat. Nanotechnol. 3 (2008) 477–481.
[35] L. Palatinus, C.A. Corrêa, G. Steciuk, D. Jacob, P. Roussel, P. Boullay, M. Klementová, M. Gemmi, J. Kopeček, M.C. Domeneghetti, F. Cámara, V. Petříček, Structure refinement using precession electron diffraction tomography and dynamical diffraction: tests on experimental data, Acta Crystallogr. B Struct. Sci. Cryst. Eng. Mater. 71 (2015) 740–751.
[36] D. Cooper, T. Denneulin, N. Bernier, A. Béché, J.-L. Rouvière, Strain mapping of semiconductor specimens with nm-scale resolution in a transmission electron microscope, Micron 80 (2016) 145–165.
[37] T. Grieb, F.F. Krause, M. Schowalter, D. Zillmann, R. Sellin, K. Müller-Caspary, C. Mahr, T. Mehrtens, D. Bimberg, A. Rosenauer, Strain analysis from nano-beam electron diffraction: influence of specimen tilt and beam convergence, Ultramicroscopy 190 (2018) 45–57.
[38] Y. Han, K. Nguyen, M. Cao, P. Cueva, S. Xie, M.W. Tate, P. Purohit, S.M. Gruner, J. Park, D.A. Muller, Strain mapping of two-dimensional heterostructures with subpicometer precision, Nano Lett. 18 (2018) 3746–3751.
[39] D. Stroppa, M. Meffert, C. Hoermann, P. Zambon, D. Bachevskaya, H. Remigy, C. Schulze-Briese, L. Piazza, From STEM to 4D STEM: ultrafast diffraction mapping with a hybrid-pixel detector, Microsc. Today 31 (2023) 10–14.
[40] K. Gjonnes, On the integration of electron diffraction intensities in the Vincent-Midgley precession technique, Ultramicroscopy 69 (1997) 1–11.
[41] C.S.Y. Own, System Design and Verification of the Precession Electron Diffraction Technique, Northwestern University, 2005.
[42] H. Klein, Precession electron diffraction of Mn2O3 and PbMnO2.75: solving structures where X-rays fail, Acta Crystallogr., Sect. A: Found. Crystallogr. 67 (2011) 303–309.
[43] W. Sinkler, C.S. Own, L.D. Marks, Application of a 2-beam model for improving the structure factors from precession electron diffraction intensities, Ultramicroscopy 107 (2007) 543–550.
[44] M. Gemini, S. Nicolopoulos, Structure solution with three-dimensional sets of precessed electron diffraction intensities, Ultramicroscopy 107 (6) (2007) 483–494.
[45] J. Hadermann, A.M. Abakumov, A.A. Tsirlin, V.P. Filonenko, J. Gonnissen, H. Tan, J. Verbeeck, M. Gemmi, E.V. Antipov, H. Rosner, Direct space structure solution from precession electron diffraction data: resolving heavy and light scatterers in $Pb_{13}Mn_9O_{25}$, Ultramicroscopy 110 (2010) 881–890.
[46] H. Klein, J. David, The quality of precession electron diffraction data is higher than necessary for structure solution of unknown crystalline phases, Acta Crystallogr., Sect. A: Found. Crystallogr. 67 (2011) 297–302.
[47] L. Reimer, H. Kohl, Transmission Electron Microscopy, Springer, 2008.
[48] C. Hammond, The Basics of Crystallography and Diffraction, Oxford University Press, 2015.
[49] A.S. Eggeman, R. Krakow, P.A. Midgley, Scanning precession electron tomography for three-dimensional nanoscale orientation imaging and crystallographic analysis, Nature 6 (2015) 7267–7274.
[50] H.X. Gao, L.M. Peng, Parameterization of the temperature dependence of the Debye–Waller factors, Acta Crystallogr. A: Found. of Crystallogr. 55 (1999) 926–932.
[51] D. Kriegner, S. Assali, A. Belabbes, T. Etzelstorfer, V. Holý, T. Schülli, F. Bechstedt, E.P.A.M. Bakkers, G. Bauer, J. Stangl, Unit cell structure of the wurtzite phase of GaP nanowires: x-ray diffraction studies and density functional theory calculations, Phys. Rev. B Condens. Matter Mater. Phys. 88 (2013) 115315.
[52] W. Sun, Y. Huang, Y. Guo, Z.M. Liao, Q. Gao, H.H. Tan, C. Jagadish, X.Z. Liao, J. Zou, Spontaneous formation of core–shell GaAsP nanowires and their enhanced electrical conductivity, J. Mater. Chem. C 3 (2015) 1745–1750.
[53] J.B. Wagner, N. Sköld, L.R. Wallenberg, L. Samuelson, Growth and segregation of GaAs–AlxIn1−xP core-shell nanowires, J. Cryst. Growth 10 (312) (2010) 1755–1760.
[54] L. Palatinus, D. Jacob, P. Cuvillier, M. Klementová, W. Sinkler, L.D. Marks, Structure refinement from precession electron diffraction data, Acta Crystallogr., Sect. A: Found. Crystallogr. 69 (2013) 171–188.
[55] P. Virtanen, R. Gommers, T.E. Oliphant, M. Haberland, T. Reddy, D. Cournapeau, E. Burovski, P. Peterson, W. Weckesser, J. Bright, S.J. van der Walt, M. Brett, J. Wilson, K.J. Millman, N. Mayorov, A.R.J. Nelson, E. Jones, R. Kern, E. Larson, C. J. Carey, İ. Polat, Y. Feng, E.W. Moore, J. VanderPlas, D. Laxalde, J. Perktold, R. Cimrman, I. Henriksen, E.A. Quintero, C.R. Harris, A.M. Archibald, A.H. Ribeiro, F. Pedregosa, P. van Mulbregt, A. Vijaykumar, A.P. Bardelli, A. Rothberg, A. Hilboll, A. Kloeckner, A. Scopatz, A. Lee, A. Rokem, C.N. Woods, C. Fulton, C. Masson, C. Häggström, C. Fitzgerald, D.A. Nicholson, D.R. Hagen, D. V. Pasechnik, E. Olivetti, E. Martin, E. Wieser, F. Silva, F. Lenders, F. Wilhelm, G. Young, G.A. Price, G.-L. Ingold, G.E. Allen, G.R. Lee, H. Audren, I. Probst, J. P. Dietrich, J. Silterra, J.T. Webber, J. Slavič, J. Nothman, J. Buchner, J. Kulick, J. L. Schönberger, J.V. de Miranda Cardoso, J. Reimer, J. Harrington, J.L. C. Rodríguez, J. Nunez-Iglesias, J. Kuczynski, K. Tritz, M. Thoma, M. Newville, M. Kümmerer, M. Bolingbroke, M. Tartre, M. Pak, N.J. Smith, N. Nowaczyk, N. Shebanov, O. Pavlyk, P.A. Brodtkorb, P. Lee, R.T. McGibbon, R. Feldbauer, S. Lewis, S. Tygier, S. Sievert, S. Vigna, S. Peterson, S. More, T. Pudlik, T. Oshima, T.J. Pingel, T.P. Robitaille, T. Spura, T.R. Jones, T. Cera, T. Leslie, T. Zito, T. Krauss, U. Upadhyay, Y.O. Halchenko, Y. Vázquez-Baeza, SciPy 1.0: fundamental algorithms for scientific computing in Python, Nat. Methods 17 (2020) 261–272.

[56] Y. Liu, J. Wang, S. Kim, H. Sun, F. Yang, Z. Fang, N. Tamura, R. Zhang, X. Song, J. Wen, B.Z. Xu, M. Wang, S. Lin, Q. Yu, K.B. Tom, Y. Deng, J. Turner, E. Chan, D. Jin, R.O. Ritchie, A.M. Minor, D.C. Chrzan, M.C. Scott, J. Yao, Helical van der Waals crystals with discretized Eshelby twist, Nature 570 (2019) 358–362.
[57] J. Ciston, B. Deng, L.D. Marks, C.S. Own, W. Sinkler, A quantitative analysis of the cone-angle dependence in precession electron diffraction, Ultramicroscopy 108 (2008) 514–522.
[58] A.S. Eggeman, T.A. White, P.A. Midgley, Is precession electron diffraction kinematical? Part II, Ultramicroscopy 110 (2010) 771–777.
[59] J.C. Meyer, A.K. Geim, M.I. Katsnelson, K.S. Novoselov, T.J. Booth, S. Roth, The structure of suspended graphene sheets, Nature 446 (2007) 60–63.
[60] F. Shao, S.Y. Woo, N. Wu, R. Schneider, A.J. Mayne, S.M. de Vasconcellos, A. Arora, B.J. Carey, J.A. Preuß, N. Bonnet, M. Och, C. Mattevi, K. Watanabe, T. Taniguchi, Z. Niu, R. Bratschitsch, L.H.G. Tizei, Substrate influence on transition metal dichalcogenide monolayer exciton absorption linewidth broadening, Phys. Rev. Mat. 6 (2022) 074005–074017.
[61] M. Belter, A. Sajnóg, D. Barałkiewicz, Over a century of detection and quantification capabilities in analytical chemistry – historical overview and trends, Talanta 129 (2014) 606–616.
[62] B. Carter, D.B. Williams, Transmission Electron Microscopy: Diffraction, Imaging, and Spectrometry, Springer, 2016.
[63] L.A. Currie, Limits for qualitative detection and quantitative determination. Application to radiochemistry, Anal. Chem. 40 (1968) 586–593.
[64] L.A. Currie, Detection and quantification limits: origins and historical overview, Anal. Chim. Acta 391 (1999) 127–134.
[65] A. Kelly, K.M. Knowles, Crystallography and Crystal Defects, Wiley, 2012.

Apêndice D

Material Suplementar ao Apêndice C

A seguir está anexado o material suplementar ao artigo que descreve o trabalho descrito no Capítulo 3 da tese. O arquivo pode ser encontrado em https://ars.els-cdn.com/content/image/1-s2.0-S0304399124000068-mmc1.docx.

Supplementary Information

High Precision Orientation Mapping from 4D-STEM Precession Electron Diffraction data through Quantitative Analysis of Diffracted Intensities

Leonardo M. Côrrea[1], Eduardo Ortega[2], Arturo Ponce[2], Mônica A. Cotta[1], Daniel Ugarte[1*]

1. Instituto de Fisica "Gleb Wataghin", Universidade Estadual de Campinas-UNICAMP, 13083-859, Campinas - SP, Brazil
2. Department of Physics and Astronomy, University of Texas, San Antonio, Texas 78249, United States

S1. Assembly of the PED-based 4D-STEM data set

The original spatially resolved data has been acquired in a detection system which was not prepared to assign the precession electron diffraction (PED) pattern and the corresponding spatial location on the nanowire (NW). The original data was acquired as movie on CMOS axial camera while PED attachment performed the precession and scanning of the electron beam. To convert the diffraction pattern series into 4D data, we have calculated virtual annular dark field images (VADF) for each pattern. The VADF pixel intensity is formed by integrating the intensity of a selected annular region of the electron diffraction pattern (ED) which contains only diffracted peaks (excluding the central peak or transmitted beam), as show in Figure S1a. The center of each cross-section of the NW will represent the center of the peaks in the VADF

intensity constructed as a movie. To determine the centers, we utilized the cross-correlation function between the formed VADF profile and an ideal wire profile (for simplicity we utilized a top-hat function, see Figure S1b). The profiles were then aligned to construct the 4D datablock (see Figure S1c), such that during the analysis is clear that the NW center is set along the datablock center. It is important to notice that this procedure is only possible due to previous knowledge about the region scanned by the electron beam, as seen in Figure 2b.

S2. Diffraction peak identification, intensity integration, indexation and calibration

The diffraction disks from each ED need to have its center determined and intensity integrated in order to exploit diffracted intensity values. To solve such issue, we have utilized the cross-correlation between each ED and an ideal diffraction disk (top-hat type, binary form, 1 inside the disk, 0 outside it). The diameter has been determined from experimental patterns, representation very closely measured diffraction spots, such that both have the same convergence angle (see Figure S2a). After the application of cross-correlation, a new ED is obtained where the intensities in the center of each diffraction disk are maximum, and the maxima have the value of the integrated spot intensity in the original pattern. The cross-correlation also smooths the diffraction peak profile, as show in see Figure S2b, such that we can easily find the disk centers by searching local maxima in the cross-correlation image (Figure S2c). This procedure is similar to the ones used by other software's of ACOM, but the properties of intensity integration is usually not explored, as the methodologies do not explicitly aim to explore intensity values (Johnstone et al., 2021; Savitzky et al., 2021).

Each peak need to be indexed to be utilized in our analysis, such that we have included an automatic peak indexation algorithm in our analysis procedure. As all diffraction patterns measured are near the $[2\bar{1}\bar{1}0]$, we need only to find:

$$h = \frac{\boldsymbol{g}\cdot\boldsymbol{v}^*}{|\boldsymbol{v}^*|^2}, k = \frac{\boldsymbol{g}\cdot\boldsymbol{c}^*}{|\boldsymbol{c}^*|^2}, i = -(i+k), l = 0 \quad (S1)$$

where $\boldsymbol{c}^*$ and $\boldsymbol{v}^* = \boldsymbol{b}^*/cos(30°)$ are the reciprocal vectors related to the $\boldsymbol{c}$ and $\boldsymbol{b}$ lattice vectors of the hexagonal primitive**,** $\boldsymbol{g}$ is the scattering vector for each identified peak. The $\boldsymbol{g}$ vector is obtained by multiplying the identified centers by the proper scale factor (obtained from the manual indexation and calibration of one the measured EDs).

S.3 Details of the Laue circle analysis.

The orientation of a crystal severely affects the observed diffraction patterns, as it alters the observed projection of reciprocal space which intercepts the Ewald sphere (known as the Laue circle). A slight tilt of the crystal away from a zone axis can significatively move the position of the center of Laue circle (O_L) from the position of the transmitted beam (T) (usually considered the diffraction pattern central spot, see Figure S3). It is possible to measure the resulting disorientation (ϕ) from the zone axis direction by determining the radius of the Laue circle (R_L), as they are directly related by: (Edington, 1975)

$$R_L\lambda = \sin(\phi) \quad (S.2)$$

where λ is the wavelength of the incident electron wave. This simple relation can be easily implemented in procedures for crystal orientation determination or alignment, as it only requires a simple fit of a circle to the diffraction peaks position (Ben-Moshe et al., 2021; Zhang et al., 2018; Zhang et al., 2020). This procedure does not require any assumptions about the

crystal structure or previous information about the sample. In our case, we can derive the angles ρ and β (see Figure S4) from the fit of the Laue circle to the binarized version of the measured diffraction patterns. This is possible as angles ρ (tilting of c axis in relation to the plane perpendicular to the optical axis of the TEM) and β (basal plane rotation) are related to the [0001] and [hki0] directions, respectively, which are identified by indexing the diffraction pattern.

For analysis, the indexed ED has been binarized by a threshold value that exclude any diffraction peak with intensity lower than 3% of the direct beam intensity. Then, a simple circle fit is performed, in which the circle equation utilized is given by:

$$(x - R_0 \cos\theta)^2 + (y - R_0 \sin\theta)^2 = {R_0}^2 \quad (S3)$$

where R_0 and θ are free parameters that minimize the distance between the circle and the diffraction points. It is possible to use Equation S.2 to obtain the angles β and ρ if the related lengths to cartesian axes (L_β and L_ρ) are determined. This can be performed by projecting the vector formed by T and $O_L = (R_0 \cos\theta\,, R_0 \sin\theta)$ into the $\boldsymbol{c}^*$ and $\boldsymbol{v}^*$ directions, as show in Figure S3. From that we can obtain β and ρ through:

$$\begin{cases} \sin(\beta) = L_\beta \lambda \\ \sin(\rho) = L_\rho \lambda \end{cases} \quad (S4)$$

S.4 Nanowire shape and size analysis.

As described in the main text, the formation of virtual VADF images is fundamental for our analysis and is important to understand the contained spatial information with the maximum possible precision. We have decided to explore VADF images, as the detection has been optimized to ensure the quality of the diffracted peaks, while the central beam is possibly

saturated and variations in it could not be related to structural features (a virtual bright field, VBF). All VADF have been generated by integrating the intensities in an annular region with 6 mrad of inner half angular opening and 23 mrad in the outer one (see Figure S5a).

The NW shape analysis has been performed in the integrated cross-section of the formed VADF (summation of all the cross-sections along the NW length), this allows an easier interpretation and better signal to noise ratio (*e.g.* in Figure S5b the error bars due to Poisson noise are smaller the points dimensions). We have tested the possibility of a cylindrical NW by calculating the VADF intensity (I^{VADF}) as a function of distance to the NW center considering a convolution between the circular profile of the NW and gaussian profile of the electron beam which scans the sample: (Carter & Willians, 2009).

$$I^{VADF}(x) = C\left[d\sqrt{1-\left(\frac{2x}{d}\right)^2} * \frac{1}{\sigma\sqrt{2\pi}}e^{-\left(\frac{x-\mu}{\sqrt{2}\sigma}\right)^2}\right] \quad (S5)$$

where d is the NW diameter, C is a scale factor, σ and μ are, respectively, the width and center of the gaussian. We can see in Figure S5b that the fit of the above expression on the measured intensity profile do not properly describe the NW VADF intensities. This is evident if we superimpose the useful region in our analysis (from a residue quality analysis, maximum distance of 15 nm to the NW center, see Figure S5c). In this region, the root mean square deviation (RMS) of a constant profile (mean value in the region) gives much lower value (0.45) than the RMS of the circular profile (0.67). This suggest the presence of faceting in the NW surface, but, as this is not a rigorous analysis of the NW shape, we will constrain ourselves to state that the measured diffracted intensities are much better described by a constant thickness than by a circular cross-section. The assessment of the NW shape can be performed by TEM image tomography (Midgley & Dunin-Borkowski) by imaging its cross sections (Sun et al., 2015; Wagner et al., 2010).

Considering the available data, we have been able to discuss ACOM precision with the intensity analysis, but we are not able to estimate the accuracy. In order to estimate accuracy, we would need a Eshelby twisted nanowire with rotation of more than 30º along the analyzed region to cross two zone-axis (e.g. $[01\bar{1}\bar{0}]$ and $[2\bar{1}10]$, see Figure 3 in (Ugarte et al., 2019)). These zone axes provide a good standard for calibration, but also require a very thin wire (~ 30 nm in diameter, torsion is inversely proportional to NW diameter), where crystal torsion is large (0.05 degrees/nm). Otherwise, the required NW length is not viable for intensity analysis ACOM: our measure region is ~ 0.07 μm in length, a 30 nm in diameter requires at least 0.5 μm and the measured NW (diameter ~ 45 nm) requires almost 1.5 μm. The NW shape must also be straight, as any thickening due to lateral growth will lower the torsion rate and increase the required length.

One of the most prominent sources of error in our analysis comes from the determination of the NW crystalline core diameter. This is due to the common imaging methods utilized (as VADF and VBF) lacking sensibility to differentiate abrupt changes from the crystalline core to the amorphous oxide layer in the NW surface (Kiss et al., 2016; Ugarte et al., 2019). An advantage of 4D-STEM techniques is the capacity of explore the measured EDs to generate different types of contrast. One alternative is to utilize the correlation or anti-correlation functions to generate contrast due to changes in the measured EDs (Kiss et al., 2016). This is especially useful to identify the position of change between amorphous and crystalline regions in the NW. We have utilized the most common definition of anti-correlation utilized in ACOM, which compares a diffraction pattern $p_{x,y}$ (x, y: spatial coordinate in the ED mapping) with its nearest neighbors ($p_{x+1,y}$ and $p_{x,y+1}$) to form contrast $C(x, y)$: (Kiss et al., 2016)

$$C(x,y) = \sqrt{\frac{\sum_{i,j}\left[p_{x,y}(i,j) - p_{x+1,y}(i,j)\right]^2 + \left[p_{x,y}(i,j) - p_{x,y+1}(i,j)\right]^2}{2n}} \quad (S.6)$$

where i, j is the coordinate of a pixel of the measured ED, white n total pixels in each one. Notice that the definition of $C(x, y)$ is anti-correlation function, although it is often referred as a correlation function (Kiss et al., 2016). The value of $C(x, y)$ is low for similar diffractions patterns and high for very distinct patterns. The correlation function (similar diffraction patterns give high value) is obtained utilizing the inverse value (inverse of contrast) of $C(x, y)$ in each pixel, as defined by (Kiss et al., 2016).

To construct such anticorrelation images some additional treatment is required, as it has been reported that those images are significatively sensitive to ED background intensity (Kiss et al., 2016). The procedure is very similar to the ones performed in other works in the literature, so only a quick description is given and we focus our attention in the quality and interpretation of our correlation images (Kiss et al., 2016). An example of our data treatment is given in Figure S6; first, the central peak is excluded by a simple circular mask in the center of our data, the mask is a little larger that the central beam diameter to ensure that no possible blooming-like effects are included. Then, we create a mask to mitigate the intensity outside the diffracted peaks by applying a local threshold method to our data. An example of the effective mask and the resulting effect in the ED are shown in Figure S6b,c.

We can observe the anti-correlation image in Figure S7a. Most of the NW center appears to have an almost homogenous value, with a gradual maximization of $C(x, y)$ (anti-correlation) in its borders and then a region of low contrast in the vacuum region (diffraction patterns are very similar to each other without diffraction peaks). The integration of the cross-sections in the image along the NW (Figure S7b) shows two peaks in the anti-correlation, which can be interpreted as the region with maximum difference between the crystalline part and the amorphous surface layer in the NW. The peak width is a transition region between crystal and amorphous and its width can be utilized to determine an uncertainty for the crystalline core diameter. From those criteria, we have obtained the NW diameter as $(48 \pm 7)nm$.

S.5 Results from the Laue circle analysis

The Laue circle approach only requires the proper indexation of each ED and a simple circle fit, from that we can obtain the angles β and ρ associate to crystal tilt for each scanned position. A low threshold value was utilized as the method requires many diffraction spots for proper fit. The Laue circle allows the characterization of a larger area of the NW (until 20 nm from NW center) than the more precise intensity residue analysis. This also implies in the inclusion of noisier data, which may lead to lower reliability. The Laue circle derived information is clearly sensible to the dislocation and torsion (see Figure 5) in the NWs, and the results indicate a high sensibility to small values of disorientation. The values of dispersion obtained are much lower than the ones in previous pattern matching reports (~ 1º) (Ugarte et al., 2019). The disorientation $\beta_{rad} = \beta - \beta_{center}$ (basal plane rotation) is shown in Figure S8, with no observable tendency variation until ~15 nm from center. This is expected as the basal plane orientation should be constant along the NW cross section perpendicular to wire axis, such that any variation is only due to noise.

S.6 Pattern matching Results (ASTAR)

The pattern matching calculation required the simulation of a large library of diffraction patterns (~50000 patterns) to cover the small changes in crystal orientation. The template-matching ASTAR procedure yields 3 Euler angles for each diffraction pattern and additional calculation is required to obtain the disorientations (see (Ugarte et al., 2019) for more details). It is clear that the ASTAR is sensible to both the core dislocation and the torsion, but with

varying quality in the observation of each structural feature. The dislocation varies continually withing a large useful area (within 16 nm from the NW center), with only a few points diverging from data point clouds. The torsion behaves in a discontinuous manner, with two clear distinct distributions that present very different torsion rates values ($(0.031 \pm 0.008)°/\mathrm{nm}$ and $(0.067 \pm 0.006)°/\mathrm{nm}$). Only a small fraction of the NW was useful for the torsion calculation, and the locations of the related PEDs present a random behavior all over the wire. This implies that the torsion seen to be much more prone to data noise, with the two populations observed being two distinct local minima distributions in the template-matching cross-correlation procedure. This last behavior has already been observed by other researchers and it is possibly due to different assumption that ASTAR utilizes in data treatment and template simulation (Cautaerts et al., 2022). The dispersion in angular disorientation (see Table 1) seen to be higher than the ones observed in previous works; this could be a consequence of our use of the ASTAR software with data acquired outside the Nanomegas suite (optical camera) for ACOM. The system is extremely well optimized to be utilized together with the non-axial optical camera, and deviations from the characteristics of the expected data (well defined narrow diffraction spots, some distortion, a gamma function applied during acquisition, *etc*.) can imply in the ASTAR software having trouble to properly process our data. Previous studies of InP nanowire based on Nanomegas ASTAR, have taken great care (*e.g.,* data denoising, scan in reduced regions for better signal, more pixels in detection) to obtain the best possible data to measure those small changes in orientation (Ugarte et al., 2019). Those steps are not reproduced in the analysis presented in this paper. Nonetheless, the analysis shows the main limitations and serves for comparison with other techniques, as is performed in the main text.

S.7 Intensity analysis: consistency and sensitivity

It is important to corroborate the robustness of our results by observing the consistency. This has been tested for torsion by looking for sudden variation of basal plane disorientation in relation to the value in the NW center (see Figure S8). No strong variations have been detected using the intensity analysis. The residue normalized by the number of peaks (see Figure S9a and Figure S9c) increases at one of NW sides (right) in relation to values for in the NW center. This is expected considering the lower information (less diffraction disks, see Figure S9b) in the EDs and also the lower signal-to-noise ratio due to the amorphous oxide shell. This residue asymmetry may be associated to thickness differences at each NW side. The analysis of residues indicate that a change in orientation of ~ 0.1° induce a residue variation of approximately 1% . Considering our angular precision of ~ 0.03°, the induced R_N changes would be 0.2% (see Fig. S10). The 2D comparison of the simulated and measured PED patterns (see Figure S11) show good visual agreement for diffraction peaks above the threshold value utilized to select peaks for optimization. However, noise appears to affect the peaks excluded from the original analysis due to the low number of counts, although the general trends are still comparable.

S.8 Code

We provide a template code (a jupyter notebook file) for the orientation determination algorithm utilized in our analysis, which takes as input a list of hkl and the related intensity for each one. The code can be found at: https://github.com/l211796/Crystal-Orientation-from-PED-Intensity-Analysis. The user must also provide every aspect related to the experiment performed, especially the parts related to the sample crystal system (crystal primitive dimensions, structure factor, Debye-Waller factors and proper indexation). Most critical are the structure factor and zone axes references. The user must provide its own rotation referential,

keeping in mind that the code is limited to 2 angles of rotation. A workflow chart for all step of the used program (Figure S12) is also provided. The code itself shows the part responsible for the determination of the crystal orientation. The code only performs the optimization of a single measured diffraction pattern, such that the user must be responsible for the generalization for an entire datablock.

S.9 References

Ben-Moshe, A., da Silva, A., Muller, A., Abu-Odeh, A., Harrison, P., Waelder, J., Niroui, F., Ophus, C., Minor, A. M., Asta, M., Theis, W., Ercius, P. & Alivisatos, A. P. (2021). The chain of chirality transfer in tellurium nanocrystals. *Science* **372**, 729–733.

Carter, B. & Williams, D. B. (2016). *Transmission Electron Microscopy: Diffraction, Imaging, and Spectrometry*. Berlin, Germany: Springer.

Cautaerts, N., Crout P., Ånes H. W., Prestat E., Jeong J., Dehm G. & Liebscher C. H. (2022). Free, flexible and fast: Orientation mapping using the multi-core and GPU-accelerated template matching capabilities in the Python-based open source 4D-STEM analysis toolbox Pyxem, *Ultramicroscopy* **237**, 113517 – 113527.

Edington, J. W. (1975). *Electron Diffraction in the Electron Microscope*. London, UK: Macmillan Education.

Johnstone, D. N., Crout, P., Nord, M., Laulainen, J., Høgås, S., Opheim, E., Martineau, B., Francis, C., Bergh, T., Prestat, E., Smeets, S., andrew-ross1, Collins, S., Hjorth, I., Mohsen, Furnival, T., Jannis, D., Cautaerts, N., Jacobsen, E., Herzing, A., Poon, T., Ånes, H. W., Morzy

J., Huang S., phillipcrout, Doherty, T., affaniqbal, Ostasevicius, T., mvonlany & Tovey, R. pyxem/pyxem: Release 0.13.2 **2021. DOI:** 10.5281/zenodo.4687011.

Midgley, P. & Dunin-Borkowski, R. (2009) Electron tomography and holography in materials science. *Nat. Mater.* **8**, 271–280.

Kiss, Á. K., Rauch, E. F. & Lábár, J. L. (2016). Highlighting material structure with transmission electron diffraction correlation coefficient maps. *Ultramicroscopy* **163**, 31–37.

Savitzky, B. H., Zeltmann, S. E., Hughes, L. A., Brown, H. G., Zhao, S., Pelz, P. M., Pekin, T. C., Barnard, E. S., Donohue, J., DaCosta, L. R., Kennedy, E., Xie, Y., Janish, M. T., Schneider, M. M., Herring, P., Gopal, C., Anapolsky, A., Dhall, R., Bustillo, K. C., Ercius, P., Scott, M. C., Ciston, J., Minor, A. M. & Ophus, C. (2021). py4DSTEM: A Software Package for Four-Dimensional Scanning Transmission Electron Microscopy Data Analysis. *Microsc. Microanal.* **4**, 712-743.

Sun, W., Huang, Y., Guo, Y., Liao, Z. M., Gao, Q., Tan, H. H., Jagadish, C., Liao, X. Z. & Zou, J. (2015). Spontaneous formation of core–shell GaAsP nanowires and their enhanced electrical conductivity. *J. Mater. Chem. C* **3**, 1745 – 1750.

Ugarte, D., Tizei, L. H. G., Cotta, M. A., Ducati, C., Midgley, P. A. & Eggeman, A.S. (2019). Analysis of structural distortion in Eshelby twisted InP nanowires by scanning precession electron diffraction. *Nano Res.* **12**, 939–946.

Wagner, J. B., Sköld, N., Wallenberg, L. R. & Samuelson, L. (2010). Growth and segregation of GaAs–AlxIn1−xP core-shell nanowires, *J. Cryst. Growth* **312**, 10, 1755-1760.

Zhang, D., Zhu, Y., Liu, L., Ying, X., Hsiung, C. E., Sougrat, R., Li, K. & Han, Y. (2018). Atomic-resolution transmission electron microscopy of electron beam–sensitive crystalline materials. *Science* **359**, 675–679.

Zhang, Y., Yan, R., Sun, T. & Ma, Y. (2020). A simple program for fast tilting electron-beam sensitive crystals to zone axes. *Ultramicroscopy* **211**, 112941.

Figure S1

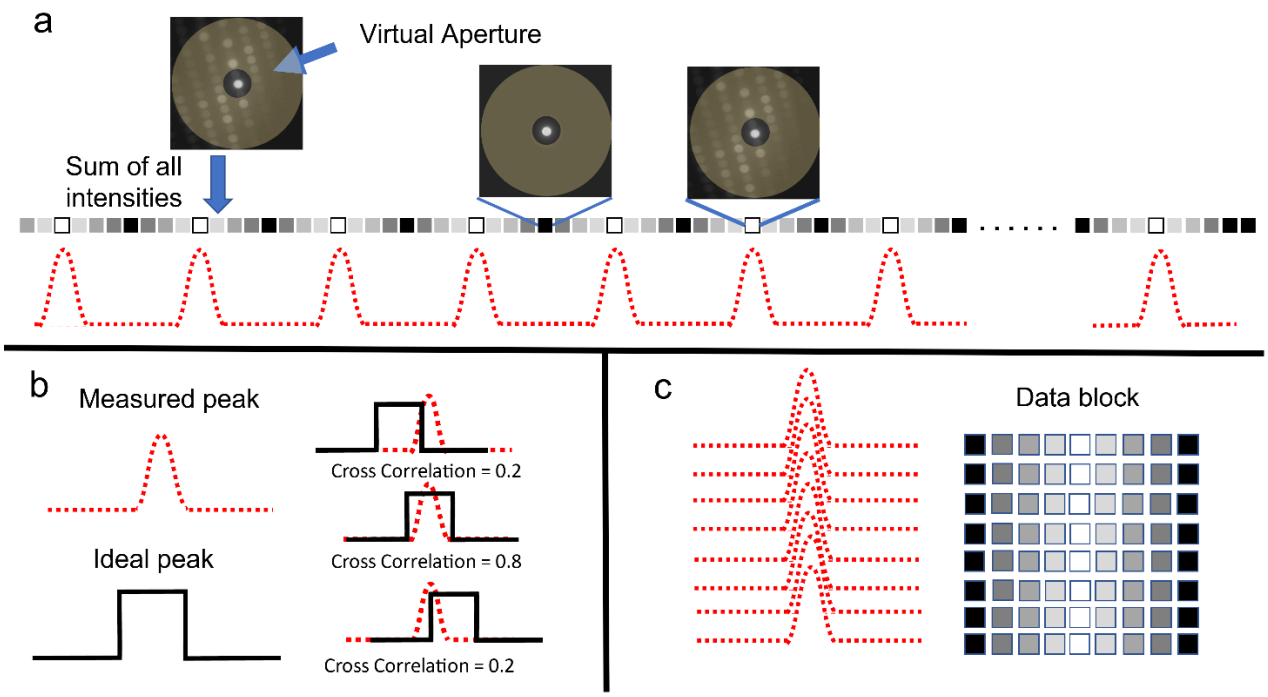

Figure S1: Schematic representation of the datablock construction from recorded PED patterns (time based). a) A virtual annular aperture selects a region in the PED pattern in which all the intensities are summed up. This integration forms a sequence of peaks in relation to time, where each peak center is related to the center of the NW position. b) The cross-correlation value between the measured peaks and an ideal peak (top-hat function) is maximum when the center of the two curves are matched. c) Then we can align the centers (and consequentially all pixels) to produce the data block.

Figure S2

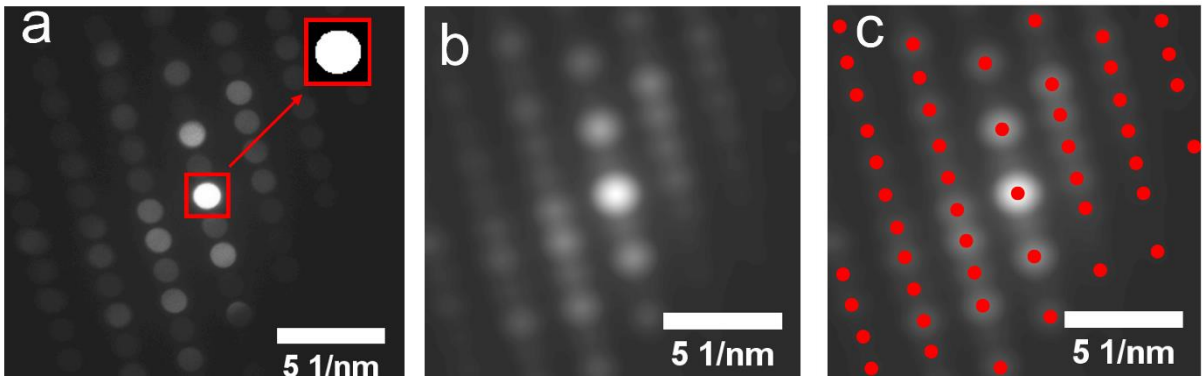

Figure S2: Example of the peak finding algorithm. a) The binarized diffraction disk corresponding to the transmitted beam is selected as an ideal peak. b) The result of the cross-correlation between the data and the ideal disk selected in (a). Notice the blurred aspect of the pattern, consequence of the smoothing effect of the cross-correlation. c) Diffraction spot centers identified by a local maxima algorithm applied to the cross-correlation image.

Figure S3

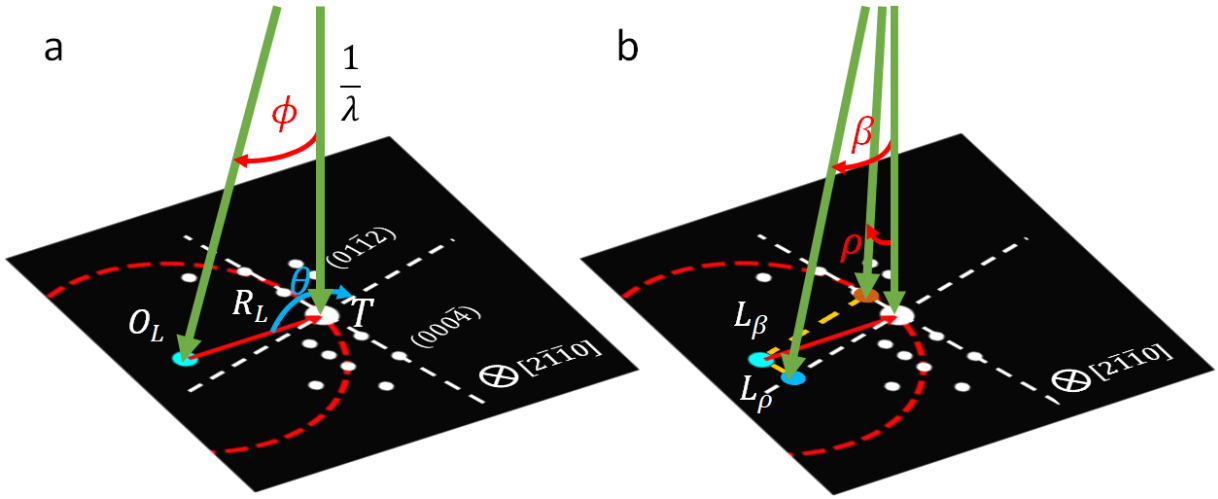

Figure S3: Application of the Laue circle fit to a diffraction pattern. a) Effect of a disorientation ϕ of the crystal in relation to a zone axis. b) It is possible to determine the disorientation in relation to a specific direction by projecting the R_L vector along those directions.

Figure S4

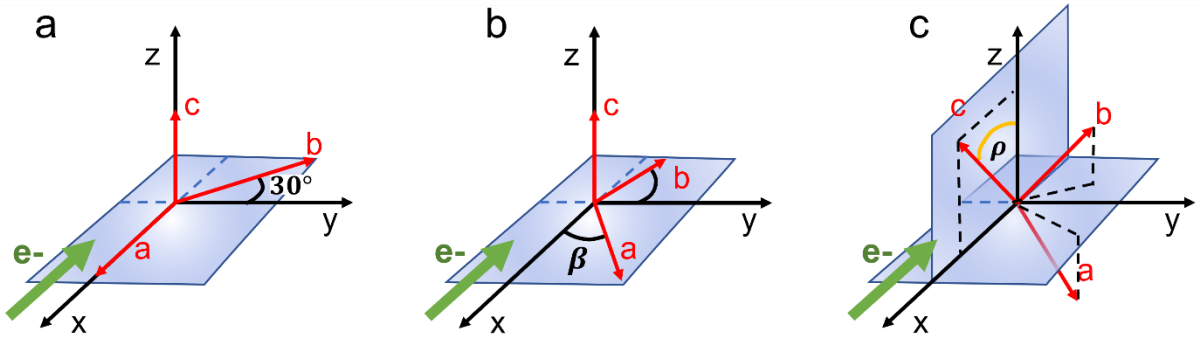

Figure S4: Crystal orientation system in relation to sample coordinates. a) Initially, the crystal is perfectly oriented along the microscope optical axis (represented by the static electron beam direction, considered along x axis). b) Rotation of basal plane (torsion) of the NW disorientates the crystal in relation to TEM optical axis (x-axis). c) The hexagonal c-axis inclination originated by the screw dislocation deformation field generates a disorientation in relation to the plane (yz plane) perpendicular to the TEM optical axis.

Figure S5

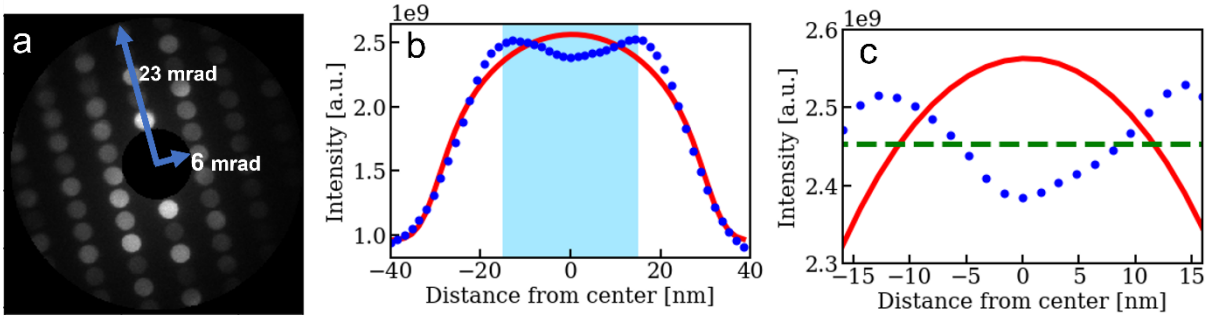

Figure S5: a) Annular region values utilized to form the VADF images. b) VADF intensity profile formed by integration of all the cross-sections profiles along the nanowire length (blue dots) and optimized circular cross-section (continuous red line). The highlighted region identifies the high quality (PED patterns) used for our orientation determination by diffracted intensity analysis. c) Closer look at the highlighted region, showing the measured (blue dots), circular cross-section NW (red line) and flat cross-sections (value used in intensity optimization dashed green line) profiles. The error bars are much smaller than the points due to the large number of counts provided by the integration (more than 10^9 counts).

Figure S6

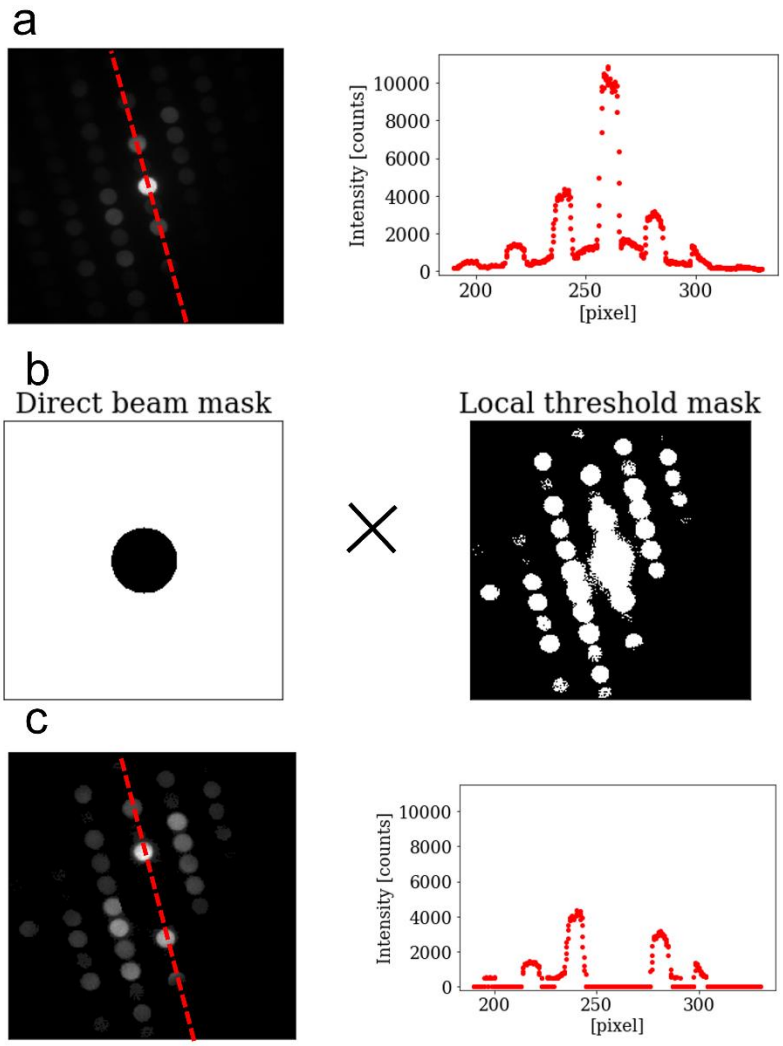

Figure S6: Example of the procedure used for maximizing the quality of the cross-correlation images utilized for NW diameter estimation. a) Raw data (left panel) shows significative influence from the central beam scattering and background; intensity profile along the [000l] direction (right panel). b) Circular mask (left panel) utilized to exclude the transmitted diffraction disk in VADF images c) Resulting mask selects only the regions inside the diffraction disks (left panel), which greatly reduces the influence of the background and transmitted beam in the resulting profile (right panel).

Figure S7

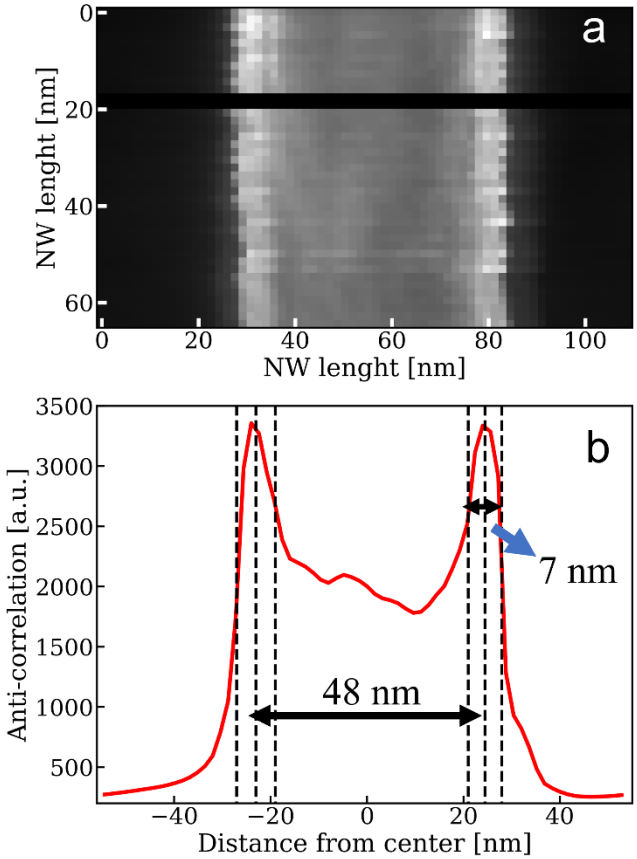

Figure S7: a) Anti cross-correlation image of the NW. Notice that a small region just before 20 nm from the NW center is excluded from image formation due to a scan instability during measurement. b) The anti-correlation profile formed by the integration of the cross-section along the NW length. The center of each extremity peak is considered the NW edge, the full width in half maximum is considered the uncertainty of the NW edge position.

Figure S8

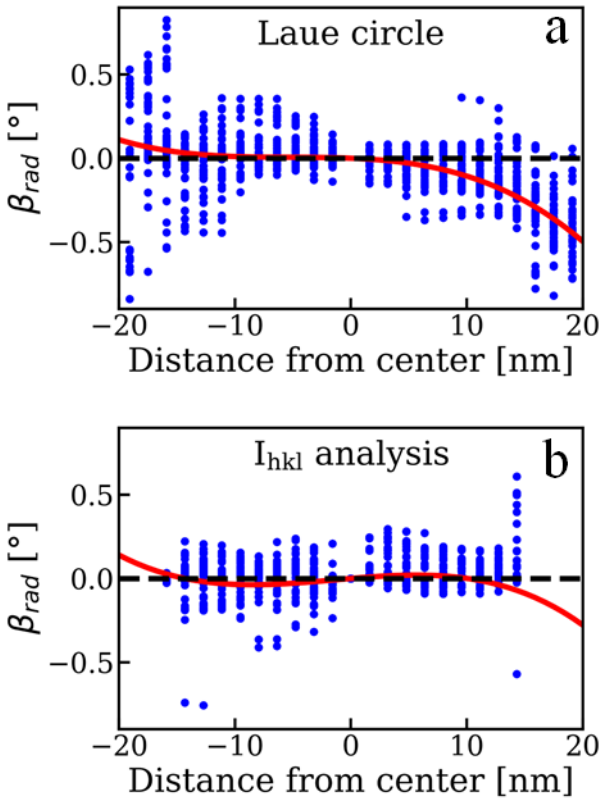

Figure S8: Basal plane vectors disorientation (points) in relation to the value at the NW center (data corresponding to all crossing lines is displayed): a) Laue circle analysis and b) diffracted intensity analysis. The polynomial fit (3rd order polynomial, continuous line) helps to observe the tendencies in the data. Notice that a flat curve should be observed in relation to the zero disorientation (see Discussion section in the main text for more details).

Figure S9

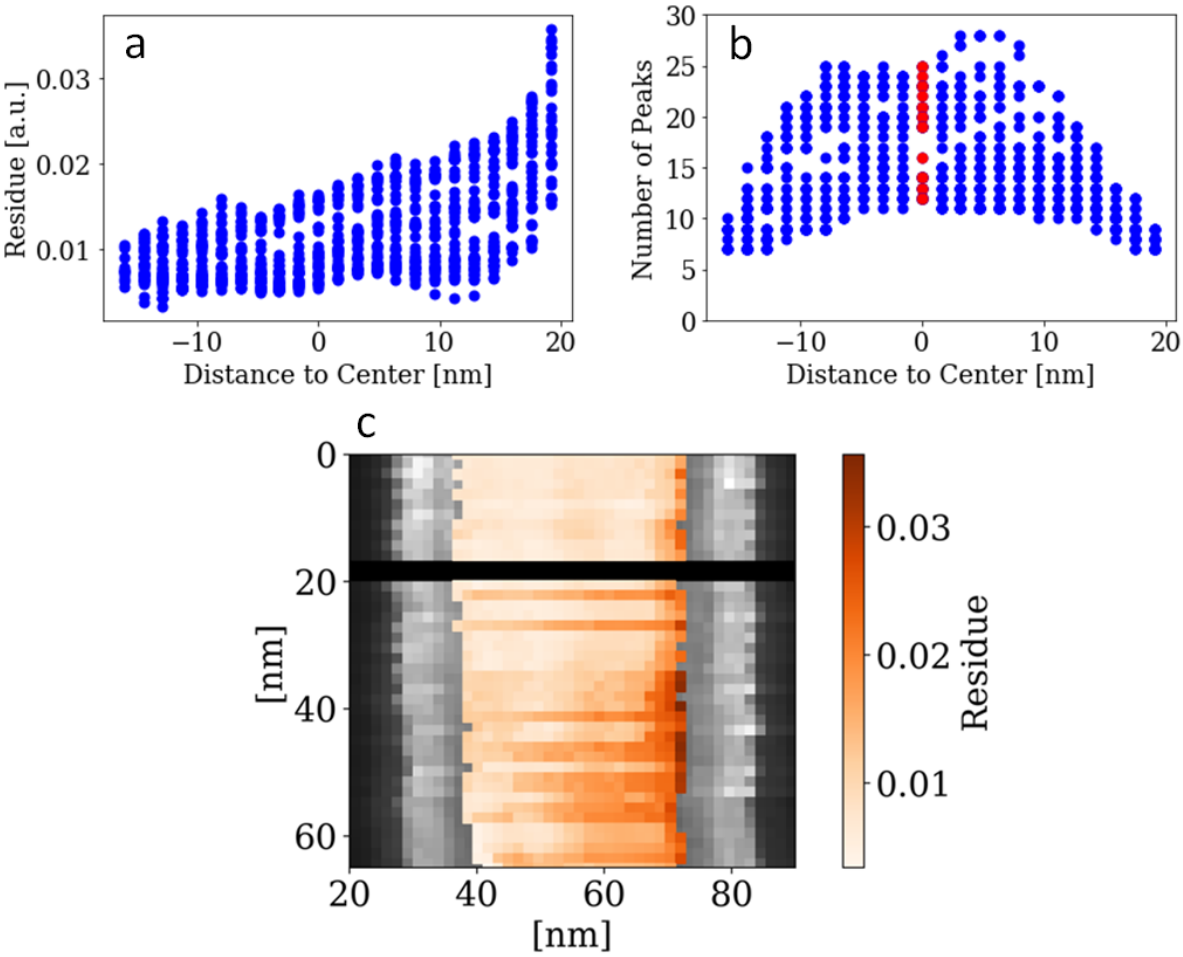

Figure S9: a) Values of the Residue normalized by the number of peaks in the PED pattern (all analyzed points over the wire). Notice that an increase of the value in the extremities of the NW would be expected. b) Number of peaks analyzed on the PED patterns. c) Colormap of the residue normalized by the number of peaks overlayed in the VADF image of the NW. The increase in residue along the NW length is related to a decreased in number of peaks (top to bottom) due larger disorientation from zone axis.

Figure S10

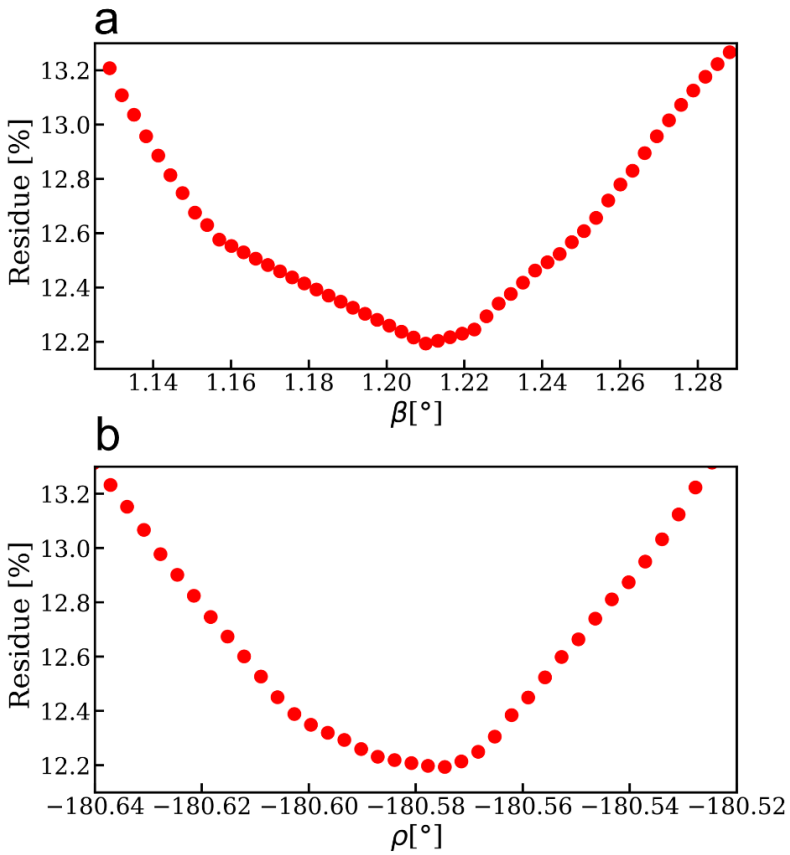

Figure S10: Analysis of the sensibility of the residue to small changes in the orientation. a) basal plane and b) hexagonal ***c*** vector (dislocation). In this work, we have considered that only residue differences above 0.2% are significative, as our precision is ~ 0.03°.

Figure S11

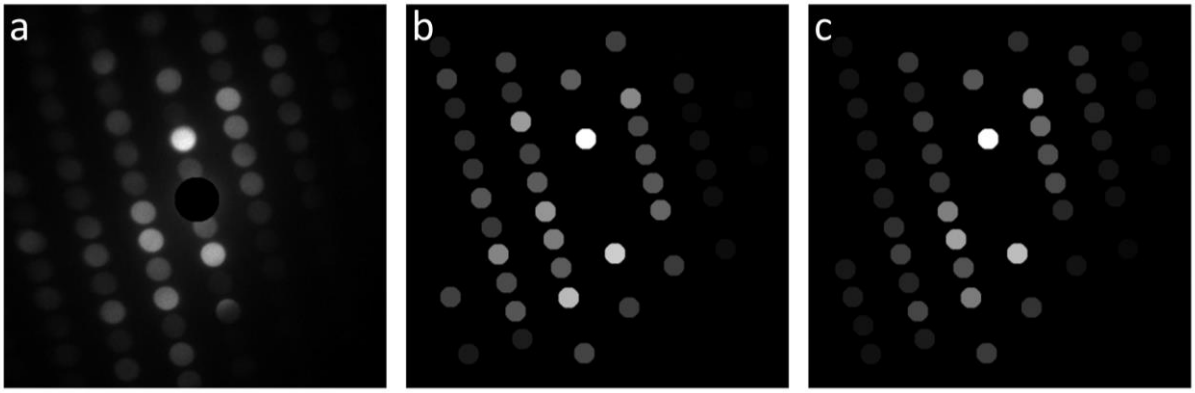

Figure S11: a) Raw diffraction pattern shown in Figure 4. b) Simulated pattern obtained after optimization procedure (in this case no threshold of peaks have been utilized to construct the image; Figure 4 shows peaks utilized for the actual optimization). c) Diffraction pattern built with spots brightness based on integrated peak intensity, derived by processing raw pattern in (a).

Figure S12

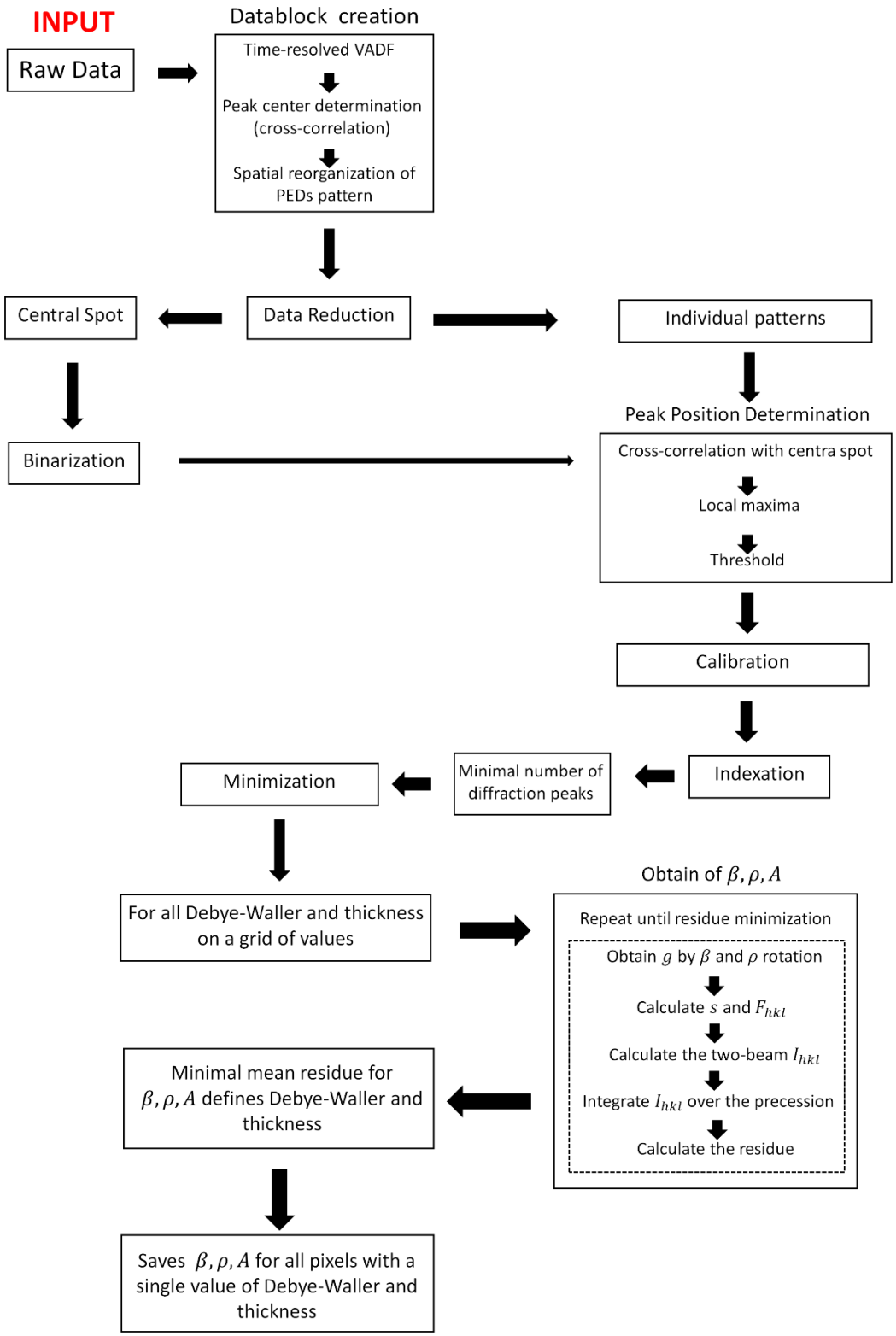

Figure S12: Workflow of the algorithm utilized in our work.

Apêndice E

Estrutura Atômica e Forma 3D de uma Nanoestrela Plasmônica Multiramificada Derivada de um Único Mapa de Difração de Elétrons Resolvido Espacialmente

A seguir está anexado o artigo nomeado "*Atomic Structure and 3D Shape of a Multibranched Plasmonic Nanostar from a Single Spatially Resolved Electron Diffraction Map*" que detalha o trabalho descrito no Capítulo 5. Ele foi publicado em 2024 na revista ACS Nano 2024, 18, 26655 – 26665. Os diretos do artigo pertencem a American Chemical Society, que permite aos autores a reprodução do artigo em teses e coleções, sobre as condições expostas em: https://pubs.acs.org/page/copyright/journals/posting_policies.html, na seção "*Reuse/Republication of the Entire Work in Theses or Collections*".

ACS NANO

www.acsnano.org

ARTICLE

Atomic Structure and 3D Shape of a Multibranched Plasmonic Nanostar from a Single Spatially Resolved Electron Diffraction Map

Leonardo M. Corrêa, Simon M. Fairclough, Kaleigh M. R. Scher, Supriya Atta, Diego Pereira dos Santos, Caterina Ducati, Laura Fabris, and Daniel Ugarte*

Cite This: *ACS Nano* 2024, 18, 26655–26665

Read Online

ACCESS | Metrics & More | Article Recommendations | Supporting Information

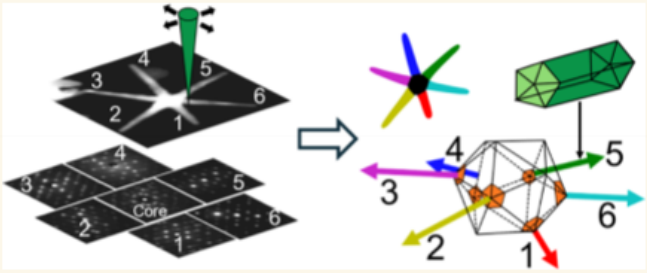

ABSTRACT: **Despite the interest in improving the sensitivity of optical sensors using plasmonic nanoparticles (NPs) (rods, wires, and stars), the full structural characterization of complex shape nanostructures is challenging. Here, we derive from a single scanning transmission electron microscope diffraction map (4D-STEM) a detailed determination of both the 3D shape and atomic arrangement of an individual 6-branched AuAg nanostar (NS) with high-aspect-ratio legs. The NS core displays an icosahedral structure, and legs are decahedral rods attached along the 5-fold axes at the core apexes. The NS legs show an anomalous anisotropic spatial distribution (all close to a plane) due to an interplay between the icosahedral symmetry and the unzipping of the surfactant layer on the core. The results significantly improve our understanding of the star growth mechanism. This low dose diffraction mapping is promising for the atomic structure study of individual multidomain, multibranched, or multiphase NPs, even when constituted of beam-sensitive materials.**

KEYWORDS: *plasmonic nanoparticles, nanostar, 4D-STEM, precession electron diffraction, crystal orientation mapping, nanoparticle morphology, nanocrystallography*

Noble metal nanoparticles (NPs) attract huge interest due to the possibility of tuning their optical properties. This usually exploits the excitation of surface plasmon resonances, which show a strong dependence on dielectric properties, morphology, size, and interparticle distance.[1] Optical metamaterials[2] and surface-enhanced Raman spectroscopy represent actual application of tuned optical response, where efficiency is deeply tied to NP morphologies. Despite its relevance, the determination of three-dimensional (3D) shapes of very complex NPs (anisotropic, branched, etc.) is an everlasting issue in nanoscience.[1] Many different morphologies of metal NPs have been synthesized and proposed to generate strong plasmonic response, such as nanospheres, nanorods, nanosheets, and nanostars (NSs).[3] Among them, multibranched plasmonic NSs display high field enhancement around the sharp tips of high-aspect-ratio legs.[1,4] The precise under-

Received: April 19, 2024
Revised: September 11, 2024
Accepted: September 13, 2024
Published: September 21, 2024

https://doi.org/10.1021/acsnano.4c05201
ACS Nano 2024, 18, 26655–26665

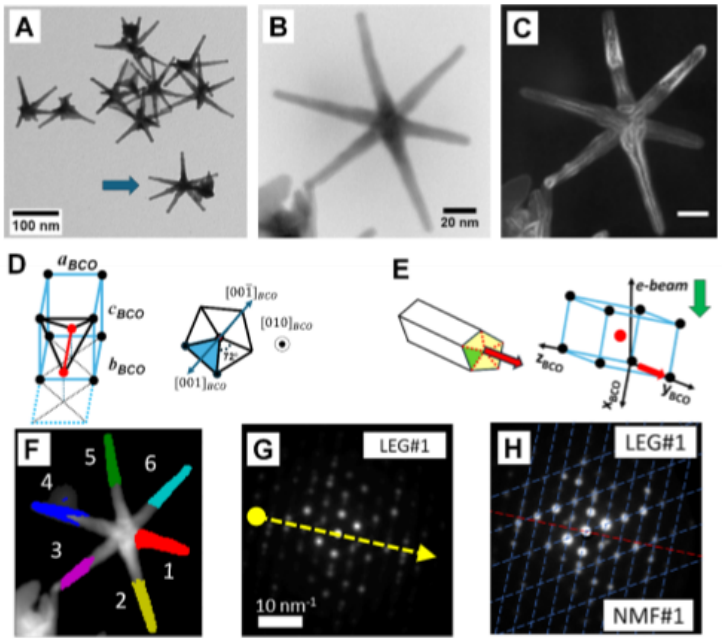

Figure 1. (A) TEM micrograph displaying general view of a high-aspect-ratio AuAg NS. (B) BF-STEM image of the NS studied in detail by 4D-STEM precession diffraction methods. (C) A virtual anticorrelation image revealing abrupt crystallographic changes between pixels (pixel step 1 nm) inside legs, which confirms their decahedral structure. (D) BCO unit cell and the relevant crystallographic directions in relation to a decahedral structure ($[010]_{BCO}$ vector points along the decahedral leg axis as derived in Figure S3). (E) The crystal orientation deduced from the ED pattern interpretation that allows the determination of LEG#1 orientation in space (b_{BCO} vector points downward in the scheme) in relation to the incident electron beam (or in sample coordinates). (F) A virtual annular dark field (VADF) image generated from the 4D-STEM data set. The colored region at legs' tips mark regions of pixels clustered by the machine learning (ML) tool *K*-means; the regions of all 6 legs have been recognized (indicated numbers are used to identify different legs in the subsequent sections of this work, see the Methods section for details and explanations). (G) A mean diffraction pattern calculated from the region on LEG#1 (the arrow indicates the leg axis on the pattern along the base−tip direction as derived from the annular VDF image). (H) Interpretation of the mean diffraction pattern of LEG#1 in (G) was rendered easier after using non-negative matrix factorization (NMF) to perform a partial demixing of the diffraction contribution from the five different crystal domains of the decahedral leg; dashed lines are used to show the manually identified ED pattern from the NMF component #1.

standing of the NS structure and 3D shape is an essential step to refine synthesis protocols, to help tailor shape, and to optimize plasmonic response.

Transmission electron microscopy (TEM) and its related scanning mode (STEM) represent the best suited tools to characterize nanomaterials due to their intrinsic high spatial resolution.[5−7] TEM (or STEM) images just provide 2D projections of the studied object, and the 3D structure can be reconstructed by applying discrete electron tomography (ET) to a series of 50−70 images taken at different tilting angles (usually in a tilt range −70 to 70°).[8] In the field of nanomaterials, ET may exploit high-angle annular dark-field (HAADF) STEM images to derive particle faceting using nanometer-wide electron probes, and atomic resolution ET reconstructions may be generated exploiting aberration-corrected instruments. This requires the generation of Angstrom-size probes with semiconvergence angles of 25−30 mrad; this convergence limits the depth of field to 5−7 nm (resolution along the longitudinal electron beam path) to avoid image resolution loss.[8−11] Therefore, atomic structure ET is restricted to particles that are thin (10−20 nm), and images must be acquired at high magnification. This limits its use to rather small regions when a large particle is studied. Despite recent progress,[8−12] STEM ET remains quite demanding considering the required beam time (typically 1 h acquisition time) and high electron irradiation doses (10^5–10^6 $e^-/Å^2$);[8] thus, beam-sensitive samples can be seriously modified.

New opportunities to study nanosystems have recently been explored by the so-called 4-dimensional scanning-TEM (4D-STEM),[13] where either an electron diffraction (ED) or a scattering pattern is stored for each image pixel position (see Figure S1). This method allows the measurement of, for example, atomic arrangement, phase, crystal orientation, and strain, with nanometer resolution[13] using a much lower irradiation dose.[14] Additionally, a 4D-STEM data set maps local crystallographic information, and it can be used to get the spatial distribution of regions that generate a particular crystal attribute in a reciprocal space (e.g., individual peaks and the related virtual dark-field images: VDF).[13,15]

https://doi.org/10.1021/acsnano.4c05201
ACS Nano 2024, 18, 26655−26665

In this work, we address the study of a complex six-branched AuAg plasmonic NS, where branches show a high aspect ratio (7−10 nm in diameters and 35−60 nm in length); the star structure attains a diameter in the 150−200 nm range. These NSs are synthesized by seed-mediated methods exploiting peculiarities of different surfactants. The deep understanding of the star optical properties and synthesis protocols requires the precise measurement of different structural aspects: (a) 3D spatial distribution of the legs, (b) atomic arrangement inside seeds and legs, and (c) how the seeds structure determines leg number and their spatial configuration. The application of ET tomography to answer all of these questions may be extremely challenging. First, atomic resolution ET cannot be used to analyze such extended objects (50−70 nm in length) because the necessary depth of field would be ∼70 nm. This will limit the convergence angle to about 1.0−1.5 mrad, and then the generated electron probe will be in the nanometer-wide range; ET using this kind of electron beams may be used to measure leg distribution but will be unable to provide atomic arrangement knowledge. Some studies have overcome these difficulties by taking a nanometer-resolution ET to determine 3D morphology and perform a second atomic resolution ET of a very reduced NP region such as the tip of a nanowire or the corner of a NP.[16] Here, we have adopted a different strategy to determine NS atomic structure with reduced electron irradiation; we show that the crystallographic information mapped by a 4D-STEM data set can provide simultaneous determination of leg 3D distribution, atomic arrangement of legs and seed, and their orientation relationships. All this NS structural information could be derived from one single 4D-STEM diffraction map using a total electron dose of ∼200 $e^-/Å^2$.

Crystalline Structure of the NS Legs. The AuAg NSs studied here display a morphology with a high aspect-ratio (Figures 1 and S2). While the sample contains stars with various leg configurations (see Figure S2), for this study, we have chosen to analyze a symmetrical NS containing 6 legs which can be efficiently produced[3,4] [see bright-field STEM image (BF) in Figure 1B]. Many studies of Ag nanowires have reported a decahedral structure, with a 5-fold axis along the wire length.[3,17,18] It is, therefore, not surprising that previous atomic resolution TEM images of NS legs are interpreted as consistent with an elongated decahedral structure containing twins along its axis.[4] From the crystallographic point of view, a decahedron is formed by the assembly of 5 tetrahedra; nevertheless, a pure face-centered cubic (FCC) structure cannot generate a compact decahedral structure (see Figure S3). Therefore, a structural distortion must occur, what leads to a body-centered orthorhombic (BCO) crystal, as discussed by Yang et al.[19] and illustrated in Figure S3.

Illuminating information can be derived by evaluating the anticorrelation between the diffraction patterns of each pixel with its neighbors in the 4D-STEM map; these images are brighter at interfaces between phase or grain boundaries.[20] The anticorrelation image in Figure 1C (and in Figure S18) reveals two points: (i) most legs display bright lines parallel to their axis, revealing the axial twin planes that confirms the decahedral structure of the legs, and (ii) several legs display clear contrast changes along their axis, suggesting a crystal modification, which may be due to growth discontinuities, slight rotation, or mechanical deformation (to be discussed later). Furthermore, the anticorrelation contrast in a cross section of the NS leg is very well described by the expected position of grain boundaries for a distribution of grains around a 5-fold axis, as shown in Figures S11 and S12. Consequentially, the 5-fold symmetry of the legs is confirmed by the reciprocal information (the BCO unit cell measured from the diffraction spot positions) and the real space information (the grain distribution observed by the anticorrelation image is consistent with the 5-fold structure).

There has been much debate on whether this deformation field is homogeneous or inhomogeneous;[18] here, we will limit our diffraction pattern analysis to a homogeneous BCO structure, as this yields good quality understanding and modeling of our experiments, as described in the Methods section. A schematic drawing of the atomic position within the BCO unit cell and its orientation in a decahedral rod is shown in Figures 1D and S3 (notice that the $[010]_{BCO}$ vector points along the wire axis, Figure 1E).

Determination of the Star Legs Orientation in Space. The measurement of the 3D leg orientation can be directly obtained by determining the $[010]_{BCO}$ crystal direction (see Figures 1D,E and S3); this is possible by indexing the diffraction patterns as described in the Methods section. A ML clustering tool (*K*-means)[21−23] has been used to easily group pixels with similar diffraction patterns that spatially corresponded to each leg tip as can be seen in Figure 1F. Note that pixels close to the core or in structurally defective regions are not grouped by the analysis algorithm. To complete the analysis of the whole star, we manually selected regions closer to the core to obtain structural information in the whole leg length, avoiding defective regions (mean ED from tips and bases are displayed in Figures S4 and S5). At this point, the task of estimating the NS shape requires measuring the crystal orientation from merely the average diffraction patterns from 10 different regions (Figures S4 and S5); information on leg lengths can be derived from the images. It is important to consider that each decahedral leg generates a complex ED pattern, as it results from the overlapping of 5 crystal grains. The grains share the same crystal direction ($[010]_{BCO}$) along the leg axis (Figure 1D), but all positioned at different orientations. The initial rough indexing and interpretation of the patterns required manual identification (see Figure S6 for details) of spots arising from one of the five BCO crystals (see examples in Figures 1H and S7−S9). Subsequently, a more precise crystal orientation has been performed with automated crystal orientation mapping (ACOM) numerical procedures to determine each leg axis ($[010]_{BCO}$) orientation with a precision of ∼0.1° (see Figure S10).[24−30]

Table 1 summarizes the leg orientation in space (vectorial directions), and their spatial distribution is graphically included in Figure 2. Most of the leg bases (#2−6) lay very close to the *xy* sample plane, with the larger deviation observed for LEG#1, which has an elevation angle of about 20.2° (downward in Figure 2). For legs #2 and #4−6, bases and tips show quite similar results with angular changes that do not exceed a few degrees. The tip of LEG#3 points up in Figure 2 showing angular change from the base to the tip of ∼39°, suggesting that this leg suffered a major mechanical deformation when deposited on the grid. In fact, the LEG#3 tip is not free, and it seems in contact with a big particle (see the lower left corner in Figures 1B,C,F and S18). In contrast, for legs #2 and #4−6, the bases and tips show quite similar crystal orientation results with angular changes that do not exceed a few degrees, so we attribute the anticorrelation image contrast changes observed in Figure 1C to instabilities that occurred during growth.

https://doi.org/10.1021/acsnano.4c05201
ACS Nano 2024, 18, 26655−26665

Table 1. Spherical Coordinates of the NS Leg Axis (Versors) Derived from Intensity Analysis[a]

leg	base			tip		
	azimuthal [deg]	elevation [deg]	length [nm]	azimuthal [deg]	elevation [deg]	length [nm]
1				9.0	20.2	34
2				64.5	3.6	55
3	142.1	16.5	19	141.5	−22.1	38
4	193.6	2.9	16	193.7	1.9	38
5	253.3	−2.1	24	255.9	0.5	32
6	314.6	1.9	17	314.3	4.9	33

[a]The azimuthal angle indicates the in-plane (xy) rotation of the legs (around z axis, starting from x axis), while the elevation angle provides the out-plane position (from the xy plane, note that in the adopted coordinate system, z-axis points down in Figure 2).

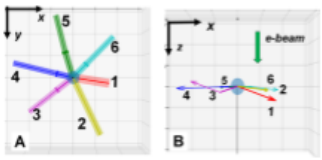

Figure 2. Orientation of the NS 6 legs deduced from ACOM results for bases and tips. (A) Top view, along electron beam direction indicating the legs' azimuthal distribution. (B) Side view [along the (−y) direction] revealing that most of the legs lay in a plane perpendicular to the electron beam direction (the z axis points downward in the plot). The background grid indicates 20 nm × 20 nm squares.

To further understand NS formation and the rather planar spatial leg configuration, it is essential to determine the NS core structure because the layout of legs, in first approximation, should be determined by the seed NP structure (or symmetry) used in the two-step NS synthesis procedure.[4,31]

Determination of the NS Core Structure. The mean diffraction pattern of the NS core was calculated by adding the contribution from all pixels at the NS central region (10 nm in radius; see Figure 3A). The mean ED pattern shows an elongated hexagonal shape that seems to be roughly close to a 2-fold symmetry with a quasi-mirror plane defined by the line crossing the diffraction spot marked E (Figure 3A). VDF images provide the spatial location of crystals generating the different diffraction spots (A–F), and we can derive several structural aspects by closely examining these VDFs (Figure 3B): (a) most images reveal crystal regions with a triangular shape at different azimuthal orientation and always showing a sharp tip at the core center and (b) some VDFs show 2 bright triangles that are diametrically opposed and sharing a pointed tip at the core center. These two features can only be explained by a multidomain structure formed by a core with icosahedral symmetry (ICO, see icosahedral schema in Figure 3C), where the noble metal FCC structure is distorted into a rhombohedral (RHO) lattice as discussed by Yang et al.[19]

The experimental ED pattern in Figure 3A shows the characteristics of the 2-fold (ICO2) and 3-fold (ICO3) diffraction patterns of icosahedral particles, such as a rough 2-fold symmetry, but also several diffraction spots (A, D, and E) associated with twin planes visible for ICO3 (Figure S15). Strong evidence of an orientation close to an ICO3 orientation is the generation of spot F, which should be observable only for this orientation. Based on the assembled crystallographic data and VDF images, we have been able to conjecture an estimate of the ICO orientation (ICO32D, Figure 3D) very close to the intermediate axis between the 2-fold and 3-fold symmetry axes (ICO32). The deduced ICO32D NS core orientation has been confirmed by the compelling good agreement between simulated and measured diffraction patterns (see detailed analysis in the Methods section and Figure 3).

Understanding How the Star Core Structure Influences Leg Spatial Configuration. The full understanding of NS atomic arrangement and shape needs the determination of the relation between the NS icosahedral core and leg spatial position and orientation (Figure 4). An ICO particle oriented along an ICO32D axis represents an interesting structure: this configuration presents four corners approximately in the plane perpendicular to the incident beam direction (Figure 4A, expected attachment position for legs #2−3 and 5−6). These ICO corners (actually 5-fold axis) constitute excellent substrates to stimulate the epitaxial formation of decahedral legs close to the xy plane (see the geometrical model in Figure 4A,B and angular measurements in Figure 3 and Table 1). This structural model also predicts that two legs (numbered #1 and #4) should grow from apexes that should point 20−30° out of the xy plane (upward or downward). LEG#3 data does not follow the previous interpretation (the measured position is indicated with a black arrow in Figure 4C), possibly due to the mechanical deformation mentioned previously. Figure 4 shows a good agreement between the ICO model and the measurement of the legs' position and orientation, with the small deviations likely related to the imperfect formation of the ICO core.

The ICO vertices represent the ideal 5-fold structured substrate for an epitaxial growth of decahedral wires, so there must be a well-determined register between angular position from the twin planes composing the legs and twins from the core 5-fold axes (Figures 1D and 4C,D). This information is straightforwardly available from the crystal orientation through the measured $[0\ 0\ -1]_{BCO}$ vectors (which are parallel to the decahedral twins). LEG#1 displays the expected twin plane pointing close to the vertical direction from the leg center (upward in Figure 4D). In contrast, LEG#5 (LEG#6) should display a twin laying close to the horizontal plane pointing left (right) from the wire center. Legs #1−3 and #5−6 show a good agreement with this detailed structural model (Figure 4D). Also, we must note that there is a small rotation in the leg structure between the base and tip, suggesting that the legs must include structural defects formed during their growth.

Three capital structural properties of a NS have been determined: (a) the core is an ICO particle; (b) the high-aspect-ratio legs are decahedral rods; and (c) the legs are attached at the vertices (5-fold) of the ICO core. Several previous growth models relate NS shape to a decahedral core, with legs growing from twins perpendicular to 5-fold axis (at 72° between them), and any additional legs (a sixth one) would be located perpendicular to that plane (along the 5-fold axis).[4,31] In contrast, our results indicate that the 6-leg NS imaged in Figure 1B,C,F grow in an utterly different configuration. Our measurements indicate azimuthal angles between NS legs around 60° (see Table 1 and Figure 3) and an icosahedral core. Previous studies have reported stars with identical branch configuration,[4] indicating that the derived structural analysis (Figure 1) must be quite general. The occurrence of an ICO core may explain many different NS leg

https://doi.org/10.1021/acsnano.4c05201
ACS Nano 2024, 18, 26655−26665

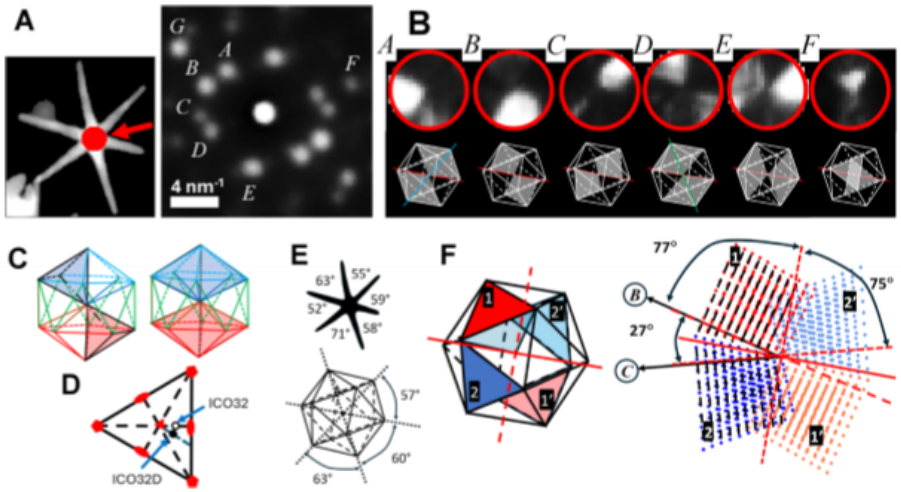

Figure 3. (A) Mean diffraction pattern from the NS core generated by summing all pixels at a distance <10 nm from the estimated core center (shown in the inset). (B) Upper image row: the VDFs derived from diffraction spots marked *A*−*F* (the circle diameter is 20 nm). Lower image row: the expected VDF contrast generated from the icosahedral geometrical model along ICO32D orientation (the red line in these images indicates the expected twin plane that would agenerate diffraction spot *E* and define the rough 2-fold symmetry of the ED pattern). The simulated VDFs show a very good agreement with the experimental data (in the upper row). Notice that the brighter regions of the VDF from spots *A*, *D*, and *E* are perpendicular to the diffraction peak direction, as expected for regions containing twin planes, providing a solid interpretation for crystal domains generating those peaks. (C) A schematic drawing of icosahedral particles, note that all tetrahedra show a tip at the particle center, and a diametrically opposed tetrahedron rotated by 60°. ICO particles include two stacked decahedra (assembly of 5 tetrahedra) rotated by 36° (2π/10) along the 5-fold axis. (D) The estimated orientation of the NS icosahedral core as observed in the experiments with the incident electron beam impinging vertically onto the page (ICO32D, see the Supporting Information for detailed explanations). (E) The azimuthal distribution of legs derived from NS images in comparison with the position of icosahedral vertices in the estimated ICO core orientation. (F) (left) Schematic drawing of an ICO oriented along ICO32D (see text for explanation). (right) In this orientation, the tetrahedral pairs marked (1 and 1′, 2 and 2′) present $\{110\}_{RHO}$ atomic planes almost parallel to the electron beam, which would generate strong diffraction spots (marked as *B* and C, respectively). This conclusion is corroborated by the excellent match between the predicted and experimental angle and intensity differences between these spots, see Figure S17.

configurations, even when formed by 5, 6, 7, or more high-aspect-ratio legs. Symmetrical 5-branched NS (angle between legs close to 72°, Figure 5g in ref 4) can be easily accounted for considering 5-fold axes of an ICO core. Some NSs display 5 legs distributed close to the 5-fold symmetry and some additional legs (arrowed NS in Figure 1A or 6c or 6g in ref 4). These additional legs (sixth, seventh, etc.) are always located close to the central angle between the legs in a 5-fold configuration (see Figures 1 and S23). An ICO particle observed along a 5-fold axis presents 10 tetrahedra sharing an edge with the axis, which can be described as two stacked decahedra which are rotated by 36° (2π/10) in relation to one another (Figures 3C and S23). Thus, the vertices from one of these decahedra support the legs in a 5-fold layout, while the additional legs at bisecting angles must grow in a different plane and from apexes located on the second decahedron (Figure S23).

Insights into NS Formation during Synthesis. The detailed AuAg NS structural information derived in this work contributes significantly to understanding NS synthesis protocols and growth mechanism. NS synthesis involves two steps: (a) seed formation and (b) a second step to induce leg growth. It has already been observed that it is necessary to increase Ag concentration (from $AgNO_3$) during the second step to improve cylindrical shape (reducing tapering) and increase the stability of the high-aspect-ratio legs after growth.[4] As all legs are decahedral rods, and they contain 5× twins parallel to the leg axis along the whole length. The increase of Ag atoms during leg growth will enhance stability by reducing the energetic contribution of the 5 twin defects (the Ag twin energy is about a factor 2 lower than the Au one[32]). From another point of view, the efficient production of high-aspect-ratio 6-branched NS is favored if the amount of ascorbic acid is raised during leg formation, which is associated with the enhancement of metal atom migration toward low energy facets as {111}.[4] In fact, the surface at the tip extremes of decahedral wires should be formed by {111} facets; in addition, leg tip surface contains 5 twins which would enhance atom attachment efficiency due to generation of steps and edges during growth. This helps to nucleate new layers, increasing kinetics in a similar way of crystal growth around screw dislocations (Frank growth model[33]).

Our results have revealed that the NS legs located at ICO vertices lay in a highly anisotropic leg distribution (lying very close to a plane, Figure 2B). This contradicts a crucial aspect of icosahedral symmetry: a regular and homogeneous spatial distribution of the 12 corners on a sphere; the ideal star leg configuration on an ICO core would be 12× legs distributed regularly in space. It is expected that the anisotropic growth through seed-mediated methods involving reducing agents,

https://doi.org/10.1021/acsnano.4c05201
ACS Nano 2024, 18, 26655−26665

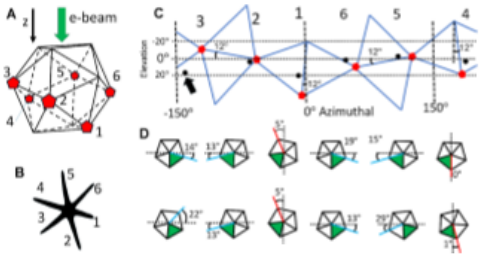

Figure 4. 3D correlation between the icosahedral core symmetry and leg orientation. Comparison of the NS measured morphology with the leg azimuthal positions and elevation angle derived from the geometrical NS model. (A) ICO32D core and the expected leg attachment positions at the 5-fold axes located at icosahedral vertices (pentagonal markers), NS legs indexing is shown below in (B). (C) A plot of elevation angle of the vertices as a function of azimuthal angle around the ICO core (pentagonal red markers) compared with measured leg base orientation (round black markers). Note that measured LEG#3 orientation (indicated with a black arrow) is not as close to the predicted position; this is expected as LEG#3 seems to have suffered a major mechanical deformation when deposited on the grid (see text for a more detailed explanation). (D) Orientation of the decahedral leg structure (five crystal domains) around their axis; darkened triangular sectors indicate domains used for leg orientation assessment.

metal salts, and passivating molecules is determined by the relative rate of metal atom deposition and surface diffusion.[34] However, it seems unlikely that kinetic factors associated with diffusion-limited growth would contribute to induce anisotropy inside the solution. Our hypothesis is that, as the NS core is formed during the first synthesis step (i.e., seed generation), the nucleation and further growth of the legs during the second synthesis step may require the unzipping of the surfactant layer on the NP.[4] Upon nucleation of the first leg on an icosahedra vertex, the surfactant layer might be disturbed, rendering the nucleation of a second leg on a neighboring apex easier. The nucleation at two neighboring apexes may be able to generate a linear crack in the surfactant layer, facilitating its further unzipping along the expanding unzipping line. Simultaneously, this may increase the pressure on the direction perpendicular to the plane defined by the unzipping line on the core; as a result, the nucleation of the out-of-plane legs could be inhibited. In this scenario, the anisotropic leg distribution could be due to an interplay between the symmetry of the icosahedral core and the crack line on the surfactant capping layer. As this is only a working hypothesis of the complex and currently unknown mechanistic events taking place during the growth of these NSs, more detailed experimental work is necessary, and it is currently the focus of our synthetic efforts.

CONCLUSIONS

The precise crystallographic analysis reported here provided a complete characterization of the NS 3D crystalline structure. We must emphasize that all structural measurements have been confirmed by the analysis of a second 4D-STEM scan with the sample holder rotated by 10°; also, this second data set provided evidence of no detectable structural damage, confirming the low dose utilized in the experiment.

We speculate that the measured NS shape and legs' spatial distribution is associated with the surfactant layer unzipping over the icosahedral core during growth. It is essential to continue to refine the chemical and structural characterization of products at different stages of the complex two-step synthesis protocol to improve the understanding. This would be fundamental for NS synthesis scale-up and technological application.

Once we have a detailed measurement of the 3D shape, it is crucial to apply this knowledge to develop more precise modeling of their optical response and a deeper understanding of their application as plasmonic antennas.[35−38] The optical response results show a very good agreement with the measured spectrum for an ensemble of NS, providing more detailed understanding of their optical properties (see Figures S24−S26).

Determining the 3D morphology of a NS represents a traditional and well-stablished application of nanometer-resolution ET; in fact, HAADF ET could have been applied as an independent verification approach. However, the derivation of atomic arrangement information from higher resolution ET experiments remains quite challenging for this kind of extended NPs. Notwithstandingly, tomography image reconstruction is more suitable for nanomaterials which are not beam sensitive, where sample thickness and height (inducing defocus) do not change significantly during the tilt series: NPs, nanorods, nanocubes, etc., within the suitable dimension size (<20 nm). This study has provided solid evidence that we have been able to derive a very detailed atomic arrangement (legs, core, and the relative spatial orientation) from an individual very complex multibranched metal plasmonic NP from a single 4D-STEM scan, which was acquired using a very low electron total dose (<200 $e^-/Å^2$ per frame). The utilized analysis is especially well suited for the characterization of objects with extended and asymmetric shape. Our study has been based on ED techniques, which demand a more complex data analysis than the intuitive visualization of a tomography 3D image. The procedures applied in our work and results obtained provide opportunities to determine the atomic structure of individual multidomain or/and multiphase NPs, even when constituted of beam-sensitive materials.

METHODS

Specimen Preparation. The Au seed NPs were initially synthesized by the addition of a freshly prepared ice-cold solution of $NaBH_4$ (0.6 mL, 0.01 M) into an aqueous solution of $HAuCl_4$ (10 mL, 0.25 mM) and Triton X 100 (0.15 M). The solution immediately turned from pale yellow to orange after the addition of $NaBH_4$. The mixture was stirred for 2 min and aged for 10 min at 4 °C before use. The star growth solution was prepared by adding 0.4 mL of 25 mM $HAuCl_4$ solution to a 20 mL Triton-X solution (0.15 M). This step was followed by the addition of ascorbic acid (1.2 mM), $AgNO_3$ (100 μM), and the Au seeds (ranging from 0.06 nM) to the growth solution. The solution was stirred for 10 min and then centrifuged at 3500g for 10 min and dispersed to a final concentration of approximately 2 nM with Ultrapure Milli-Q water (18.2 MΩ cm). Samples of the produced 6-branched NSs with high-aspect-ratio legs were then drop-cast on a holey carbon Cu grid (Figures 1 and S2).

Electron Microscopy Experiments. A Thermo Fischer Spectra 300 electron microscope operated at 300 kV equipped with a probe spherical aberration corrector and a Quantum Detector Merlin 256 × 256 pixels direct detection camera was used for recording STEM and 4D-STEM data. Precession ED (PED) at 1 kHz with a precession angle of 1° was generated using a Nanomegas hardware and TopSpin software. Data acquisition used a 2 nm-wide electron probe of 1.0

https://doi.org/10.1021/acsnano.4c05201
ACS Nano 2024, 18, 26655−26665

mrad half-convergence angle and a dose of <200 $e^-/Å^2$ per frame; the pixel step was 1 nm, and the dwell time was 1 ms. Low-resolution study of the sample was based on a 200 kV using a Topcon 002B TEM. More detailed description of the PED experiment can be found in the Supporting Information.

Calculation of Virtual Images (VDFs) from 4D-STEM Maps. The interpretation of virtual images was fundamental for this work; thus, it was important to understand the contained spatial information with the maximum possible precision. Different kind of images has been calculated: (a) VADF, where the intensity in annular areas of the diffraction patterns (including many diffraction peaks) is added to generated images, or (b) VDF by selection of individual diffraction peaks to generate specific sample regions associated with a particular diffraction spot (see Figure 1).[13,15]

We have utilized anticorrelation images to visualize grain distribution in the NS; they were constructed with the common definition of anticorrelation utilized in 4D-STEM work, which compares a diffraction pattern $p_{x,y}$ (x,y: spatial coordinate in the ED mapping) with its nearest neighbors ($p_{x+1,y}$ and $p_{x,y+1}$) to form contrast $C(x,y)$[20]

$$C(x,y) = \sqrt{\frac{\sum_{i,j}[p_{x,y}(i,j) - p_{x+1,y}(i,j)]^2 + [p_{x,y}(i,j) - p_{x,y+1}(i,j)]^2}{2n}} \quad (1)$$

where i,j is the coordinate of a pixel in the measured ED, with n total pixels in each one.[20] The value of $C(x,y)$ is low when neighboring pixels show similar diffractions patterns and high when patterns change significantly from pixel to pixel; this is a very efficient tool to identify crystal grain boundaries and twins (see Figure 1).

Details of 4D-STEM Diffraction Data Processing and Simulation. The 6-branch star is quite an open nanostructure, in which the area that it occupies (a circle with a diameter of ~120 nm, the distance from a leg tip to the opposite one) is much larger than the effective projected area that the NS fills. Then, most pixels in the original 200 × 200 map just contain information from the carbon substrate (amorphous), not the NS (crystal). To reduce data volume, we have binarized a VADF image and selected all bright pixels to build a reduced data set containing just the pixels (~3200) inside the 2D projection image of the NS (a 92% reduction in data size). ML tools were applied using the Hyperspy open package.[23] Intensity profiles were derived using the ImageJ free software.[39] Orientation analysis was based on the Pyxem open software,[24] and PED intensity analysis has been previously developed and applied using a homemade Python software.[29,30]

Background Subtraction. The data block has been processed to reduce the effect of nonspecific (substrate or inelastic) intensity. A simple background subtraction was applied: a threshold was utilized in the VADF image to separate crystalline (inside NS) and amorphous (carbon substrate) regions. A background mean diffraction pattern was utilized as a template, which was rescaled for each pixel as a PED background and finally subtracted.

Clustering and ML. Clustering has been applied to our 4D-STEM diffraction maps by utilizing algorithms available in the Hyperspy suit,[23] whose efficiency has already been well established for treatment of diffraction data.[21,22] A gamma function has been applied to enhance the influence of low intensity peaks for ML algorithm processing, and a threshold value was utilized to exclude peaks with excessively low intensity. The K-means method identified 8 clusters, which resulted in 6 clusters spatially localized in the NS leg tips, and the other ones displayed mixed contribution of the NS core and the leg bases. Only LEG#1, highlighted in red in Figure 1F, could be fully clustered from the core to the tip by ML (the mean ED pattern from this region is shown in Figure 1G); this leg seems to be different from the other 5 legs, being shorter (~30 vs 50 nm) and slightly wider (12−15 vs 7−10 nm). We have also selected regions close to the NS core (indicated as base regions, see Figure S5) to ensure the characterization of the whole leg. The mean diffraction patterns of tip and base regions have been calculated (see Figure 1 main text and Figures S4 and S5) and analyzed in the same way. This procedure has drastically reduced the number of diffraction patterns that can be interpreted to just 10 patterns in total.

For each leg, the final step of interpretation of crystal orientation involved the manual recognition of the geometrical pattern of spots arising from one of the five BCO composing the decahedral leg; this allowed us to perform a rough crystal indexation with the common procedure (see Figure S6 for an example) to ensure the reliability of the crystal identification. When manual identification was rather difficult, we have also applied NMF (from Hyperspy[23]) to a data block generated by pixels in each individual region grouped by clustering (no intensity modification procedure, as scaling and gamma function, has been utilized here). The NMF was not able to isolate or recognize each of the 5 crystals forming the decahedral leg; nevertheless, it was useful in a few cases (LEG#1) to render easier the subsequent manual interpretation of diffraction spots (see Figures 1H, S6, and S7).

Crystal Orientation Determination. The use of conventional template matching is the most straightforward method to measure crystal orientation; however, the complexity of our sample implied the need of a more robust approach.[24−26] The polycrystalline nature of the legs (diameter <15 nm) implied that the observed diffraction pattern results from the contribution of several superimposed crystals (5, each with its own zone axis); this leads to an ineffective automated determination of crystal orientation using the standard procedures. Therefore, an additional manual identification protocol has been required, which can be performed by the traditional indexation of ED patterns.

We must identify diffraction spots from one of the 5 crystal domains forming the decahedral leg, so they can be selected by using a series of masks (shown in Figure S9). After masking, a gamma function is utilized to enhance the influence of diffraction peaks with low intensities; then, spots above a threshold value are selected to generate a binarized diffraction pattern. We have utilized the Pyxem software[24] to perform template-matching ACOM and retrieve the $[010]_{BCO}$ and $[001]_{BCO}$ directions. The template library has been simulated for a Au BCO crystal with the primitive cell dimensions measured from the diffraction pattern and calibrated from a Si calibration sample in the same experimental conditions (a = 0.265 nm, b = 0.271 nm, c = 0.358 nm, space group = *Immm*, #71). It is important to notice that the indexation can be performed with high precision due to the capacity to differentiate between the three main axes of the cell (a,b,c). The c-axis ($[001]_{BCO}$) is significantly distinct from the a-axis ($[100]_{BCO}$) and (b-axis $[010]_{BCO}$), and we can differentiate the b-axis by observing the direction of the leg in the virtual images formed by the diffraction patterns. In general, ACOM is very reliable in less symmetrical crystals, for example, the orthorhombic or hexagonal crystals, which simplifies the identification of a specific direction by reducing the multiplicity of each direction.

Pattern-matching ACOM results indicate that most leg axes ($[010]_{BCO}$) are confined to the xy plane, and the only major difference in orientation is the azimuthal angle of each one. This loss of some 3D information is probably the consequence of the binarization of intensities, as usually applied in pattern matching algorithms.

The diffraction spot intensity provides precise 3D information, as observable in the intensity profiles. For example, looking at extracted profiles from LEG#2 along the leg axis (Figure S4, left to right follows the core to tip direction), we can notice that diffracted beams on the left (core) side of the transmitted beam display higher intensity than beams on the right (tip) side. Then, the Ewald sphere construction and the Laue circle in diffraction physics[40] easily explains this intensity difference, what unambiguously indicates a leg oriented with its tip moving (down) along the electron beam traveling direction. Notice that the sample coordinate system indicated in Figure 2 implies in a e-beam traveling along the z direction (downward), a common coordinate reference system utilized in ACOM softwares.[24−26] We would like to mention that LEG#1 displays an elevation angle of 20° so that it has not been possible to exploit Laue

https://doi.org/10.1021/acsnano.4c05201
ACS Nano 2024, 18, 26655−26665

circle construction to determine if the leg is pointing downward or upward (phenomenon described as 180° duality of SAED). Then, a second diffraction map (Figure S18) taken at a different incident angle to the NS plane has been necessary to determine unambiguously that this leg points downward.

First, we obtain crystal orientation from pattern-matching as a starting point, where the angular resolution is at best limited to ~1−2° (see Figure S9); this is a common value for methods based on cross-correlation between experimental patterns and a library of kinetically simulated ED patterns.[24−26,29,30] Subsequently, a second higher precision ACOM was applied, in which the quantitative analysis of diffraction beam intensity is exploited (for this step, we used raw intensities after background subtraction, without any further intensity modification); the crystal orientation is measured through a residual metric (Rietveld-like comparison of experimental and simulated beam intensity, as illustrated in Figure S6) that allows angular resolution to be improved by at least 1 order of magnitude. We estimate that crystal orientation angles have been determined with a precision of ~0.1° (see Figure S10). The quality of the optimization is assessed by the residue value,[29,30] our results indicate the value in an acceptable range (20−40%),[41] considering the complexity of the NS structure and the unavoidable overlap between diffraction peaks from different crystal domains in the legs.

Overall, measurement of crystal orientation of the NS legs is a challenging case for both the peak position based and the intensity-based methodologies. The small crystal thickness (at maximum ~10 nm) implies large excitations errors, and peaks can be excited even with a large disorientation (<5°) from ideal diffraction condition, this is evidenced by the high symmetry of the measured PED patterns (see Figures S8 and S9). This probably implies that template matching cannot identify changes in orientation in this rather large angular range. This is corroborated by our results, where template matching provided many NS leg orientation restricted to the *xy* plane (0° elevation angle), but using diffracted intensity analysis intensities, we have revealed *xy* plane disorientation of the legs up to 5° (see Table 1). Furthermore, quantitative analysis of intensities must be performed with care as many of the observed PED peaks are resulting from the superposition of reflections from different crystals, affecting proportions between diffracted peaks in unpredictable ways. Consequentially, residues are higher than expected for a single crystalline case, and the angular resolution (~0.1°) is higher than previously reported efforts (<0.05°).[29,30]

NS Core Structure. Noble metal NPs can form different types of so-called multiple-twinned particles (MTPs) including a 5-fold axis; the decahedral structure is one of them, and its orthorhombic atomic arrangement has been extensively discussed to analyze leg structure (Figure 1D). The second type of MTPs is the icosahedron, frequently observed in Au or Ag NP samples.[19,42−44] An ICO is formed by the assembly of 20 tetrahedra sharing the tip at the center (Figure 3C). To fill the space, the cubic FCC unit cell is compressed along the [111] direction to generate a rhombohedral unit cell (RHO, space group = *R*32, #155, $a = 0.289$ nm).[19] From the point symmetry, ICO particles present 6× 5-fold axes (located at corner), 10× 3-fold axes (center of triangular faces), and 15× 2-fold axes (center of edges).[19] There are many reports of atomic resolution images of ICO NPs along 2- and 3-fold axes (hereafter noted as ICO2 and ICO3 respectively), and image contrast may be rather complex, but they can be easily understood considering some tetrahedra oriented correctly along the crystal zone axis (Figure S15).[43,44] The diffraction pattern originated by a system of 20 crystalline domains has revealed to be too complex to be solved by our manual analysis or by trying to unmix information by ML methodologies. Thus, we have not been able to calculate precisely the ICO orientation directly from the diffraction pattern as previously realized for the decahedral legs (see Table 1). However, when an ICO is oriented along an axis at the intermediate direction between a 2-fold and a 3-fold axis (an angular distance of 10.5° from both axes, Figure S16), the diffraction spots should display an elongated hexagonal configuration as observed in our experiments, in agreement with the analysis by Reyes-Gasga et al.[43] (see more details in the Supporting Information). Furthermore, an icosahedron oriented as ICO32D would display some tetrahedral units (marked 1, 1′ and 2, 2′ in Figure 3F), which will present atomic planes almost parallel to the electron beam and that will generate strong diffraction spots (*B* and *C*). From that, we can determine an ICO slight outside the intermediary orientation by looking at the projected atomic positions of these pairs of tetrahedra (Figure 3F). Notice that in this case, 2,2′ crystals are slightly more misoriented (3° off) from the electron beam direction than 1,1′ crystals. Consequentially, diffraction beams associated with 2,2′ tetrahedra will show lower intensity than the ones from the 1,1′; our model predicts that spot *C* in Figure 3F should be weaker than spot *B*; this is in full agreement with experimental data (simulated diffraction patterns is shown in Figure S17).[45] If the incident direction is along the line connecting the 2-fold and 3-fold axis, the intensity of spots *B* and *C* should be alike (both crystal pairs become nearly identically oriented along the e-beam direction, Figures S13 and S21).

Verification of Robustness and Accuracy of the Structural Results. To analyze the reproducibility of the applied procedure, we have acquired an additional data set by tilting the TEM sample holder by 10° and, subsequently, performing identical data processing and analysis. Unfortunately, the second 4D-STEM data set shows significant effects of amorphous carbon deposition after acquisition of data at 0°; thus, the quality of recorded diffraction data was lower (see Figure S18). Usually, this level of contamination would represent a serious difficulty for atomic resolution imaging; however, ED is a much more robust methodology to reveal atomic arrangement information under these sample conditions. The anticorrelation image from the data set taken at 10° (Figure S18) reveals easily that all twins associated with the decahedral structure of the legs have been conserved, confirming the low-dose profile of the present study (no radiation damage effects have been detected). More importantly, all of the crystallographic conclusions obtained from the second experiment (see details in the Supporting Information, Figures S18−S22) fully agreed within experimental error with the original study, confirming the leg spatial distribution and the icosahedral structure of the NS core and its estimated orientation.

Simulation of the Optical Response. The electromagnetic extinction calculated through the discrete dipole approximation[46] qualitatively agrees with the optical characterization of the sample (see Figures S24 and S25). Below 600 nm, the optical responses in both experimental and simulated extinction spectra are very similar and are dominated by the plasmonic response of the gold spherical core (~520 nm) and interband transitions (background). Two broad resonances are observed in the experimental data at 670 and 830 nm. In the simulated spectrum, we were also able to observe two resonances, namely, mode#1 (~630 nm) and mode#2 (~750 nm). The observed resonances are blue-shifted and considerably narrower than the experimental observations. These discrepancies can be attributed to different factors: (i) the real sample is composed of a distribution of NP shapes, whereas only one structure is considered in the simulation,[47−49] (ii) the simulated structure must yet be improved to reproduce a nanostructure with such a diversity of intricate features, (iii) possible local refractive index effects due to molecular adsorbates from the synthesis were not included, (iv) a possible difference in composition for the legs, containing non-negligible Ag, was also not considered. Nevertheless, the observation of two modes in the simulated spectrum is an important realization and is in good qualitative agreement with the more complex experimental spectrum. The polarization vectors for each dipole are presented in Figure S26 and suggest that mode#1 is composed of dipole oscillations localized mainly on 2 legs (LEG#2 and LEG#6) for the incident polarization, whereas in mode#2, the contribution of four legs can be observed (LEG#2, LEG#3, LEG#5, and LEG#6). The results suggest a high degree of plasmon resonance and near-field tunability by controlling the number and aspect ratio of legs in AuAg NSs.

https://doi.org/10.1021/acsnano.4c05201
ACS Nano 2024, 18, 26655−26665

ASSOCIATED CONTENT

Data Availability Statement

Supporting Information is available in the online version of the paper. The data sets utilized in this work is available at https://redu.unicamp.br/dataset.xhtml?persistentId=doi:10.25824/redu/YYUUDW. This data is registered with the DOI: doi:10.25824/redu/YYUUDW.

Supporting Information

The Supporting Information is available free of charge at https://pubs.acs.org/doi/10.1021/acsnano.4c05201.

TEM micrographs of the sample; operational principles of 4D-STEM diffraction mapping and precession electron diffraction; atomic arrangement of decahedral particles; clustering (*K*-means) grouped pixels, the resulting mean diffraction patterns and diffracted intensity profiles; manual identification of zone axis and crystal orientation; mean diffraction pattern of LEG#1 and the result of NMF analysis; manual identification of the zone axes for LEG#1 and crystal orientation with template-matching; quality, sensitivity and precision of the intensity analysis through residue minimization; evidence of 5-fold symmetry of the NS legs; mean diffraction pattern for the NS core; structural aspects associated to ICO particles structure; deduction orientation of the NS icosahedral core; simulation of the NS core diffraction pattern; VADF and correlation-image of the NS after sample rotation; determination of the rotation axis and NS 3D reconstruction and core orientation after sample rotation; measured PED pattern; ;icosahedral core for NS showing 5-fold symmetry in leg orientation; UV-Vis-NIR spectra, DDA-simulated extinction spectra and polarization vectors of the derived structure (PDF)

AUTHOR INFORMATION

Corresponding Author

Daniel Ugarte − *Instituto de Física Gleb Wataghin, Universidade Estadual de Campinas, Campinas 13083-859, Brazil;* orcid.org/0000-0003-3332-9139; Email: dmugarte@ifi.unicamp.br

Authors

Leonardo M. Corrêa − *Instituto de Física Gleb Wataghin, Universidade Estadual de Campinas, Campinas 13083-859, Brazil;* orcid.org/0000-0002-0823-4085

Simon M. Fairclough − *Department of Materials Science and Metallurgy, University of Cambridge, Cambridge CB3 0FS, U.K.;* orcid.org/0000-0003-3781-8212

Kaleigh M. R. Scher − *Department of Materials Science and Engineering, Rutgers University, Piscataway, New Jersey 08854, United States*

Supriya Atta − *Department of Biomedical Engineering, Duke University, Durham, North Carolina 27708, United States;* orcid.org/0000-0001-5489-268X

Diego Pereira dos Santos − *Instituto de Química, Universidade Estadual de Campinas, Campinas 13083-859, Brazil;* orcid.org/0000-0001-9468-7293

Caterina Ducati − *Department of Materials Science and Metallurgy, University of Cambridge, Cambridge CB3 0FS, U.K.;* orcid.org/0000-0003-3366-6442

Laura Fabris − *Department of Applied Science and Technology, Politecnico di Torino, Turin 10129, Italy;* orcid.org/0000-0002-7089-5175

Complete contact information is available at: https://pubs.acs.org/10.1021/acsnano.4c05201

Author Contributions

S.M.F., L.F., K.S., and S.A. prepared the specimen and performed the initial optical and TEM experimental investigation. S.M.F., L.M.C., D.U., and C.D. planned and contributed to 4-D-STEM + PED data acquisition. L.M.C. and D.U. interpreted the experimental results using PED diffraction simulations and ML tools. D.P.d.S. performed optical response calculations. L.M.C., D.U., L.F., and C.D. wrote the manuscript. All the authors discussed the results and commented on the manuscript.

Funding

The Article Processing Charge for the publication of this research was funded by the Coordination for the Improvement of Higher Education Personnel - CAPES (ROR identifier: 00x0ma614).

Notes

The authors declare no competing financial interest.

ACKNOWLEDGMENTS

We acknowledge the use of the Thermo Fisher Spectra 300 TEM funded by EPSRC under grant EP/R008779/1. L.F. and K.S. acknowledge the support from the Busch Biomedical Grant Program at Rutgers University. D.U. acknowledges the financial support from the Brazilian Agencies FAPESP (2014/01045-0), CNPq (402571/2016-9, 306513/2017-0, 402676/2021-1, and 303025/2022-0), and FAEPEX-UNICAMP (2632/17). L.M.C. acknowledges the financial support from CAPES (1765876/2018) and CNPq (140596/2020-8). D.P.d.S. acknowledges FAPESP (2016/21070-5, 2022/11983-4), FAEPEX/UNICAMP (3034/23) and CNPq (405087/2021-7) for financial support.

REFERENCES

(1) Langer, J.; Jimenez De Aberasturi, D.; Aizpurua, J.; Alvarez-Puebla, R. A.; Auguié, B.; Baumberg, J. J.; Bazan, G. C.; Bell, S. E. J.; Boisen, A.; Brolo, A. G.; Choo, J.; Cialla-May, D.; Deckert, V.; Fabris, L.; Faulds, K.; García de Abajo, F. J.; Goodacre, R.; Graham, D.; Haes, A. J.; Haynes, C. L.; Huck, C.; Itoh, T.; Käll, M.; Kneipp, J.; Kotov, N. A.; Kuang, H.; Le Ru, E. C.; Lee, H. K.; Li, J.-F.; Ling, X. Y.; Maier, S. A.; Mayerhöfer, T.; Moskovits, M.; Murakoshi, K.; Nam, J.-M.; Nie, S.; Ozaki, Y.; Pastoriza-Santos, I.; Perez-Juste, J.; Popp, J.; Pucci, A.; Reich, S.; Ren, B.; Schatz, G. C.; Shegai, T.; Schlücker, S.; Tay, L.-L.; Thomas, K. G.; Tian, Z.-Q.; Van Duyne, R. P.; Vo-Dinh, T.; Wang, Y.; Willets, K. A.; Xu, C.; Xu, H.; Xu, Y.; Yamamoto, Y. S.; Zhao, B.; Liz-Marzán, L. M. Present and Future of Surface-Enhanced Raman Scattering. *ACS Nano* **2020**, *14* (1), 28−117.

(2) Rho, J. Metasurfaces: Subwavelength nanostructure arrays for ultrathin flat optics and photonics. *MRS Bull.* **2020**, *45*, 180−187.

(3) Xia, Y.; Xiong, Y.; Lim, B.; Skrabalak, S. E. Shape-Controlled Synthesis of Metal Nanocrystals: Simple Chemistry Meets Complex Physics? *Angew. Chem., Int. Ed.* **2009**, *48* (1), 60−103.

(4) Atta, S.; Beetz, M.; Fabris, L. Understanding the Role of AgNO3 Concentration and Seed Morphology in the Achievement of Tunable Shape Control in Gold Nanostars. *Nanoscale* **2019**, *11* (6), 2946−2958.

(5) Carter, C. B.; Williams, D. B. *Transmission Electron Microscopy*; Springer International Publishing: Cham, 2016.

(6) Zuo, J. M.; Spence, J. C. H. *Advanced Transmission Electron Microscopy*; Springer: New York, NY, 2017.
(7) De Graef, M. *Introduction to Conventional Transmission Electron Microscopy*; Cambridge University Press: Cambridge, 2003.
(8) Zhou, J.; Yang, Y.; Ercius, P.; Miao, J. Atomic Electron Tomography in Three and Four Dimensions. *MRS Bull.* **2020**, *45* (4), 290−297.
(9) Hovden, R.; Muller, D. A. Electron Tomography for Functional Nanomaterials. *MRS Bull.* **2020**, *45* (4), 298−304.
(10) Hovden, R.; Ercius, P.; Jiang, Y.; Wang, D.; Yu, Y.; Abruña, H. D.; Elser, V.; Muller, D. A. Breaking the Crowther Limit: Combining Depth-Sectioning and Tilt Tomography for High-Resolution, Wide-Field 3D Reconstructions. *Ultramicroscopy* **2014**, *140*, 26−31.
(11) Albrecht, W.; Bals, S. Fast Electron Tomography for Nanomaterials. *J. Phys. Chem. C* **2020**, *124* (50), 27276−27286.
(12) Thomas, J. M.; Leary, R. K.; Eggeman, A. S.; Midgley, P. A. The Rapidly Changing Face of Electron Microscopy. *Chem. Phys. Lett.* **2015**, *631*−*632*, 103−113.
(13) Ophus, C. Four-Dimensional Scanning Transmission Electron Microscopy (4D-STEM): From Scanning Nanodiffraction to Ptychography and Beyond. *Microsc. Microanal.* **2019**, *25*, 563−582.
(14) Macpherson, S.; Doherty, T. A. S.; Winchester, A. J.; Kosar, S.; Johnstone, D. N.; Chiang, Y.-H.; Galkowski, K.; Anaya, M.; Frohna, K.; Iqbal, A. N.; Nagane, S.; Roose, B.; Andaji-Garmaroudi, Z.; Orr, K. W. P.; Parker, J. E.; Midgley, P. A.; Dani, K. M.; Stranks, S. D. Local Nanoscale Phase Impurities Are Degradation Sites in Halide Perovskites. *Nature* **2022**, *607* (7918), 294−300.
(15) Rauch, E. F.; Véron, M. Virtual Dark-Field Images Reconstructed from Electron Diffraction Patterns. *Eur. Phys. J. Appl. Phys.* **2014**, *66*, 10701.
(16) Ni, B.; Mychinko, M.; Gómez-Graña, S.; Morales-Vidal, J.; Obelleiro-Liz, M.; Heyvaert, W.; Vila-Liarte, D.; Zhuo, X.; Albrecht, W.; Zheng, G.; González-Rubio, G.; Taboada, J. M.; Obelleiro, F.; López, N.; Pérez-Juste, J.; Pastoriza-Santos, I.; Cölfen, H.; Bals, S.; Liz-Marzán, L. M. Chiral Seeded Growth of Gold Nanorods Into Fourfold Twisted Nanoparticles with Plasmonic Optical Activity. *Adv. Mater.* **2023**, *35* (1), 2208299.
(17) Reyes-Gasga, J.; Elechiguerra, J. L.; Liu, C.; Camacho-Bragado, A.; Montejano-Carrizales, J. M.; Jose Yacaman, M. On the Structure of Nanorods and Nanowires with Pentagonal Cross-Sections. *J. Cryst. Growth* **2006**, *286* (1), 162−172.
(18) Rogers, B.; Lehr, A.; Velázquez-Salazar, J. J.; Whetten, R.; Mendoza-Cruz, R.; Bazan-Diaz, L.; Bahena-Uribe, D.; José Yacaman, M. Decahedra and Icosahedra Everywhere: The Anomalous Crystallization of Au and Other Metals at the Nanoscale. *Cryst. Res. Technol.* **2023**, *58* (4), 2200259.
(19) Yang, C. Y.; Yacamán, M.; Heinemann, K. Crystallography of Decahedral and Icosahedral Particles. *J. Cryst. Growth* **1979**, *47*, 283−290.
(20) Kiss, Á. K.; Rauch, E. F.; Lábár, J. L. Highlighting Material Structure with Transmission Electron Diffraction Correlation Coefficient Maps. *Ultramicroscopy* **2016**, *163*, 31−37.
(21) Eggeman, A. S.; Krakow, R.; Midgley, P. A. Scanning Precession Electron Tomography for Three- Dimensional Nanoscale Orientation Imaging and Crystallographic Analysis. *Nat. Commun.* **2015**, *6*, 7267.
(22) Martineau, B. H.; Johnstone, D. N.; Van Helvoort, A. T. J.; Midgley, P. A.; Eggeman, A. S. Unsupervised Machine Learning Applied to Scanning Precession Electron Diffraction Data. *Adv. Struct. Chem. Imaging* **2019**, *5*, 3.
(23) de la Peña, F.; Prestat, E.; Tonaas Fauske, V.; Burdet, P.; Lähnemann, J.; Jokubauskas, P.; Furnival, T.; Carter, F.; Nord, M.; Ostasevicius, T.; MacArthur, K. E.; Johnstone, D. N.; Sarahan, M.; Taillon, J.; Thomas, A.; pquinn, dls.; Migunov, V.; Eljarrat, A.; Caron, J.; Nemoto, T.; Poon, T.; Stefano, M.; actions, u.; Tappy, N.; Cautaerts, N.; Somnath, S.; Slater, T.; Walls, M.; pietsjoh; Ramsden, H. *Hyperspy/Hyperspy: V2.0.1*; Zenodo, 2024.
(24) Cautaerts, N.; Crout, P.; Ånes, H. W.; Prestat, E.; Jeong, J.; Dehm, G.; Liebscher, C. H. Free, Flexible and Fast: Orientation Mapping Using the Multi-Core and GPU-Accelerated Template Matching Capabilities in the Python-Based Open Source 4D-STEM Analysis Toolbox Pyxem. *Ultramicroscopy* **2022**, *237*, 113517.
(25) Ophus, C.; Zeltmann, S. E.; Bruefach, A.; Rakowski, A.; Savitzky, B. H.; Minor, A. M.; Scott, M. C. Automated Crystal Orientation Mapping in py4DSTEM Using Sparse Correlation Matching. *Microsc. Microanal.* **2022**, *28* (2), 390−403.
(26) Rauch, E. F.; Portillo, J.; Nicolopoulos, S.; Bultreys, D.; Rouvimov, S.; Moeck, P. Automated Nanocrystal Orientation and Phase Mapping in the Transmission Electron Microscope on the Basis of Precession Electron Diffraction. *Z. Kristallogr.* **2010**, *225* (2−3), 103−109.
(27) Midgley, P. A.; Eggeman, A. S. Precession Electron Diffraction − A Topical Review. *IUCrJ* **2015**, *2*, 126−136.
(28) Vincent, R.; Midgley, P. A. Double Conical Beam-Rocking System for Measurement of Integrated Electron Diffraction Intensities. *Ultramicroscopy* **1994**, *53*, 271−282.
(29) Corrêa, L. M.; Ortega, E.; Ponce, A.; Cotta, M. A.; Ugarte, D. High Precision Orientation Mapping from 4D-STEM Precession Electron Diffraction Data Through Quantitative Analysis of Diffracted Intensities. *Ultramicroscopy* **2024**, *259*, 113927.
(30) Palatinus, L.; Brázda, P.; Jelínek, M.; Hrdá, J.; Steciuk, G.; Klementová, M. Specifics of the Data Processing of Precession Electron Diffraction Tomography Data and Their Implementation in the Program PETS2.0. *Acta Crystallogr., Sect. B: Struct. Sci., Cryst. Eng. Mater.* **2019**, *75* (4), 512−522.
(31) Velázquez-Salazar, J. J.; Bazán-Díaz, L.; Zhang, Q.; Mendoza-Cruz, R.; Montaño-Priede, L.; Guisbiers, G.; Large, N.; Link, S.; José-Yacamán, M. Controlled Overgrowth of Five-Fold Concave Nanoparticles into Plasmonic Nanostars and Their Single-Particle Scattering Properties. *ACS Nano* **2019**, *13* (9), 10113−10128.
(32) Werner, K. V.; Niessen, F.; Li, W.; Lu, S.; Vitos, L.; Villa, M.; Somers, M. A. J. Reconciling Experimental and Theoretical Stacking Fault Energies in Face-Centered Cubic Materials with the Experimental Twinning Stress. *Materialia* **2023**, *27*, 101708.
(33) Burton, W. K.; Cabrera, N.; Frank, F. C. The Growth of Crystals and the Equilibrium Structure of Their Surfaces. *Philos. Trans. R. Soc., A* **1951**, *243*, 299−358.
(34) Xia, X.; Xie, S.; Liu, M.; Peng, H.-C.; Lu, N.; Wang, J.; Kim, M. J.; Xia, Y. On the Role of Surface Diffusion in Determining the Shape or Morphology of Noble-Metal Nanocrystals. *Proc. Natl. Acad. Sci. U.S.A.* **2013**, *110* (17), 6669−6673.
(35) Fabris, L. Gold Nanostars in Biology and Medicine: Understanding Physicochemical Properties to Broaden Applicability. *J. Phys. Chem. C* **2020**, *124*, 26540−26553.
(36) Dardir, K.; Wang, H.; Martin, B. E.; Atzampou, M.; Brooke, C. B.; Fabris, L. SERS Nanoprobe for Intracellular Monitoring of Viral Mutations. *J. Phys. Chem. C* **2020**, *124* (5), 3211−3217.
(37) Cristiano, M. N.; Tsoulos, T. V.; Fabris, L. Quantifying and Optimizing Photocurrent via Optical Modeling of Gold Nanostar-Nanorod-and Dimer-Decorated MoS2 and MoTe2. *J. Chem. Phys.* **2020**, *152*, 014705.
(38) Atta, S.; Pennington, A. M.; Celik, F. E.; Fabris, L. TiO2 on Gold Nanostars Enhances Photocatalytic Water Reduction in the Near-Infrared Regime. *Chem* **2018**, *4*, 2140−2153.
(39) Schneider, C. A.; Rasband, W. S.; Eliceiri, K. W. NIH Image to ImageJ: 25 years of image analysis. *Nat. Methods* **2012**, *9*, 671−675.
(40) De Graef, M.; McHenry, M. E. *Structure of Materials: An Introduction to Crystallography, Diffraction and Symmetry*; Cambridge University Press: Cambridge, 2012.
(41) Palatinus, L.; Corrêa, C. A.; Steciuk, G.; Jacob, D.; Roussel, P.; Boullay, P.; Klementová, M.; Gemmi, M.; Kopeček, J.; Domeneghetti, M. C.; Cámara, F.; Petříček, V. Structure Refinement Using Precession Electron Diffraction Tomography and Dynamical Diffraction: Tests on Experimental Data. *Acta Crystallogr., Sect. B: Struct. Sci., Cryst. Eng. Mater.* **2015**, *71* (6), 740−751.
(42) Marks, L. D. Experimental Studies of Small Particle Structures. *Rep. Prog. Phys.* **1994**, *57*, 603−649.
(43) Reyes-Gasga, J.; Tehuacanero-Nuñez, S.; Montejano-Carrizales, J. M. Simulation of the Experimental HRTEM Contrast of Icosahedral

https://doi.org/10.1021/acsnano.4c05201
ACS Nano 2024, 18, 26655−26665

Gold Nanoparticles of Different Sizes. *Acta Microsc.* **2009**, *18*, 304–315.
(44) Flüeli, M.; Spycher, R.; Stadelmann, P. A.; Buffat, P. A.; Borel, J.-P. High-Resolution Electron Microscopy (HREM) on Icosahedral Gold Small Particles: Image Simulation and Observations. *Europhys. Lett.* **1988**, *6*, 349–352.
(45) Seto, Y.; Ohtsuka, M. ReciPro: Free and Open-Source Multipurpose Crystallographic Software Integrating a Crystal Model Database and Viewer, Diffraction and Microscopy Simulators, and Diffraction Data Analysis Tools. *J. Appl. Crystallogr.* **2022**, *55*, 397–410.
(46) Gallinet, B.; Butet, J.; Martin, O. J. F. Numerical Methods for Nanophotonics: Standard Problems and Future Challenges. *Laser Photonics Rev.* **2015**, *9*, 577–603.
(47) Tsoulos, T. V.; Han, L.; Weir, J.; Xin, H. L.; Fabris, L. A Closer Look at the Physical and Optical Properties of Gold Nanostars: an Experimental and Computational Study. *Nanoscale* **2017**, *9*, 3766–3773.
(48) Tsoulos, T. V.; Fabris, L. Interface and Bulk Standing Waves Drive the Coupling of Plasmonic Nanostar Antennas. *J. Phys. Chem. C* **2018**, *122*, 28949–28957.
(49) Tsoulos, T. V.; Atta, S.; Lagos, M. J.; Beetz, M.; Batson, P. E.; Tsilomelekis, G.; Fabris, L. Colloidal Plasmonic Nanostar Antennas with Wide Range Resonance Tunability. *Nanoscale* **2019**, *11* (40), 18662–18671.

https://doi.org/10.1021/acsnano.4c05201
ACS Nano 2024, 18, 26655–26665

Apêndice F

Material Suplementar ao Apêndice E

A seguir está anexado o material suplementar ao artigo que descreve o trabalho descrito no Capítulo 5 da tese. O arquivo pode ser encontrado em: https://pubs.acs.org/doi/10.1021/acsnano.4c05201.

Supplementary Information

Atomic structure and 3D shape of a multi-branched plasmonic nanostar from a single spatially resolved electron diffraction map

Leonardo M. Corrêa[a], Simon M. Fairclough[b] , Kaleigh M. R. Scher[c] , Supriya Atta[d] , Diego Pereira dos Santos[e], Caterina Ducati[b], Laura Fabris[f], Daniel Ugarte[a*]

[a] Instituto de Física Gleb Wataghin, Universidade Estadual de Campinas, Campinas, 13083- 859, Brazil.

[b] Department of Materials Science and Metallurgy, University of Cambridge, Cambridge, CB3 0FS, UK.

[c] Department of Materials Science and Engineering, Rutgers University, Piscataway, NJ 08854,USA.

[d] Department of Biomedical Engineering, Duke University, Durham, NC 27708, USA.

[e] Instituto de Química, Universidade Estadual de Campinas, Campinas, 13083- 859, Brazil.

[f] Department of Applied Science and Technology, Politecnico di Torino, Turin, 10129, Italy.

* Email: dmugarte@ifi.unicamp.br

Precession electron diffraction (PED)

The interpretation of electron diffraction (ED) is rather complicated due to the strong electron-matter interaction (a phenomenon described as dynamical diffraction) that leads to nonlinear effects on the diffracted beam intensities such that the data can only be correctly modelled through slow and complex numerical simulations (*1-3*).

Vicent & Midgley (*4*) have proposed a method of precession electron diffraction in which the ED pattern is acquired while the electron beam precesses around the microscope optical axis (forming a hollow cone, Fig. S1). This beam manipulation reduces dynamical diffraction effects, such that beam diffraction patterns can be quantitively understood using a simpler x-ray crystallography modelling, which is the so-called kinematical theory (*4-8*). Scanning precession electron diffraction (SPED) is also widely used in materials science for texture analysis by means of the so-called automated crystal orientation mapping (ACOM) (*5,9,10*). We have obtained a higher precision measurement of crystal orientation by a quantitative analysis of diffracted beam intensities (*11,12*), which will be discussed in more detail in the crystal orientation determination section.

The use of PED implies that events of double scattering will be significantly reduced such that, in the case of crystal superposition, we can analyze the final diffraction pattern as the incoherent addition of each crystal scattering (each crystal can be treated as isolated). This has been exploited for crystal tomography and the reconstruction of precipitates in superalloys based on PED diffraction mapping by Eggeman et al. (*13*).

Determining the NS core atomic structure

The core mean diffraction pattern has been obtained by averaging all patterns from the nanostar (NS) centre (circular region of 10 nm in radius, Fig. 3 main text and Fig. S13). This pattern shows an elongated hexagonal distribution of spots, roughly close to a 2-fold symmetry.

The spot distribution reminds a face centred cubic crystal (FCC) crystal containing 2 non-parallel twins (Fig. S14) as described in the transmission electron microscopy (TEM) textbook by De Graef (*19*). Nevertheless, this explanation can be easily ruled out by taking virtual dark field (VDF) images of diffractions spots in our experiment (Fig. 3 main text), which are quite different from the expected VDFs image contrast for FCC twinned crystal (Fig. S14). Looking carefully at VDFs from the NS core (Fig. 3 main text), we can recognize that most VDFs reveal crystal regions with a triangular shape at different azimuthal orientation and always showing a sharp tip at the core centre. These characteristics can only be explained by an icosahedral structure (ICO, see geometrical schema at Fig. 3), with rhombohedral (*RHO*) atomic arrangement.

The roughly 2-fold nature of the core mean ED pattern (Fig. 3 and Fig. S13) suggests an icosahedral particle observed along 2-fold axis (ICO2 observation). However the pattern also shows very clear attributes of an ICO3 (Fig. S15): a) an angle of 60 degrees between spots marked *D* and *E* ($(110)_{RHO}$ planes, Fig. S13); and b) the occurrence of the spot marked *F* ($(\bar{1}10)_{RHO}$ or $(121)_{RHO}$ planes, or {220} planes in the undeformed FCC lattice, Fig. S13) aligned with the same direction as spot *D*. The interplane distance associated with spot *F* is much smaller (~1.4 Å) than the ones originating *A-D* spots (~2.2 Å, see Fig. S13), so these planes require a much more precise crystal orientation to be measured (expected diffraction patterns from ICO2 and ICO3 are displayed in Fig. S15). The simulated VDF for spot *F* shows a bright contrast at the particle centre in full agreement with the experimental VDF image expected for an icosahedral particle observed along 3-fold axis (ICO3 observation) (Fig. 3 main text).

Unfortunately, we have not been able to calculate precisely the ICO orientation directly from the diffraction pattern as previously realized for the decahedral legs (see Table 1). The experimental ED shows characteristics of the 2-fold and 3-fold diffraction pattern. The intermediate direction between a 2-fold and 3-fold axis (ICO32, noted 32 in Fig. S16) at angular distance of 10.5 degrees from both axes. To preserve a good orientation of atomic planes originating the diffraction spot marked *F*, the ICO must be rotated along a direction close to normal to these planes (see lower part of the Fig. S16) in such a way that the 2-fold nature of the diffraction pattern is preserved. We have conjectured a possible observation direction to fulfil all experimental constrains (arrowed in Fig. S16), which will be called ICO32D; letter *D* is included to describe a deviation for the intermediate position (ICO32) between ICO2 and ICO3 orientations. It is important to note

that an icosahedron along the ICO32D orientation yields a complete consistent explanation for all experimental data (VDF images in Fig. 3) and predicted diffraction spots, see Fig. S13 and S17).

Taking ICO32D orientation as the reference, we can geometrically model the orientation of different tetrahedra forming the ICO core, estimate their diffraction pattern and their spatial location through VDF images. Some domains (marked 1,1' and 2,2' in Fig. 3F) will present atomic planes almost parallel to the electron beam and should generate strong diffraction spots. Fig. 3F shows the projected atomic positions of these tetrahedra; note that tetrahedra 1 and 1' display a family of (110)$_{RHO}$ planes very well oriented along the electron beam direction generating a strong diffraction spot (disk marked *B* in experiment). In contrast, domains 2 and 2' display a similar family of planes that are, however slightly misoriented (misorientation of about 3 degrees with the electron beam), which would generate much weaker spots (disk *C*). The predicted spot position, intensity and their relative angle is in excellent agreement with measurements (see Fig. S13). Concerning the intense spot *G* (not shown), its VDF image does not follow a contrast pattern that can be associated with an ICO core; we attribute its occurrence to a region of metal overgrown on the ICO seed during the NS leg growth and it will be neglected in our analysis.

We must emphasize that we have been able to predict the spot positions, angular distance, and intensity differences from the ICO23D model (see Fig. 3, Fig. S13 and S17). Briefly, a precise understanding of the NS core atomic arrangement has been derived by the combination of electron diffraction and virtual images. All major diffraction spots (*A-F*) from the NS core have been explained through well founded arguments.

Verification of the robustness and accuracy of the structural results

The crystallographic analysis of ED patterns may seem rather difficult, and thus it may raise questions and doubts on the robustness of the procedures. To provide an answer to the potential questions on precision, accuracy, and reproducibility, we have used the tilting capacity of TEM sample holders to acquire a second set of data after rotation of 10 degrees. Subsequently, we have applied the same data analysis procedures. Unfortunately, the quality of recorded diffraction data resulted much lower due to a significant deposition of carbon contamination (see Fig. S18), which reduced the precision of derived structural parameters. It is important to emphasize that the NS images taken at 0 and 10 degrees do not show major difference, but ED data from legs or the NS core show major changes (Fig. S19 & S21). Fig. S18c displays the anticorrelation image after 10 degrees tilt, where twins from the leg decahedral structure are clearly visible (bright lines along legs) implying that the decahedral atomic arrangement has been conserved, and thus confirming the low dose profile of this study.

To test the quality of our crystal orientation assessment, we have compared first and second assessment of leg spatial position considering the applied 10 degrees rotation. We have analysed LEG#4 and LEG#6 which should show the maximum orientational changes as these two legs are located at high angle (closer to perpendicular) from the sample holder rotation axes (approximatively along vertical direction). The [010]$_{BCO}$ direction has been determined for these legs: a) LEG 4 = [-0.965, -0.221,-0.143]; b) LEG 6 = [0.644, -0.7352, 0.222]. The rotation axis (dashed line in Fig. S19) has been determined by optimizing the azimuthal angle to the axis, such that experimental measurements result from an applied rotation angle of 10 degrees. The angle between legs ($\alpha_{4\text{-}6}$) has determined by using the scalar product between the vector indicating the axis of the decahedral structures by using the crystallographic analysis of the experimental PED patterns. The results show full agreement within experimental errors: a) 0 degrees experiment $\alpha_{4\text{-}6}$= (120.3 ± 0.1) deg.; b) 10 degrees experiment $\alpha_{4\text{-}6}$= (119,4 ± 0.4) deg. Furthermore, data quality (ex. presence of saturated diffraction spots) has hindered the analysis of diffraction intensities, so we have perform a simpler orientation analysis for the other legs (reduced angular precision in the few degrees range). The results are shown in Figure S20 and Table S1 and confirm unambiguously the planar leg configuration. However, the angular resolution for legs 1, 2, 3 and 5 is at best limited to the resolution provided by PYXEM (~ 1°), which is optimistic considering that sample characteristics (mainly the sample thickness, ~ 5 nm of crystallite size) restrict the methods (only peak position is taken into account). This is evidenced in LEG#1, where we have only been able to identify only a major axis ([-2 -1 1]$_{BCO}$), a deviation of 5 degree from the expected axis ([-8 -5 4]$_{BCO}$) calculated from the measured axis of the original data. Consequentially, we decide to utilize a 5 degrees value as a conservative

estimation of the angular resolution. Although the reduced precision, it is still to corroborate the planar leg configuration obtained with the original data (before carbon contamination occurrence).

Table S1: Spherical coordinates of the NS leg axis (versors) derived from the intensity (Leg#4 & Leg#6) and with template-matching (1, 2, 3 & 5) have distinct angular resolution. The table follows the same conventions than Table 1 in the main text.

Leg	Azimuthal [deg]	Elevation [deg]
1	9.6	28 ± 5
2	66.1	9 ± 5
3	140.6	18 ± 5
4	192.9	-8.2 ± 0.3
5	253.2	-7 ± 5
6	313.2	12.8 ± 0.2

Concerning the NS core, we evaluated the mean ED pattern from the central region (Fig. S21) from the 10 degrees rotated NS. Surprisingly, the general appearance of the pattern is very similar to the unrotated sample one, showing again an elongated hexagonal distribution of spots roughly close to a 2-fold symmetry, but the mirror plane seems rotated azimuthally. This is due to a change of the ICO32D icosahedral to another 2-fold axis surrounding the central point of an icosahedral triangular facet (see Fig. S21b). This result is not surprising because the icosahedral point group shows high density of high symmetry axes. The mirror dividing the hexagonal configuration of the diffraction pattern follows the plane determined by spot marked *T*. Spot marked *U* is associated to $(10\bar{1})_{RHO}$ planes that should observed when an icosahedron is oriented along ICO3 axis. As spots *T* and *U* are aligned along the mirror plane, we must conclude that the ICO orientation is located approximatively along the line connecting 2-fold and 3-fold axes. This is confirmed by the fact that diffraction spots *S* and *R* show almost identical intensity (equivalent spots in the original ICO32D orientation were marked *B* and *C*, but they showed quite different intensity). The geometrical reconstruction of an icosahedron confirms this analysis (compare Fig. 3 and Fig. S21 & S22). Tetrahedra originating both diffraction spots should show atomic planes along the electron incident direction and will generate intense electron diffraction spots of similar intensities. Additionally, the measured and expected contrast of VDF generated from *S* and *R* spots show a remarkable agreement.

Summarizing, all the crystallographic conclusions from the second experiment fully agreed with the original study, confirming leg spatial distribution and the icosahedral structure of the NS core and its estimated orientation (ICO32D).

Analysis of 6-branched or 7-branched NSs showing 5-fold symmetry.

The results showed unambiguously that the core of the 6-branched NS is an icosahedral nanoparticle; however, previous reports indicate that the core is more akin to decahedral. This is mostly based in the fact that the legs of many NS follow a 5-fold layout: 5 legs nucleate with a 72 degree between neighbouring legs which are correlated to the decahedra 5 twin positions. An alternative explanation can be derived from the present work that demonstrated unambiguously an icosahedral particle as the NS core. An ICO particle observed along a 5-fold axis presents 10 tetrahedra with an edge parallel to the 5-fold axis. These 10 tetrahedra can be grouped and described as two stacked decahedra; the two decahedra are rotated by 36 degrees ($2\pi/10$) in relation to one the other (Fig. 3C and Fig. S23). Thus, assuming that the legs in a 5-fold layout are, all the five, located on the vertices of one of these decahedra, the additional leg at bisecting angles (36 degrees) must grow in a different plane and from apexes located on the second decahedron. Fig. S23 shows a TEM image of a particle (arrowed in Fig. 1A) displaying 5 legs azimuthally distributed close to 5-fold symmetry and a 6th leg (located close to the central angle between two legs defining the 5-fold symmetry). This leg configuration represents also a layout expected for an icosahedral NS core (see Fig. S23).

Absorption measurement and simulation

Absorption spectra were collected on a Thermo Scientific Evolution 300 UV-Visible spectrophotometer using a quartz cuvette with a 1 cm path. Simulated extinction spectrum for the measured nanostar 3D morphology has been calculated using DDA approach (*15*).

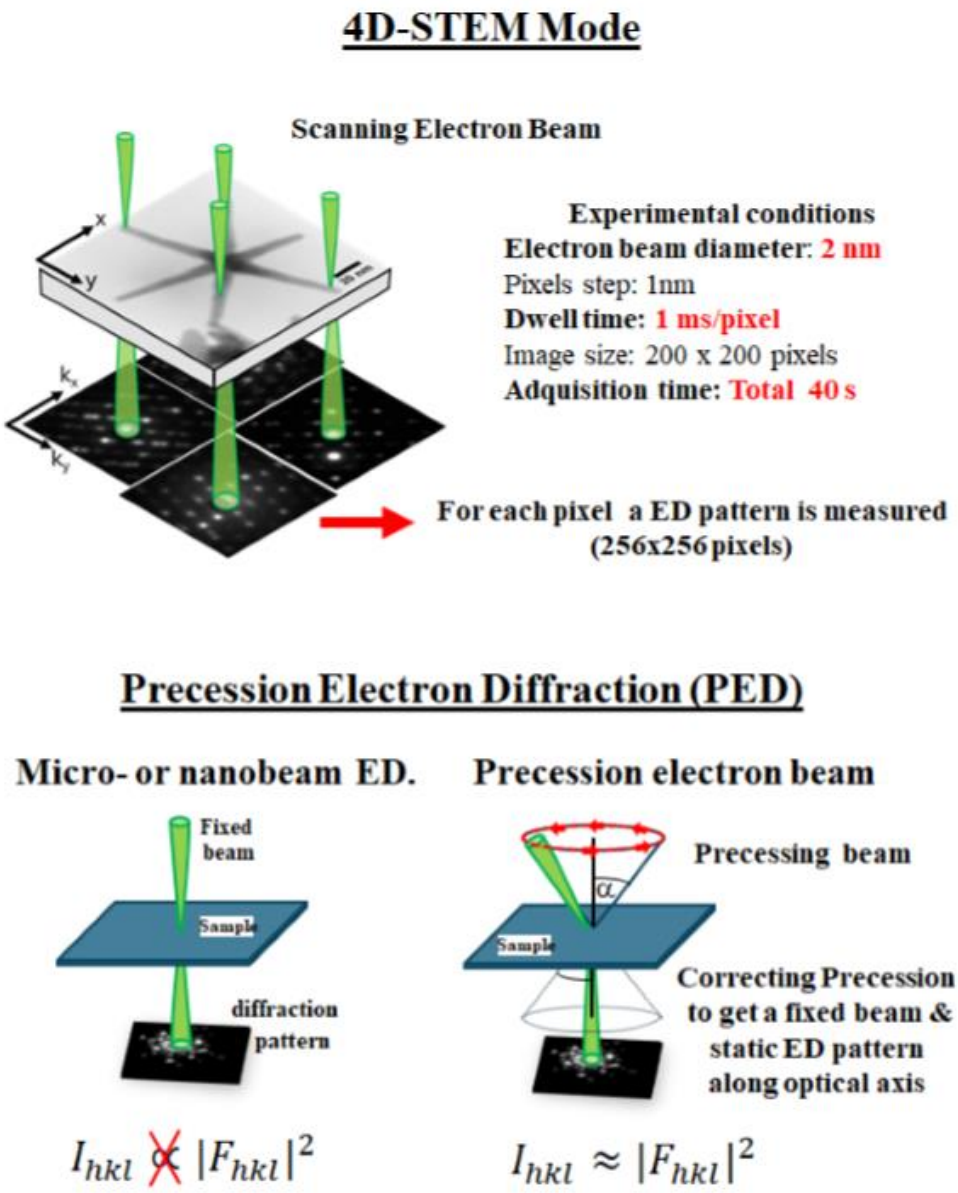

Figure S1. Scheme showing operational principles of 4D-STEM diffraction mapping (top) and comparison between fixed beam nano- or microdiffraction with precession electron diffraction (bottom).

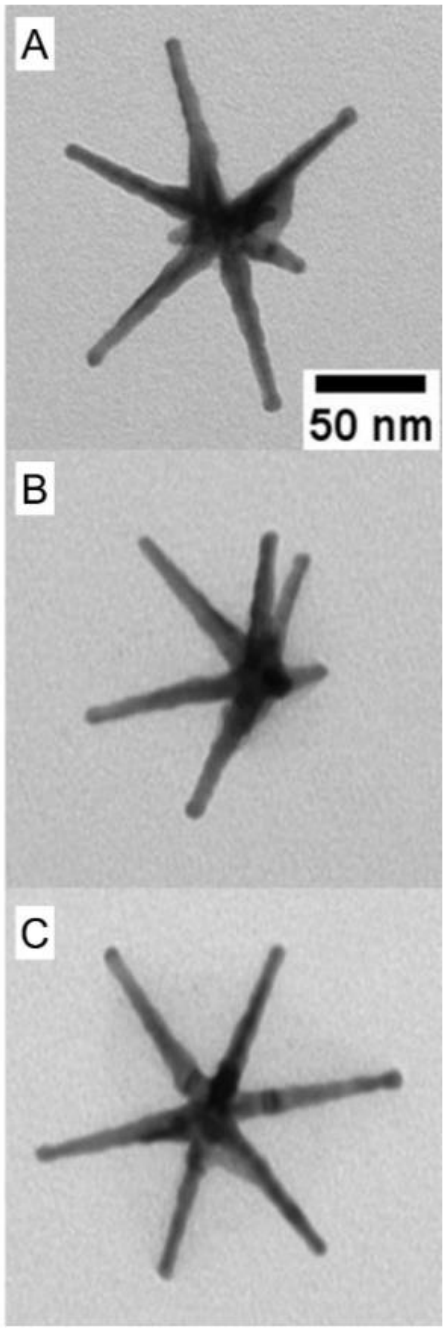

Figure S2. a-c) TEM micrographs showing a general view of 6-branched noble metal nanostar showing high aspect-ratio legs.

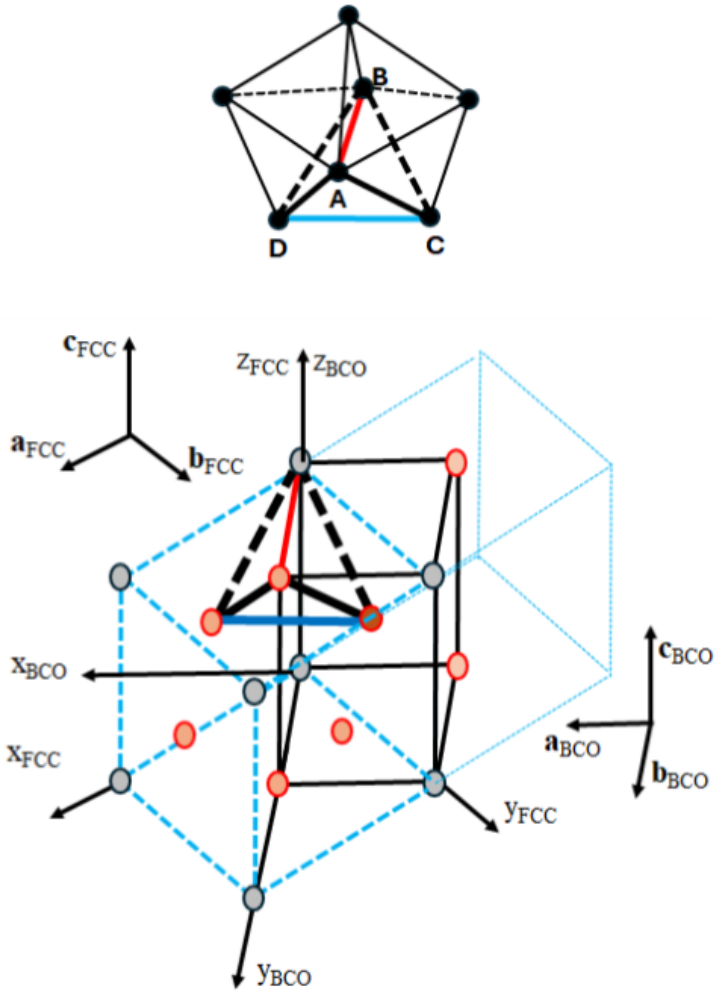

Figure S3. The atomic arrangement of decahedral particles may be described as the assembly of five tetrahedra along a common 5-fold axis. Face centered cubic (FCC) structure is the bulk atomic arrangement for noble metals, but filling space requirement induce an expansion of the DC distance to reach 72 degrees between triangles ABD and ABC. This expansion generates a body centered orthorhombic unit cell as described by Yang (16). The bottom part of the figures shows the geometrical relation between the FCC and BCO unit ells.

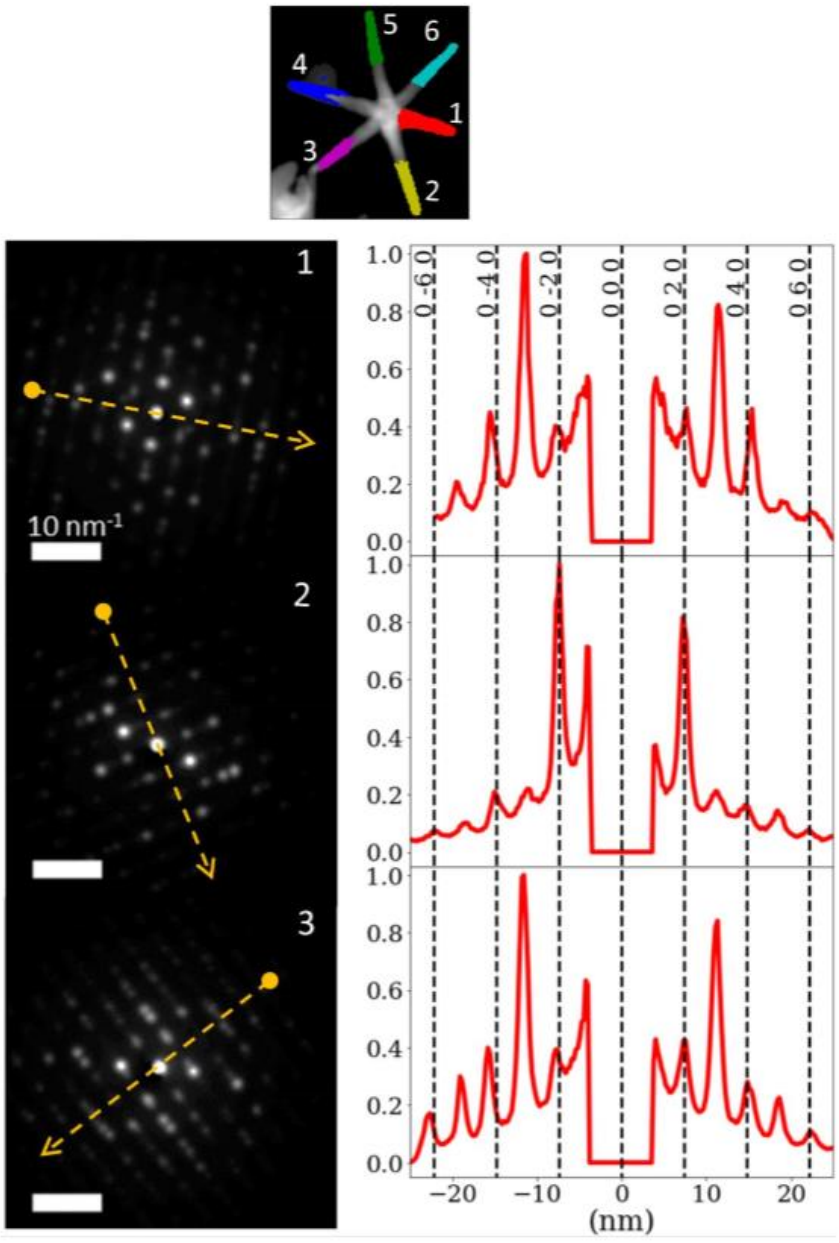

Figure S4a (continues next page). Top: Grouped pixels showing similar diffraction patterns clustered by the ML tool K-means (*17*) superimposed on the NS VDF. Below, we show, on the left side, the mean diffraction pattern calculated from region on LEG#1-6 respectively (arrows indicates leg axis on patterns and also the core to leg tip direction). On the right, we show the diffracted intensity profiles extracted along the arrows (left-to-right indicates core-tip direction). Scale bars are 10 1/nm.

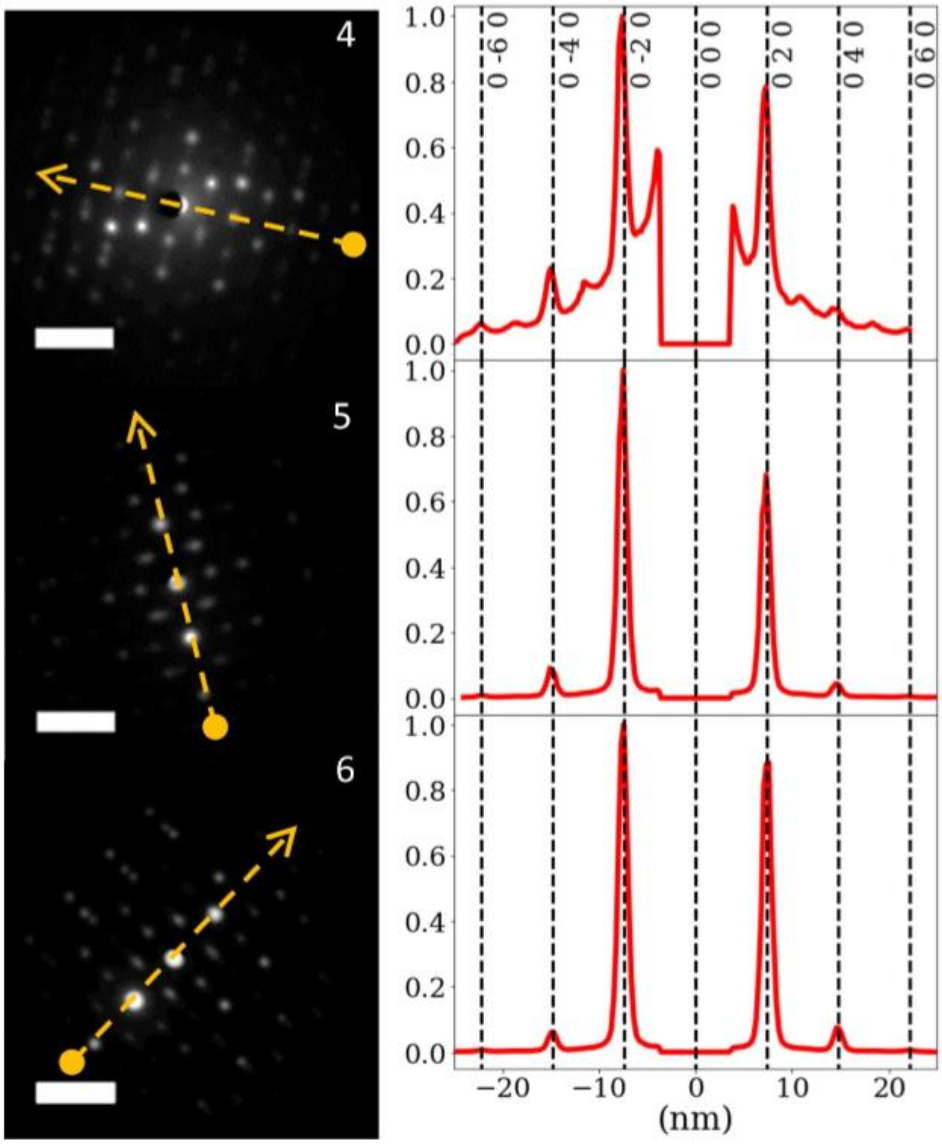

Figure S4b. Second page of Figure S4.

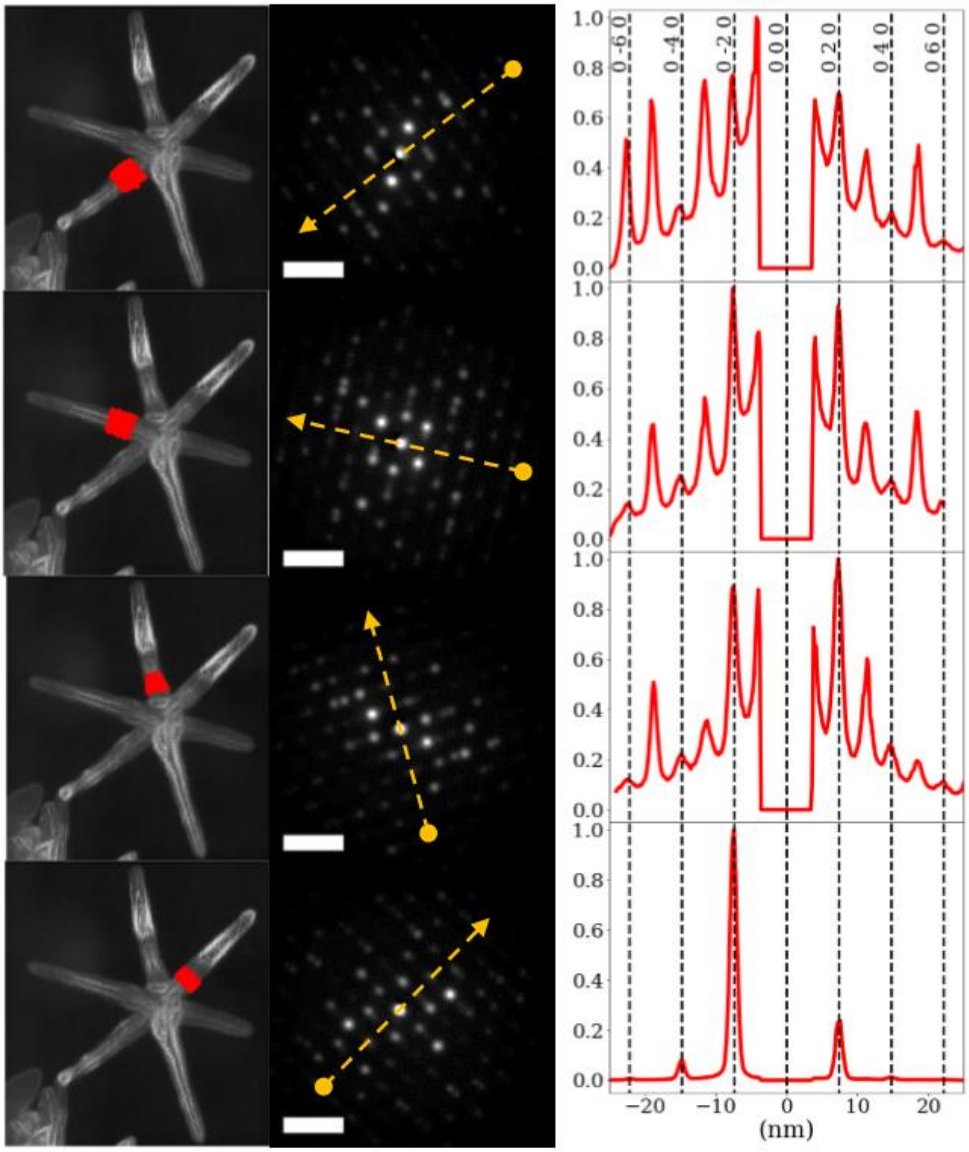

Figure S5. Mean diffraction patterns and diffracted intensity profiles (extracted along the arrows, left-to-right indicates core-tip direction). From manually selected pixel regions (leg bases) close to the NS core centre from on LEG#3-6. Scale bars are 10 1/nm.

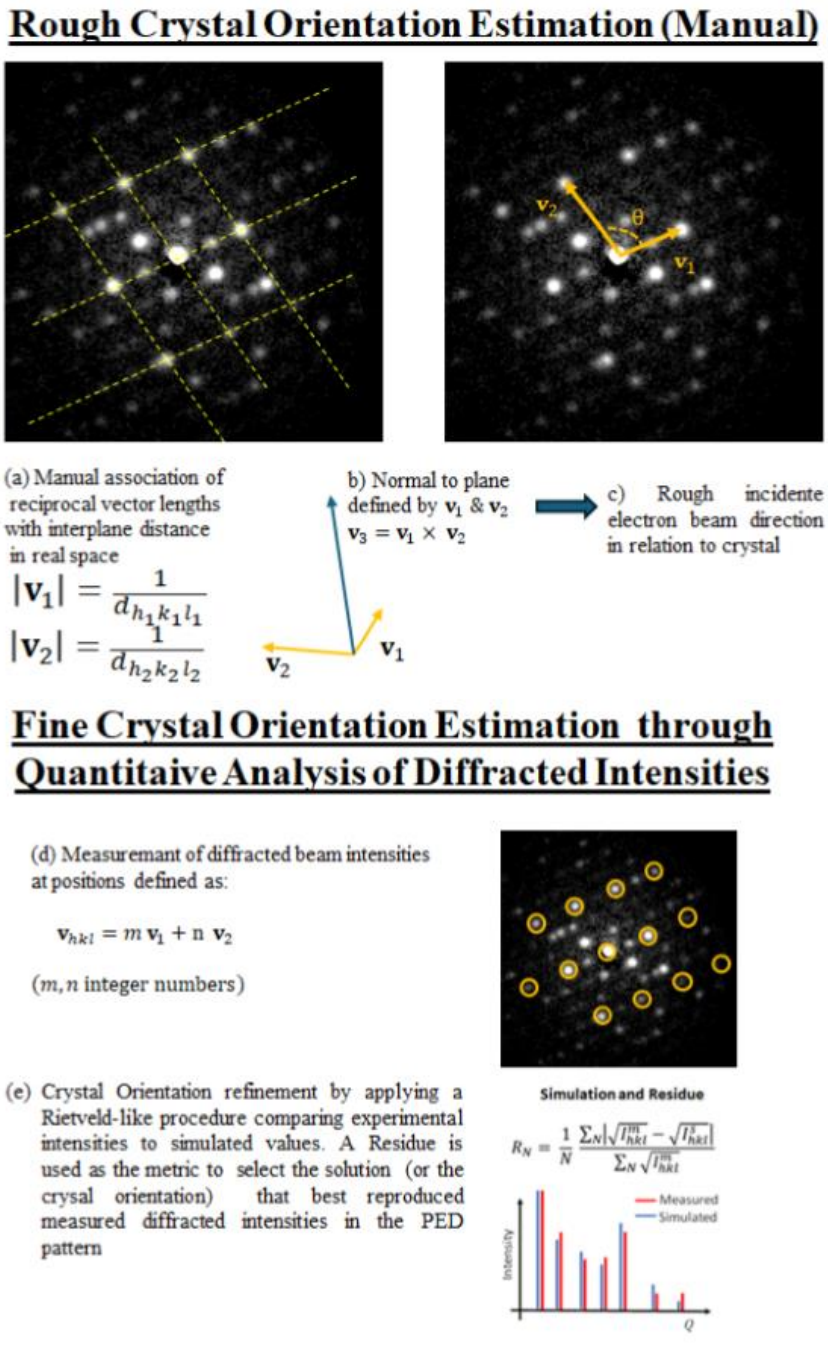

Figure S6. Top: Schematic representation of the manual identification of zone axis from a PED pattern. Bottom: procedure adopted to make a fine measurement of crystal orientation in relation to the incident electron beam, using the intensities from the diffraction spots obtained from the geometrical pattern identified by visual observation (top).

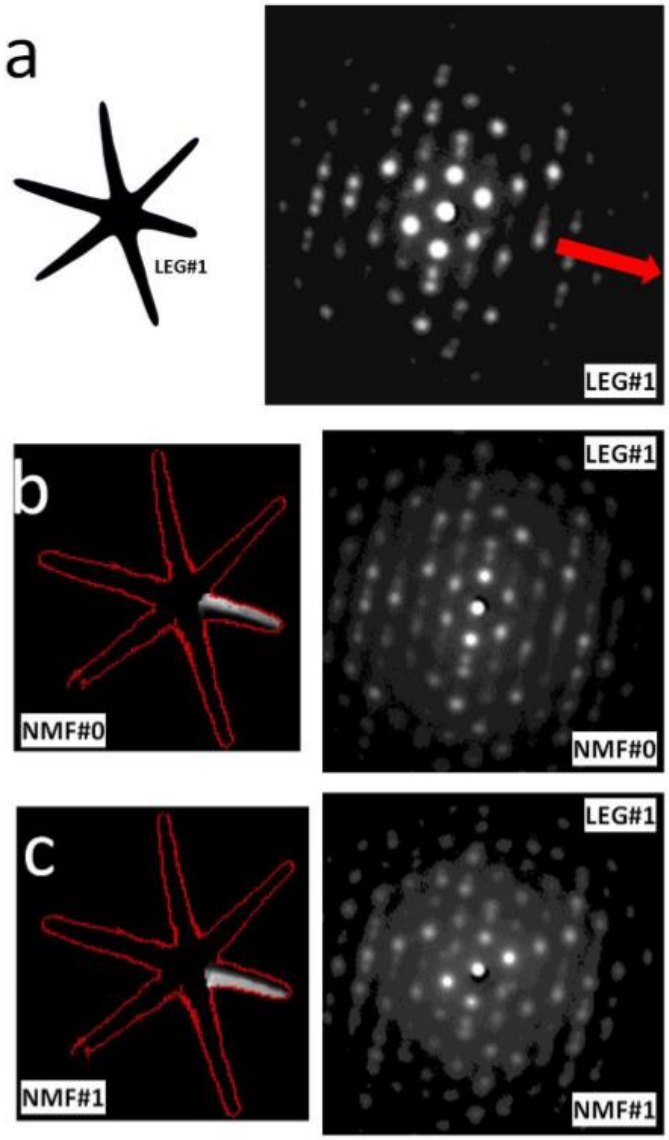

Figure S7. a) Mean diffraction pattern of LEG#1, where it is not possible to observe the peaks related to the decahedral axis $[010]_{BCO}$. Non-negative matrix factorization (NMF) has been applied to the data block formed by the LEG #1 diffraction patterns; only two components have been utilized to ensure the convergence of the method. b - c) The resulting ED patterns are very different, as well as their spatial arrangement. Notice a regular spot distribution is clearly easily recognized in component NMF#1(see details in Fig. S8).

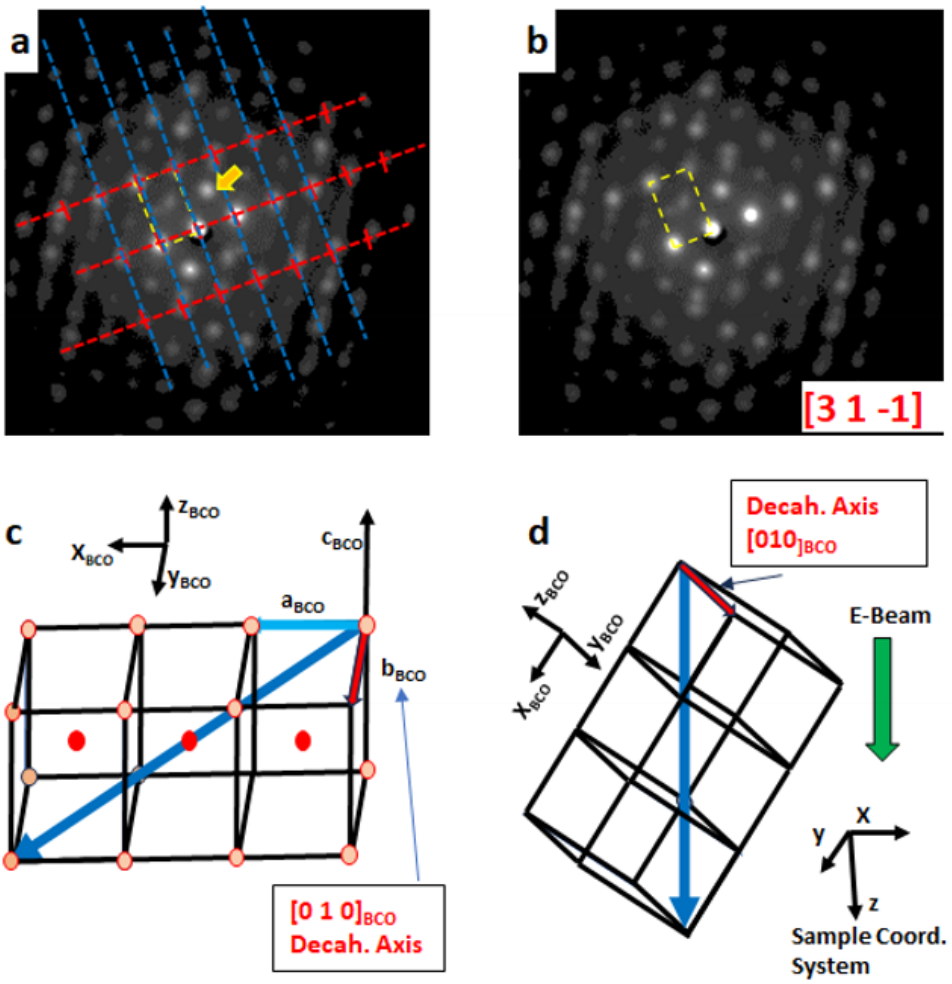

Figure S8. Analysis of ED pattern obtained as component NMF#1. a,b) A rectangular spot distribution is manually identified in this diffraction pattern, which can be indexed and a $[31\bar{1}]_{BCO}$ orientation along electron beam. c) Schematic drawing showing the identified direction in a BCO crystal; this figure also points out the expected direction of the decahedral leg ($[010]_{BCO}$). d) Deduced orientation of the leg crystal showing that the decahedral leg should point down at an elevation angle of ~17.3 degrees with the plane perpendicular to the electron beam direction. The arrow in (a) indicates a very intense diffraction spot that cannot be explained by a decahedral leg rotation of the identified BCO crystal around the leg axis to reproduce all decahedral sections of the leg. Therefore, this leg seems to be defective with a crystal in registry with the decahedral leg crystals; maybe the growth of this additional crystal may explain why this leg is slightly shorter than the other NS spikes.

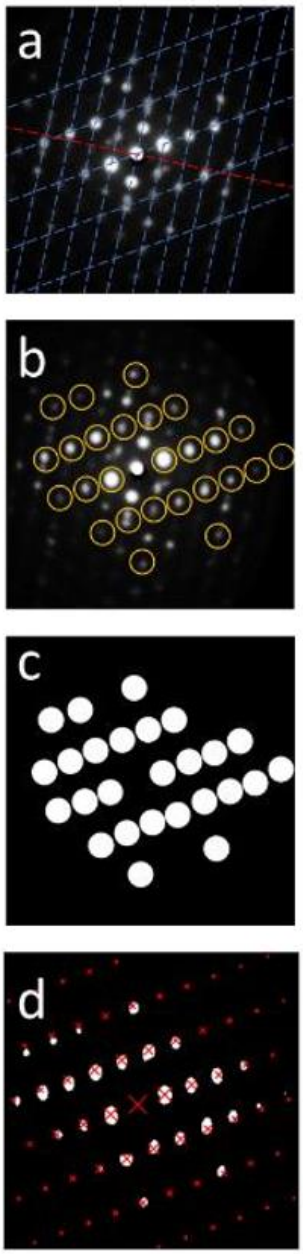

Figure S9. a) Manual identification of one of the zone axes contributing to LEG#1 after partial demixing using NMF tool. The grid represents the expected position of the peaks for a determined zone axis. b) Manual selection of the peaks for the formation of the mask in c). d) Resulting template-matching identification using Pyxem software (*17*), the crosses represent the position of the peaks for the template that best matches our data.

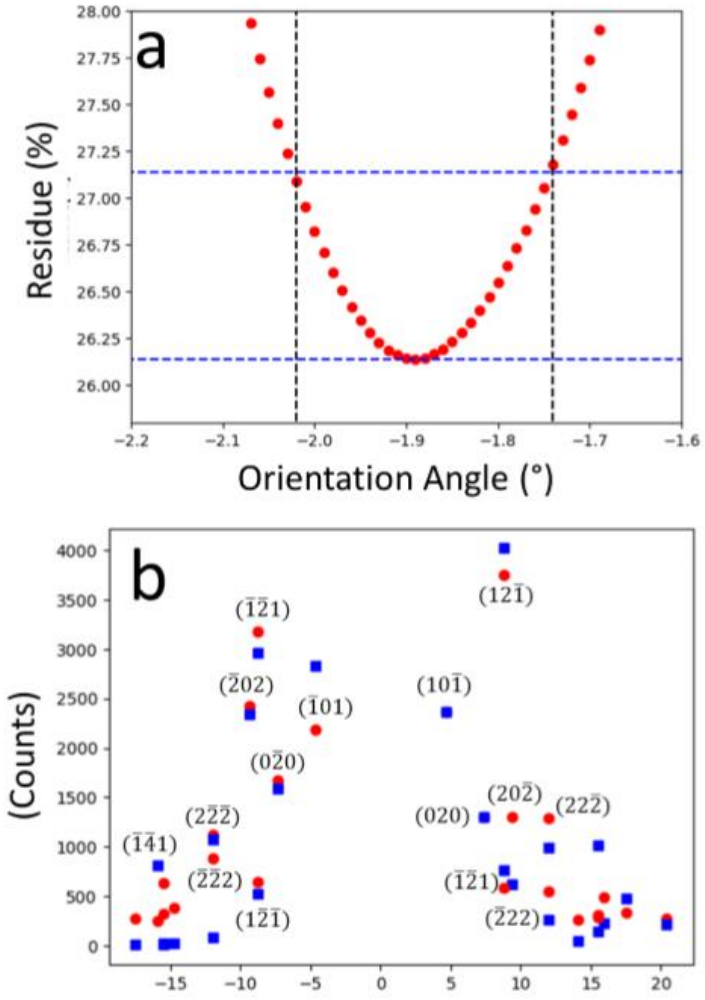

Figure S10. a) Sensitivity of the residue in relation to the elevation angle; the lines show the 1% change in residue in relation the minima. b) Comparison of the measures PED beams (circles) to the optimized values (squares).

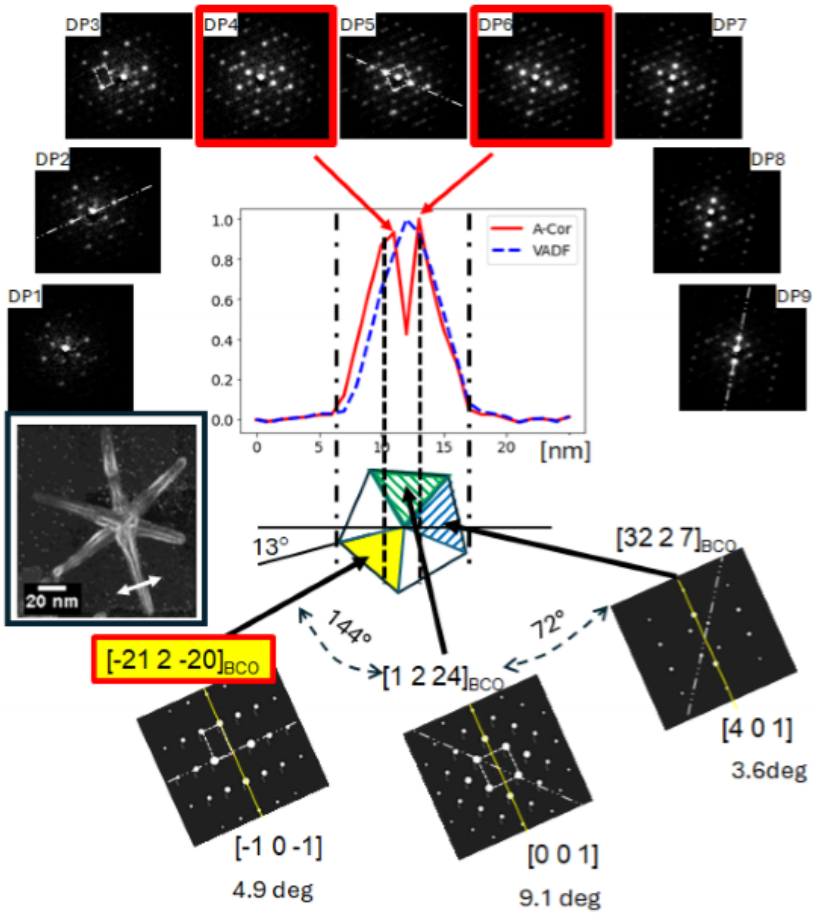

Figure S11. Analysis of diffraction patterns from individual pixels extracted along a line perpendicular to the tip of Leg#2 (see inset at the left of the figure). Top: individual diffraction patterns, note the clear changes of spots distribution from left to right; dashed lines in DP2, DP5 and DP9 provide a guide to identify the alignment direction of high intensity spots. Center: profiles of VADF and anti-correlation image intensity across Leg#2 at the same position than the DPs. Bottom: the orientation of this leg was measured from the region colored yellow at the lower left sector of the pentagonal schema (identified zone axis $[-21, 2, -20]_{BCO}$). If we rotate this crystal by 144 degrees clockwise (two 72 degrees rotation), the new zone axis is $[1,2,24]_{BCO}$; further 72 degrees rotation leaves the crystal at the $[32,2,7]_{BCO}$ zone axis. The bottom of the figure show electron diffraction patterns simulated using kinematical theory (ReciPro software (18)), and along low index zone axes close to the experimentally derived ones ($[-1,0, -1]_{BCO}$, $[0,0,1]_{BCO}$ and $[4,0,1]_{BCO}$). Their angular deviation from the directions identified from experiments at the top of the figure is indicated. The solid yellow line in simulated pattern indicates the $[0,1,0,]_{BCO}$ direction, which should be the decahedral structure axis, and dashed white lines indicate the line of high intensity spots in agreement with experimental measurements from individual pixels DPs. These simulations help to understand diffraction spots from the individual pixels, for example, the rectangular (square) geometrical distribution of spots in the simulated $[-1,0, -1]_{BCO}$ ($[0,0,1]_{BCO}$) patterns is clearly observed in DP3 (DP5). Finally, high intensity spots in DP7-DP9 are aligned close to a vertical line whose angle with the $[020]_{BCO}$ direction is ~35 degrees, as can be measured from the simulated patter along $[4,0,1]_{BCO}$ pattern. The very good agreement between experimental data and simulations provides a solid basis for the interpretation of the legs as decahedral wires.

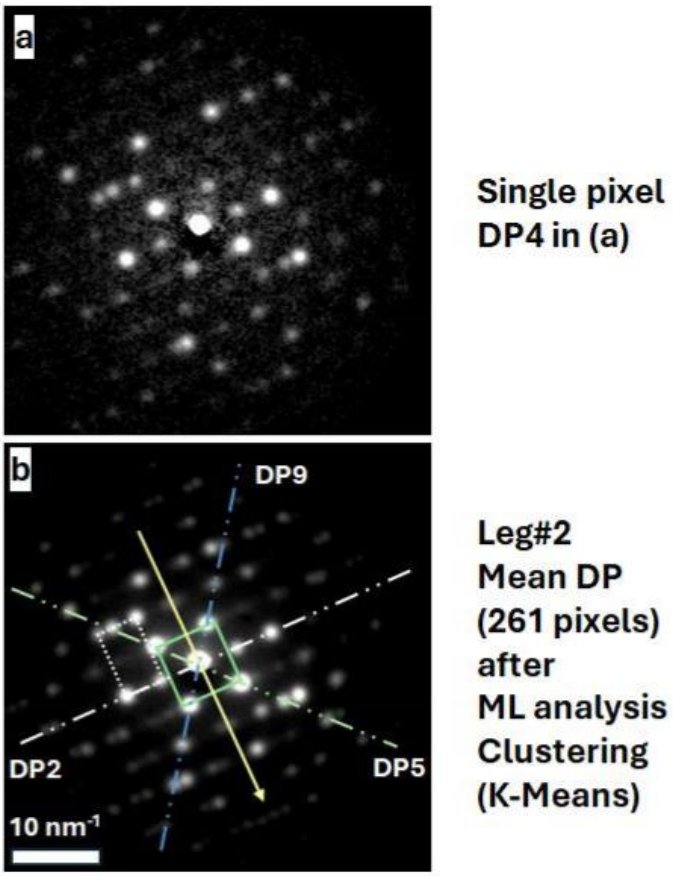

Figure S12. Comparison between the individual pixel diffraction pattern marked DP4 in (a) and the average diffraction pattern generated by ML tools in (K-Means for the tip of leg#2). The interpretation of this kind of patterns is rather complex because it is generated from the superposition of 5 different crystals from the decahedral leg. Dashed white lines indicate the direction of high intensity spots in (DP2, DP5 and DP9); the rectangular square distribution of spots as well as their orientation can be easily correlated with simulation in Fig. S11

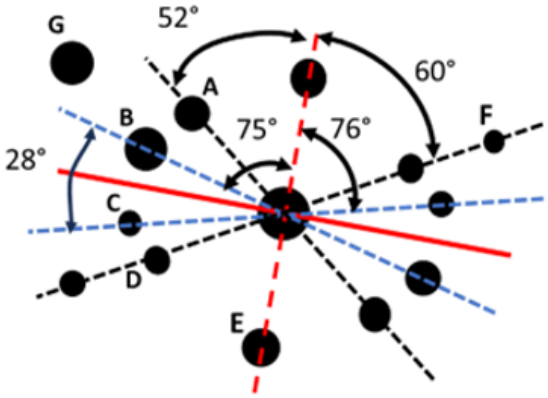

Real Space Distances

SPOTG	d_{hkl} [Å] (±0.05)
A	2.23
B	1.94
C	1.93
D	2.23
E	2.23
F	1.42
G	1.17

Figure S13. A schematic draw of the mean diffraction pattern from NS central region derived from diffraction spots from the mean diffraction pattern from the core (4D-STEM pixels at a radial distance < 10 nm). Measured values of angles between diffraction peaks and the correspondent real space distances are shown.

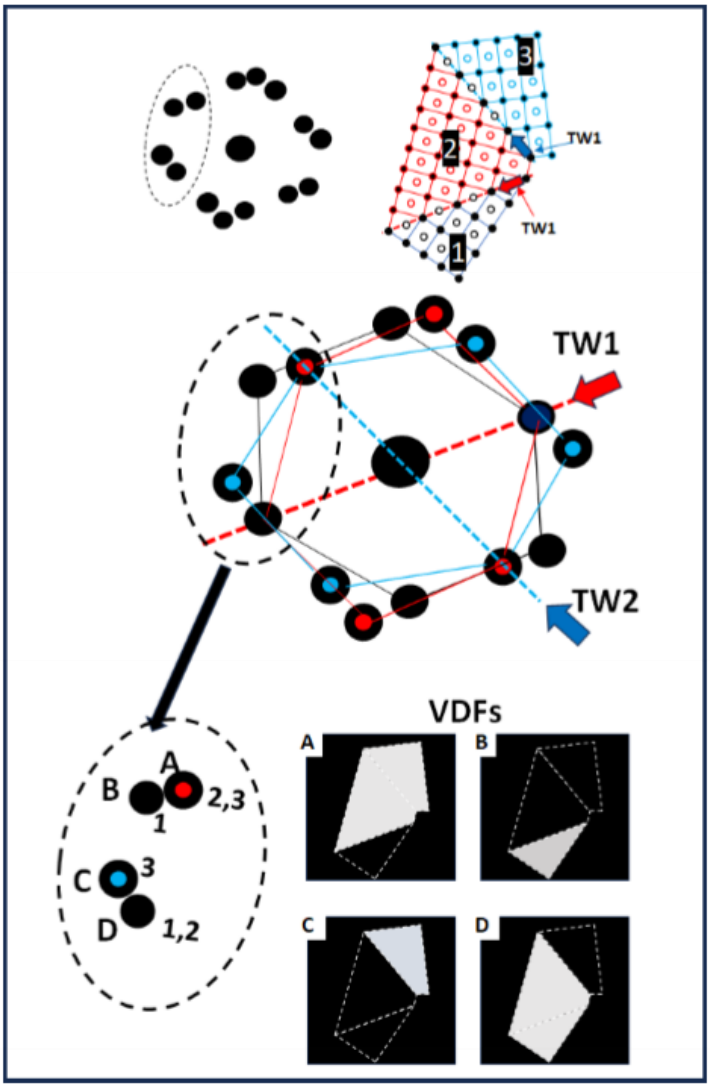

Figure S14. A schematic illustration showing the expected SAED pattern generated from face-centred-cubic (FCC) lattice oriented along [110] axis including three crystals (1-3) connected by two mirror twins (TW1 and TW2). A simple analysis of the diffraction pattern allows the identification of twin positions and the correlation between crystal number (bottom part of the figure) and diffracted spot (see Figures 9.3 and 9.4 from pages 524 and 525 from book by Graef (19)). For example, a VDF generated by spot A should show crystal #2 and #3, while a VDF from spot C must only show crystal #3. Then, we can use a series of VDF images displayed in Fig. 3 exclude the twinned FCC crystal occurrence.

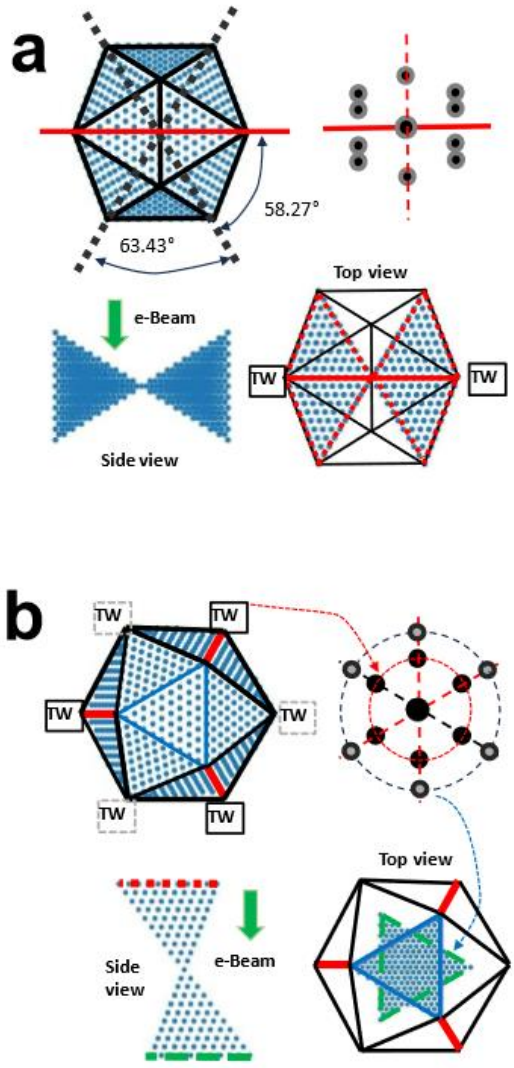

Figure S15. Schematic drawing of the structural aspects associated to ICO particles oriented along 2-fold and 3-fold axes including projection images (top- and side-views) and diffraction patterns. a) Along the 2-fold axis, the ICO ED appears to be a twinned crystal, because groups 2 tetrahedra at each side of the ICO are oriented on zone axis. Along the 3-fold axis (shown in (b)), the diffraction pattern shows an apparent 6-fold symmetry where two different families of spots (or arising from different crystal) are perfectly aligned to each other. The inner ED spots are associated to 6 twins that become parallel to the electron beam; the larger circle of diffraction spots (or shorter real space distances) is associated to two tetrahedra located at the centre of the ICO image whose $(111)_{RHO}$ facets are perpendicular to the incident direction.

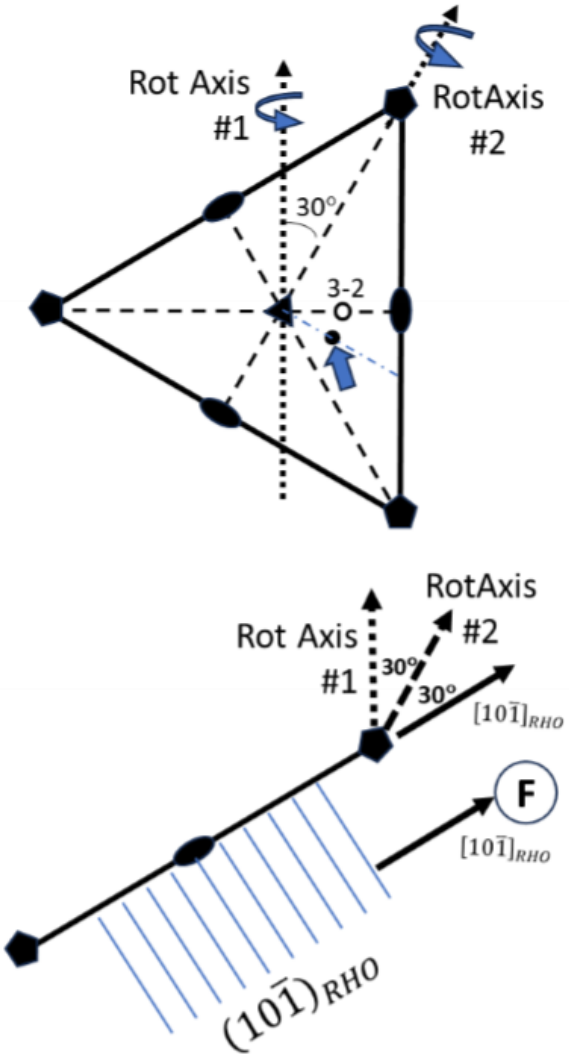

Figure S16 A schematic drawing indicating high symmetry axes of the icosahedra by observing a regular triangular facet. Axes with 5-fold symmetry are located at facet corners, 3-fold axes at the triangle centre, and 2-fold axes are located at the centre of edges. Just by rotating the particle around the vector noted Axis#1, we can move between the three types of axes. The intermediate direction between a 2-fold and 3-fold axis (noted 32, 10.5 degrees from both axes). To preserve a good orientation of planes generating the diffraction spot marked F, the ICO must be rotated along their normal (or the reciprocal vector $[101]_{RHO}$, see lower part of the figure). This axis is located at 60 degrees from Axis#1, and a rotation around this axis will strongly diminish the influence of the 2-fold axis in the final ICO diffraction pattern, in contrast with experiments. We have explored the crystallographic characteristic of an ICO particle rotated around an axis (Axis#2) at an intermediate position between Axis#1 and $[101]_{RHO}$. This orientation (arrowed in the drawing) will be called ICO32D, to note a deviation for the intermediate position between ICO2 and ICO3.

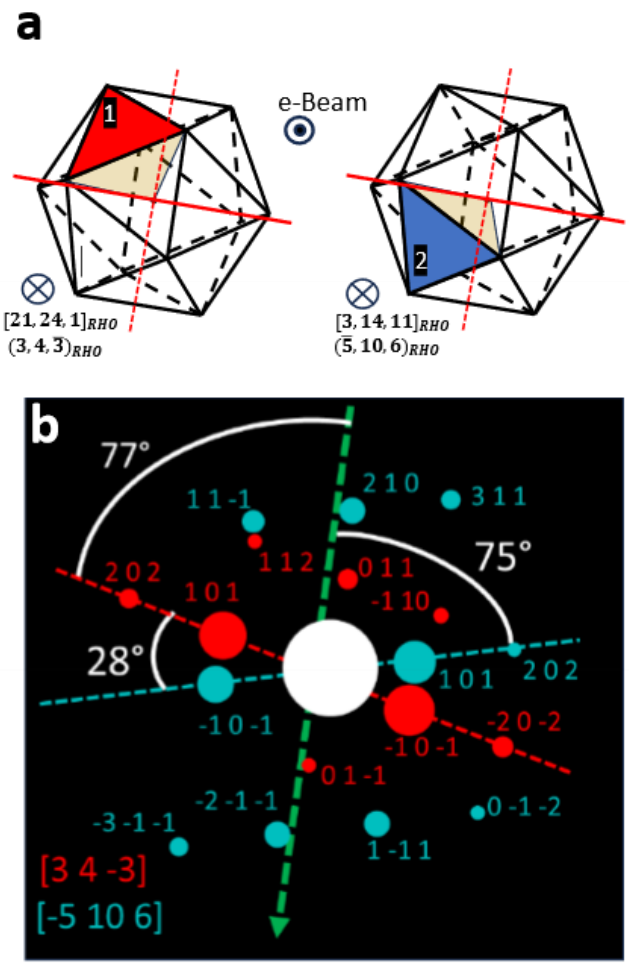

Figure S17. a) The expected orientation of the core in between the ICO23D direction which implies that the tetrahedron marked #1 is oriented along the [21 24 1]$_{RHO}$ direction in real space ([3 4 -3]$_{RHO}$ in reciprocal space. Simultaneously, tetrahedron #2 is oriented along the [3 14 11]$_{RHO}$ direction in real space ([-5 10 6]$_{RHO}$ in reciprocal space). Kinematical simulation of the rhombohedral lattice oriented along [3 4 -3]$_{RHO}$ and [-5 10 6]$_{RHO}$ zone axis obtained with ReciPro software (*18*). Notice that peaks along the [101]$_{RHO}$ directions are dominant in both zone axis, with an angle of ~75° with the *y* direction (defined as the normal to twin plane perfectly oriented when ICO is oriented along ICO32 direction). The intensities of the [3 4 -3$_{RHO}$ are higher than the ones for the [-5 10 6]$_{RHO}$, as predicted for the model orientation (see Fig. S16) and in agreement with the experiment (see Figure 3 and S13).

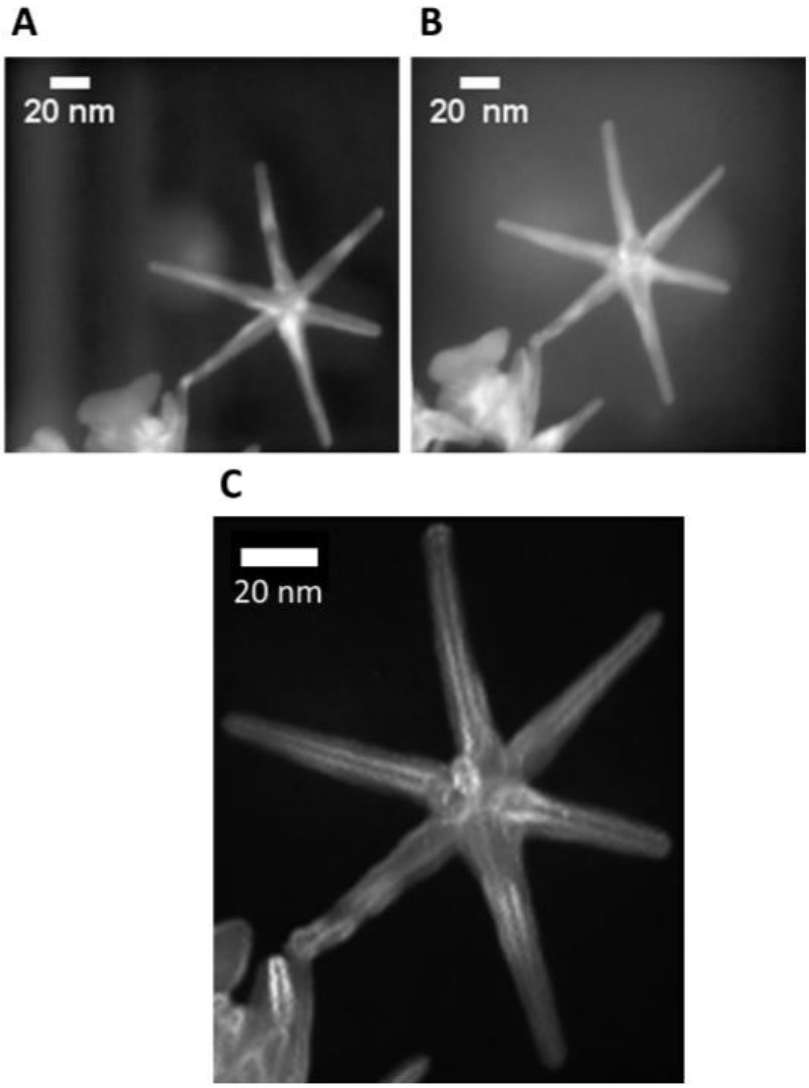

Figure S18. VADF of the nanostar: a) 0 degrees and b) 10 degrees dataset. Notice that the image in (b) shows an increased background intensity due to a-C contamination. c) Anti-correlation image of the nanostar from the 10 degrees data set, where the polycrystalline nature of the legs is clearly evident (bright lines along legs indicate twin positions), implying that the decahedral atomic arrangement of the thin high-aspect ratio legs has been preserved after data acquisition.

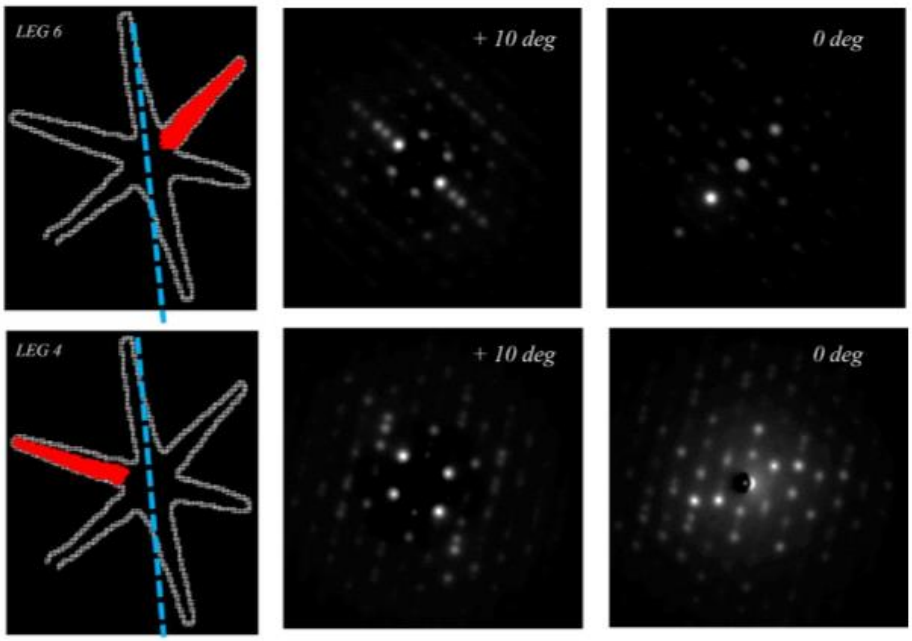

Figure S19: Legs 4 (upper) and 6 (lower) after a sample rotation of +10 degrees using the TEM goniometer (nominal value). The +10 degrees dataset has been analysed with the same procedure previously described. A clustering procedure has been capable of differentiating and isolating each leg (the left image shows the clustered regions for legs 4 and 6). The mean diffraction patterns of each leg changes significatively after rotation.

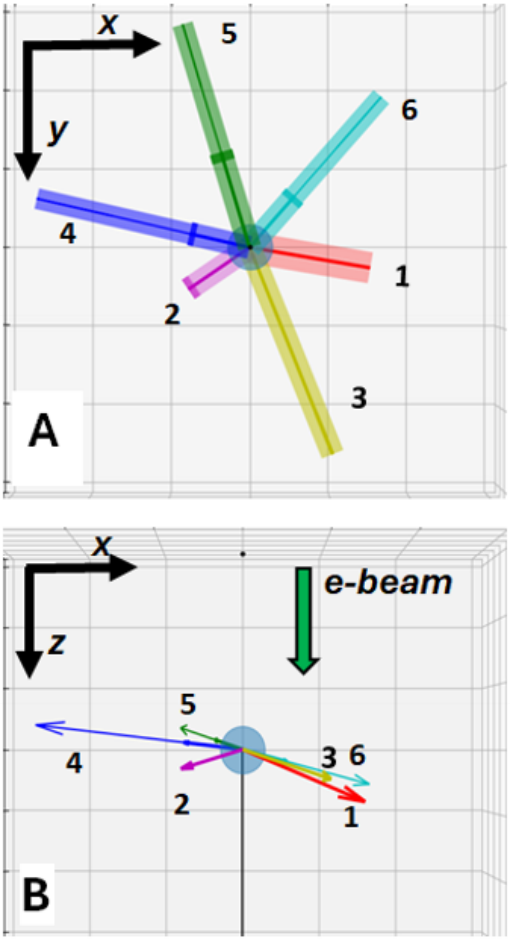

Figure S20: Nanostar 3D reconstruction for the tilted data (10 degrees). Legs#4 and 6 orientations have been measured with the PED intensity analysis, Legs#2, #3, #5 have utilized only the template-matching analysis and leg 1 has utilized only manual indexation. The angular resolution of Legs#1, 2, 3, 5 is significantly affected in relation to Leg# 4 & 6, but the legs are still restricted to a tilted plane, as expected for a planar leg distribution.

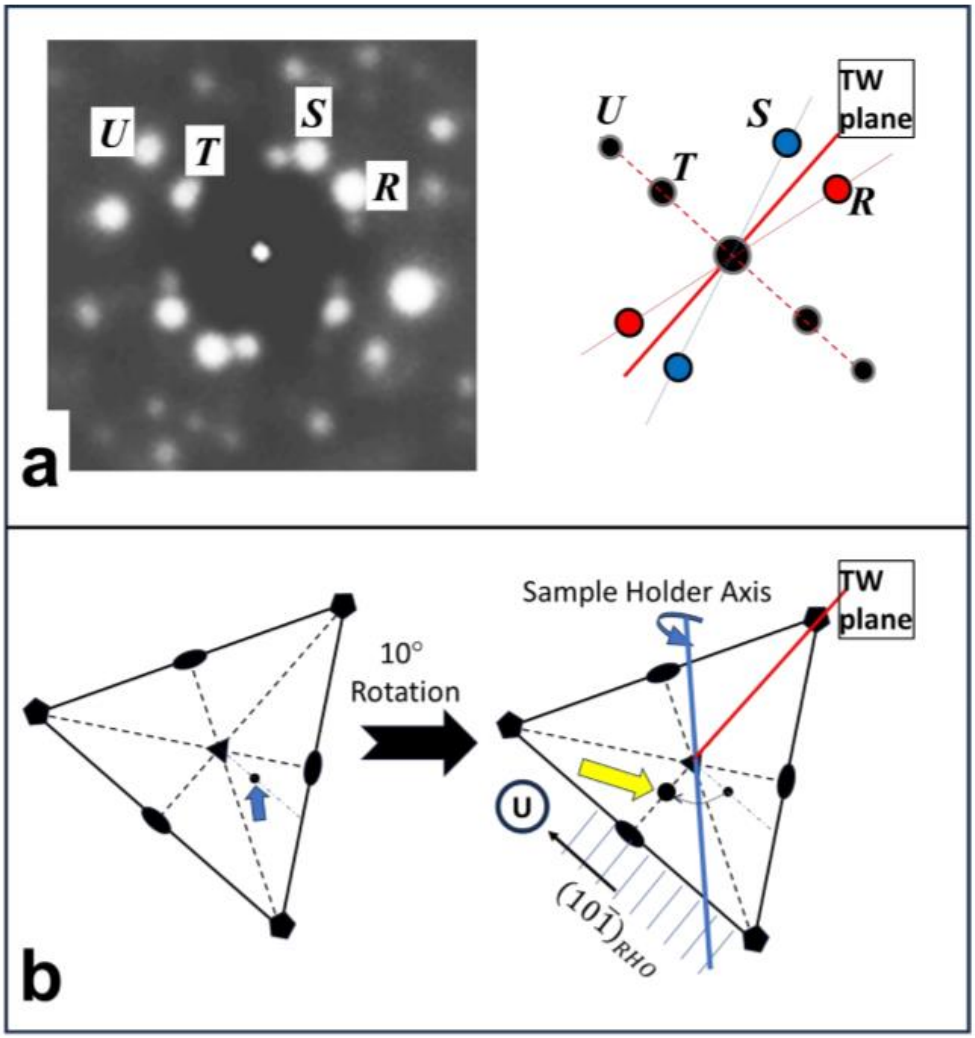

Figure S21. a) Measured PED pattern for the core of the NS for the 10 degrees dataset. b) Orientation of the NS core in relation to the ICO symmetry sites for the 0 degrees (left) and 10 degrees (right) datasets. The circle represents the estimated orientation (arrowed), ellipses the 2-fold symmetry sites, triangles the 3-fold sites and pentagon the 5-fold sites.

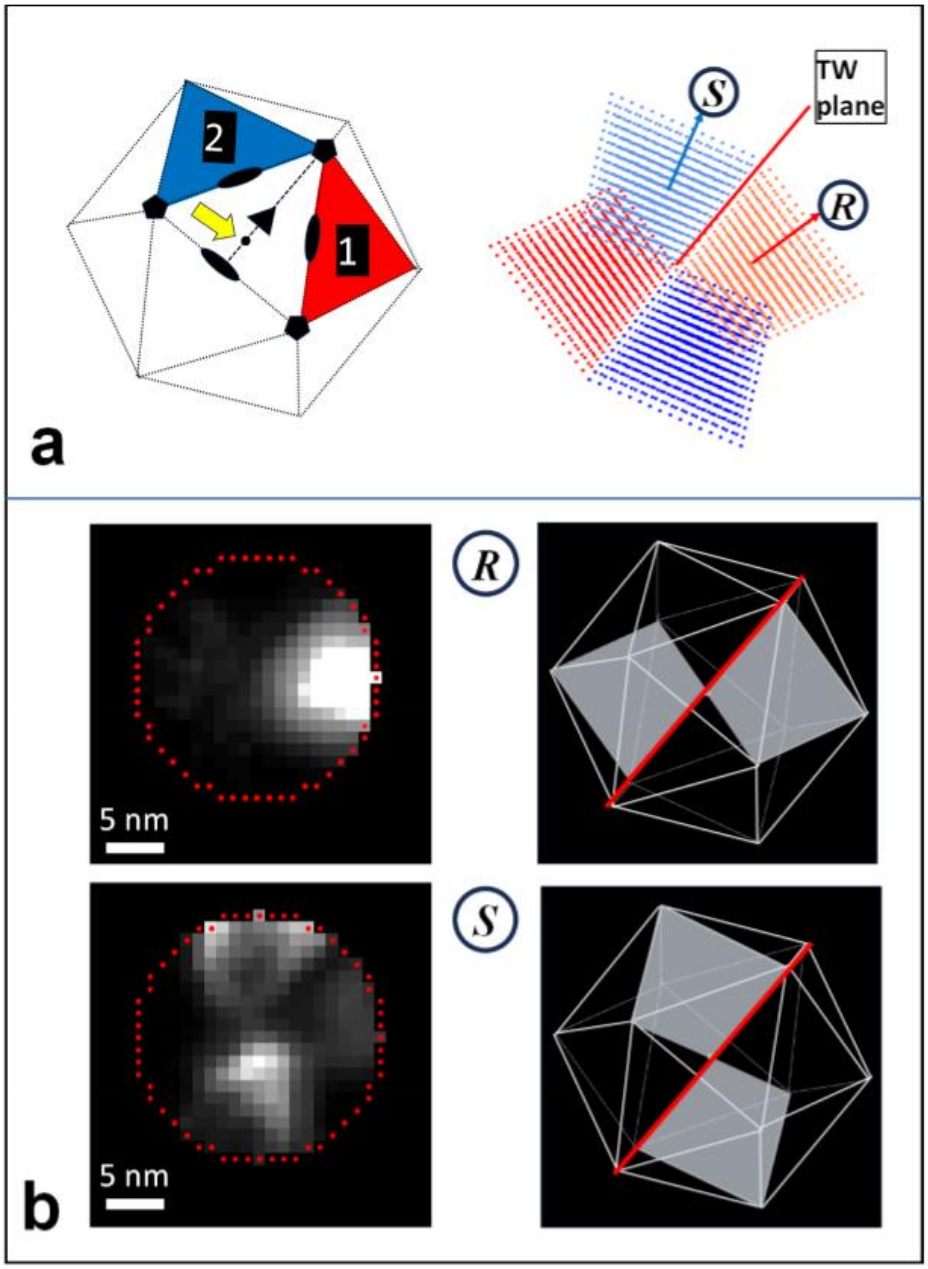

Figure S22. A) deduced orientation of the NS icosahedral core after the +10 degrees rotation; in this configuration two pairs of tetrahedra show atomic planes oriented along the electron beam direction. These planes should generate diffraction spots (*S* and *R*) of identical intensity, in full agreement with experimental data. b) Comparison of experimental and expected VDF images for diffracted beam *S* and *R*, that again show an excellent agreement.

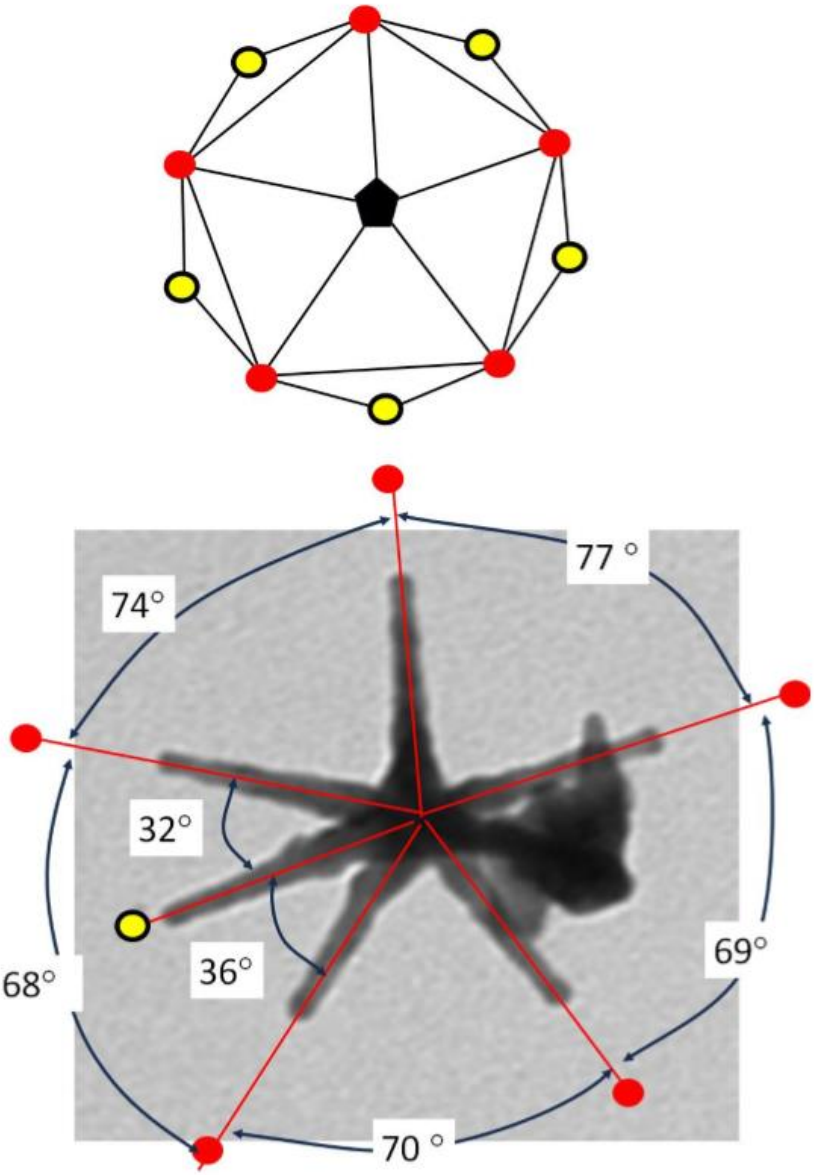

Figure S23. Image of a NS showing an ensemble of legs displaying a 5-fold symmetry distribution (marked with red disks). A 6th leg (marked with a yellow disk) is located close to the bisecting angle between legs (left lower region); this 6th leg must be growing from an icosahedral apex located along the second stacked decahedron of the icosahedral NS core (see schematic drawing included at the top).

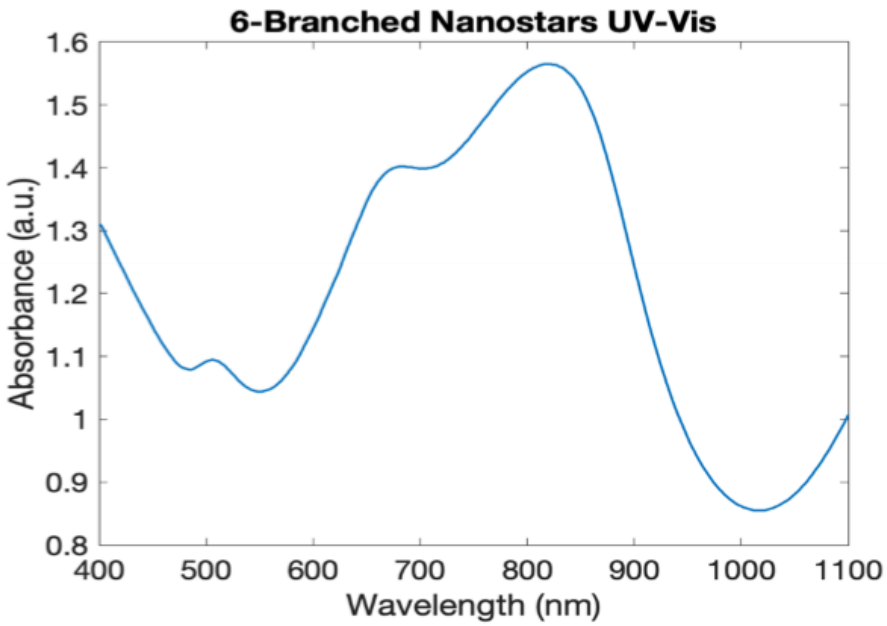

Figure S24. a) UV-Vis-NIR spectra of the 6-legs noble metal NS sample. The resulting UV-Vis-NIR spectra is characterized by prominent LSPR modes at 670 nm and 830 nm in this wavelength range.

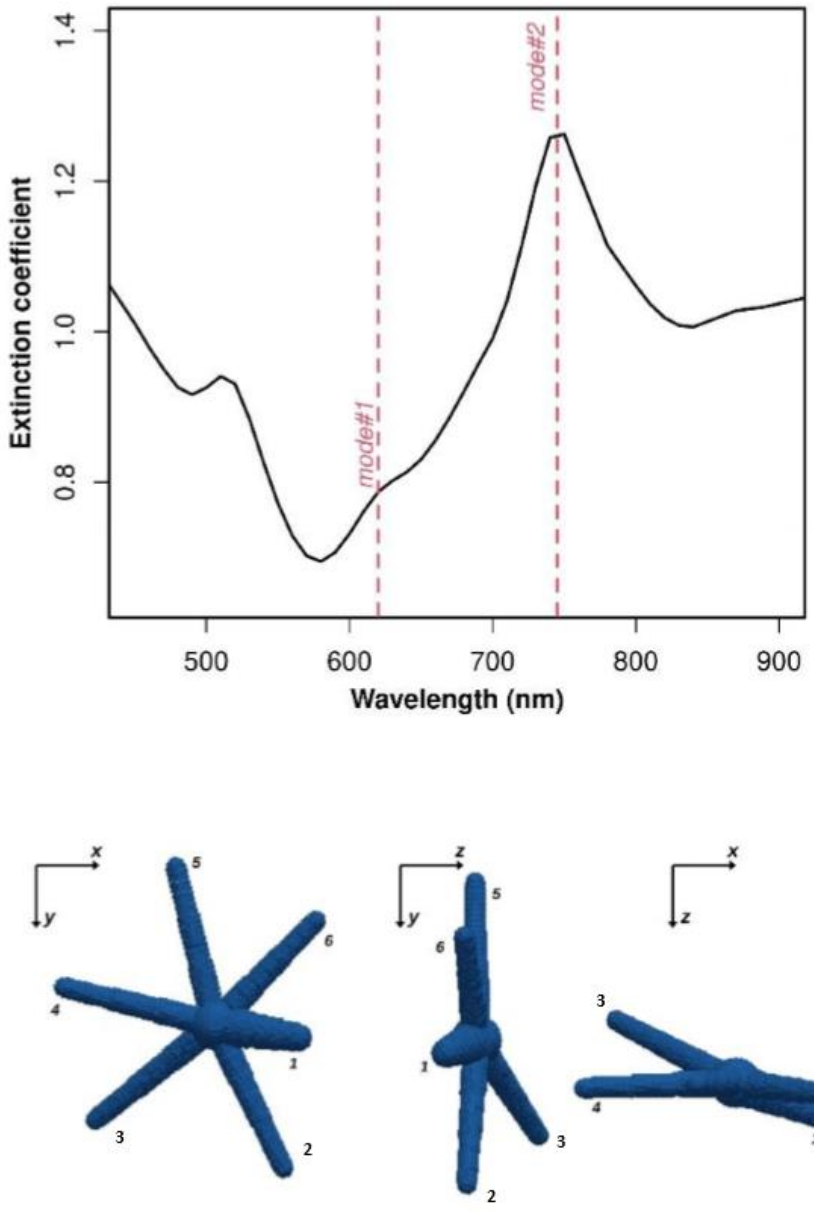

Figure S25. Top: DDA simulated extinction spectra for the measured nanostar 3D morphology. Bottom DDA simulated nanoparticle shape presented by three orientations, axis representation and leg numbering as used in Figure 1.

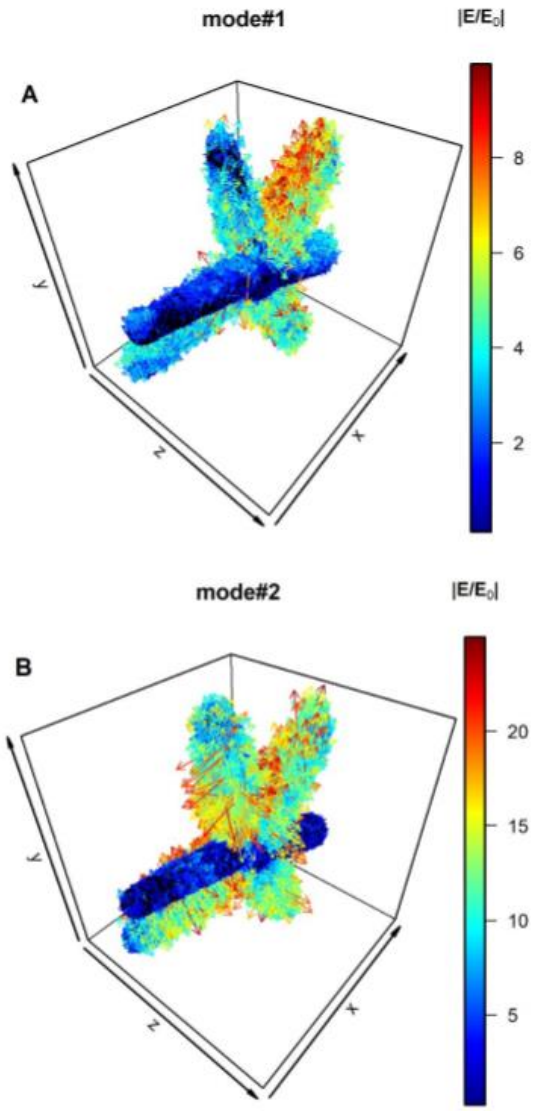

Figure S26. Polarization vectors representation in terms of the real part of the electric field at the dipole positions for mode#1 (A) and mode#2 (B). Colors represent the electric field enhancement.

References

1. C. B. Carter, D. B. Williams, Eds., *Transmission Electron Microscopy* (Springer International Publishing, Cham, 2016).

2. J. M. Zuo; J. C. H. Spence; *Advanced Transmission Electron Microscopy* (Springer New York, New York, NY, 2017).

3. E. J. Kirkland, *Advanced Computing in Electron Microscopy* (Springer International Publishing, Cham, 2020).

4. Vincent, R.; Midgley P. A. Double Conical Beam-Rocking System for Measurement of Integrated Electron Diffraction Intensities. Ultramicroscopy 1994, 53, 271–282.

5. Rauch, E. F.; Portillo, J.; Nicolopoulos, S.; Bultreys, D.; Rouvimov, S.; Moeck, P. Automated Nanocrystal Orientation and Phase Mapping in the Transmission Electron Microscope on the Basis of Precession Electron Diffraction. Z. Kristallogr. 2010, 225 (2–3), 103–109.

6. Midgley, P. A.; Eggeman, A. S. Precession Electron Diffraction – A Topical Review. IUCrJ 2015, 2, 126–136.

7. P. Oleynikov, S. Hovmöller, X. D. Zou, Precession electron diffraction: Observed and calculated intensities. *Ultramicroscopy* **107**, 523–533 (2007).

8. Own, C. S.; Marks, L. D.; Sinkler, W. Precession electron diffraction 1: multislice simulation. *Acta Crystallogr. A Found. Crystallogr.* **2006**, 62, 434–443.

9. Cautaerts, N.; Crout, P.; Ånes, H. W.; Prestat, E.; Jeong, J.; Dehm, G.; Liebscher, C. H. Free, Flexible and Fast: Orientation Mapping Using the Multi-Core and GPU-Accelerated Template Matching Capabilities in the Python-Based Open Source 4D-STEM Analysis Toolbox Pyxem. Ultramicroscopy 2022, 237, 113517.

10. Ophus, C.; Zeltmann, S. E.; Bruefach, A.; Rakowski, A.; Savitzky, B. H.; Minor, A. M.; Scott, M. C. Automated Crystal Orientation Mapping in py4DSTEM Using Sparse Correlation Matching. Microsc Microanal 2022, 28 (2), 390–403.

11. Corrêa, L. M.; Ortega, E.; Ponce, A.; Cotta, M. A.; Ugarte D. High Precision Orientation Mapping from 4D-STEM Precession Electron Diffraction Data Through Quantitative Analysis of Diffracted Intensities. Ultramicroscopy 2024, 259, 113927.

12. Palatinus, L.; Brázda, P.; Jelínek, M.; Hrdá, J.; Steciuk, G.; Klementová, M. Specifics of the Data Processing of Precession Electron Diffraction Tomography Data and Their Implementation in the Program PETS2.0. Acta Crystallogr. B Struct. Sci. Cryst. Eng. Mater. 2019, 75 (4), 512–522.

13. Eggeman, A. S.; Krakow, R.; Midgley, P. A. Scanning Precession Electron Tomography for Three-Dimensional Nanoscale Orientation Imaging and Crystallographic Analysis. Nat. Commun. 2015, 6, 7267.

14. M. De Graef, *Introduction to Conventional Transmission Electron Microscopy* (Cambridge University Press, ed. 1, 2003)

15. Gallinet, B.; Butet, J.; Martin, O. J. F. Numerical Methods for Nanophotonics: Standard Problems and Future Challenges. Laser Photonics Rev. 2015, 9, 577–603.

16. Yang, C. Y. Crystallography of Decahedral and Icosahedral Particles. J. Cryst. Growth 1979, 47, 274–282.

17. Francisco de la Peña; Eric Prestat; Vidar Tonaas Fauske; Pierre Burdet; Jonas Lähnemann; Petras Jokubauskas; Tom Furnival; Carter Francis; Magnus Nord; Tomas Ostasevicius; Katherine E. MacArthur; Duncan N. Johnstone; Mike Sarahan; Joshua Taillon; Thomas Aarholt; pquinn-dls; Vadim Migunov; Alberto Eljarrat; Jan Caron; T. Nemoto; Timothy Poon; Stefano Mazzucco; actions-user; Nicolas Tappy; Niels

Cautaerts; Suhas Somnath; Tom Slater; Michael Walls; pietsjoh; Hugh Ramsden. Hyperspy/Hyperspy: V2.0.1, 2024. https://doi.org/10.5281/ZENODO.10709941.

18. Seto, Y.; Ohtsuka, M. ReciPro: Free and Open-Source Multipurpose Crystallographic Software Integrating a Crystal Model Database and Viewer, Diffraction and Microscopy Simulators, and Diffraction Data Analysis Tools. *J. Appl. Crystallogr.* **2022**, 55, 397–410.

19. De Graef, M. & McHenry, M. E. Structure of Materials: *An Introduction to Crystallography, Diffraction and Symmetry*; Cambridge University Press, Cambridge, 2012.

Apêndice G

Artigo da Metodologia Desenvolvida para PED + ePDF

A seguir está anexado o artigo intitulado "*Quantitative Structural Analysis of AuAg Nanoparticles Using a Pair Distribution Function Based on Precession Electron Diffraction: Implications for Catalysis*", publicado em 2021 na revista ACS Applied Nano Materials: ACS Appl. Nano. Mater. 2021, 4, 12541-12551. Os diretos do artigo pertencem a American Chemical Society, que permite aos autores a reprodução do artigo em teses e coleções, sobre as condições expostas em: https://pubs.acs.org/page/copyright/journals/posting_policies.html, na seção "*Reuse/Republication of the Entire Work in Theses or Collections"*.

ACS APPLIED NANO MATERIALS

www.acsanm.org Article

Quantitative Structural Analysis of AuAg Nanoparticles Using a Pair Distribution Function Based on Precession Electron Diffraction: Implications for Catalysis

Leonardo M. Corrêa, Murilo Moreira, Varlei Rodrigues, and Daniel Ugarte*

Cite This: *ACS Appl. Nano Mater.* 2021, 4, 12541−12551 Read Online

ACCESS | Metrics & More | Article Recommendations | Supporting Information

ABSTRACT: Nanostructured materials and nanoparticles (NPs) probably represent the most promising system to develop technological applications and devices. The atomic arrangement of nanosystems can be quite different from the corresponding bulk material; the access to reliable and quantitative structural characterization tools for this size regime is still an open issue. Transmission electron microscopy (TEM) results are many times qualitative and hardly fulfill the requirement for quantitative statistics. This is particularly critical for many nanocatalysts displaying polycrystalline agglomerated NPs with significant size dispersion. Herein, we report a method for structural refinement and quantitative analysis of nanomaterial atomic arrangement based on an electron pair distribution function (ePDF) derived from precession electron diffraction (PED) patterns. We have shown that a high-quality and reliable structural refinement, whose residue values (∼15%) are similar to synchrotron-based nanosystem studies, can be obtained from catalyst complex nanostructure samples using a low-profile LaB_6-gun TEM. The mass of the sample used in our experiment is extremely small, below the picogram range, and the measurements required a total electron dose of ∼10 $e^-/Å^2$; this indicates that the ePDF displays a huge potentiality to analyze quantitatively beam-sensitive materials. Although a complex sample and sophisticated simulation, including size dispersion, the number of free fitting parameters was kept to a rather low value (only 3), guaranteeing that the low-residue values are realistic, accurate, and not an effect of overfitting. Our results show that a PED-based ePDF may provide a wealth of quantitative structural information for complex nanostructured materials as used in technological applications as supported catalysts. We anticipate that a PED-based PDF will become a reliable approach to analyze quantitatively the statistical properties of complex nanostructured samples, which are rather difficult to identify by 2D projection atomic resolution TEM images.

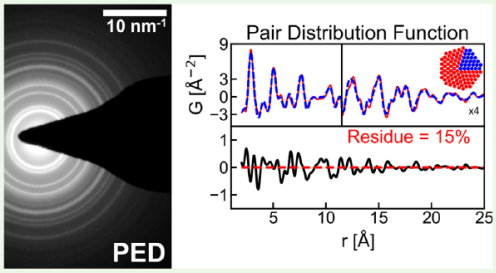

KEYWORDS: *pair distribution function (PDF), nanoparticles, structural refinement, transmission electron microscopy (TEM), precession electron diffraction (PED), statistics, quantitative characterization*

I. INTRODUCTION

Nanoparticles (NPs) are used to increase the performance of devices and industrial processes in many different areas, for example, as catalysts, optical and electronic sensors, biomedical materials, and so forth.[1−3]

In particular, nanostructured heterogeneous catalysts enhance the efficiency of many industrial processes and lower the quantity of necessary expensive metals in them. Desired properties for catalysis can be achieved by manipulating NP structural properties such as size, crystallinity, and shape. Additional control can be obtained by alloying and/or controlling the elemental distribution inside NPs (solid solution, concentration gradients, and segregated structures such as Janus-type or core−shell particles).[1]

Precise control of NPs chemical and structural properties is usually achieved with wet-chemical synthesis, a high-throughput and affordable method, but which may demand complex multistep procedures.[3] Also, physical synthesis using gas-phase condensation may be applied, which is certainly very appealing for catalysis as the particles are not accompanied by subproducts such as surfactants and reagents.[4,5] Furthermore, NPs and surface/substrate interaction can be utilized to enhance catalytic efficiency.[6,7]

The development of optimized nanomaterial synthesis demands precise characterization approaches to understand differences between nanostructures and their macroscopic

Received: September 23, 2021
Accepted: October 12, 2021
Published: October 26, 2021

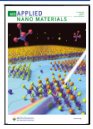

https://doi.org/10.1021/acsanm.1c02978
ACS Appl. Nano Mater. 2021, 4, 12541−12551

counterparts. The atomic arrangement inside NPs may be quite different from the bulk one because surface energy becomes an important factor in the total energy balance.[8] For example, multiple-twinned particles (MTPs) are frequently observed in noble metals such as Au and Ag; these particles are formed by the assembly of many tetrahedra, which may form decahedral (Dh) and icosahedral (Ih) NPs, displaying fivefold axes.[9]

Bulk crystals display a long-range atomic order; then, X-ray diffraction (XRD) analysis has for a long time fulfilled many of the requirements of precision, simplicity, and convenience.[10,11] However, crystalline nanomaterials are in between amorphous systems (only short-range order) and bulk crystals (long-range order). Nanocrystal diffraction patterns are prone to information loss due to peak broadening, low signal, high background, and thermal movement of the atoms.[11] This leads, as postulated by Billinge and Levin, to the so-called "nanostructure problem": a lack of sufficient constrains (diffraction peaks) to the required free variables (atomic positions).[12] The implementation of structural refinement methods allowing a quantitative comparison of nanostructure crystal arrangement with different models is a yet unsolved issue. This issue is even more challenging for catalysts displaying a complex spatial arrangement of tiny metal NPs randomly distributed on larger support materials (alumina, glassy carbon, titanium oxide, *etc.*)

A notable improvement to the "nanostructure problem" has been achieved by applying optimization and refinement to real-space pair distribution function (PDF), a function that describes the probability of finding a pair of atoms separated by the distance r.[13,14] PDF measurements are frequently derived from synchrotron-based X-ray powder diffraction (XRPD) patterns or neutron diffraction.[15] The quantitative comparison with the simulated PDF from a structural model can be applied to evaluate the residual square difference used as the metric for optimization.[14,16]

From another point of view, transmission electron microscopy (TEM) is certainly one of the most utilized techniques to characterize NPs due to its intrinsic higher spatial resolution, providing information of particle morphology, atomic arrangement, and elemental distribution with angstrom resolution (see example in Figure 1).[17] One of the main sensitive aspects of TEM work is that conclusions are frequently derived from few pinpointed examples in the sample; then, it must not be considered with solid statistical validity from the point of view of a general sample evaluation. Most electron-based studies of nanosystems exploit the much stronger electron-matter cross section allowing the analysis of small volumes of matter. Then, the use of electron diffraction (ED) represents an appealing case to derive an electron-based PDF (ePDF) of tiny NP samples. In many regards, the ePDF may be considered an accessible technique due to the high number of TEM in research laboratories and also the availability of several open-source data treatment packages.[18−22]

ED physics is significantly different from the XRD one; while kinematical diffraction (or single scattering assumption) can be straightforwardly applied to XRD, multiple scattering events occur in ED even in weakly scattering material or small metal NPs.[23,24] When multiple scattering is important, the so-called "dynamical regime" arises and a small variation in crystal size or orientation may cause dramatic changes in diffraction peak positions and intensity. Theoretical methods to simulate

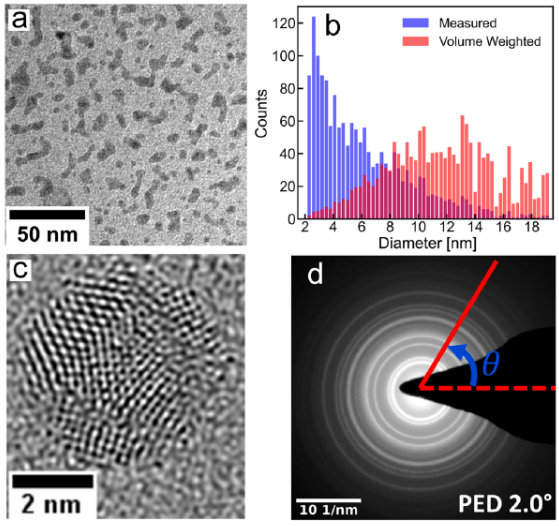

Figure 1. TEM characterization of metal alloy AuAg nanoparticles generated in a gas-aggregation source. (a) Low-magnification TEM image showing NP distribution on the substrate. (b) Size distribution weighted by diameter or volume. (c) HRTEM of a nanoparticle displaying a complex polycrystalline atomic arrangement. (d) Typical SAED ring-pattern acquired using a precessing incident beam, which will be used for PDF calculation.

dynamical diffraction are complex and time-consuming, which inhibit their practical use in ED structure refinement.[25]

Electron microscopy methods have shown impressive progress during the 21st century; among them, precession electron diffraction (PED) has become an essential tool for electron crystallography by recovering somehow a simpler relation between experimental ED intensity and kinematical diffraction theory.[26,27] PED diffraction can be described as a "quasi-kinematical" regime, which is neither kinematical nor dynamical, but preserves several characteristics of the former.[28] This technique can be simplified as a two-step electron beam manipulation: (i) the electron beam is tilted around the microscope optical axis to form a hollow cone before interacting with the sample; (ii) after passing through the sample, the beam is tilted back to the optical axis, to form a static diffraction pattern. PED methods have become popular in the materials science community as a scanning diffraction approach to map phases and crystal orientation in polycrystalline samples.[27] However, the traditional parallel beam selected area ED (SAED) measurements have gained huge interest when acquired using a wide precessing parallel beam. Deviations from kinematical intensities are small enough that structural refinement procedures have been viable from PED−SAED data,[29,30] which has had a huge impact on crystallographic solution of structures.[27]

Recently, Hoque *et al.*[31] have shown the high potential of associating PED and ePDF for the quantitative characterization of Au NPs synthesized by the wet-chemical method, where the sample is very close to ideal ones, showing narrow size distribution and non-agglomerated particles on the substrate. This study involved data analysis procedures adapted from XRPD, which do not account for several factors exclusive to ED. Actual nanostructured materials utilized in many technological processes, as an example in catalysis, may be

https://doi.org/10.1021/acsanm.1c02978
ACS Appl. Nano Mater. 2021, 4, 12541−12551

Scheme 1. Illustration of How Structural Information of Complex Nanoparticle Samples (Showing Size Distribution and Apparent Agglomeration) Can Be Derived From PED-Based ePDF Analysis[a]

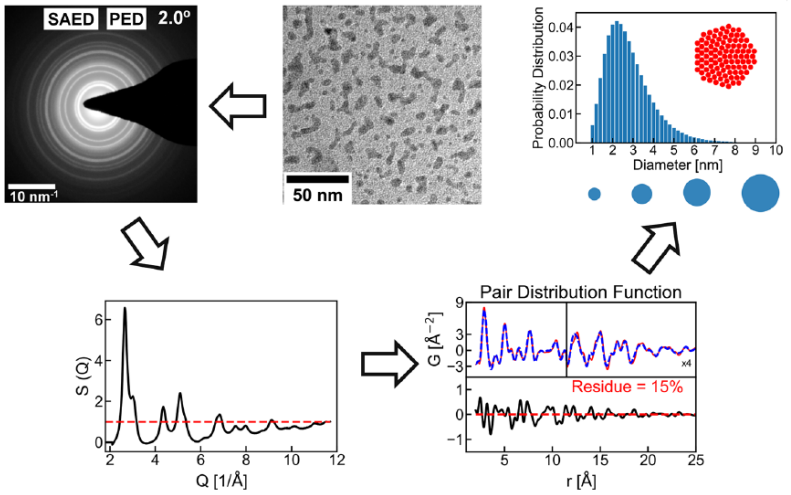

[a]First, a PED pattern acquired using a low-profile TEM is processed to obtain the sample electron powder diffraction pattern [and the normalized version $S(Q)$]. Then, a Fourier transform is utilized to obtain real-space information through the ePDF. A structural refinement analysis is performed by minimizing a residual factor, providing quantitative structural information of the NP atomic arrangement, crystallite size, and the particle size distribution.

very complex, showing agglomeration, substrate-induced structural deformation, size dispersion, and so forth.[1,6,32−36] These characteristics frequently hinder the straightforward application of traditional TEM imaging techniques, which require well-oriented crystals without superposition. These issues are independent of synthesis type (chemical or physical) as catalyst preparations are complex multistep procedures such that NPs can be synthesized to form ideal samples for TEM characterization, but the catalyst itself (usually NPs plus substrate) will be much more complex.[1,32,35] Furthermore, the design of the catalyst must also account for degradation during the reaction due to the increase in NP size dispersity and agglomeration; this demands sample comparison pre- and post-catalytic reaction, in which the NP sample may have evolved into a much more complex nanostructure.[35,36] In this work, we will address the quantitative structural characterization of complex few-nanometer-wide polycrystalline metal NPs generated by a gas cluster source and deposited on a substrate. This sample mimics reasonably well the rather complex nature of the as-prepared- or post-reaction-supported heterogeneous catalysts, which are frequently extremely challenging to be analyzed in depth using traditional imaging approaches. This kind of sample shows agglomeration and apparent coalescence such that the traditional atomic resolution images cannot render precise structural information (Figure 1), and sample mass is insufficient to measure a high-quality XRPD pattern. Our results show that ePDF structural refinement based on PED and kinematical simulations may allow a structural assessment of very high quality, where residue values are equivalent to ones reported from synchrotron PDF measurements (see Scheme 1 for an illustration of the analysis process). In addition, ED data may be acquired with very small electron dose minimizing electron-beam-induced sample modification.

II. PDF CALCULATION

The calculation of a PDF curve requires as initial input a powder diffraction pattern $I_{raw}(Q)$ (where $Q = 4\pi \sin\theta/\lambda$ is the magnitude of the scattering vector, θ is the scattering angle, and λ is the wavelength of the incident wave). Subsequently, a proper background subtraction is used to obtain the coherent diffraction contribution $I(Q)$.[15,16] The total structure scattering function, $S(Q)$ (eq 1), can be derived normalizing $I(Q)$ by the scattering power of the sample

$$S(Q) = 1 + \frac{I(Q) - \langle f(Q)\rangle^2}{f^2(Q)} \tag{1}$$

where $\langle f(Q)\rangle$ is the atomic scattering factor ($f(Q)$) of the material weighted by its composition.[16]

The reduced PDF, $G(r)$, can be directly derived from $S(Q)$ through a Fourier transform (eq 2) between the minimal (Q_{min}) and maximum (Q_{max}) measured values of Q (examples of $S(Q)$ and $G(r)$ curves are shown in Figure 2).

$$G(r) = \frac{2}{\pi}\int_{Q_{min}}^{Q_{max}} Q[S(Q) - 1]\sin(Qr)dQ \tag{2}$$

The $G(r)$ function contains most of the available structural information in a PDF (excluding the coordination number) and it is the most commonly used real-space PDF derived from the diffraction data [for simplicity, hereafter, we will note the $G(r)$ function as PDF]. The $G(r)$ curve contains structural information in several length scales for NP samples (see Figure 2b): (a) local order, usually associated with the primitive cell (commonly <10 Å); (b) domain size; and (c) average particle size (or diameter).[15]

The evaluation of $I(Q)$ requires a background subtraction step for the measured diffraction intensity, $I_{raw}(Q)$, ($I(Q) = I_{raw}(Q) - B(Q)$), where $B(Q)$ represents contributions from the sample substrate or matrix, instrumentation, and

https://doi.org/10.1021/acsanm.1c02978
ACS Appl. Nano Mater. 2021, 4, 12541−12551

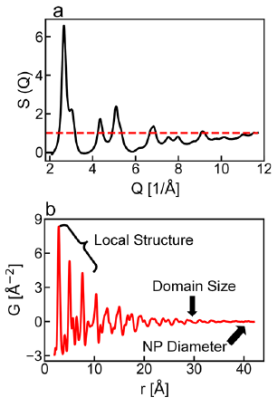

Figure 2. a) Total structure scattering function $[S(Q)]$ obtained by a proper normalization of a powder PED−SAED pattern. The dashed line shows the asymptotic behavior of $S(Q)$ toward 1. (b) Real-space PDF curve $G(r)$ generated by Fourier transformation. Note that this latter curve allows a direct access to short-, medium-, and long-range order regions.

incoherent scattering (see Figure S2).[15,16] The background subtraction is far more complex than needed for a Rietveld analysis because it must fulfill the constrains of diffraction physics in order to calculate a PDF curve.[37] First, the total integrated scattered signal of $I(Q)$ must agree with the integrated scattering power from the material $f^2(Q)$.[18,38] Second, the asymptotic behavior at high Q should be incoherent such that high Q scattered intensity must fulfil $I(Q)/f^2(Q) \rightarrow 1$.[10,18,38]

These constrains represent concrete bounds for any type of scattering radiation, but we must consider that the physics of neutrons, X-ray, and electron scattering are very different, which implies different challenges for background subtraction. In XRD, background subtraction is usually performed in steps; first, the scattering due to substrate/instrumentation is measured and removed from the sample diffraction signal. Subsequently, the incoherent scattering signal, described as a slowly variating function, can be subtracted to obtain $I(Q)$.[15,38,39] The first step is usually the main concern, requiring a precise scaling of the substrate scattering in relation to the sample one. As discussed by Banerjee,[40] the result of this subtraction is highly dependent on a time-consuming manual user intervention, where decision is taken qualitatively on the basis of expected outcomes. The author emphasizes that it is critical to develop automated background subtraction because this represents an important hurdle in PDF studies of weakly scattering materials.

In ED measurements, the main contribution to the background is related with incoherent scattering; consequentially, signal extraction procedures differ significantly from X-ray studies.[41] Several softwares are available for ePDF derivation from ED, and although numerical procedures may be different, most of them include slowly variating function to model the diffraction pattern background (or not displaying structured scattering profile from a substrate), which is optimized to ensure fulfillment of the physical scattering constrains mentioned above.[18−22] A simultaneous subtraction of both contributions (incoherent and substrate/matrix) is rather complex as their strong scattering intensity superposes in low Q (there is no common equivalents in XRPD).[10,38] Overall, ED background subtraction suffers similar automatization problems than X-ray and how to minimize such adverse effects still is an open question. In this work, we have tackled this problem and we suggest an algorithm to perform a more user-independent background removal considering an experimental substrate scattering contribution.

III. MATERIALS AND METHODS

III.I. NP Synthesis. Metal NPs have been produced in a homemade gas aggregation cluster source.[42] A cylindrical magnetron is used to sputter atoms from a metal wire target, which are carried by a flux of Ar gas and subsequently cooled by adiabatic expansion. In particular, this source has been specially designed to generate metal alloy NPs aiming technological studies involving catalysts and magnetic systems. The cluster size can be controlled with the aid of ion optics and it can be measured *in situ* by time-of-flight mass spectroscopy. Clusters from the molecular beam are directly deposited on the electron microscopy grid (a-C: amorphous carbon film on a lacey carbon support, nominal thickness 30 Å, TED Pella) with low kinetic energy (<0.5 eV/atom), in the so-called "soft-landing" regime.[4,43,44] The sample analyzed here was composed of binary Au_xAg_{1-x} alloy NPs ($x \approx 0.7$) in order to look for the possible formation of a core−shell structure (chemical gradient).[45] This chemical ordering was not detected during our work, may be it is a minor effect or it is below the sensitivity of our measurement; for future modeling, we will only consider a random chemical order due to the high miscibility of these chemical elements.

III.II. Electron Microscopy. We have used an FEI TECNAI G2 STwin LaB6-gun TEM operated at 200 keV coupled with ASTAR (Nanomegas) beam precession (Lab. de Caract. Estr.-LCE, Dept. Materiais, UFSCar, São Carlos, Brazil). ED patterns were acquired using a Gatan Orius CCD detector (14 bits, 2048 × 2048 pixels). HRTEM images were taken using a JEM 2100F FEG operated at 200 keV (Brazilian Nat. Nanotech. Lab.- LNNANO, Campinas, Brazil). A very careful alignment of the beam precession is essential to derive a high-quality PDF (see the Supporting Information for details). The ED measurements have been performed in a selected area region of about 0.5 μm in diameter, containing approximately 2000 NPs. The a-C film scattering pattern from the sample substrate was measured using a pristine a-C grid.

III.III. Data Analysis Procedure. The calculation of the PDF curve from ED ring patterns requires additional steps associated with diffraction generation and measurement in TEM. First, it is necessary to correct optical system aberrations (mostly twofold astigmatism, see Figure S1).[46−48] Second, background subtraction must account precisely for the contribution from the substrate supporting the sample (Figures S2). In particular, the optimization of background subtraction used in this work has been a key step to attain lower residues during the PDF analysis, so it will be described briefly. The incoherent background in ED patterns represents a much higher portion of the measured total intensity than in XRD,[41] and this scattering may be modeled by a smooth function. High caution is required for analyzing few-nanometer-wide particles whose diameter is similar to the support/matrix thickness (*e.g.*, amorphous carbon 50−100 Å thick) as it generates a substantial signal contributing to the ED background.[49]

Usually, the support or matrix scattering contribution is first subtracted tentatively, and second, the constrains that PDF require are applied to $S(Q)$.[18−20,37,39] In contrast, we have decided to incorporate the two steps in a single iterative optimization procedure yielding the coherent scattering intensity which fulfils the constrains of diffraction physics (see the Supporting Information for more details and a pseudo-code describing our algorithm). The background model considers simultaneously both a-C experimental profile and a smooth function decreasing with Q, as described in eq 3

$$B(Q) = a_{a\text{-}C}B_{a\text{-}C}(Q) + b_1 + \frac{b_2}{Q} + \frac{b_3}{Q^2} + \frac{b_4}{Q^3} \quad (3)$$

https://doi.org/10.1021/acsanm.1c02978
ACS Appl. Nano Mater. 2021, 4, 12541−12551

where b_i (i = 1, 2, 3, 4) are the parameters of the incoherent scattering model, $B_{a\text{-}C}(Q)$ is an experimental a-C diffraction pattern (see Figure S3a) and $a_{a\text{-}C}$ is its scale factor. The final background shows a strong Q dependence, which may generate clear differences in diffraction peak height and position (see Supporting Information and Figure S3).

III.IV. Calculating the Residue and Simulations from Model Structures. The structural refinement follows a regular procedure, requiring the quantitative comparison of the measured PDF, $G_{mes}(r)$, with the simulated one from a structural model, $G_{sim}(r)$. A residual square difference R (eq 4) is used as the metric for optimization.[14,31]

$$R^2 = \frac{\sum (G_{mes} - G_{sim})^2}{\sum G_{mes}^{\ 2}} \quad (4)$$

To build a reliable ePDF structural refinement, generating reproducible and reliable residues, the simulations of ePDF curves must be efficient and precise. A simple approach to estimate NP PDF functions is to derive $G(r)$ using a bulk crystal curve (based on the known unit cell) which is attenuated by the real space form factor of the NPs.[50,51] Our simulations have been based on the kinematical Debye scattering equation (DSE), which allows the calculation of powder diffraction patterns (yielding peak height, width, and position) without any assumption of the atomic position structural order (as the existence of a unit cell),[52] which may be very useful in future studies aiming at potential structure deformation.

We have developed software in Python language, which performs all the ED processing steps and structural refinement based on the ePDF curve (a schematic workflow algorithm of all processing steps is presented in Figure S4). The numerical Fourier transform of $I(Q)$, used to calculate $G(r)$, and structural refinement procedure (DSE simulation and residue optimization) are similar to those found in common diffraction analysis programs.[53−55] It is essential to emphasize that we have aimed to perform structural refinement involving the minimal number of free parameters: spherical NP diameter and isotropic Debye−Waller factor ($M = 8\pi^2 U_{iso}$, where U_{iso} is the mean quadratic displacement of the atoms).[10] This is important to ensure physically realistic and accurate models, and reliable residues, because the plethora of parameters usually utilized in PDF analysis can provide models that are resulting from overfit of $G(r)$ features.

The range of interatomic distances considered for residue evaluations starts just before the first $G(r)$ peak (associated to the nearest neighbor). The upper limit, r_{max}, was set at the value where noise starts to dominate the PDF curve (information limit); our analysis yielded $r_{max} \approx 40$ Å for our ED setup experiment. We have performed different tests on suitable models and we have observed that our PDF measurements do not allow us to reliably determine small changes in shape; this agrees with previous reports that PDFs lack sensitivity to reveal the presence of facets or small changes in shape, both in electron-based and X-ray-based PDFs.[13,56] Consequentially, we have only considered spherical-shaped particles displaying a random chemical order (expected due to the high miscibility of these chemical elements). On the basis of these simpler models, we have been able to perform a very efficient comparison of particles with distinct crystallographic features (domain structure and organization, *e.g.*, monocrystalline, twinned, *etc.*).

IV. RESULTS

The low-magnification TEM image of the NP sample shows that there are many cluster agglomerates (Figure 1a); in fact, our experiments required a high density of particles to guarantee a good signal-to-noise ratio for the ED measurements using the available detector (CCD). The measured NP mean diameter is ≈60 Å, but as a diffraction signal is proportional to the number of atoms, it is better to look at the NP distribution weighted by volume (Figure 1b). More importantly, this complex arrangement of apparently coalesced NPs is a good imitation of a situation found in catalysts or plasmonic devices; this kind of nanosystem seems rather challenging concerning the assessment of crystallographic and detailed structural information. In fact, atomic resolution images indicate complex polycrystalline particles (Figure 1c) such that it is not possible to derive any additional quantitative information of the atomic arrangement from this kind of micrographs.

As the sample contains multidomain particles (Figure 1c), twinned and MTPs represent a reasonable trial model. Therefore, Dh, Ih, twinned face-centered cubic (fcc) (ST, twin at an NP center), and monocrystalline fcc structures will be the basis of our structural analysis (examples of powder ED pattern and PDF for these particles are shown in Figure S5). Table 1 summarizes the structural refinement results, and the comparison of optimized curves is shown in Figure 3. Dh NPs (≈30 Å in diameter) generate the smallest residue; we must note that previous studies based on XRD have indicated that the PDF represents a very strong tool to identify MTPs.[13] Our PED−PDF study has attained a residue value of ≈20%, which is very close to synchrotron-based measurements (12−17%), suggesting a very good ability of the ePDF for quantitative NP structural analysis.[13] This is very encouraging considering that ED measurements have been obtained with low-profile TEM and an apparently agglomerated NP sample. Finally, an important result is that PED yields a smaller residue (≈4%) than conventional SAED for all studied cases. This corroborates the findings of Hoque *et al.*[31] for the ePDF using a much more performant instrumental setup. Our residue reduction is rather modest, while Hoque *et al.*[31] have reported around 20% reduction, probably due to differences in sample

Table 1. Optimization Results for SAED/PED Measurements[a]

parameter	fcc	ST	Dh	Ih
R (%)	31/27	30/26	23/20	64/58
Ø (Å)	21/18	27/24	32/28	24/24
U_{iso} (Å^2)	0.033/0.027	0.033/0.029	0.031/0.030	0.049/0.043

[a]The a-C substrate contribution has been considered during background subtraction for all displayed results (Ø optimized NP diameter).

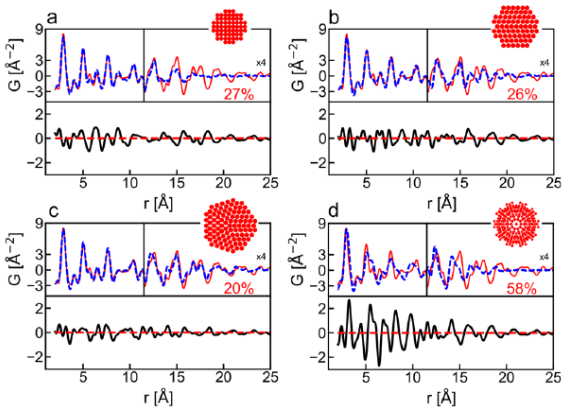

Figure 3. Comparison between measured (continuous line) and optimized ePDF (dashed line) for the four different model nanostructures: (a) fcc, (b) single twinned, (c) Dh, and (d) Ih.

https://doi.org/10.1021/acsanm.1c02978
ACS Appl. Nano Mater. 2021, 4, 12541−12551

homogeneity, as they show narrow size distribution, well-formed particles, and no apparent agglomeration/superposition. Physically, the observed residue reduction is due to the fact that powder PED diffraction intensities are much better described by kinematical theory, as observed for diffraction from monocrystalline samples.[27] Our study corroborates that PED should play a fundamental role for further development of electron-based PDF methods and other electron crystallography methods because it represents a practical and efficient tool to deal with the intrinsic difficulty of dynamical ED effects.

A clear example of the unique capability of PDF methods is the direct access in a single real-space curve to the whole structural information in different spatial ranges (*i.e.*, local-, medium-, and long-range order).[16] To exploit this whole structural characterization power, the simulations must be able to describe accurately any arrangement of atoms (periodic or aperiodic structures, also including defects, strain, *etc.*). Luckily, the DSE calculations are able to fulfil this essential step, which allows us to analyze the sensitivity of the proposed ePDF refinement analysis to subtle structural modifications. Our results have indicated that a 30 Å Dh NP provides the best description of experimental data (R = 20%); this kind of particle is composed of five identical tetrahedrals whose fcc atomic arrangement suffers a slight homogeneous distortion into a body-centered orthorhombic (bco) to form a compact atomic arrangement.[57]

The structural optimization using a spherical fcc model yields the best fit (R = 27%) for an NP ≈20 Å in diameter. This is approximately the size of an individual tetrahedral domain of the Dh, which is expected as diffraction measurements will mainly provide information on the crystallite structure and domain size, or, more specifically, the structural coherence of a material.[15] Figure 4a shows that the optimized fcc model describes correctly the local order (r < 10 Å) but fails to account for the medium- and long-range order (r > 15 Å). Alternatively, if we use spherical bco NPs for optimization, a slightly larger NP (24 Å) is indicated; the quality of the fit is similar (R = 27%), reproducing fairly well the local order with a light improvement for PDF peaks for distances around 15 Å (Figure 4b). In spite of this last apparent gain, the bco model does not provide significant residue reduction, suggesting that the stronger PDF oscillations due to the local order tend to dominate the final residue value. The fcc and bco structures belong to different point groups but with a very close local order; unfortunately, the measured PDF has not been able to properly discriminate them through the residue calculation.

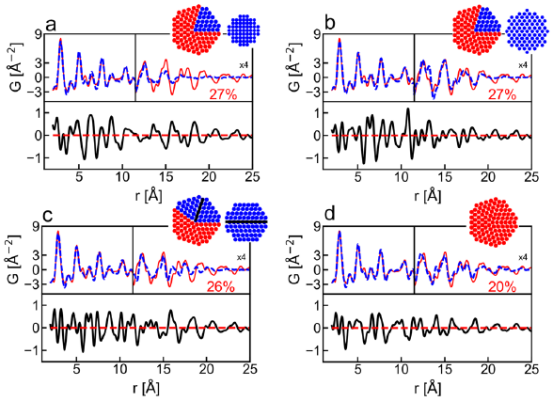

Figure 4. Comparison between measured (continuous line) and optimized (dashed line) ePDF curves for: (a) fcc monocrystal; (b) bco monocrystal; (c) fcc twinned; and (d) Dh. The inset images illustrate the relation of the optimized monocrystalline and twinned structure as the composing parts of the Dh. The region between 11.5 and 25 Å was scaled by a factor 4× to render easier the visualization of differences; below each $G(r)$ plot, the difference curves are shown.

Dh NPs display five twin planes; then, we have also analyzed how twinning influences the structural optimization. When performing a structural optimization using a twinned fcc particle (ST), the residue shows a subtle reduction to 26%. This provides some gain in the short-range region but worsens the description of the medium-range (r ≈ 15 Å) when compared with pure bco NPs (see the difference curve in Figure 4c). We must keep in mind that a twin defect establishes a precise structural local order around the twinning plane (actually a mirror plane for the staking of fcc (111) atomic layers) which is different from fcc or bco pristine crystals; this information seems to have been captured by the experimental ePDF curve, explaining the residue improvement. In the light of the precedent discussion, we must conclude that Dh NPs yield a much lower residue (20%, Figure 4d) because they provide the correct balance of local order (associated with point group and twins) and medium-range order information, both of them have been very precisely expressed in the experimental ePDF.

The results show that PED clearly contributes to get smaller residues during the quantitative comparison of experimental ePDF with kinematical diffraction approximation modeling. However, at this point, it is essential to emphasize that the major factor influencing residue reduction has been the correct inclusion of a-C substrate scattering during background subtraction (35 to 23% for SAED and 28 to 20% for PED). Then, the lower residues obtained are results of both: improvement of input experimental data (through PED) and the careful isolation of the NP coherent scattering pattern by the proposed automated optimization of substrate contribution to background.

V. DISCUSSION

Our results show that the quantitative ePDF methods applied to the agglomerated NP sample, as shown in Figure 1, allow the estimation of a dominant Dh atomic arrangement (diameter ≈ 30 Å). The obtained depth of structural information characterization derived from the ePDF cannot be derived or deduced from atomic resolution images. We must remind that several models of NP formation in gas aggregation sources suggest a high probability of Dh structures due to oriented attachment of smaller cluster in-flight; our ePDF results seem to confirm these models.[4,58] As for NP size distribution, electron-based PDF size seems smaller than TEM data (volume weighted mean diameter ≈ 120 Å for the wide size distribution, Figure 1b); also, experimental data show an information limit at ≈40 Å (detectability limit for PDF oscillations). The analyzed NPs come from a molecular beam which can carry clusters in the 10−50 Å diameter range as indicated by time-of-flight mass spectrometry measurements;[42] then, 30 Å NPs represent a good estimation of the average cluster size formed by the source. Although a high degree of coalescence can be observed in Figure 1, good agreement between mass spectroscopy and ePDF size assessment

https://doi.org/10.1021/acsanm.1c02978
ACS Appl. Nano Mater. 2021, 4, 12541−12551

represents a clear indication of a successful "soft-landing" process (without major structural modification of the original clusters).[42−44] Again, this essential information has become available in a quantitative way due to the use of ePDF methods.

A major concern when studying small NPs is the effect of electron beam irradiation that can induce structural modifications in the sample during observation. Using the beam current measurement from the microscope screen, we estimate that the total electron dose during ED data acquisition was around 10 $e^{-}/Å^2$. This is a very low dose for metallic NPs, so we are confident that such values do not induce structural changes; this suggestion is also consistent with the detection of successful "soft-landing" without further structure modification.

Hitherto, we have implemented the PDF structural refinement considering as a model a single spherical particle structure (or ideal monodisperse NP sample). Any NP generating enough diffracted signal to overcome background or noise will contribute to the measured diffracted pattern and the derived ePDF curve.[59,60] In this case, the model can be easily extended to describe more complex situations (multiple structures or size distribution). We can then model the diffraction pattern of a polydisperse sample as the linear combination of the ED patterns $I_i(Q)$ from NPs with a well-defined diameter

$$I(Q) = \sum_i w_i I_i(Q) \tag{5}$$

where w_i are the weight coefficients of the linear combination.

In practice, it is quite difficult to get an efficient and reliable convergence if many sizes (or variables to be optimized) are included in the refinement calculation. To overcome this difficulty, we have assumed a lognormal distribution (the frequent distribution generated in our cluster source)[42] and the width and center of the distribution were considered as optimization parameters. The choice of optimizing a well-defined size distribution function also is extremely helpful to keep the number of degrees of freedom included in the model to a minimum (total 3, we have used a single Debye−Waller factor for all sizes). The refinement considered Dh NPs with diameters between 1 and 10 nm (diameter step 2 Å), leading to 45 different NP sizes used for optimization.

The optimized polydisperse parameters (mean diameter of 28 Å and U_{iso} = 0.030 $Å^2$) are similar to those derived in the monodisperse model optimization. The resulting residue has shown a significant improvement (see curves in Figure 5), attaining a value of R = 15%, which is equivalent to the ones obtained in X-ray studies,[13] and we have obtained such high-quality optimization using a model just considering three adjustable parameters. As expected, the inclusion of a size distribution (and larger NPs) allows a great improvement in the description of PDF oscillation for r > 20 Å (see Figures 5c and S6c,d). As larger particles must show stronger dynamical diffraction effects, their inclusion can be problematic when models are based on kinematic theory. It is important to note that the high r range of the ePDF curve derived from normal SAED diffraction is not properly described even using a model considering size distribution. In contrast, the PED-based PDF seems to be very well-described for the whole high r range (this high performance is clearly revealed through difference curves in Figure S6), which gives strong support for PED application in ePDF methods.

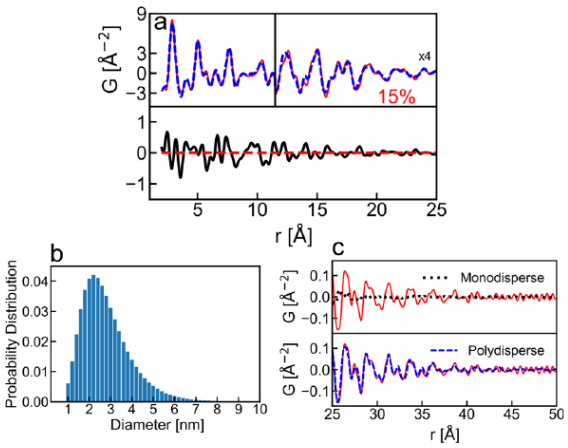

Figure 5. (a) Comparison between measured (continuous line) and optimized ePDF derived from the size distribution in (b) (dashed line). In the interval 11.5−25 Å, the upper curves were scaled by a factor 4 to emphasize differences; the difference curve is shown below. (b) Optimized size distribution for the Dh nanoparticles. (c) Difference in high r range between the experimental data (continuous line) and the ePDF optimized with a monodisperse model (upper panel) and a polydisperse one (lower panel).

Some previous experimental studies have explored the use of PED to improve structural refinement analysis of ED patterns or ePDF curves.[31,61] Despite the positive results, the physical origins of observed progress by incorporating PED are still under debate and should be analyzed in more detail because the dynamical characteristic of ED is always present.[30] In simple terms, dynamical diffraction may influence the ED powder pattern in three ways: (i) modification of the relative intensities of diffraction peaks; (ii) distortions of their profile (width and position); and (iii) presence of forbidden reflections (peaks hkl where the structure factor is zero, $F_{hkl} \equiv 0$). Hall and collaborators[24] have studied in detail the powder ED of few-nanometer-wide Ag NPs using full dynamical multislice simulations and they have clearly detected the occurrence of the two first effects. In fact, our experimental data show slight shifts without much modification of width of diffractions peaks when comparing PED and SAED (Figure S7).

As discussed by Hoque *et al.*,[31] the correct mathematical description of a ring ED pattern is a summatory of diffraction intensities from the patterns of individual nanocrystals (all in different orientations). The "quasi-kinematical" nature of PED intensities implies that the pattern from each individual nanocrystal will be closer to kinematical theory. Consequentially, it is straightforward to deduce that the final summatory (or diffraction ring intensity) will also become closer to kinematical simulated values. This explains the lower residues obtained from PED experiments during ePDF refinement.

For an unexperienced TEM user, it is important to emphasize that a PED pattern is actually the average of an ensemble of static beam diffraction patterns taken at each incident beam direction in the precession cone (Figure S7). Then, if one beam direction in the cone is found under the strong dynamical condition (this means along a high symmetry zone axis of the crystal), the influence of this particular diffraction pattern is reduced by averaging. Just a crystal tilt of 0.1−0.2° drastically changes the ED patterns in conventional

https://doi.org/10.1021/acsanm.1c02978
ACS Appl. Nano Mater. 2021, 4, 12541−12551

TEM diffraction work, while the beam precession angle (or cone opening half-angle) should be around 1−2° or higher for ePDF work. High angles guarantee the low statistical weight of any highly dynamical condition. At these precession angles, forbidden reflection, generated by dynamical diffraction, shows an intensity reduction from 1−2 orders of magnitude, when compared with standard ED measurements.[62]

We have been able to implement a structural refinement using a PED-based ePDF approach. The question rises if this performance can be further enhanced, for example, using larger detectors (to attain larger scattering vector values) or reducing inelastic scattering contribution to the ED pattern (energy filtering). The value of the maximum scattering vector (Q_{max}) is directly associated with resolution (as expected for any Fourier transform-based calculation). In our experimental setup (2048 × 2048 CCD camera), we have managed to obtain $Q_{max} \approx 12$ Å^{-1}, which is considered reasonable for ePDF analysis (usual values are 12 Å$^{-1} \leq Q_{max} \leq 24$ Å^{-1}).[63] At present, many cameras attain 4096 × 4096 pixel size, so this clearly indicates that doubling Q_{max} represents an attainable instrumental target assuming that the whole ring pattern is measured simultaneously without changing TEM optical configuration (which may induce additional electron optics aberrations and distortion to diffractions rings). We have already tested the evaluation of the ePDF from energy-filtered PED diffraction, and it reduces significantly incoherent scattering background; unfortunately, the available bidimensional detector had insufficient pixel number and limited excessively the Q_{max} that could be attained. At present, the progress of TEM instrumentation is realized at high speed, so the coupling of PED, energy filtering, and improved detectors (sampling and quantum efficiency) will become available soon. This will allow us to use the ePDF to tackle more challenging structural issues (*e.g.* chemical gradients, strain, *etc.*).

Our results were derived using an acceptable but rather low Q_{max}(≈12 Å^{-1}); a comparison with simulated PDF derived using different Q_{max} values is shown in Figure S8. These calculations show that, although a clear loss of resolution occurs, our PED-based measurements generate most of the PDF peaks. Then, we are confident that we have been able to extract the majority of the available structural information, as evidenced by the obtained excellent residue values. In addition, little difference is observed in the simulated PDF curve from a 30 Å Dh, when Q_{max} is increased from 20 to 30 Å^{-1}; in fact, no coherent intensity peak is observable after 25 Å^{-1} due to thermal vibrations at room temperature (assuming the Au bulk Debye−Waller value).

Many researchers may wonder about the precision of the present approach to measure the interatomic spacing, for example, to tackle size-dependent effects such as compression/expansion or strain distributions.[64] In our refinement procedure, the local order was assumed to be bco; then, both considering the PED calibration and lattice parameter optimization, we have estimated that the precision of our results is around ≈0.1−0.2% (considering that detection means a residue change of ∼1%). We think that there are many instrumental fronts to be explored for a better detection and acquisition of PED patterns (and attaining higher Q_{max}), providing further improvement to the ePDF refinement precision and accuracy in a short future.

For decades, noble metal Dh NPs have been the object of study concerning the occurrence of homogeneous or inhomogeneous strain in the space-filling fivefold NPs.[57,64−66] Most of the studies are based on TEM images (dark field or atomic resolution ones), where information is axis-averaged along the beam direction (2D projection) and derived from particles oriented close to the five fold axis.[57,64−66] The assessment of strain in 3D may yield new light on the validity of different models; the ePDF methods tested here may contribute to this issue. Work is in progress to increase the precision of the method and try to provide deeper structural information.

As examples of potential applications, we can mention several wet-chemical synthesis involving seeded growth or alloy NPs where inclusion of a different metal precursor may generate significant morphology differences in the generated NPs.[67] Another interesting issue is the quantitative analysis if abrupt core shells or chemical gradients occur in multimetal NPs generated by gas aggregation sources.[4,45] Although TEM images may provide qualitative guidance to develop models, no effective quantitative confrontation has been possible.

VI. CONCLUSIONS

We have shown that the PED-based ePDF allows for a high-quality and reliable structural refinement procedure for apparently agglomerated NP samples and nanostructured materials, which is confirmed by residue values (≈15%) similar to synchrotron-based nanosystem studies.[13] Quantitative atomic ordering information was derived for several spatial range scales and from a sample which is far from the idealized ones usually utilized for TEM structural characterization. Although the studied system was composed of polycrystalline agglomerated NPs with apparent size dispersion, we have been able to derive the dominant NP atomic arrangement (Dh, 30 Å in diameter) from a sample mimicking reasonably well the rather complex nature of supported heterogeneous catalysts.

We anticipate that PED−PDF will become a reliable approach to analyze quantitatively and identify the mean 3D atomic structure of nanocatalyst samples, which are rather difficult to perform in the 2D projection atomic resolution images. For example, it is frequent to characterize nanocatalyst samples by dissociating NPs and the actual catalyst analysis. In this way, the isolated NP information is extrapolated to interpret the catalyst, instead of the direct characterization needed. The ePDF method shows a high potential to provide a much deeper understanding of the as-prepared or post-reaction catalyst samples that are usually too complex to be analyzed in depth using traditional imaging approaches.

Our study has confirmed the "soft-landing" deposition of NPs from the molecular beam on the substrate; this information could not have been obtained without the PDF structural refinement and this suggests that the PED-based ePDF may provide a wealth of quantitative structural information for complex nanostructured materials, as used in technological applications.

In order to achieve the reported low-residue ePDF analysis, we have developed a different approach to a few numerical data processing steps to calculate the ePDF (mainly astigmatism correction and background subtraction optimization). Despite the rather complex NP sample and more sophisticated simulation (inclusion of size dispersion), the number of free fitting parameters was kept to a low value (only 3) when compared to usual quantification efforts. This guarantees that the good residue values are not an effect of over fitting, and it has deep implications to ensure that models utilized are realistic and accurate. These results represent a

https://doi.org/10.1021/acsanm.1c02978
ACS Appl. Nano Mater. 2021, 4, 12541−12551

remarkable achievement considering that we have used a low-profile LaB_6-gun TEM to measure a sample mass in the pico- to atto-gr range. As for the electron beam dose, the reported experiments on metal NPs required a total dose of ≈10 $e^-/Å^2$, which indicates that the ePDF displays a huge potentiality to analyze quantitatively beam-sensitive materials.

Additional work is in progress to apply the ePDF methodology to quantitatively provide answers to other complex NP characterization issues.

■ ASSOCIATED CONTENT

Supporting Information

The Supporting Information is available free of charge at https://pubs.acs.org/doi/10.1021/acsanm.1c02978.

TEM experiments, PED, data processing, kinematical simulation of NP ED patterns, PDF interpretation details, and pseudocode is included for the background subtraction algorithm (PDF)

■ AUTHOR INFORMATION

Corresponding Author

Daniel Ugarte − *Instituto de Física "Gleb Wataghin", Universidade Estadual de Campinas-UNICAMP, Campinas - SP CEP 13083-859, Brazil;* orcid.org/0000-0003-3332-9139; Email: dmugarte@ifi.unicamp.br

Authors

Leonardo M. Corrêa − *Instituto de Física "Gleb Wataghin", Universidade Estadual de Campinas-UNICAMP, Campinas - SP CEP 13083-859, Brazil;* orcid.org/0000-0002-0823-4085

Murilo Moreira − *Instituto de Física "Gleb Wataghin", Universidade Estadual de Campinas-UNICAMP, Campinas - SP CEP 13083-859, Brazil;* orcid.org/0000-0002-9209-4993

Varlei Rodrigues − *Instituto de Física "Gleb Wataghin", Universidade Estadual de Campinas-UNICAMP, Campinas - SP CEP 13083-859, Brazil;* orcid.org/0000-0003-0073-3186

Complete contact information is available at: https://pubs.acs.org/10.1021/acsanm.1c02978

Notes

The authors declare no competing financial interest.

■ ACKNOWLEDGMENTS

We thank D. Coimbrão from LCE-DEM-UFSCar for his invaluable assistance during TEM experiments. We also acknowledge Dr. Duncan Johnstone from University of Cambridge for illuminating discussions on PED diffraction applications. D.U. acknowledges financial support from the Brazilian Agencies FAPESP (no. 2014/01045-0), CNPq (402571/2016-9 and no. 306513/2017-0), and FAEPEX-UNICAMP. V.R. acknowledges funding from FAPESP (2007/01722-9) and CNPq (555647/2006-4 and 577046/2008-0). L.M.C. acknowledges financial support from CAPES (no. 1765876/2018) and CNPq (no. 140596/2020-8). M.M. thanks funding from CNPq (no. 162541/2018-0). Access to the FEG-TEM/STEM from the Brazilian Nanotechnology National Laboratory is acknowledged (LNNANO, grant no. ME - 22329).

■ REFERENCES

(1) Astruc, D. *Nanoparticles and Catalysis*; Wiley-VHC: Weingeim, 2008; pp 1−37.

(2) Kim, M.; Lee, J. H.; Nam, J. M. Plasmonic Photothermal Nanoparticles for Biomedical Applications. *Adv. Sci.* **2019**, *6*, 1900471−1900494.

(3) Ferrando, R. *Structure and Properties of Nanoalloys*; Elsevier: Oxford, 2016; pp 13−45.

(4) Huttel, Y. *Gas-phase Synthesis of Nanoparticles*; Wiley-VCH: Weinheim, 2017; pp 3−18.

(5) Grammatikopoulos, P.; Steinhauer, S.; Vernieres, J.; Singh, V.; Sowwan, M. Nanoparticle Design by Gas-Phase Synthesis. *Adv. Phys.: X* **2016**, *1*, 81−100.

(6) Vassalini, I.; Borgese, L.; Mariz, M.; Polizzi, S.; Aquilanti, G.; Ghigna, P.; Sartorel, A.; Amendola, V.; Alessandri, I. *Angew. Chem., Int. Ed.* **2017**, *56*, 6589−6593.

(7) Ellis, P. R.; Brown, C. M.; Bishop, P. T.; Ievlev, D.; Yin, J.; Cooke, K.; Palmer, R. E. High-Selectivity Palladium Catalysts for the Partial Hydrogenation of Alkynes by Gas-Phase Cluster Deposition onto Oxide Powders. *Catal., Struct. React.* **2018**, *4*, 1−8.

(8) Markov, I. V. *Crystal Growth for Beginners*; World Scientific: Hackensack, 2017; pp 1−75.

(9) Marks, L. D. Experimental Studies of Small Particle Structures. *Rep. Prog. Phys.* **1994**, *57*, 603−649.

(10) Warren, B. E. *X-Ray Diffraction*; Dover Publications Inc.: New York, 1990; pp 116−150.

(11) Holder, C. F.; Schaak, R. E. Tutorial on Powder X-Ray Diffraction for Characterizing Nanoscale Materials. *ACS Nano* **2019**, *13*, 7359−7365.

(12) Billinge, S. J. L.; Levin, I. The Problem with Determining Atomic Structure at the Nanoscale. *Science* **2007**, *316*, 561−565.

(13) Banerjee, S.; Liu, C.-H.; Lee, J. D.; Kovyakh, A.; Grasmik, V.; Prymak, O.; Koenigsmann, C.; Liu, H.; Wang, L.; Abeykoon, A. M. M.; Wong, S. S.; Epple, M.; Murray, C. B.; Billinge, S. J. L. Improved Models for Metallic Nanoparticle Cores from Atomic Pair Distribution Function (PDF) Analysis. *J. Phys. Chem. C* **2018**, *122*, 29498−29506.

(14) Christiansen, T. L.; Cooper, S. R.; Jensen, K. M. Ø. There's No Place Like Real-Space: Elucidating Size-Dependent Atomic Structure of Nanomaterials Using Pair Distribution Function Analysis. *Nanoscale Adv.* **2020**, *2*, 2234−2254.

(15) Egami, T.; Billinge, S. J. L. *Underneath the Bragg Peaks Structural Analysis of Complex Materials*; Elsevier: Oxford, 2003; pp 25−51.

(16) Billinge, S. Local Structure from Total Scattering and Atomic Pair Distribution Function (PDF) Analysis. In *Powder Diffraction: Theory and Practice*; Dinnebier, R. E., Billinge, S. J. L., Eds.; Royal Society of Chemistry: Cambridge, 2008; pp 464−493.

(17) Carter, B.; Williams, D. B. *Transmission Electron Microscopy: Diffraction, Imaging, and Spectrometry*; Springer: Switzerland, 2016; pp 343−372.

(18) Tran, D. T.; Svensson, G.; Tai, C.-W. SUePDF: a program to obtain quantitative pair distribution functions from electron diffraction data. *J. Appl. Crystallogr.* **2017**, *50*, 304−312.

(19) Shi, H.; Luo, M.; Wang, W. ePDF Tools, a Processing and Analysis Package of the Atomic Pair Distribution Function for Electron Diffraction. *Comput. Phys. Commun.* **2019**, *238*, 295−301.

(20) Gorelik, T. E.; Neder, R.; Terban, M. W.; Lee, Z.; Mu, X.; Jung, C.; Jacob, T.; Kaiser, U. Towards Quantitative Treatment of Electron Pair Distribution Function. *Acta Crystallogr., Sect. B: Struct. Sci., Cryst. Eng. Mater.* **2019**, *75*, 532−549.

(21) La Peña, F. D.; Prestat, E.; Fauske, V. T.; Burdet, P.; Furnival, T.; Jokubauskas, P.; Nord, M.; Ostasevicius, T.; MacArthur, K. E.; Johnstone, D. N.; Sarahan, M.; Lähnemann, J.; Taillon, J.; pquinn-dls; Aarholt, T.; Migunov, V.; Eljarrat, A.; Caron, J.; Mazzucco, S.; Martineau, B.; Somnath, S.; Poon, T.; Walls, M.; Slater, T.; actions-user; Tappy, N.; Cautaerts, N.; Winkler, F.; Donval, G.; Myers, J. C. *Hyperspy/hyperspy*: Release V1.6.1; Hyperspy, 2020.

https://doi.org/10.1021/acsanm.1c02978
ACS Appl. Nano Mater. 2021, 4, 12541−12551

(22) Johnstone, D. N.; Crout, P.; Nord, M.; Laulainen, J.; Høgås, S.; Opheim, E.; Martineau, B.; Francis, C.; Bergh, T.; Prestat, E.; Smeets, S.; andrew-ross; Collins, S.; Hjorth, I.; Mohsen; Furnival, T.; Jannis, D.; Cautaerts, N.; Jacobsen, E.; Herzing, A.; Poon, T.; Ånes, W. H.; Morzy, J.; Huang, S.; phillipcrout; Doherty, T.; affaniqbal; Ostasevicius, T.; mvonlany; Tovey, R. *pyxem/pyxem*: Release 0.13.2; pyxem, 2021.
(23) Cowley, J. M. *Diffraction Physics*; Elsevier: Amsterdam, 1995; pp 93−121.
(24) Hall, B. D.; Ugarte, D.; Reinhard, D.; Monot, R. Calculations of the dynamic Debye-Scherrer diffraction patterns for small metal particles. *J. Chem. Phys.* **1995**, *103*, 2384−2394.
(25) Kirkland, E. J. *Advanced Computing in Electron Microscopy*; Springer: Cham, 2020; pp 197−239.
(26) Vincent, R.; Midgley, P. A. Double Conical Beam-Rocking System for Measurement of Integrated Electron Diffraction Intensities. *Ultramicroscopy* **1994**, *53*, 271−282.
(27) Midgley, P. A.; Eggeman, A. S. Precession electron diffraction - a topical review. *IUCrJ* **2015**, *2*, 126−136.
(28) Sinkler, W.; Marks, L. D. Characteristics of Precession Electron Diffraction Intensities from Dynamical Simulations. *Z. Kristallogr. - Cryst. Mater.* **2010**, *225*, 47−55.
(29) Klein, H.; David, J. The Quality of Precession Electron Diffraction Data is Higher than Necessary for Structure Solution of Unknown Crystalline Phases. *Acta Crystallogr., Sect. A: Found. Adv.* **2011**, *67*, 297−302.
(30) Palatinus, L.; Jacob, D.; Cuvillier, P.; Klementová, M.; Sinkler, W.; Marks, L. D. Structure Refinement from Precession Electron Diffraction Data. *Acta Crystallogr., Sect. A: Found. Crystallogr.* **2013**, *69*, 171−188.
(31) Hoque, M. M.; Vergara, S.; Das, P. P.; Ugarte, D.; Santiago, U.; Kumara, C.; Whetten, R. L.; Dass, A.; Ponce, A. Structural Analysis of Ligand-Protected Smaller Metallic Nanocrystals by Atomic Pair Distribution Function Under Precession Electron Diffraction. *J. Phys. Chem. C* **2019**, *123*, 19894−19902.
(32) Fiuza, T. E. R.; Gonçalves, D. S.; Gomes, I. F.; Zanchet, D. CeO2-Supported Au and AuCu Catalysts for CO Oxidation: Impact of Activation Protocol and Residual Chlorine on the Active Sites. *Catal. Today* **2021**, *381*, 171−180.
(33) Chamorro-Coral, W.; Caillard, A.; Brault, P.; Baranton, S.; Coutanceau, C. Binary and Ternary Pt-based Clusters Grown in a Plasma Multimagnetron-Based Gas Aggregation Source: Electrocatalytic Evaluation Towards Glycerol Oxidation. *Nanoscale Adv.* **2021**, *3*, 1730−1740.
(34) Whang, H. S.; Lim, J.; Choi, M. S.; Lee, J.; Lee, H. Heterogeneous Catalysts for Catalytic CO2 Conversion into Value-Added Chemicals. *BMC Chem. Eng.* **2019**, *1*, 9−28.
(35) Niu, Z.; Peng, Q.; Zhuang, Z.; He, W.; Li, Y. Evidence of an Oxidative-Addition-Promoted Pd-Leaching Mechanism in the Suzuki Reaction by Using a Pd-Nanostructure Design. *Chem.—Eur. J.* **2012**, *18*, 9813−9817.
(36) Goodman, E. D.; Schwalbe, J. A.; Cargnello, M. Mechanistic Understanding and the Rational Design of Sinter-Resistant Heterogeneous Catalysts. *ACS Catal.* **2017**, *7*, 7156−7173.
(37) Peterson, P. F.; Božin, E. S.; Proffen, T.; Billinge, S. J. L. Improved Measures of Quality for the Atomic Pair Distribution Function. *J. Appl. Crystallogr.* **2003**, *36*, 53−64.
(38) Guinier, A. X-Ray Diffraction. *Crystals, Imperfect Crystals, and Amorphous Bodies*; Dover Publications Inc.: San Francisco, 1963; pp 27−81.
(39) Juhás, P.; Davis, T.; Farrow, C. L.; Billinge, S. J. L. PDFgetX3: A Rapid and Highly Automatable Program for Processing Powder Diffraction Data into Total Scattering Pair Distribution Functions. *J. Appl. Crystallogr.* **2013**, *46*, 560−566.
(40) Banerjee, S. Improved Modeling of Nanocrystals from Atomic Pair Distribution Function Data. Ph.D. Thesis, Columbia University: New York, NY, 2020.
(41) Cowley, J. M.; GjØnnes, J. K. Diffuse Scattering in Electron Diffraction. In *International Tables for Crystallography Volume B: Reciprocal Space*; Shmueli, U., Ed.; Kluwer Academic Publishers: Dordrecht, 1991; pp 443−448.
(42) de Sá, A. D. T.; Abrao Oiko, V. T.; di Domenicantonio, G.; Rodrigues, V. New Experimental Setup for Metallic Clusters Production Based on Hollow Cylindrical Magnetron Sputtering. *J. Vac. Sci. Technol., B: Nanotechnol. Microelectron.: Mater., Process., Meas., Phenom.* **2014**, *32*, 061804−061812.
(43) Bromann, K.; Brune, H.; Félix, C.; Harbich, W.; Monot, R.; Buttet, J.; Kern, K. Hard and Soft Landing of Mass Selected Ag Clusters on Pt(111). *Surf. Sci.* **1997**, *377*−*379*, 1051−1055.
(44) Popok, V. N.; Barke, I.; Campbell, E. E. B.; Meiwes-Broer, K.-H. Cluster-surface interaction: From soft landing to implantation. *Surf. Sci. Rep.* **2011**, *66*, 347−377.
(45) Huttel, Y.; Martínez, L.; Mayoral, A.; Fernández, I. Gas-Phase Synthesis of Nanoparticles: Present Status and Perspectives. *MRS Commun.* **2018**, *8*, 947−954.
(46) Mahr, C.; Müller-Caspary, K.; Ritz, R.; Simson, M.; Grieb, T.; Schowalter, M.; Krause, F. F.; Lackmann, A.; Soltau, H.; Wittstock, A.; Rosenauer, A. Influence of Distortions of Recorded Diffraction Patterns on Strain Analysis by Nano-Beam Electron Diffraction. *Ultramicroscopy* **2019**, *196*, 74−82.
(47) Niekiel, F.; Kraschewski, S. M.; Müller, J.; Butz, B.; Spiecker, E. Local Temperature Measurement in TEM by Parallel Beam Electron Diffraction. *Ultramicroscopy* **2017**, *176*, 161−169.
(48) Lábár, J. L. Electron Diffraction Based Analysis of Phase Fractions and Texture in Nanocrystalline Thin Films, Part II: Implementation. *Microsc. Microanal.* **2009**, *15*, 20−29.
(49) Williams, D. B.; Carter, C. B. *Transmission Electron Microscopy: A Textbook for Materials Science*; Springer Science: Boston, 2009; pp 3−22.
(50) Gilbert, B. Finite Size Effects on the Real-Space Pair Distribution Function of Nanoparticles. *J. Appl. Crystallogr.* **2008**, *41*, 554−562.
(51) Farrow, C. L.; Billinge, S. J. L. Relationship between the atomic pair distribution function and small-angle scattering: implications for modeling of nanoparticles. *Acta Crystallogr., Sect. A: Found. Crystallogr.* **2009**, *65*, 232−239.
(52) Debye, P. Zerstreuung von Röntgenstrahlen. *Ann. Phys.* **1915**, *351*, 809−823.
(53) Cervellino, A.; Frison, R.; Bertolotti, F.; Guagliardi, A. DEBUSSY 2.0: The New Release of a Debye User System for Nanocrystalline and/or Disordered Materials. *J. Appl. Crystallogr.* **2015**, *48*, 2026−2032.
(54) Juhás, P.; Farrow, C. L.; Yang, X.; Knox, K. R.; Billinge, S. J. L. Complex Modeling: A Strategy and Software Program for Combining Multiple Information Sources to Solve Ill Posed Structure and Nanostructure Inverse Problems. *Acta Crystallogr., Sect. A: Found. Adv.* **2015**, *71*, 562−568.
(55) Hall, B. D.; Monot, R. Calculating the Debye-Scherrer Diffraction Pattern for Large Clusters. *Comput. Phys.* **1991**, *5*, 414−417.
(56) Usher, T.-M.; Olds, D.; Liu, J.; Page, K. A Numerical Method for Deriving Shape Functions of Nanoparticles for Pair Distribution Function Refinements. *Acta Crystallogr., Sect. A: Found. Adv.* **2018**, *74*, 322−331.
(57) Yang, C. Y. Crystallography of Decahedral and Icosahedral Particles. *J. Cryst. Growth* **1979**, *47*, 274−282.
(58) Song, M.; Zhou, G.; Lu, N.; Lee, J.; Nakouzi, E.; Wang, H.; Li, D. Oriented Attachment Induces Fivefold Twins by Forming and Decomposing High-Energy Grain Boundaries. *Science* **2020**, *367*, 40−45.
(59) Zanchet, D.; Hall, B. D.; Ugarte, D. Structure Population in Thiol-Passivated Gold Nanoparticles. *J. Phys. Chem. B* **2000**, *104*, 11013−11018.
(60) Gamez-Mendoza, L.; Terban, M. W.; Billinge, S. J. L.; Martinez-Inesta, M. Modelling and Validation of Particle Size Distributions of Supported Nanoparticles Using the Pair Distribution Function Technique. *J. Appl. Crystallogr.* **2017**, *50*, 741−748.

https://doi.org/10.1021/acsanm.1c02978
ACS Appl. Nano Mater. 2021, 4, 12541−12551

(61) Song, K.; Kim, Y.-J.; Kim, Y.-I.; Kim, J.-G. Application of Theta-Scan Precession Electron Diffraction to Structure Analysis of Hydroxyapatite Nanopowder. *J. Electron Microsc.* **2012**, *61*, 9−15.
(62) Eggeman, A. S.; White, T. A.; Midgley, P. A. Is Precession Electron Diffraction Kinematical? Part II. *Ultramicroscopy* **2010**, *110*, 771−777.
(63) Cockayne, D. J. H. The Study of Nanovolumes of Amorphous Materials Using Electron Scattering. *Annu. Rev. Mater. Res.* **2007**, *37*, 159−187.
(64) Marks, L. D.; Peng, L. Nanoparticle Shape, Thermodynamics and Kinetics. *J. Phys.: Condens. Matter* **2016**, *28*, 053001−053049.
(65) Howie, A.; Marks, L. D. Elastic Strains and the Energy Balance for Multiply Twinned Particles. *Philos. Mag. A* **1984**, *49*, 95−109.
(66) Johnson, C. L.; Snoeck, E.; Ezcurdia, M.; Rodríguez-González, B.; Pastoriza-Santos, I.; Liz-Marzán, L. M.; Hÿtch, M. J. Effects of Elastic Anisotropy on Strain Distributions in Decahedral Gold Nanoparticles. *Nat. Mater.* **2008**, *7*, 120−124.
(67) Atta, S.; Beetz, M.; Fabris, L. Understanding the role of $AgNO_3$ concentration and seed morphology in the achievement of tunable shape control in gold nanostars. *Nanoscale* **2019**, *11*, 2946−2958.

https://doi.org/10.1021/acsanm.1c02978
ACS Appl. Nano Mater. 2021, 4, 12541−12551

Apêndice H

Material Suplementar ao Apêndice G

A seguir está anexado o material suplementar ao artigo que descreve a metodologia a metodologia de PDF. O arquivo pode ser encontrado em: https://pubs.acs.org/doi/10.1021/acsanm.1c02978.

Supporting Information

Quantitative Structural Analysis of AuAg Nanoparticles Using a Pair Distribution Function Based on Precession Electron Diffraction: Implications for Catalysis.

Leonardo M. Corrêa[1], Murilo Moreira[1], Varlei Rodrigues[1] and Daniel Ugarte[1,*]

1 Instituto de Física "Gleb Wataghin", Universidade Estadual de Campinas-UNICAMP, CEP 13083-859, Campinas - SP, Brazil

*Corresponding Author: dmugarte@ifi.unicamp.br

Content:

d) Additional figures describing TEM experiments, Precession electron diffraction, Data processing, Kinematical simulation of nanoparticle electron diffraction patterns, Pair distribution function interpretation details.

PED: optical alignment

Most manuals of precession diffraction operation are written for scanning PED (SPED) techniques, optimizing pre-sample beam rocking movement (scan) and post-sample cancelling the beam movement (de-scan), such that they occur in the same position at the sample plane.[1-3] The high-quality intensity measurement using an axial CCD camera has revealed that significant misalignment of the de-scan setup may remain undetected. To overcome such limitations, we have divided the PED alignment procedure in two steps: i) perform a standard SPED alignment using a sample which generating nice diffraction patterns and high contrast images (*e.g.*, semiconductor InP nanowires);[4] ii) insert the NP sample and perform fine tuning of de-scan on the ED ring pattern directly observed on the CCD camera. This procedure has allowed us to obtain high quality pattern under PED conditions which are very well suited for quantitative ePDF analysis.

Correction of 2-fold astigmatism of the ED ring pattern

The bi-dimensional powder ED pattern should be formed by concentric circular rings; but, if 2-fold astigmatism is present, diffraction rings are actually elliptical, and the azimuthal integration generates broader peaks with reduced intensity. Recently, several effective post-measurement distortion correction procedures have successfully demonstrated to correct remaining astigmatism aberration by mapping the ring intensity maximum position as a function of azimuthal angle θ (see Figure 1d). [5-7] It is necessary to take into account that when a peak is mounted on an intense and quickly varying background, the peak maximum, may not correspond to the actual peak center. Instead, our approach consists in extracting radial intensity profiles for azimuthal angles and, subsequently, we determine the peak center by fitting a Gaussian (or Lorentzian) profile added to a polynomial function (Figure S1a). The plot of the peak position as a function of azimuthal angle

shows a clear sinusoidal function, characteristic of 2-fold astigmatism (eq S1, see Figure S1c). Finally, the distortion is corrected and the ring (radius ρ_0) is azimuthally integrated (Figure S1b and c) to increase signal-noise-ratio, particularly displaying a high counting in the high Q region.

$$d(\theta) = A\,sin(2\theta + \delta) + \rho_0 \qquad (S1)$$

A troublesome point of correcting 2-fold astigmatism is the precise determination of the diffraction pattern center. But we noted that when the center is shifted from the ideal position, the distribution of points do not follow properly the expected sinusoidal function for 2-fold astigmatism. Then, we have used the quality of sinusoidal fit for different center positions as a quantifiable parameter to implement an automatic centering procedure with single pixel sensitivity.

Detailed description of Background subtraction

The calculation of a reliable PDF function is strongly dependent on the background subtraction procedure. We must emphasize that the major factor influencing residue reduction in this work has been the correct inclusion of a-C substrate scattering during background subtraction. Due to high relevance of this step, we have dedicated more attention to optimize it than frequently considered in conventional diffraction studies.

Electrons interact more strongly with matter, then the incoherent background represents a much higher portion of the measured total intensity than in XRD.[8] ED incoherent scattering is usually modelled by smooth functions (usually polynomial functions on Q^{-1}, that show high value at low Q and approach 0 as Q grows); this kind of simple functions are preferred in order to guarantee operation for non-specialized users.[9] In many cases, such approach may be a good approximation to the total background; none withstanding, high caution is require for analyzing few-nm-wide particles whose

diameter is similar to the support film thickness, because it neglects any contributions from the TEM sample substrate. The usual TEM support is amorphous carbon film with thickness in the range of 50 - 100 Å, that generates a substantial signal background to ED patterns or HRTEM images from NP samples.[10,11]

The PDF calculation requires a background subtraction which yield a diffraction pattern ($I(Q)$, coherent scattering) that is highly constrained and the processing is far more complex than needed for a conventional diffraction study.[12] The first constrain regards the normalization of $I(Q)$, the total scattered signal from a material is fully described by $f^2(Q)$ and it is independent of atomic arrangement. The arrangement of the atoms generate preferential scattering directions (diffraction peaks), but conserves the total scattered intensity.[10,13,14] The second constrain implies that the asymptotic behavior of $I(Q)$ should be incoherent at high Q. Small deviations from perfect crystalline arrangement inhibit the occurrence of constructive interference, the high Q scattered intensity must be close to $f^2(Q)$.[15] Both conditions can be summarized by the following equations (eq S2 and S3 respectively):[9,15]

$$\int_{Q_{min}}^{Q_{max}} I\,(Q)dQ = \int_{Q_{min}}^{Q_{max}} \langle f^2(Q)\rangle\, dQ \qquad (S2)$$

$$\int_{Q_{tail}} [I(Q) - \langle f^2(Q)\rangle]\, dQ = 0 \qquad (S3)$$

Usually, the blank support or matrix scattering is firstly measured; secondly this contribution is subtracted tentatively. Finally, the constrained background subtraction to derive $I(Q)$ is applied. A trial-and-error interaction is performed until a qualitative acceptance criterion is set by the user. In contrast, we have decided to incorporate the last two steps in a single optimization by in a single iterative optimization procedure, yielding the coherent scattering intensity fulfilling constrains of

diffraction physics. The background model considers simultaneously both a-C experimental profile and an smooth function decreasing with Q (eq S4.):

$$B(Q) = a_{a-C}B_{a-C}(Q) + b_1 + \frac{b_2}{Q} + \frac{b_3}{Q^2} + \frac{b_4}{Q^3} \quad \text{(S4)}$$

where b_i $(i = 1, 2, 3, 4)$ are the parameters of the incoherent scattering model, $B_{a-C}(Q)$ an experimental a-C diffraction pattern (see Figure S3) and a_{a-C} its scale factor. The experimental a-C scattering pattern was acquired under identical electron optical conditions that the sample diffraction pattern; subsequently, it was centered and azimuthally integrated.

Regions without diffraction peaks are used as input data points for the procedure. It is important to emphasize that a conventional fit is not sufficient to respect the physical constrains of the scattering function (eq S2 and eq S3), as it may generate a function where $I_{tail}(Q) = 0$. To ensure proper behavior in the tail regions, we subtracted the tail data points of $I_{raw}(Q)$ by a constant, such that after fit $I_{tail}^{fit}(Q) > 0$; this parameter was also consider in the multi-parameter optimization and multi-step background subtraction procedure. After subtracting the total background, the remaining intensity ($I_{fit}(Q) = I_{raw}(Q) - B(Q)$) was rescaled such that the final diffraction pattern results in $I(Q) = c\, I_{fit}(Q) + d$ (where c and d are parameter optimized to ensure the scattering constrains).

To test if background optimization is successful, we observe carefully some quality tests. For example, the a-C scale factor should be close but < 1 because, for data acquired with identical electron optical conditions, some electrons will be scattered by the metal NPs, and carbon contribution should diminish. Another verification considers if $I_{fit}(Q)$ is not excessively rescaled by parameters c and d. A high rescaling may modify the proportion between low and high Q diffraction peaks, yielding an incorrect PDF (these constant yielded results 1.07 and -2.2 for c and d respectively, final curve shown in Figure S3). Furthermore, the scale factor a_{a-C} can tell the degree of influence of the a-C contribution in the total background (0.5 for fits shown in Figure S3). If this value is close to 0, the a-C substrate has little influence on the background and can be ignored. Another possible consistency

test is the comparison of the ratio of total integrated intensities ($\int_{Q_{min}}^{Q_{max}} I_{raw}(Q)dQ / \int_{Q_{min}}^{Q_{max}} B_{a-C}(Q)dQ$) which should be around unity considering the small mass of nanoparticles dispersed on the continuous carbon substrate (this ratio is ≈ 0.9 in Figure S3a). The final background profile after this procedure shows a strong Q dependence (see dashed line Figure S3a). This is a clear demonstration that a wrong inclusion or even neglecting the substrate contribution may cause serious deviations of the diffraction pattern and the ePDF assessment (Figure S3c), where clear differences in peak height and positions can be observed.

Pseudo-code for the Background Subtraction Procedure

Begin ()

```
\\ Input
Q          \\  measured scattering vector
Iraw       \\  measured NP diffraction
Bac        \\  measured a-C diffraction
Fsquare    \\ mean square value of the scattering power

\\ define points for background fit between n intervals, must include the final values of Q (tail)
Qfit = Q [n]
Ifit = Iraw [n]
Bfit = Bac [n]

\\ define total background function Back
ac                  \\ Bac scale factor
b1, b2, b3, b4      \\ incoherent scattering function parameters
x                   \\ scattering vector values where background will be calculated
DEF Back (Input (x, Bac); Variable (ac, b1, b2, b3, b4)):
        RETURN ac*Bac + b1 + (b2/x) + (b3/(x*x)) + (b4/(x*x*x))

\\  define function (Resub) that will calculate background subtraction residue
a > 0          \\ value that will be subtracted from Ifit and Bfit in the final values of Qfit (tail)
w, w_tail      \\ weights for each n chosen intervals
DEF Resub (Input (Qfit,  Ifit, Bfit, a, w, w_tail); Variable (ac, b1, b2, b3, b4)):
```

```
        Ifit_out = Ifit [Qout]          \\ Outside the final Q interval (tail)
        Ifit_tail = Ifit [Qtail] - a    \\ Inside the final Q interval (tail)
        \\ minimum square difference (MinSquare) for each interval of points
        res_out = MinSquare (Ifit_out – Back (Qout, Bfit, ac, b1, b2, b3, b4))
        res_tail = MinSquare (Ifit_tail – Back (Qtail, Bfit, ac, b1, b2, b3, b4))
        RETURN  w*res_w +  w_tail*res_tail


\\ define function (Backsub) that will be minimize for background subtraction
c   \\ multiplicative factor to ensure scattering physics constrains
d    \\ additive factor to ensure scattering physics constrains
DEF Backsub (Input (Q, Iraw, Fsquare, Bac, Qfit,  Ifit, Bfit, w, w_tail); Variable (a, c, d, ac, b1, b2, b3, b4)):
        ac, b1, b2, b3, b4 = Minimization (Resub)       \\ background parameters determination
        Isub = Iraw – Back (Q, Bac, ac, b1, b2, b3, b4)   \\ initial subtracted intensity
        Isca = c*Isub + d                                 \\ rescaled intensity
        norm = Integral (Fsquare) / Integral (Isca)       \\ normalization to ensures that Condition 1 is respected
        \\ Chose Condition 2 for minimization
        \\ In tail region
        I_tail = norm*Isca[Qtail]
        F_tail = Fsquare [Qtail]
        RETURN Integral((I_tail – F_tail)* (I_tail – F_tail))

\\ Parameters are obtained
c, d, ac, b1, b2, b3, b4  =  Minimization (Backsub)
\\ Final Background
B = Back (Q, Bac, ac, b1, b2, b3, b4)
\\ Initial Subtracted Intensity
Isub = Iraw – B
\\Scaled Subtracted Intensity
Isca = c*Isub + d
\\ Final Intensity
norm = Integral (Fsquare) / Integral (Isca)
I = norm*(c*Isca + d)
End()
```

References

(1) Liao, Y.; Marks, L. D. On the Alignment of Precession Electron Diffraction. *Ultramicroscopy* **2012**, 117, 1-6.

(2) Barnard, J. S.; Johnstone, D. N.; Midgley P. A. High-Resolution Scanning Precession Electron Diffraction: Alignment and Spatial Resolution. *Ultramicroscopy* **2017**, 174, 79-88.

(3) Rauch, E. F.; Portillo, J.; Nicolopoulos, S.; Bultreys, D.; Rouvimov, S.; Moeck, P. Automated Nanocrystal Orientation and Phase Mapping in the Transmission Electron Microscope on the Basis of Precession Electron Diffraction, *Z. Kristallogr. Cryst. Mater.* **2010**, 225, 103-109.

(4) Ugarte, D.; Tizei, L. H. G.; Cotta, M. A.; Ducati, C.; Midgley, P. A.; Eggeman, A. S. Analysis of Structural Distortion in Eshelby Twisted InP Nanowires by Scanning Precession Electron Diffraction. *Nano Res.* **2019**, 12 (4), 939–946.

(5) Mahr, C.; Müller-Caspary, K.; Ritz, R.; Simson, M.; Grieb, T.; Schowalter, M.; Krause, F. F.; Lackmann, A.; Soltau, H.; Wittstock, A.; Rosenauer, A. Influence of Distortions of Recorded Diffraction Patterns on Strain Analysis by Nano-Beam Electron Diffraction. *Ultramicroscopy* **2019**, 196, 74–82.

(6) Niekiel, F.; Kraschewski, S. M.; Müller, J.; Butz, B.; Spiecker, E. Local Temperature Measurement in TEM by Parallel Beam Electron Diffraction. *Ultramicroscopy* **2017**, 176, 161-169.

(7) Lábár, J. L. Electron Diffraction Based Analysis of Phase Fractions and Texture in Nanocrystalline Thin Films, Part II: Implementation. *Microsc. Microanal.* **2009**, 15 (1), 20-29.

(8) Cowley, J. M; GjØnnes, J. K. Diffuse Scattering in Electron Diffraction. In International Tables for Crystallography Volume B: Reciprocal Space; Shmueli, U., Eds.; Kluwer Academic Publishers: Dordrecht, 1991; pp 443-448.

(9) Tran, D. T.; Svensson, G.; Tai, C.-W. SUePDF: A Program to Obtain Quantitative Pair Distribution Functions from Electron Diffraction Data. *J. Appl. Crystallogr.* **2017**, *50* (1), 304-312.

(10) Williams, D. B.; Carter, C. B. *Transmission Electron Microscopy: A Textbook for Materials Science*; Springer Science: Boston, 2009; pp 3-17

(11) Ayache, J.; Beaunier, L.; Boumendil, J.; Ehret, G.; Laub, D. Sample Preparation Handbook for Transmission Electron Microscopy: Techniques; Springer: New York, 2010; pp 92-106.

(12) Peterson, P. F.; Božin, E. S.; Proffen, T.; Billinge, S. J. L. Improved Measures of Quality for the Atomic Pair Distribution Function. *J. Appl. Crystallogr.* **2003**, *36* (1), 53-64.

(13) James, R. W. The Optical Principles of The Diffraction of X-Rays; G. Bell and Sons: London, 1948; pp 93-101.

(14) Guinier, A. X-Ray Diffraction: In Crystals, Imperfect Crystals, and Amorphous Bodies; Dover Publications Inc.: San Francisco, 1963; pp 27-81.

(15) Billinge, S. J. L. Local Structure from Total Scattering and Atomic Pair Distribution Function (PDF) Analysis. In Powder Diffraction: Theory and Practice; Dinnebier, R. E., Billinge, S. J. L., Eds.; Royal Society of Chemistry: Cambridge, 2008; pp 464-493.

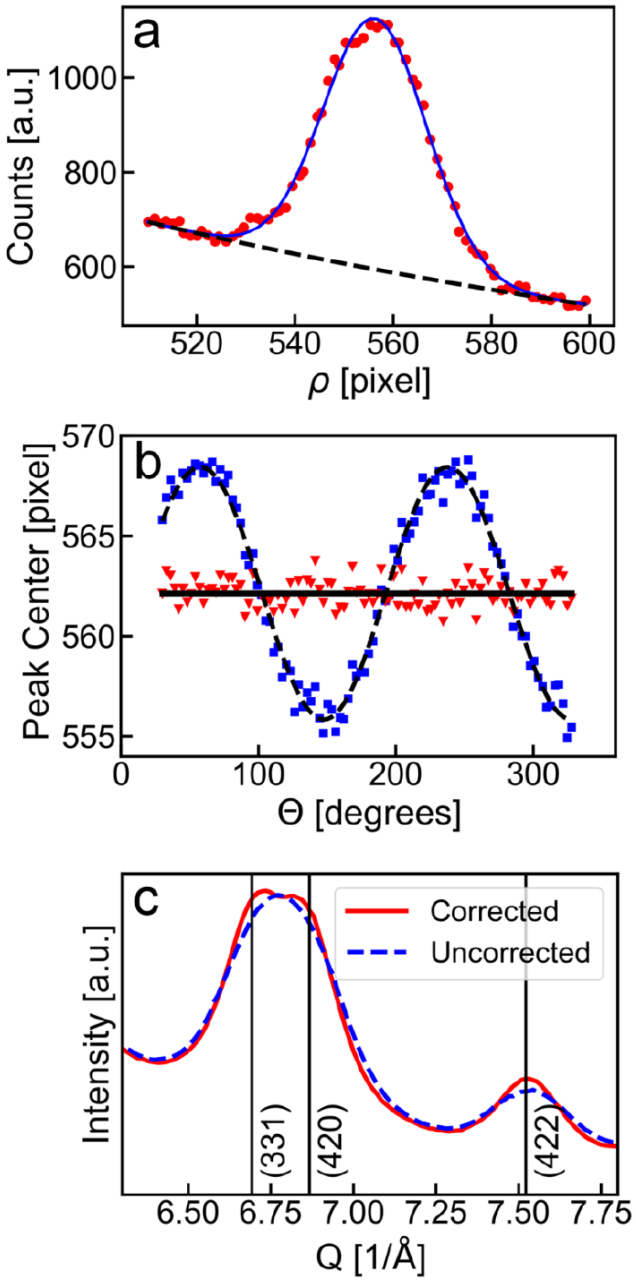

Figure S1. a) Fitting of a diffraction peak obtained from radial profile extracted from an ED ring pattern. b) Plot of the peak position as a function of azimuthal angle showing a clear sinusoidal function characteristic of 2-fold astigmatism (raw data-squares, eq 10 fit-dashed line, corrected value-triangles). c) Effect of the 2-fold astigmatism correction on the azimuthally integrated diffraction peaks.

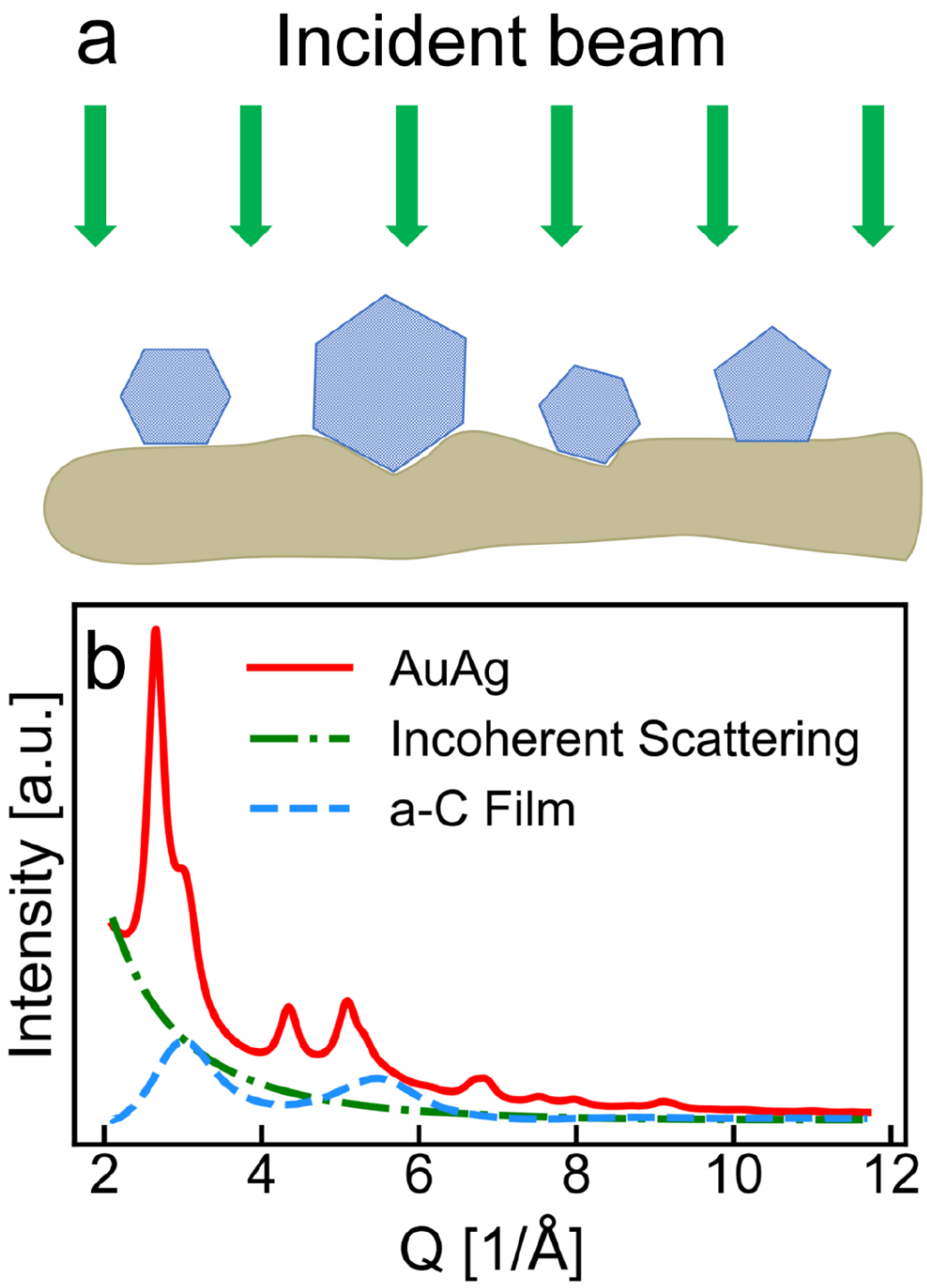

Figure S2. a) Illustration of a common parallel electron beam diffraction experiment on a NP sample. The thickness of the amorphous carbon substrate is usually comparable with the particle diameter. b) Measured powder ED pattern ($I_{raw}(Q)$) and the two components composing the background (a-C film scattering curve and, incoherent scattering described by a slow varying function).

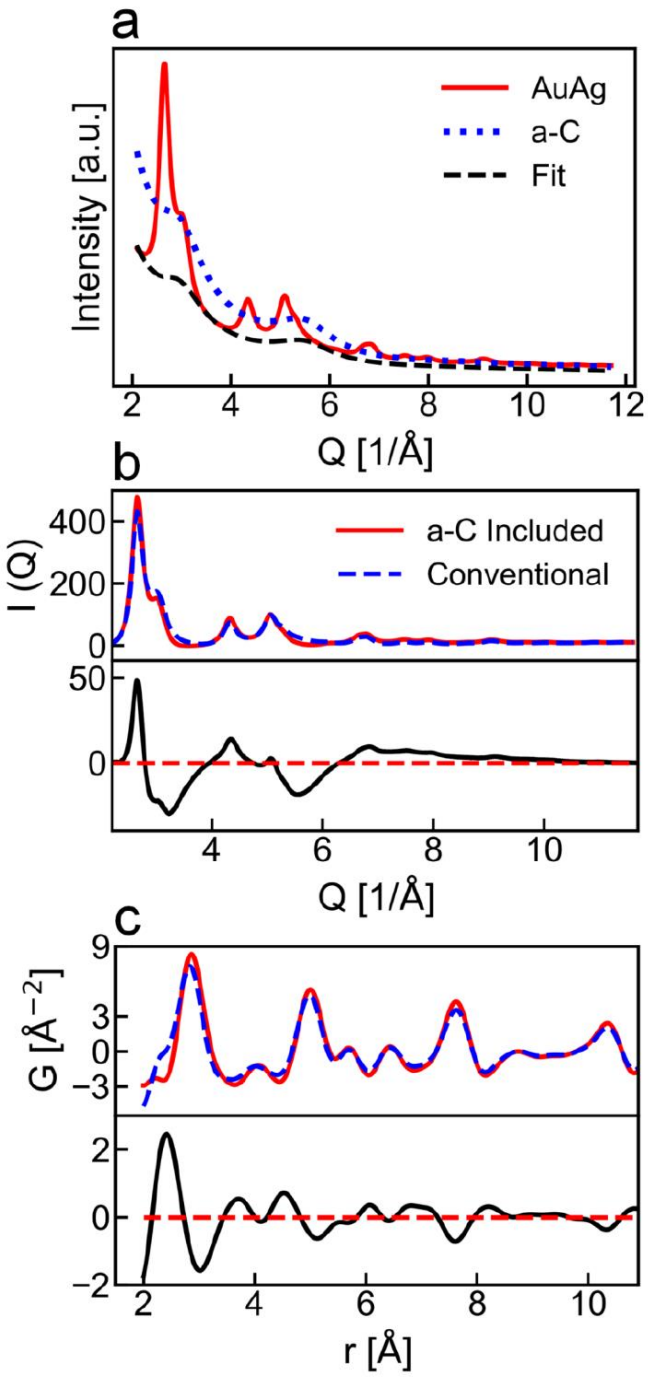

Figure S3. a) Comparison of the experimental measurement of the ED pattern from the NPs and the a-C film scattering curve; note the final form of the background calculated with our procedure (and actually subtracted from raw data) shows a strong variation with the scattering vector Q. b) and c) show the large differences that are observed when the sample substrate is neglected for coherent scattering $I(Q)$ and the PDF respectively (the bottom plot using black lines represent the difference curve).

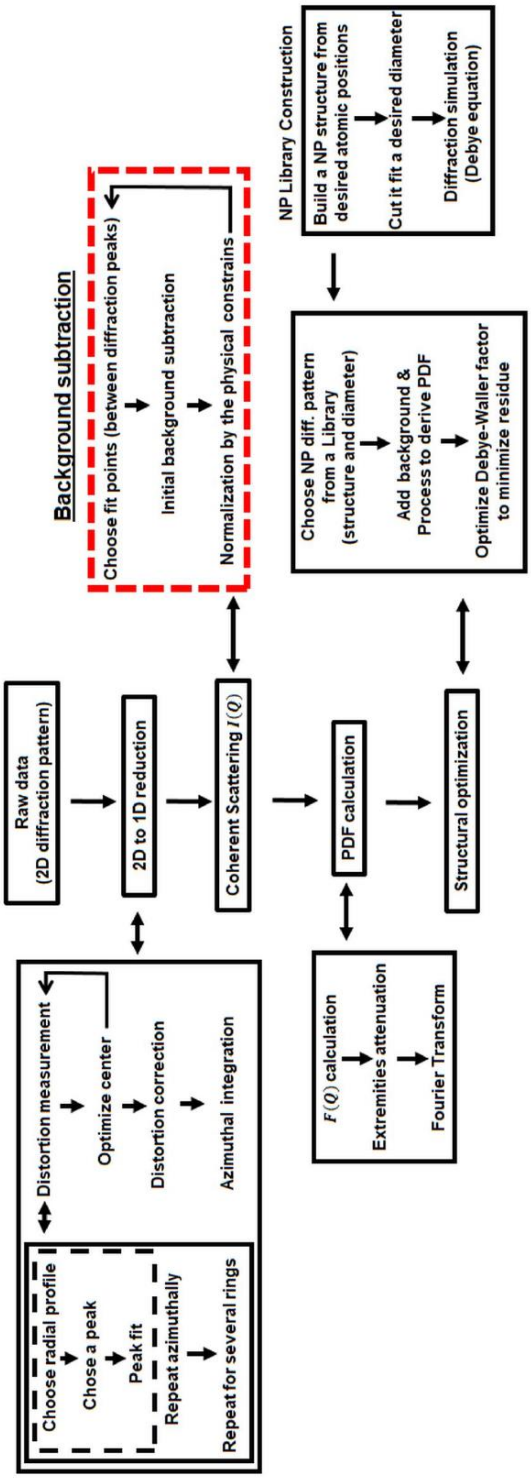

Figure S4. Schematic workflow algorithm of all processing steps from raw electron diffraction data to structural refinement through ePDF.

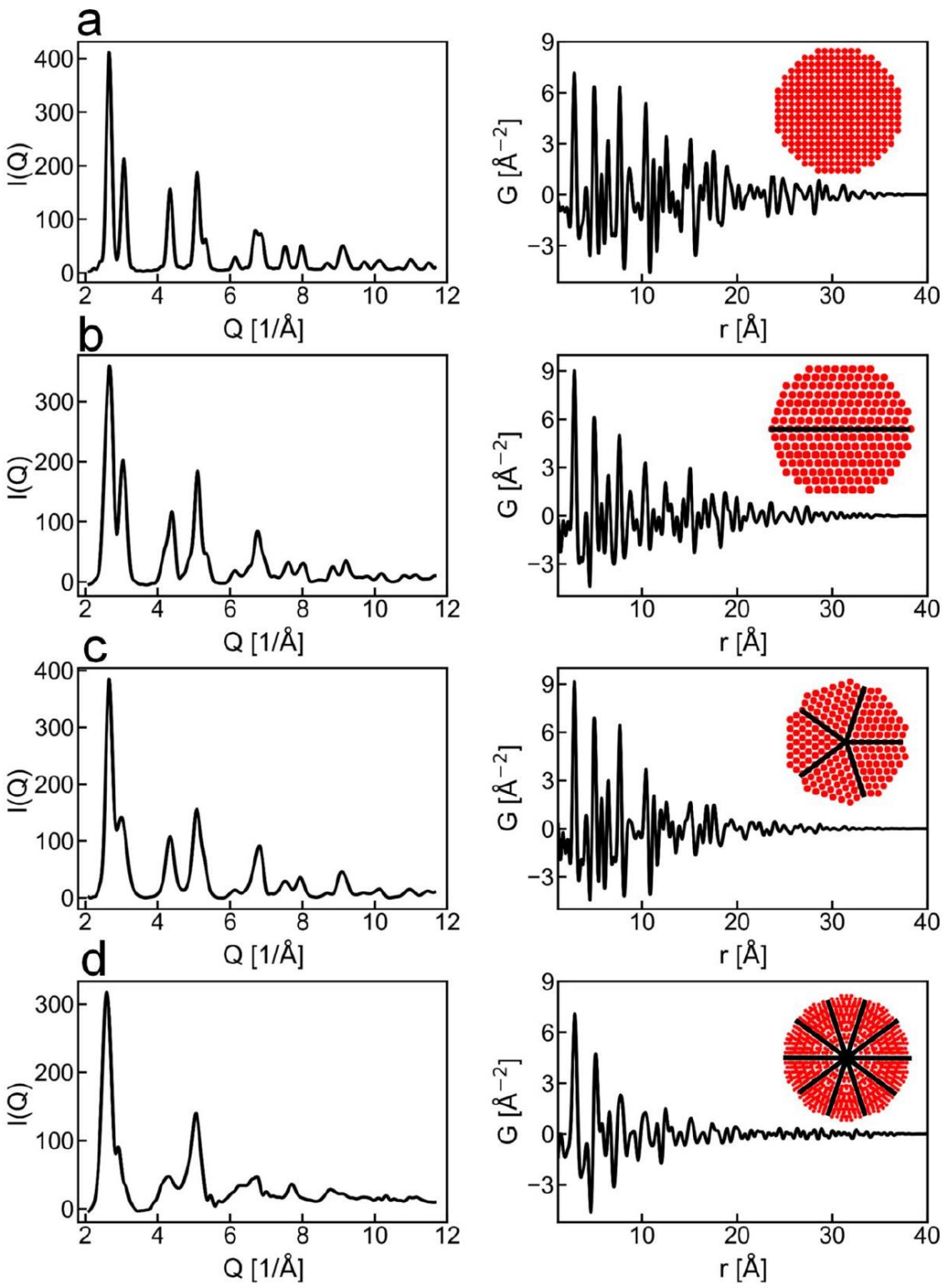

Figure S5. Electron powder diffraction patterns obtained from the DSE formulation and the derived PDF curves for spherical particles 40Å in diameter. a) fcc (monocrystalline), b) single twinned, c) Dh and d) Ih.

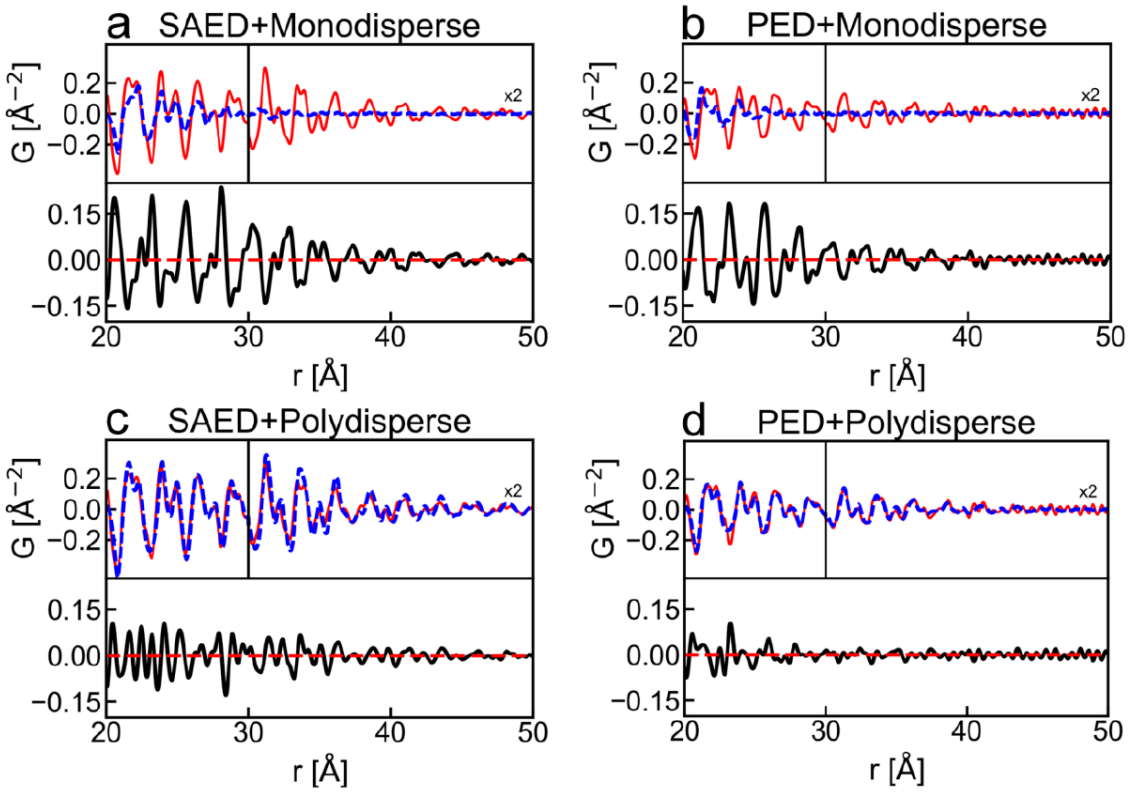

Figure S6. Comparison of the effect of including a size polydisperse model for the analysis of SAED- and PED-based PDF, in the region corresponding to high r values (20 – 50 Å). Experiments are shown with continuous lines, while optimized simulation are represented with dashed lines. Simulations are performed with monodisperse model (a-b) and size distribution model (c-d). The (a) and (c) are relative to SAED measurements, (b) and (d) to PED. The region between 30 - 50 Å is multiplied by a factor 2 to highlight the differences in the region. Below each comparison is plotted the respective difference curves.

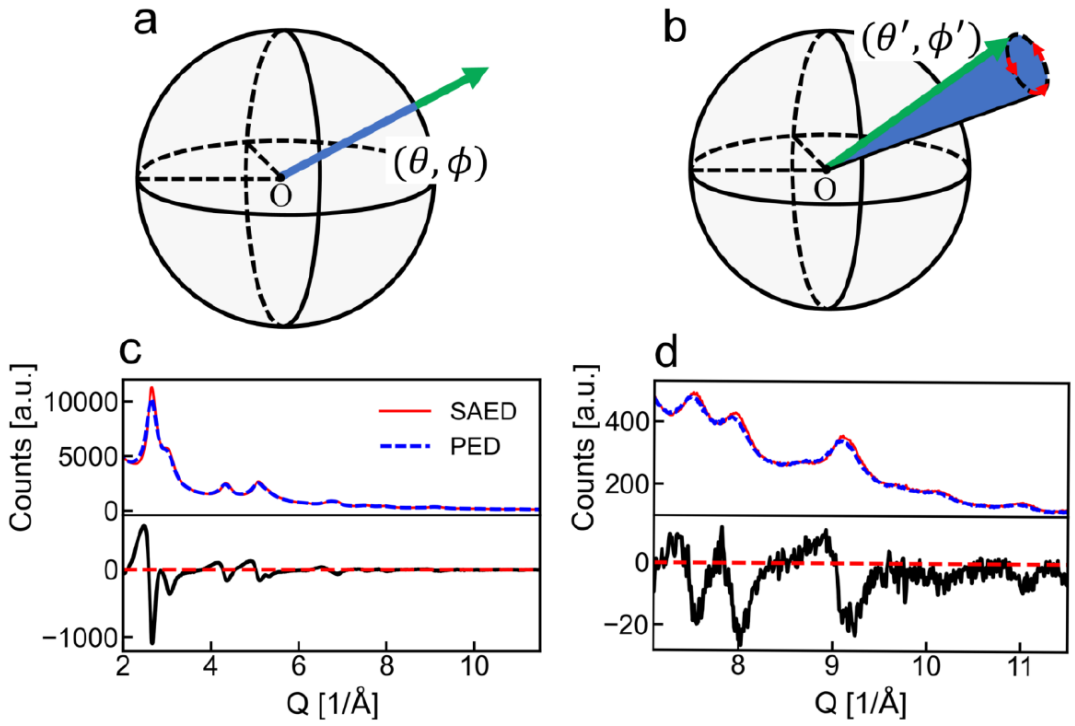

Figure S7. a) Generic orientation of NP with incident electron beam direction determined by the angles (θ, ϕ) in the spherical coordinate system; a powder diffraction considers the average for many NPs oriented randomly along all directions of the whole solid angle of 4π. b) In PED powder diffraction the beam also scan the orientation (θ', ϕ') in the hollow cone generated by the precessing beam around the direction. c) Comparison between the standard powder electron diffraction (SAED) and powder PED in the whole Q range. d) Comparison the powder electron diffraction in SAED and PED for the high Q range. This experimental data shows the diffraction peaks with small changes in intensity and they are slightly shifted without significant modifications of width.

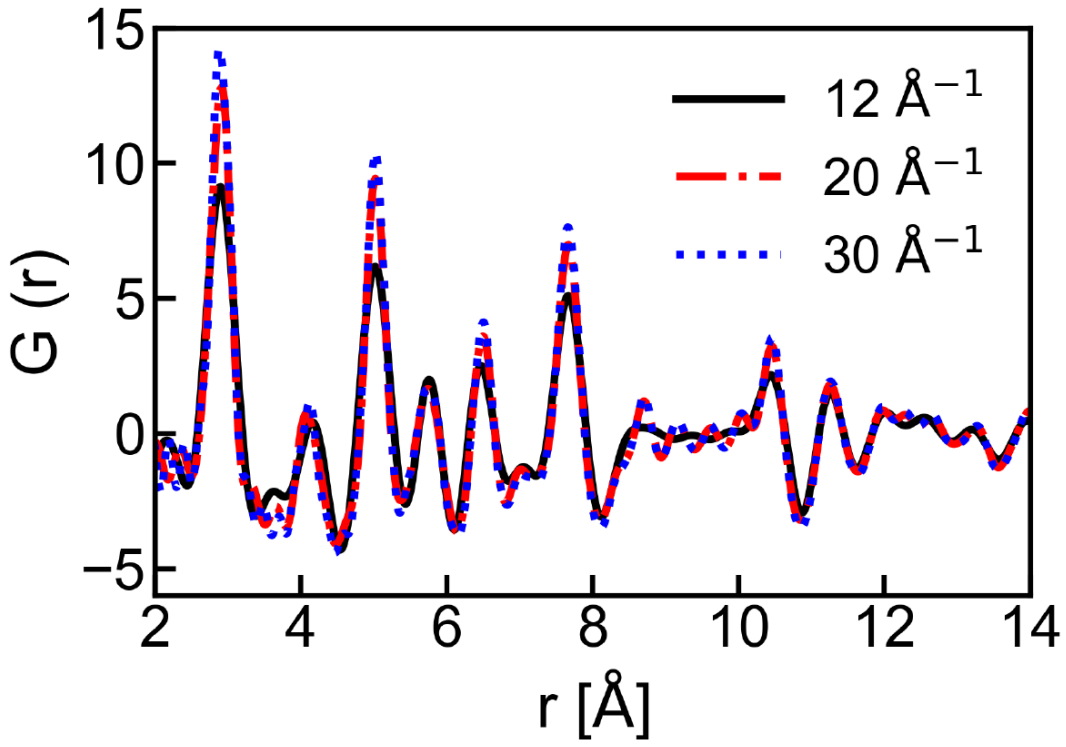

Figure S8. Simulated real space PDF functions for several Q_{max} values (spherical Dh NP, 30 Å in diameter). Comparison of the derived PDF for 3 different Q_{max}. For our experimental parameters $Q_{max} = 12$ Å^{-1}, a loss of resolution (broader peaks) arises; however, the overall tendency of the curve is maintained and most of the peaks are still identifiable. Little difference is observable in the derived PDF curve when Q_{max} in increased from 20 Å^{-1} to 30 Å^{-1}; due to thermal vibration, no coherent intensity peak is observable after 25 Å^{-1} (assuming Au bulk room temperature Debye-Waller).